

**Constraints on Early-Type Galaxy Structure from
Spectroscopically Selected Gravitational Lenses**

by

Adam Stallard Bolton

B.A. Physics
San Francisco State University, 1999

Submitted to the Department of Physics
in partial fulfillment of the requirements for the degree of

Doctor of Philosophy

at the

MASSACHUSETTS INSTITUTE OF TECHNOLOGY

June 2005

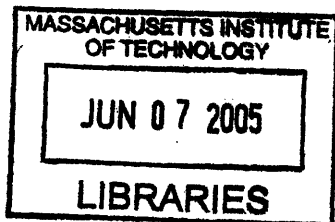
© Adam Stallard Bolton, MMV. All rights reserved.

The author hereby grants to MIT permission to reproduce and distribute publicly
paper and electronic copies of this thesis document in whole or in part.

Author
Department of Physics
5 May 2005

Certified by
Scott Burles
Assistant Professor of Physics
Thesis Supervisor

Accepted by
Thomas Greytak
Professor of Physics
Associate Department Head for Education



ARCHIVES



Constraints on Early-Type Galaxy Structure from Spectroscopically Selected Gravitational Lenses

by
Adam Stallard Bolton

Submitted to the Department of Physics
on 5 May 2005, in partial fulfillment of the
requirements for the degree of
Doctor of Philosophy

Abstract

This thesis describes all aspects of a unique spectroscopic survey for strong galaxy-galaxy gravitational lenses: motivation, candidate selection, ground-based spectroscopic follow-up, *Hubble Space Telescope* imaging, data analysis, and results on the radial density profile of the lens galaxies. The lens candidates are selected from within the spectroscopic database of the Sloan Digital Sky Survey (SDSS) based on the appearance of two significantly different redshifts along the same line of sight, and lenses are confirmed within the candidate sample by follow-up imaging and spectroscopy. The sample of ≈ 20 early-type lenses presented in this thesis represents the largest single strong-lens galaxy sample discovered and published to date. These lenses probe the mass of the lens galaxies on scales roughly equal to one-half effective radius. We find a dynamical normalization between isothermal lens-model velocity dispersions and aperture-corrected SDSS stellar velocity dispersions of $f = \sigma_{\text{lens}}/\sigma_{\text{stars}} = 0.95 \pm 0.03$. By combining lens-model Einstein radii and de Vaucouleurs effective radii with stellar velocity dispersions through the Jeans equation, we find that the logarithmic slope γ of the density profile in our lens galaxies ($\rho \propto r^{-\gamma}$) is on average slightly steeper than isothermal ($\gamma = 2$) with a modest intrinsic scatter. Parameterizing the intrinsic distribution in γ as Gaussian, we find a maximum-likelihood mean of $\bar{\gamma} = 2.22^{+0.07}_{-0.07}$ and standard deviation of $\sigma_{\gamma} = 0.13^{+0.07}_{-0.05}$ (68% confidence, for isotropic velocity-dispersion models). Our results rule out a single universal logarithmic density slope at $> 99.995\%$ confidence. The success of this spectroscopic lens survey suggests that similar projects should be considered as an explicit science goal of future redshift surveys.

Thesis Supervisor: Scott Burles
Title: Assistant Professor of Physics

Acknowledgments

First and foremost I must thank my wife Marsha for her love and support over the last five years. This thesis closes the chapter of our lives that began with all our possessions packed in a truck and California in the rear-view mirror.

Next I want to thank my advisor Scott Burles for paying me to work on such an interesting project, and for being so generous with his time and energy. Meeting Scott was definitely the best thing to happen for me at MIT.

I also wish to thank Paul Schechter for his care and interest, and for whipping me into shape as an astronomer.

Thanks to Ed Bertschinger for his expert advice throughout the thesis process.

Thanks to Hsiao-Wen Chen and Rob Simcoe for being such great mentors and observing partners on multiple trips to Las Campanas.

A wide-field thank-you to everyone who made Magellan, SDSS, Gemini, and *HST* happen. Special thanks to Alan Dressler et al. for IMACS, to the Durham Astronomical Instrumentation Group for the IFUs, and to David Schlegel for the SDSS spectro reductions.

Thanks to Léon Koopmans, Tommaso Treu, and Lexi Moustakas for making the SLACS survey happen.

Special IDLnik thanks to all who have made IDLUTILS and IDLSPEC2D what they are.

Thanks to my family for believing that my finishing the Ph.D. was a foregone conclusion, because I certainly never believed that.

Last but not least, thanks to all my graduate student comrades at MIT, past and present.

This thesis is based on:

- Data from the Sloan Digital Sky Survey (SDSS) archive. Funding for the creation and distribution of the SDSS Archive has been provided by the Alfred P. Sloan Foundation, the Participating Institutions, the National Aeronautics and Space Administration, the National Science Foundation, the U.S. Department of Energy, the Japanese Monbukagakusho, and the Max Planck Society. The SDSS Web site is <http://www.sdss.org/>. The SDSS is managed by the Astrophysical Research Consortium (ARC) for the Participating Institutions. The Participating Institutions are The University of Chicago, Fermilab, the Institute for Advanced Study, the Japan Participation Group, The Johns Hopkins University, Los Alamos National Laboratory, the Max-Planck-Institute for Astronomy (MPIA), the Max-Planck-Institute for Astrophysics (MPA), New Mexico State University, University of Pittsburgh, Princeton University, the United States Naval Observatory, and the University of Washington.
- Observations obtained with the 6.5-m Walter Baade and Landon Clay telescopes of the Magellan Consortium at Las Campanas Observatory.
- Observations obtained under program GN-2004A-Q-5 at the Gemini Observatory, which is operated by the Association of Universities for Research in Astronomy, Inc., under a cooperative agreement with the NSF on behalf of the Gemini partnership: the National Science Foundation (United States), the Particle Physics and Astronomy Research Council (United Kingdom), the National Research Council (Canada), CONICYT (Chile), the Australian Research Council (Australia), CNPq (Brazil) and CONICET (Argentina).
- Observations made with the NASA/ESA Hubble Space Telescope, obtained at the Space Telescope Science Institute (STScI), which is operated by the Association of Universities for Research in Astronomy, Inc., under NASA contract NAS 5-26555. These observations are associated with program #10174. Support for program #10174 was provided by NASA through a grant from STScI.

Contents

List of Figures	10
List of Tables	11
1 Introduction and Motivation	13
1.1 Conventions Observed in the Thesis	15
1.2 Structure and Content of the Thesis	16
2 Spectroscopic Discovery of Intermediate-Redshift Star-Forming Galaxies Behind Foreground Luminous Red Galaxies	19
2.1 Introduction	19
2.2 Search Sample	21
2.3 Candidate Selection	22
2.3.1 Initial Emission Feature Detection	22
2.3.2 Multi-Line Background Systems: Detection, Fitting, and Rejection	23
2.4 Noise Modeling	25
2.5 Candidate Systems	26
2.5.1 Catalog	26
2.5.2 Lenses or Not?	28
2.5.3 Lens Candidates in Context	32
2.6 Conclusions	33
3 Integral-Field Spectroscopic Observations of Strong Gravitational Lens Candidates	35
3.1 Introduction	35
3.2 Instrumentation	35
3.3 Calibration and Reduction of IFU Data	37
3.3.1 Bias Subtraction and Data Formatting	38
3.3.2 Flat-field Modeling and Tracing	38
3.3.3 Scattered-Light Subtraction	41
3.3.4 Wavelength Calibration	41
3.3.5 Extraction	42
3.3.6 Sky Subtraction	45
3.3.7 Rectification and Combination	46
3.4 Gravitational-Lens Modeling with IFU Data	47
3.4.1 Narrowband Image Reconstruction	47
3.4.2 Lens Modeling	47
3.4.3 The Lenses	51

3.5	Initial Conclusions	69
3.6	Constraining the Density Profile with Aperture Masses and Velocity Dispersions	70
3.6.1	Mass, Light, and Velocity	70
3.6.2	Mass Normalization from Lensing	73
3.6.3	Observational Power-Law Index Constraints	76
4	The Sloan Lens ACS Survey: Hubble Space Telescope Imaging of Spectroscopic Gravitational-Lens Candidates	81
4.1	Introduction	81
4.2	The Survey	82
4.2.1	Candidate Selection	82
4.2.2	ACS Image Processing	82
4.3	Observed Systems and New Lenses	85
4.4	Statistics	86
4.4.1	Magnification Bias	86
4.4.2	Are Our Lenses Special?	89
4.5	Discussion and Conclusions	90
5	Mass Profile Constraints from HST Lensing and Photometry	93
5.1	Why HST?	93
5.2	Aperture Masses and Velocity Dispersions, Revisited	93
5.2.1	The Stellar Distribution	93
5.2.2	Lensing Aperture-Mass Constraints	94
5.2.3	Power-Law Constraints from SDSS Velocity Dispersions	95
5.3	Mass Profile Constraints from Lensing Alone	101
5.4	Conclusions and Future Work	104
A	SDSS Lens-Candidate Parameters	107
B	SDSS Lens-Candidate Spectra	111
C	SDSS Lens-Candidate Imaging	125
D	IFU Lens-Candidate Data Catalog	137
E	HST-ACS Lens-Candidate Imaging	145

List of Figures

2-1	LRG sample median line-flux noise spectrum.	22
2-2	Median rest-frame spectrum of background galaxies	28
2-3	MagIC images and difference images of SDSSJ0037 and SDSSJ0216	29
2-4	Comparison of lens-candidate LRGs to full LRG sample	32
2-5	Comparison of candidate LRG lens galaxies to known early-type lenses	34
3-1	IFU focal-plane to detector-plane mapping	37
3-2	Factorization of IFU spectroscopic flat-field image	39
3-3	IMACS-IFU model flatfield cross section	39
3-4	IMACS- $f/4$ He-Ne-Ar IFU image subsection	42
3-5	IFU pixel-to-fiber association diagram	44
3-6	Optimal extraction of IMACS- $f/2$ IFU data	45
3-7	IFU night-sky background subtraction	46
3-8	Narrowband spectral component modeling	50
3-9	SDSSJ0037 IFU spectra	52
3-10	SDSSJ0037 IFU imaging	53
3-11	SDSSJ2238 IFU spectra	54
3-12	SDSSJ2238 IFU imaging	55
3-13	SDSSJ2321 IFU spectra	56
3-14	SDSSJ2321 IFU imaging	57
3-15	SDSSJ2302 IFU spectra	58
3-16	SDSSJ2302 IFU imaging	59
3-17	SDSSJ0044 iso-wavelength emission-line image sequence	60
3-18	SDSSJ0044 IFU spectra	61
3-19	SDSSJ0044 IFU imaging	62
3-20	SDSSJ0737 IFU spectra	63
3-21	SDSSJ0737 IFU imaging	64
3-22	SDSSJ1402 IFU spectra	65
3-23	SDSSJ1402 IFU imaging	66
3-24	SDSSJ1630 IFU spectra	67
3-25	SDSSJ1630 IFU imaging	68
3-26	Lensing velocity dispersion versus stellar velocity dispersion	71
3-27	Power-law mass model constraints from IFU lensing and SDSS velocity-dispersion measurements	78
4-1	<i>HST</i> and IFU image comparison for SDSSJ1402+6321	87
4-2	Kolmogorov-Smirnov tests of lens-galaxy observables	91

5-1	Effective radius measurements: SDSS versus <i>HST</i>	95
5-2	Power-law index versus stellar velocity dispersion	97
5-3	Mass power-law index versus light power-law index	99
5-4	Projected likelihood of power-law index distribution parameters	100
5-5	<i>HST</i> -ACS gravitational-lens modeling of SDSSJ0912+0029	103
B-1	SDSS LRG spectra with background-galaxy emission	112
B-1	(continued)	113
B-1	(continued)	114
B-1	(continued)	115
B-1	(continued)	116
B-1	(continued)	117
B-1	(continued)	118
B-1	(continued)	119
B-1	(continued)	120
B-1	(continued)	121
B-2	More SDSS lens-candidate spectra	122
B-2	(continued)	123
C-1	SDSS color images of lenses and lens candidates	127
C-1	(continued)	129
C-1	(continued)	131
C-1	(continued)	133
C-1	(continued)	135
D-1	SDSSJ0216–0813 IFU spectrum and narrowband imaging	139
D-2	SDSSJ0805+3037 IFU spectrum and narrowband imaging	139
D-3	SDSSJ0928+4400 IFU spectrum and narrowband imaging	140
D-4	SDSSJ0956+5100 IFU spectrum and narrowband imaging	140
D-5	SDSSJ1029+6115 IFU spectrum and narrowband imaging	140
D-6	IFU rotation-curve image sequence of SDSSJ1029+6115	141
D-7	SDSSJ1128+5835 IFU spectrum and narrowband imaging	141
D-8	SDSSJ1155+6237 IFU spectrum and narrowband imaging	141
D-9	SDSSJ1259+6134 IFU narrowband imaging	142
D-10	SDSSJ1409+6105 IFU spectrum and narrowband imaging	142
D-11	SDSSJ1416+5136 IFU spectrum and narrowband imaging	142
D-12	SDSSJ1521+5805 IFU spectrum and narrowband imaging	143
D-13	SDSSJ1547+5719 IFU spectrum and narrowband imaging	143
D-14	SDSSJ1550+5217 IFU spectrum	143
D-15	SDSSJ1702+3320 IFU spectrum and narrowband imaging	144
D-16	SDSSJ2251–0926 IFU spectrum and narrowband imaging	144
E-1	<i>HST</i> -ACS lens images	147
E-1	(continued)	149
E-1	(continued)	151
E-1	(continued)	153
E-2	<i>HST</i> -ACS possible-lens images	155
E-3	<i>HST</i> -ACS non-lens/non-detection images	157

List of Tables

1.1	Approximate overall properties of lens sample	15
1.2	Common optical emission lines in air and vacuum	17
3.1	IFU spectrograph configurations used	37
3.2	Power-law index distribution parameters from IFU lens sample	79
5.1	Comparison of IFU and <i>HST</i> Einstein radii	96
5.2	Partition of <i>HST</i> -ACS lens sample into velocity-dispersion bins	97
5.3	Maximum-likelihood power-law indices under varying assumptions	98
5.4	Power-law index distribution parameters from <i>HST</i> lens sample	100
A.1	SDSS lens-candidate photometric and spectroscopic parameters	108
A.1	(continued)	109
A.1	(continued)	110
D.1	Other IFU observations	138

Chapter 1

Introduction and Motivation

In the currently favored cosmological scenario, the matter content of the universe is dominated by a cold and dark component of unknown particle species whose only significant interaction with the smaller baryonic matter fraction occurs through the gravitational force. This “cold dark matter” (CDM) picture is most strongly required by observations on the largest scales. The CDM scenario holds that galaxies form within the potential wells of extended dark-matter halos which began their collapse while baryonic matter was still ionized. In disk galaxies, this view is supported by direct evidence for dark matter from the observation of rotational velocities that remain approximately constant out to radii at which the stellar galactic component makes a diminishing contribution.

Unlike disk galaxies, early-type galaxies (E and S0 in the Hubble sequence) are pressure-supported stellar systems which do not generally have directly observable circular-velocity profiles, and as such their density profiles are more difficult to determine. The density structure of early-type galaxies is nevertheless of great interest for numerous reasons. First, their structure constitutes a physical record of their formation and evolution processes. Hierarchical CDM galaxy-formation theories hold that early-type galaxies are built through the merging of late-types (Kauffmann, White, and Guiderdoni 1993; Baugh, Cole, and Frenk 1996), which should have predictable consequences for the structure of the merger products. The most stringent test of these theories will require precise observational measurements of early-type mass profiles. Second, early-type galaxies exhibit great regularity in their photometric and kinematic properties, as described by the well-known “fundamental plane” (FP) relation between velocity dispersion, effective radius, and surface brightness (Djorgovski and Davis 1987; Dressler et al. 1987). The tilt of the FP relative to the simple expectation based on the virial theorem can be understood in terms of a dependence of the total mass-to-light ratio upon mass. However, additional constraints on the mass structure of early-type galaxies are needed in order to distinguish between the various effects of differing stellar populations, differing density profiles (or “structural nonhomology”), and differing dark-matter fractions in giving rise to the FP. Finally, detailed measurement of the structure of high-surface-brightness early-type galaxies will enable quantitative tests of the CDM theory on scales where baryonic and radiative processes have significant effects upon the structure of the host dark-matter halo (e.g. Blumenthal et al. 1986), altering it significantly relative to the form expected to result from pure dark-matter collapse (e.g. Navarro et al. 1996; Moore et al. 1998).

On larger scales, conclusive evidence for the dominance of dark matter in early-type galaxy halos comes from observation of X-ray halo temperatures (e.g. Loewenstein and

White 1999) and from statistical signals of weak galaxy-galaxy lensing (e.g. Hoekstra et al. 2004). On smaller scales, observational results are less conclusive. Stellar-dynamical measurements of local elliptical galaxies (e.g. Gerhard et al. 2001), the statistics of early-type gravitational-lens galaxies (e.g. Rusin et al. 2003b), and combined lensing and dynamical measurements of the few systems amenable to such study (Koopmans and Treu 2002, 2003; Treu and Koopmans 2002, 2003, 2004, hereafter KT) all argue for the presence of a significant amount of dark matter even on the scale of the half-light radius, leading to an approximately constant circular velocity with increasing radius as in disk galaxies. A conflicting picture is put forward by Romanowsky et al. (2003), who analyzed the dynamics of satellite planetary nebulae of several nearby elliptical galaxies and claim to find little evidence for dark matter. Furthermore, Kochanek (2003) has pointed out an apparent conflict between the expected CDM galaxy halo structure and several well-measured gravitational-lens time delays under the assumption of $H_0 \approx 70 \text{ km s}^{-1} \text{ Mpc}^{-1}$. Due to this persistent uncertainty about the mass structure and diversity of early-type galaxies (see also Kochanek 2004b), it is important to exploit any and all available techniques to constrain their properties.

Strong gravitational lensing provides the most direct probe of mass in early-type galaxies: a measurement of the mass enclosed within the Einstein radius. Unfortunately, strong lenses are a rare phenomenon, and new lenses are generally discovered in small numbers through great luck or great effort. The number of currently known galaxy-scale strong gravitational lenses is on the order of one hundred¹, but many of these lenses are not suitable for studying the properties of the lensing galaxy. Some of these lens galaxies are either too faint or too overwhelmed by the light of lensed quasars to be studied in detail. Other systems lack confirmed redshifts for the lens and/or source, seriously limiting their utility as astrophysical tools. Finally, the sample of known lenses as a whole has an extremely heterogeneous discovery history that makes their selection difficult to characterize.

This thesis presents the results of a survey for strong galaxy-galaxy gravitational lenses, which has produced a sample of more than 20 previously unknown early-type strong galaxy-galaxy gravitational lenses. These lenses have all been selected spectroscopically from within the Sloan Digital Sky Survey (SDSS) database, and are confirmed by spatially resolved follow-up observations with ground-based integral-field spectroscopy and/or *Hubble Space Telescope* (*HST*) imaging. The details of the selection and confirmation of these lenses will be presented in subsequent chapters; the approximate overall properties of the lens sample are given for reference here in Table 1.1.

The new lenses we present here are of great interest for numerous reasons. First, both lens and source redshifts are known from the outset for all of our gravitational lenses. Second, our lenses are all amenable to accurate photometric and stellar-dynamical measurements. Thus the Einstein radii of lenses can be combined with a measurement of the line-of-sight velocity dispersion profile and the shape of the luminosity density of the lens galaxy to derive powerful constraints on the radial density profile of the lens galaxy through the Jeans equation. Only a handful of previously known strong lenses are amenable to this type of analysis (see KT). In addition, the extended lensed source galaxy images in our systems offer more constraints on the lensing galaxy mass profile than can generally be obtained from quasar lenses. Finally, the technique by which we select our lenses is relatively easily characterized, and thus statistical tests of the lens sample should be tractable.

The power of extended lensed images to constrain the gravitational potential of the lensing mass was originally considered in the context of radio lenses (e.g. Kochanek et al. 1989;

¹see the CASTLES gravitational-lens database at <http://cfa-www.harvard.edu/castles/>

Quantity		Median \pm Standard Deviation
z_{lens}	\approx	0.21 ± 0.08
z_{source}	\approx	0.53 ± 0.13
R_e	\approx	$2''.1 \pm 0''.9$
	\approx	7.5 ± 3.1 kpc
r -magnitude	\approx	17.4 ± 0.7
σ_v	\approx	276 ± 47 km s $^{-1}$
θ_E	\approx	$1''.25 \pm 0''.28$
M_E	\approx	$2.6 \pm 1.3 \times 10^{11} M_{\odot}$

Table 1.1: Approximate overall properties of the sample of new lenses presented in this thesis. Given are the approximate median and standard-deviation values for various quantities. R_e is the de Vaucouleurs-model effective radius, σ_v is the luminosity-weighted stellar velocity dispersion as measured by SDSS, θ_E is the isothermal lens-model Einstein radius, and M_E is the lensing mass enclosed by the Einstein radius. With the exception of z_{source} and θ_E , all values given apply to the lens (foreground) galaxy rather than the source (background) galaxy.

Langston et al. 1990; Kochanek and Narayan 1992), which often show spatially resolved lobes at high resolution, and has also been used to model strong-lensing galaxy clusters with resolved lensed images of background galaxies (e.g. Tyson et al. 1998). Strong galaxy-galaxy lenses such as we present have not previously been known in large enough numbers to constitute a significant class of object, but the promise and formalism of strong galaxy-galaxy lensing has also been developed in the literature. Miralda-Escude and Lehar (1992) have estimated that there should be approximately 100 optical Einstein rings per square degree down to a source-magnitude limit of $B = 26$. Kochanek et al. (2001) develop a method for using the extended infrared Einstein ring images of lensed-quasar host galaxies to break degeneracies in lens models based only on the quasar-image astrometry. Warren and Dye (2003) describe a method for modeling lenses with extended source images that is non-linear in the lens parameters but linear in the source surface-brightness distribution, which is applied by Dye and Warren (2005) to the lens system 0047–2808 (Warren et al. 1996), perhaps the most well-known strong galaxy-galaxy lens (also spectroscopically discovered).

1.1 Conventions Observed in the Thesis

Here we describe a number of terminological and notational conventions that will be used throughout the thesis, including several “reserved symbols” that will refer always to the same quantities.

Throughout this thesis, we will be concerned with both two-dimensional (projected onto the plane of the sky) and three-dimensional galactocentric² radial coordinates. We will consistently refer to the 2D radial coordinate as R and to the 3D radial coordinate as r . Note however that depending upon the context, R may be considered in angular units or in physical units. We will also work extensively with both 2D and 3D power-law density

²not Galactocentric

models, of the form

$$\Sigma(R) \propto R^{-\eta} , \quad \rho(r) \propto r^{-\gamma} . \quad (1.1)$$

We will consistently refer to the 2D power-law exponent as η and to the 3D exponent as γ . These exponents will also be called “power-law indices” and “logarithmic slopes” somewhat interchangeably. Note the adopted sign convention, such that positive η and γ give densities that decrease with increasing radius, with larger η and γ giving more steeply falling (or centrally concentrated) densities. Also note that, as may be verified trivially, a model with a particular γ value has $\eta = \gamma - 1$ in projection, though expressing the relationship between the 2D and 3D normalization factors requires either numerical integration or evaluation of the hypergeometric function ${}_2F_1$.

The astronomical systems that are the subject of this thesis show two redshifts along the same line of sight: we denote the foreground redshift by z_{FG} and the background redshift by z_{BG} . We will often avoid the common notation z_{L} and z_{S} (for “lens” and “source”), since not all systems necessarily exhibit strong lensing. We refer to the luminosity-weighted velocity dispersion of the foreground galaxy as measured by SDSS within a seeing-blurred circular aperture of $3''$ diameter as σ_v . The effective (or half-light) radii of de Vaucouleurs models fitted to galaxy imaging data are denoted by R_e , and are quoted at the intermediate axis (the geometric mean of the major and minor axes) for elliptical models. The minor-to-major axis ratio of elliptical mass and light models is denoted by q , with $0 < q \leq 1$ by definition.

The spectroscopic data in this thesis have all been reduced with respect to a vacuum wavelength baseline and a heliostationary (a.k.a. heliocentric) reference frame. The official motive behind this choice is that redshifts apply in the strict sense to wavelengths in vacuum and not in air, although the nonlinearity of the air-to-vacuum correction is essentially negligible at our spectroscopic resolutions. (The errors incurred by redshifting air rather than vacuum wavelengths would be $\leq 3 \text{ km s}^{-1}$, or 5% of an SDSS pixel.) The practical motive is that the reduced SDSS spectra that are the starting point for this research are expressed in vacuum wavelengths. In the text we will refer to the atomic transitions of astronomical emission lines by their common air-wavelength names; spectroscopic plot annotations use vacuum values for consistency with the data. Table 1.2 gives the air and vacuum wavelengths of atomic transitions commonly seen as optical emission lines, related through the air-to-vacuum transformation of Morton (1991).

Throughout this thesis, we assume a cosmological model with $\Omega_M = 0.3$, $\Omega_\Lambda = 0.7$, and $H_0 = 70h_{70} \text{ km s}^{-1} \text{ Mpc}^{-1}$ (with $h_{70} = 1$).

1.2 Structure and Content of the Thesis

This thesis is organized into chapters corresponding to distinct stages of a survey for new gravitational lenses. The content is the original work of the author (ASB), with much advice from the supervisor (SB). Chapter 2 describes the method used for the systematic spectroscopic selection of strong gravitational lens candidates, and was published in similar form as Bolton et al. (2004). This project was originally suggested by SB as a survey for lensed Lyman- α emitting galaxies within the SDSS luminous red galaxy spectroscopic database; a pilot project was presented by Burles et al. (2000). The idea to re-orient the survey toward more abundant, lower-redshift multi-emission-line lens candidates was conceived by ASB, and all novel methods presented in Chapter 2 were conceived and implemented by ASB.

Chapter 3 presents the results of an observational campaign to confirm and model

Line Name	Air Wavelength (Å)	Vacuum Wavelength (Å)
[O II] 3727	3725.94, 3727.24	3727.00, 3728.30
H δ	4101.734	4102.892
H γ	4340.464	4341.684
H β	4861.325	4862.683
[O III] 4959	4958.911	4960.295
[O III] 5007	5006.843	5008.239
[N II] 6548	6548.05	6549.86
H α	6562.801	6564.614
[N II] 6583	6583.45	6585.27
[S II] 6716	6716.44	6718.29
[S II] 6730	6730.82	6732.68

Table 1.2: Common optical emission lines in air and vacuum

strong lenses from the candidate sample using high-resolution integral-field units (IFUs) on the Gemini and Magellan telescopes. The successful proposals to obtain this data were written and submitted by ASB. The observations were planned and the targets selected by ASB, in consultation with SB. Most Magellan IFU data were obtained directly by ASB during classical observing runs; GMOS IFU data was obtained through queue-scheduled observations following phase II specification by ASB. The dedicated IDL-based IFU data-reduction software described in Chapter 3 was written almost entirely by ASB, with some code contributions from SB. Much of the IFU software calls upon pre-existing lower-level routines included in the IDLUTILS and IDLSPEC2D software distributions³. The b-spline strategy for fitting the night-sky spectrum to the non-rebinned spectral data is implemented in the SDSS spectroscopic pipeline, and the flatfielding and extraction strategy implemented for the IFU data was suggested by SB. The IFU narrowband imaging and gravitational-lens modeling techniques presented in Chapter 3 were all conceived and implemented by ASB. The idea to consider a spherical de Vaucouleurs model embedded in a power law potential was suggested within the context of collaboration with Leon V. E. Koopmans, Tommaso Treu, Leonidas A. Moustakas, and SB; a similar calculation carried out by LVEK was included in Bolton et al. (2005). The implementation and exposition of this method in Chapter 3, and the inclusion of the mass-normalization considerations of § 3.6.2, are the work of ASB.

Chapter 4 presents observational results from a *Hubble Space Telescope* (*HST*) Snapshot Survey targeting spectroscopic gravitational lens candidates identified by ASB. This survey is a collaboration between ASB, SB, LVEK, TT, and LAM. Chapter 4 consists of the material of the first paper from the survey, currently in preparation. All material in this chapter is the work of ASB. The b-spline+multipole galaxy fitting technique used to achieve nearly Poisson-limited residual images was suggested by ASB, coded by SB, and applied to the *HST*-ACS data by ASB.

Chapter 5 makes use of singular isothermal ellipsoid Einstein-radius parameters measured from residual ACS lens images by LVEK. All other analysis in the chapter is by ASB, although as in Chapter 3 the de Vaucouleurs+power law calculation was suggested by collaborators.

³http://spectro.princeton.edu/idlspec2d_install.html

Chapter 2

Spectroscopic Discovery of Intermediate-Redshift Star-Forming Galaxies Behind Foreground Luminous Red Galaxies

In this chapter we describe our method for selecting spectroscopic gravitational lens candidates from within the Sloan Digital Sky Survey database, which produced an initial catalog of 49 lens candidates selected from a sample of 50996 luminous red galaxies and published in Bolton et al. (2004). We identify this sample of potentially lensed star-forming galaxies through the presence of background oxygen and hydrogen nebular emission lines in the spectra of massive foreground galaxies. This multi-line selection eliminates the ambiguity of single-line identification and provides a very promising sample of candidate galaxy-galaxy lens systems at low to intermediate redshift, with foreground redshifts ranging from 0.16 to 0.49 and background redshifts from 0.25 to 0.81. As well as describing the spectroscopic selection algorithm, we present a noise modeling technique that we use to control the incidence of false-positive emission line detections. We present ground-based imaging of two candidates that show evidence for strong gravitational lensing, and make an approximate calculation of the number of bona fide strong lenses expected within the candidate sample.

2.1 Introduction

In its strongest form, gravitational lensing produces unmistakably distorted, amplified, and multiple images of distant astronomical objects. It is therefore not surprising that the majority of known galaxy-scale gravitational lens systems have been discovered through imaging observations. However, a small number of lenses have been discovered spectroscopically, with the spectrum of a targeted galaxy showing evidence of emission from a background source and follow-up imaging revealing lensing morphology. The three most secure examples are the lensed quasars 2237+0305 (Huchra et al. 1985) and SDSS J0903+5028 (Johnston et al. 2003) and the lensed Lyman- α emitting galaxy 0047–2808 (Warren et al. 1996). Several authors have made predictions for the frequency of lensed quasar discoveries

in galaxy redshift surveys (Kochanek 1992; Mortlock and Webster 2000, 2001). Others, inspired by the discovery of 0047–2808, have undertaken spectroscopic searches for lensed Lyman- α -bright galaxies (Hewett et al. 2000; Willis 2000; Hall et al. 2000; Burles et al. 2000). The idea behind such searches is that a massive foreground galaxy should act as an effective gravitational lens of *any* object positioned sufficiently far behind it and at small enough impact parameter, and any emission features from such lensed objects should be detectable in the spectra of the foreground galaxy. Therefore a search for discrepant emission features in galaxy spectra can lead to a sample of gravitational lens systems that would not be discovered in broadband imaging searches due to faintness of source relative to lens. This “lenses-looking-for-sources” approach is complementary to lens searches such as the recently completed Cosmic Lens All-Sky Survey (CLASS; Myers et al. 2003; Browne et al. 2003) which proceed by targeting sources and looking for evidence of an intervening lens. In addition to the optical Einstein ring 0047–2808 mentioned above, Hewett et al. (2000) have published one more spectroscopic galaxy-lens candidate. In contrast to the spectroscopic discovery method, *Hubble Space Telescope* (*HST*) imaging has had some success in detecting strong galaxy-galaxy lenses, as described by Crampton et al. (2002), Ratnatunga et al. (1999), and Fassnacht et al. (2004); spectroscopic confirmation remains a challenge in most cases.

With its massive scale and quality of data, the spectroscopic component of the Sloan Digital Sky Survey (SDSS) provides an unprecedented opportunity for spectroscopic galaxy-galaxy gravitational lens discovery. Here we describe the first results of such a search within a sample of $\sim 51,000$ SDSS luminous red galaxy (LRG) spectra (Eisenstein et al. 2001 hereafter E01): a catalog of candidate lensed star-forming galaxies at intermediate redshift. The lens candidates we present were detected by the presence of not one but (at least) three emission lines in the LRG spectra identified as nebular emission from a single background redshift: [O II] 3727 and two out of the three of H β , [O III] 4959, and [O III] 5007. This implies a maximum redshift of $z \sim 0.8$ for any candidate lensed galaxies: at higher redshifts, [O III] emission moves redward of the SDSS spectroscopic wavelength coverage.

The lensing cross section of a particular foreground galaxy is lower for intermediate-redshift sources than high-redshift sources, and in this sense the lens survey we describe here is at a disadvantage relative to searches for lensed high-redshift Lyman- α emitters. However, the identities of the emission lines in the sample we present here are absolutely unambiguous. This cannot be said for spectroscopic Lyman- α lens candidates, which are typically detected as single discrepant emission lines and are difficult to distinguish from lower-redshift emission or (in the case of a huge survey such as the SDSS) non-astrophysical spectral artifacts. Our spectroscopic lens survey based on multiple-line detection has further advantages. First, the source redshift of any lensed galaxies will be known from the outset, along with the redshift of the lens galaxy. This is a tremendous advantage because knowledge of both redshifts in a strong lens system is needed to establish the cosmic geometry and fix the absolute mass scale of the lensing constraints, but obtaining both of these redshifts is typically a major observational hurdle. Second, for a given limiting line flux, star-forming galaxies at intermediate redshift are more numerous on the sky than Lyman- α emitters at high redshift (see Hippelein et al. 2003; Maier et al. 2003), and hence strong lensing events could be more frequent despite decreased lensing cross sections. Correspondingly, the non-lensed source population should be more amenable to study and characterization (Hogg et al. 1998; Drozdovsky et al. 2005 for example), facilitating lens statistical analysis. Finally, intermediate-redshift lensed galaxies will probe the mass distribution of the lens population in a systematically different manner than do high-redshift sources.

2.2 Search Sample

The Sloan Digital Sky Survey is a project to image roughly one-quarter of the sky in five optical bands and obtain spectroscopic follow-up observations of $\sim 10^6$ galaxies and 10^5 quasars. York et al. (2000) provide a technical summary of the survey, Gunn et al. (1998) describe the SDSS camera, Fukugita et al. (1996), Hogg et al. (2001), and Smith et al. (2002) discuss the photometric system and calibration, Pier et al. (2003) discuss SDSS astrometry, Blanton et al. (2003) present the spectroscopic plate tiling algorithm, and Stoughton et al. (2002) and Abazajian et al. (2003) describe the survey data products. Approximately 12% of the galaxy spectroscopic fibers are allocated to the LRG sample (E01), selected to consist of very luminous ($\gtrsim 3L_*$), and hence massive, early-type galaxies at higher redshift than the galaxies of the MAIN sample (Strauss et al. 2002). We expect these LRGs to be particularly effective gravitational lenses of any objects positioned suitably behind them, and we concentrate our initial spectroscopic lens survey on them. We also note that LRGs should have little dust, and therefore any lensed background galaxies should suffer minimal extinction. The initial sample for our study consists of 50996 spectra taken between 5 March 2000 and 27 May 2003 of SDSS imaging objects flagged as `GALAXY_RED` by the photometric pipeline (Lupton et al. 2001) for passing the LRG “cut 1” described by E01, reduced by the SDSS spectroscopic pipeline (J. Frieman et al., in preparation), and selected to have redshifts between 0.15 and 0.65 as determined by the `specBS` redshift-finding software (D. J. Schlegel et al., in preparation). The low-redshift cutoff is needed because less massive galaxies start to pass the photometric cuts below $z \lesssim 0.15$ and pollute the volume-limited LRG sample; see the discussion in E01 and the bimodal LRG sample redshift histogram in Stoughton et al. (2002 Fig. 14). Later in this thesis we will also present follow-up observations of lens candidates selected by similar techniques from within the SDSS MAIN sample.

In addition to being much more massive than the average galaxy, LRGs have another property that makes them well suited to a spectroscopic lens survey: their spectra are extremely regular and well-characterized (see Eisenstein et al. 2003). To determine the spectroscopic redshift of an SDSS target galaxy with observed specific flux f_λ and one-sigma sky+source noise spectrum σ_λ , the `specBS` program employs a small set of galaxy eigenspectra (four in the reductions for this study) derived from a rest-frame principal-component analysis (PCA) of 480 galaxy spectra taken on SDSS plate 306, MJD 51690. This eigenbasis is incrementally redshifted, and a model spectrum is generated from the best-fit linear combination to the observed spectrum at each trial redshift, with the final redshift assignment given by the trial value that yields the overall minimum χ^2 . Although redshift is the primary output of this procedure, a byproduct of `specBS` is the best-fit model spectrum itself, \tilde{f}_λ . In the case of LRGs, \tilde{f}_λ typically provides a very detailed and accurate fit to f_λ , with a reduced χ^2 of order unity over almost 4000 spectral pixels (roughly 1600 spectral resolution elements) attained with only 8 free parameters: a redshift, the four eigen-galaxy coefficients, and the three terms of a quadratic polynomial to fit out spectrophotometric errors and extinction effects, both of which exist at the few-percent level¹. This extremely regular spectral behavior allows us to form residual LRG spectra

$$f_\lambda^{(r)} \equiv f_\lambda - \tilde{f}_\lambda \quad (2.1)$$

¹The `specBS` reductions of public SDSS data are available from the website <http://spectro.princeton.edu>.

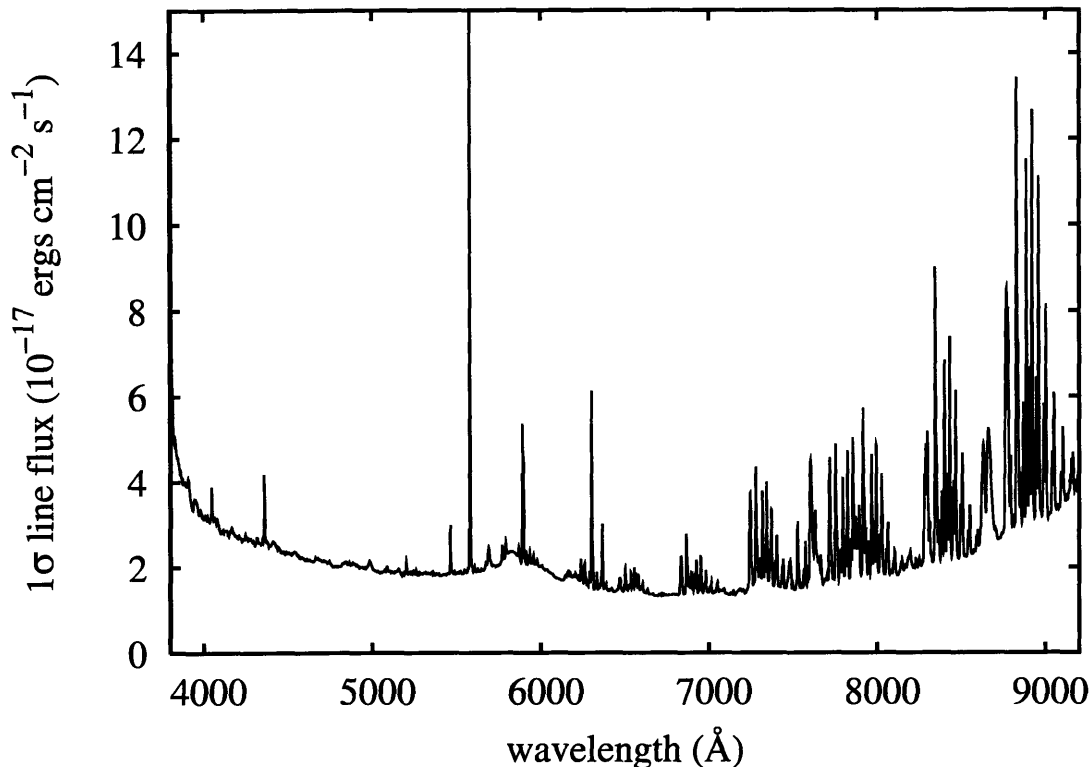


Figure 2-1: LRG sample median line-flux noise spectrum. Shown is the $1\text{-}\sigma$ noise on best-fit line fluxes for optimally matched Gaussian-shaped residual emission features with spectral width $\sigma = 1.2\text{-pixel}$ ($\simeq 83 \text{ km s}^{-1}$). Reported pixel flux variances have been rescaled as described in § 2.4 prior to the calculation of this noise spectrum.

that are in principle realizations of σ_λ . Nebular emission lines from galaxies along the line of sight other than the target LRG will not be modeled by `specBS` and should appear as significant features localized in wavelength within these residual spectra. Figure 2-1 shows the median $1\text{-}\sigma$ line flux sensitivity within our LRG residual spectrum sample as a function of wavelength. The (20th, 50th, 80th)-percentile LRG spectra themselves have a median signal-to-noise per pixel of (3.3, 5.1, 9.6) at the SDSS resolution of $\lambda/\Delta\lambda \approx 1800$.

2.3 Candidate Selection

This section describes our candidate selection routine in detail. Briefly stated, we select as initial candidates those spectra that show *both* blended [O II] 3727 at $S/N > 3$ and two out of the three lines H β , [O III] 4959, and [O III] 5007 at $S/N > 2.5$, then cull the candidate list by applying cuts based on more detailed fits to the presumed emission features, and finally remove any obviously spurious detections. This selection process yields a substantial number of promising systems without an excess of obvious false positives.

2.3.1 Initial Emission Feature Detection

The key element in the first step of our lens candidate selection (described fully in § 2.3.2 below) is a straightforward matched-filtering procedure to search for significant emission

features by fitting a Gaussian line profile at each point in the residual spectrum (Pratt 1978; Hewett et al. 1985). We describe our implementation here so as to be explicit. Let $f_j^{(r)}$ be the residual flux in pixel j and σ_j^2 be the statistical variance of $f_j^{(r)}$ ². Also let $\{u_i\}$ describe a Gaussian kernel, centered on $i = 0$, with i running from $-i_{\text{lim}}$ to i_{lim} , and normalized such that $\sum_i u_i = 1$. The maximum-likelihood estimator \bar{A}_j for the line flux A_j of any $\{u_i\}$ -shaped residual emission feature centered on pixel j is that which minimizes

$$\chi_j^2 = \sum_{i=-i_{\text{lim}}}^{i_{\text{lim}}} \left(A_j u_i - f_{(j+i)}^{(r)} \right)^2 / \sigma_{(j+i)}^2 . \quad (2.2)$$

Differentiating (2.2) with respect to A_j , setting the resulting expression to zero, and solving yields

$$\bar{A}_j = C_j^{(1)} / C_j^{(2)} , \quad (2.3)$$

where we have defined the convolutions

$$C_j^{(1)} \equiv \sum_i f_{(j+i)}^{(r)} u_i / \sigma_{(j+i)}^2 , \quad (2.4)$$

$$C_j^{(2)} \equiv \sum_i u_i^2 / \sigma_{(j+i)}^2 . \quad (2.5)$$

The variance of \bar{A}_j (under the assumption of uncorrelated Gaussian errors in $f_j^{(r)}$ as described by σ_j^2) is given by

$$\sigma_{\bar{A},j}^2 = 1 / C_j^{(2)} . \quad (2.6)$$

The signal-to-noise ratio for a fitted Gaussian profile centered on pixel j is therefore

$$(S/N)_j = C_j^{(1)} / \sqrt{C_j^{(2)}} . \quad (2.7)$$

Our null hypothesis is an absence of emission features in the residual spectra that should manifest as the $\{(S/N)_j\}$ being Gaussian-distributed about zero with unit variance: this should hold at most wavelengths in most spectra. We approach the initial search for emission lines in the residual spectra as a search for significance peaks with (S/N) greater than some threshold value. Although insensitive to goodness-of-fit, this convolution-based detection scheme executes quickly (≈ 15 s per 1000 spectra including file reads on a 2.53GHz Pentium 4 Linux PC) and is therefore well suited to the initial search for residual emission features within our large spectral sample. We implement the algorithm in the IDL language. Section 2.4 describes a noise-rescaling process that we employ to control the incidence of false-positive emission-feature detections (due primarily to imperfect sky subtraction) without masking regions of the spectrum.

2.3.2 Multi-Line Background Systems: Detection, Fitting, and Rejection

Multiple emission features at the same redshift will have redshift-independent wavelength ratios. The fully reduced SDSS spectra have been re-binned at a constant-velocity pixel scale

²Conversion from units of $\text{ergs cm}^{-2} \text{s}^{-1} \text{\AA}^{-1}$ to units of $\text{ergs cm}^{-2} \text{s}^{-1} \text{pixel}^{-1}$ is made using the re-binned SDSS spectroscopic pixel scale relation $d\lambda = \lambda \times 10^{-4} \ln(10) d(\text{pixels})$.

of 69 km s^{-1} , giving a redshift-independent pixel offset between features. Our operational scheme is thus to search for coincident (S/N) peaks between multiple copies of a single filtered residual spectrum that have been shifted relative to one another. For [O II] 3727 detection, we filter each residual spectrum with a $\sigma = 2.4$ -pixel Gaussian kernel (matched to the typical width of blended [O II] 3727 emission seen in SDSS starburst galaxies). We take copies of the same residual spectrum “blueshifted” by integer pixel amounts so as to place H δ , H γ , H β , [O III] 4959, [O III] 5007, [N II] 6548, H α , [N II] 6583, [S II] 6716, and [S II] 6730 as close as possible to the geometric-mean wavelength of the [O II] 3727 doublet. These shifted spectra are filtered with a $\sigma = 1.2$ -pixel Gaussian kernel (matched to the typical width of SDSS starburst [O III] 5007 emission), with the sub-pixel part of the line offset relative to [O II] 3727 incorporated by offsetting the kernel. Any pixel in the filtered S/N spectra with value greater than 3 for [O II] 3727 and value greater than 2.5 for two out of H β , [O III] 4959, and [O III] 5007 is tagged as a “hit”. A group of adjacent “hit” pixels is reduced to the single pixel with the greatest quadrature-sum S/N for lines detected above the threshold (in effect, the pixel most inconsistent with the null hypothesis). Spectra with more than one isolated hit are rejected. The spectra are only searched in regions that would correspond to emission from $\gtrsim 5000 \text{ km s}^{-1}$ behind the targeted LRG.

The choice to require two significant line detections (rather than just one) in addition to [O II] 3727 was made in order to control the incidence of false-positive detections. For Gaussian statistics, the probability of a $3\text{-}\sigma$ or greater positive noise deviation (i.e. $S/N > 3$) is $P(> 3\sigma^+) \simeq 0.0013$; for a $2.5\text{-}\sigma$ positive deviation the probability is $P(> 2.5\sigma^+) \simeq 0.0062$. Thus the probability of a $3\text{-}\sigma$ or greater deviation at one wavelength *and* a $2.5\text{-}\sigma$ or greater deviation at one of three possible other specified wavelengths is

$$P_{\text{hit}} = 3 \times P(> 3\sigma^+) \times P(> 2.5\sigma^+) \simeq 2.4 \times 10^{-5} . \quad (2.8)$$

For a sample such as ours with 51,000 spectra and ≈ 1000 spectral resolution elements in the searchable redshift range for each spectrum, we would expect on the order of 1000 such noise detections in the sample. Requiring *two* additional significant detections at the three possible other wavelengths leads to

$$P_{\text{hit}} = 3 \times P(> 3\sigma^+) \times [P(> 2.5\sigma^+)]^2 \simeq 1.5 \times 10^{-7} , \quad (2.9)$$

and we now expect only on the order of a few to ten false-positive detections within the sample. In principle requiring two additional lines would miss systems with only one additional line even if that line was detected at very high significance. In practice this is not much of a concern since [O III] 4959 and [O III] 5007 always occur with an intensity ratio of 1:3, and a highly significant detection of one will entail a detection of the other as well.

The preceding selection leads to 163 single-hit galaxies within our 51,000 spectra. For each hit, we explore a grid of redshift and intrinsic emission-line-width values for the background galaxy to find a best-fit model. At each grid point we fit a Gaussian profile to any emission line initially detected above a $2.0\text{-}S/N$ threshold, with the line center determined by the trial redshift and line-width given by the quadrature sum of the trial intrinsic line-width and the wavelength-dependent spectrograph resolution as measured from arc lines by the SDSS pipeline. [O II] 3727 is fit with a double-Gaussian profile. We adopt as best values for background redshift z_{BG} and (Gaussian- σ) intrinsic line-width σ_{line} those that give the minimum χ^2 over all detected lines. The z_{BG} extent of our grid corresponds to ± 2 pixels, and the explored σ_{line} range runs from 0 to 2 pixels (0 to 138 km s^{-1}).

Following these fits, we subject the candidate sample to several cuts that are designed to be a quantitative expression of our own judgements about which candidate systems look real upon spectrum inspection and which do not. First, we reject any system where no convergent (minimum χ^2) value for z_{BG} is found within the explored ± 2 -pixel range. This cut tends to reject detections associated with the wings of poorly subtracted night-sky emission lines. Similarly, we cut systems with no convergent σ_{line} between 0 and 2 pixels. This cut tends to reject systems associated with extended wavelength ranges over which the template model underestimates the galaxy continuum. Next, we compute a total signal-to-noise ratio for the fit, defined as the total best-fit flux in [O II] 3727 and all other lines initially detected at $S/N \geq 2.5$ divided by the quadrature-sum of the $1\text{-}\sigma$ noise from those line fits, and impose a cut in the total- S/N - χ_r^2 plane (χ_r^2 being the χ^2 per degree of freedom in the fit). We cut any system with a total S/N less than the greater of 6 and $6 + 3(\chi_r^2 - 1)$. This removes both low- S/N candidates and candidates whose χ_r^2 values are too high to be explained by high- S/N emission features showing significant non-Gaussian structure. This cutting procedure reduces the 163 hits to 61 candidate systems. Finally, we prune 12 candidates from the list that survive the automated culling but are clearly explained by either over-fit LRG stellar absorption, under-modeled LRG line emission, exceptionally poor data quality, or a generally flawed template fit, leaving 49 good candidate systems.

This search for background galaxy emission lines digs rather deep into the noise of our spectroscopic sample. To gauge the incidence of false positives in our final candidate list, we make a parallel run of the detection, fitting, and automated rejection procedure with the following rest-wavelength perturbations: $\text{H}\beta \rightarrow 4833$, [O III] 4959 \rightarrow 4945, and [O III] 5007 \rightarrow 5023. These perturbations alter all of the redshift-independent wavelength ratios among these lines and between all of them and [O II] 3727; this modified detection procedure no longer selects for real multi-line emission, but only for noise features. The “false candidates” that result from this perturbed procedure are randomly shuffled along with the candidates from the original procedure, and all are examined together when making the final pruning judgements. The perturbed procedure yields 88 hits and 7 post-cut candidates; all 7 are pruned upon inspection without knowledge of their intrinsic falseness. This implies that the vast majority of our candidates are indeed background galaxies and not simply noise features.

2.4 Noise Modeling

If the model of a purely Gaussian noise spectrum described by σ_λ were correct, then the distribution of scaled residual specific fluxes

$$x_\lambda \equiv f_\lambda^{(r)}/\sigma_\lambda \quad (2.10)$$

across all spectra would be Gaussian with unit variance for all wavelengths λ . This is unfortunately not the case in our sample. Imperfect night-sky emission-line subtraction and other miscellaneous effects give rise to an excess of high-significance outliers beyond the predictions of a Gaussian model, leading to a deluge of false-positive astronomical emission-line candidates when the procedure described in § 2.3.1 is applied, particularly in the 7000–9000-Å region of the spectrum where the [O III] 5007 line at redshifts $z \approx 0.4$ – 0.8 appears. The most drastic solution is simply to mask all sky-afflicted wavelengths. Rather than concede such vast spectral coverage (which would drastically reduce our survey volume), we describe the observed distribution of scaled residual specific fluxes x_λ within the

LRG sample with a more detailed empirical noise model. The generally Gaussian behavior of scaled residuals at low significance combined with the excess of high-significance residuals is well described by a mixture of Gaussian and Laplace distributions, expressed parametrically as

$$p(x) dx = [a \exp(-x^2/2\sigma_g^2) + b \exp(-|x|/\sigma_e)] dx \quad (2.11)$$

(For history and applications of the Laplace distribution, see Kotz, Kozubowski, and Podgórski 2001) The parameters of this distribution are wavelength-dependent, but we suppress this dependence in our notation. The values of a and b are related by normalization:

$$\int_{-\infty}^{+\infty} p(x) dx = \sqrt{2\pi}\sigma_g a + 2\sigma_e b = 1 \quad (2.12)$$

We also fix the following relations between parameters, based on strong correlations observed in free-parameter fits to the distribution at each wavelength:

$$\sigma_e = \sigma_g - 0.38 \quad (2.13)$$

$$b = 0.09 \times \sigma_g(a + b) \quad (2.14)$$

The result is a one-parameter noise model to fit to the distribution of x_λ across the sample at each wavelength. (The numerical values 0.38 and 0.09 are fixed by minimizing the sum of binned χ^2 values for fits across all wavelengths.) We relax conditions (2.13) and (2.14) and fit freely for σ_e and b at a few isolated locations in the spectrum, where the effects of sky-subtraction residuals are especially strong and the correlations that suggest (2.13) and (2.14) break down—regions near 5577 Å, 5894 Å, 6305 Å, and 6366 Å. Additionally, some regions of some spectra are characterized by extreme and correlated excess variance, so for each spectrum we convolve $|x_\lambda|$ capped at 5 (to limit the influence of single pixels) with a 100-pixel boxcar filter and exclude from the noise-modeling sample any pixels within a boxcar whose value exceeds 1.25.

We use our fitted noise model to re-scale the reported σ_λ values such that the new distribution $p(x) dx$ of scaled residual flux values at each wavelength becomes Gaussian, while preserving the position of individual x -values within the cumulative distribution, then proceed as described in § 2.3.1. Both the reported noise σ_λ and the measured residual flux values $f_\lambda^{(r)}$ contain information about the actual error in the presence of imperfect subtraction, so it is sensible to base an effective noise rescaling on their ratio x_λ in this manner. By fitting the noise distribution parameters independently at each wavelength, we also model the localized effects of individual night-sky lines.

2.5 Candidate Systems

2.5.1 Catalog

Here we discuss our initial catalog of 49 candidate lensed star-forming galaxies selected to have [O II] 3727 emission at S/N of 3 or higher and emission from two out of the three of H β , [O III] 4959, and [O III] 5007 each at S/N of 2.5 or higher, at a redshift significantly greater than that of the primary target LRG. Table A.1 lists various properties of the candidate lens systems, together with those of candidates subsequently selected from within the SDSS MAIN spectroscopic sample by similar techniques and targeted for follow-up observation (Chapters 3 and 4). LRG de Vaucouleurs model magnitudes and effective

radii are determined from SDSS imaging and photometric reduction. LRG redshifts and velocity dispersions are as provided by `specBS`; the software fits for velocity dispersions σ_v using a set of 24 stellar eigenspectra derived from a PCA of the ELODIE spectral library (Prugniel and Soubiran 2001). These velocity-dispersion measurements have been used successfully to construct the fundamental plane (Bernardi et al. 2003), to measure the velocity function of early-type galaxies (Sheth et al. 2003) and to make a model-based comparison of stellar and dynamical mass estimates of elliptical galaxies (Padmanabhan et al. 2004). We report all σ_v values from the database, although some are likely unreliable; see the notes of Table A.1. We also report emission-line redshifts of the detected background galaxies. Using the observed LRG and background redshifts and the observed LRG σ_v , and assuming a singular isothermal sphere (SIS) LRG luminous+dark matter distribution, we calculate a “best guess” for the angular scale of any lensing that might be present in these systems as $\Delta\theta = 8\pi(\sigma_v^2/c^2)(D_{LS}/D_S)$. (D_{LS} and D_S are angular-diameter distances from lens to source and from observer to source.) This is the separation between the two images of a strongly lensed object in the SIS model; it is also the radius of the strong-lensing region of the image plane, and twice the radius of ring images of compact sources directly behind the lens (e.g. Narayan and Bartelmann 1996). For each candidate system we also report the detected background [O II] 3727 line flux from the best-fit double Gaussian profile. The reported background line fluxes are simply the fluxes captured by the 3''-diameter SDSS spectroscopic fiber: the shapes and spatial alignments of the background-galaxy images are unknown, and the spectroscopic fibers will in general only record a fraction of their line fluxes. Figure B-1 shows the SDSS discovery spectra and best-fit model spectra, along with close-up views of the residual (data – model) spectra in the wavelength ranges corresponding to redshifted background [O II] 3727, H β , [O III] 4959, and [O III] 5007.

Although we detect line emission clearly, evidence of background galaxy *continuum* in the residual spectra of our candidate systems is scarce. This is not surprising, for three reasons. One, the LRG sample was selected for particular broadband color and luminosity, and significant background continuum would likely perturb an LRG out of the sample. Two, any faint background continuum present in an LRG spectrum will largely project onto the LRG-redshift eigenspectrum set and low-order polynomial fit used by `specBS`, and will be subtracted along with the LRG model when forming the residual spectrum. Three, these background galaxies are likely to be high-equivalent-width star-forming systems, and since their line fluxes are detected just above the noise threshold, the associated continuum will typically be lost in the noise. Nevertheless, we may obtain a higher signal-to-noise picture of the background galaxies that we detect by constructing a median residual spectrum as follows. First we transform the residual spectra of our candidate systems (i.e. spectra from which template models of the foreground continuum have been subtracted) into units of $\text{erg cm}^{-2} \text{s}^{-1} \text{pixel}^{-1}$, which is a redshift-independent quantity since the rebinned SDSS pixels are of constant velocity width. We then shift these residual spectra into the rest frame of the background galaxy, rounded to the nearest whole pixel, and transform back to $\text{erg cm}^{-2} \text{s}^{-1} \text{\AA}^{-1}$. Next we renormalize the spectra by dividing each one by its best-fit [O II] 3727-flux value. We then take the median value at each pixel, and restore physical normalization by multiplying this median spectrum by the sample-median best-fit [O II] 3727-flux value. The resulting median spectrum is shown in Figure 2-2. Although there is no discernible continuum in the individual residual spectra, we can see a 4000- \AA continuum break in the median spectrum; we also see H γ , H α , [N II] and [S II] emission lines in addition to the lines for which we select. This gives further evidence that we have successfully detected and identified real background emission features.

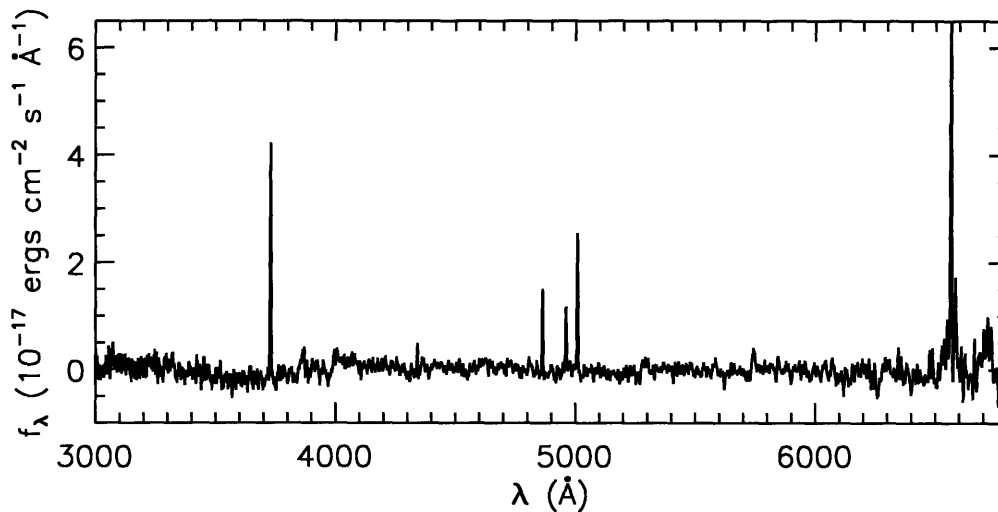


Figure 2-2: Median rest-frame spectrum of background galaxies detected in our residual LRG spectra, created as described in the text and smoothed with a 5-pixel boxcar. Note the continuum break at 4000Å and the absorption feature at 5270Å, which are not discernible in the individual residual spectra. Also evident are the emission lines H γ , H α , [N II] 6548, [N II] 6583, [S II] 6716, and [S II] 6730, in addition to the emission lines for which we select.

2.5.2 Lenses or Not?

We have certainly detected emission from galaxies behind foreground LRGs. For a system to be a strong gravitational lens, the background galaxy must be located at sufficiently small impact parameter relative to the LRG center. The true incidence of lensing within our sample can best be determined and studied with either narrow-band imaging or integral-field spectroscopy. Such observations could spectrally isolate the background line flux and resolve it spatially to reveal any lensing morphology. SDSS broadband imaging offers some hope for answering the lensing question, but in general Sloan images do not detect late-type galaxies at redshift $z \sim 0.5$ at very high S/N . Figure C-1 shows $40'' \times 40''$ SDSS r postage-stamp images centered on the candidate systems, with linear gray-scaling from -3σ sky noise to peak LRG surface brightness. Evidence of significantly offset neighboring broadband emission is seen in some images, but it would be difficult to rule out many systems as definite non-lenses based on SDSS-quality images. In the spirit of a purely spectroscopic survey, we present as candidates all systems selected spectroscopically. Furthermore, we note that many of these LRGs live in high-density group/cluster environments, and neighboring images may be at the LRG redshift and not the source of the background emission that we detect.

In preparation for integral-field spectroscopic follow-up, we obtained broadband reconnaissance images of 14 of our candidate systems (as indicated in Table A.1) using the Magellan consortium's 6.5-m Clay telescope at Las Campanas Observatory. These short g - and i -band exposures (120s each) were taken on the nights of 2003 August 1 and 2 with the Magellan Instant Camera (MagIC) CCD imager and active telescope optics (Schechter et al. 2003). Conditions were similar on both nights: non-photometric due to cirrus clouds, and with $\sim 0''.8$ median FWHM seeing. For the majority of these systems, the images present no

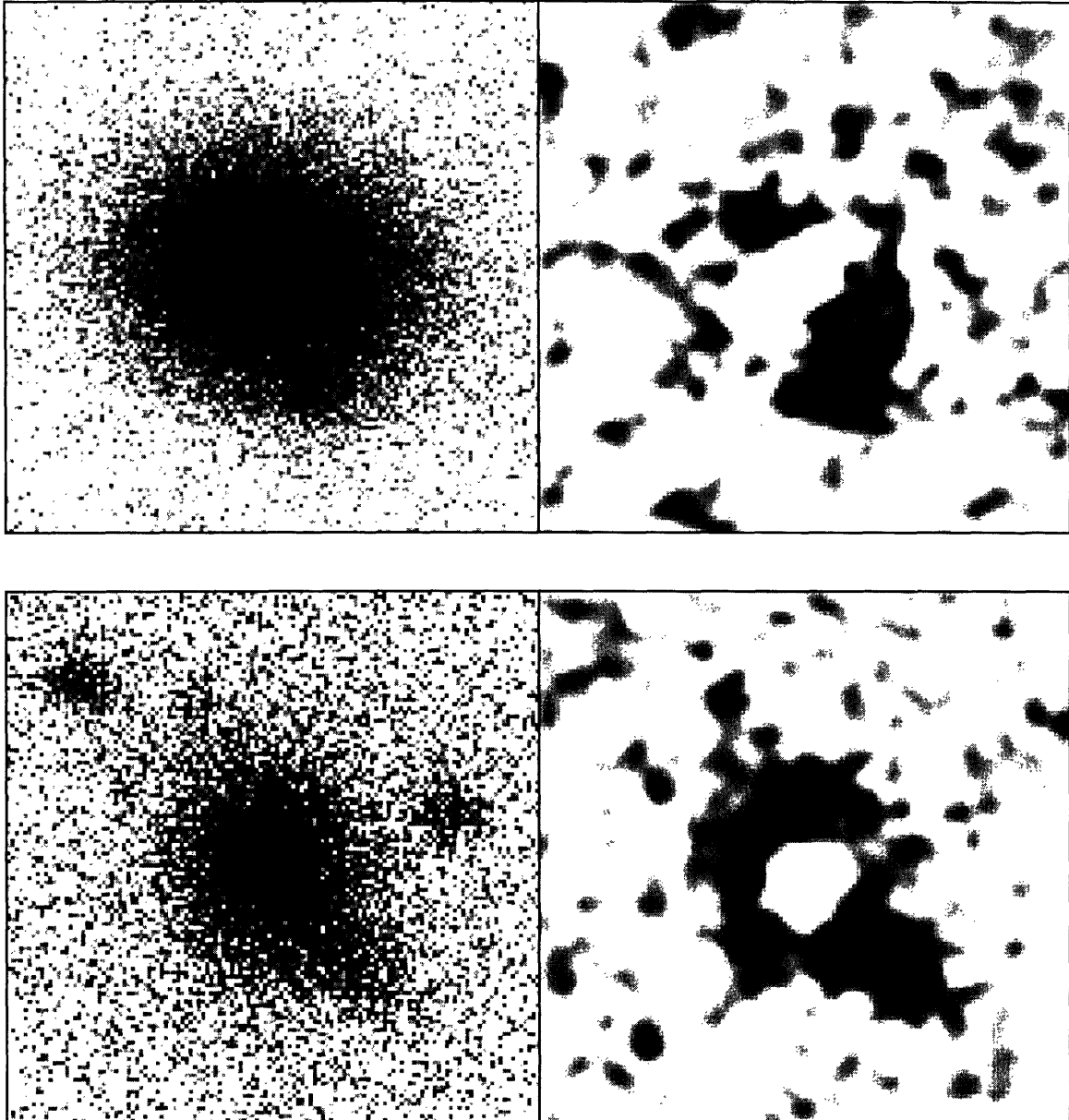


Figure 2-3: MagIC $8''8 \times 8''8$ images and difference images of lens candidates SDSSJ0037 (top) and SDSSJ0216 (bottom). Left-hand panels show 120-s g -band images of the two systems; right-hand panels show smoothed $g - i$ difference images created as described in the text. Note the evidence for multiply imaged, relatively blue objects in the difference images. (In these images, North is left and East is up—reversed parity from what is seen on the sky.)

significant evidence for or against the presence of strong lensing; we describe the exceptions here. One system, SDSSJ0035, is almost certainly not a strong lens: a relatively g -bright galaxy can be seen clearly in the images, approximately $2''.6$ offset from the LRG. This far exceeds the anticipated lensing scale of about $0''.4$ reported in Table A.1. The images of SDSSJ2147 reveal a bluer galaxy approximately $1''.3$ to the South, about at the limit of the estimated lensing scale. We see no particular evidence for strong lensing, but deeper

observation of this system could be of interest. Two systems, SDSSJ0037 and SDSSJ0216, show evidence of multiple imaging. Figure 2-3 shows g -band images of these two systems, along with difference images created by smoothing aligned i -band images with a Gaussian kernel in order to suppress noise and match the slightly worse g -band seeing, then fitting this smoothed i -band LRG image to the g -band image and subtracting it. The difference images are then smoothed with a Gaussian kernel of FWHM $\approx 0''.4$ in order to bring out coherent features; they show strong evidence of multiply imaged, relatively blue sources. SDSSJ0037 seems likely to be a double-image lens. It is tempting to identify quadruple-image morphology in the SDSSJ0216 difference image, but the level of noise recommends caution. Narrow-band imaging or integral-field spectroscopy should permit quantitative study of these systems and of those for which broadband imaging is inconclusive. *HST* imaging of any confirmed lenses using the narrow-band ramp filter set of the *Advanced Camera for Surveys* could also be pursued to obtain a highly resolved picture of lensed line-emitting regions and permit even more detailed study of the lensing mass distributions³.

The degree of lensing that will be present in a particular system will depend on the impact parameter (angular offset) of the background galaxy in the source plane relative to the center of the LRG: the smaller the impact parameter, the more lensing will be seen. To obtain a rough estimate of the number of lenses within our sample, we can guess at the unlensed surface brightness distribution of our background galaxies, compute lensed images under an assumed lens model, smear to account for seeing, and integrate over the $3''$ -diameter SDSS spectroscopic fiber, then compare to the [O II] line flux values that we have observed. To interpret the results in terms of lensing probabilities we must also invoke an [O II] 3727 luminosity function (LF). Below we describe the details of a lensing probability calculation of this nature that we have carried out. The results suggest that a total of 19 out of 49 of our original candidate systems are likely to be strong lenses—that is, we expect approximately 19 systems to have source-galaxy impact parameters less than the critical value for multiple imaging. It is important to recognize, though, that the “lenses-or-not” question does not have as straightforward an answer for extended sources as it does for point sources. Different regions of our background galaxies will be lensed by different amounts, and in general some but not all of the galaxy can be multiply imaged. It is more appropriate to ask *how much* lensing is present in any given system. Strong lensing constraints may still be derived from a galaxy-galaxy lens system even if the point of peak surface brightness is not multiply imaged.

Our strategy for assessing lensing probabilities in our sample involves the construction of an approximated probability density $p(b) db$ for the unknown impact parameter b of the background galaxy in each system. The following observed quantities are input to the calculation: the LRG and background redshifts, the LRG velocity dispersion, the background [O II] 3727 line flux received by the $3''$ -diameter spectroscopic fiber, and the median seeing for the spectroscopic plate under consideration. We also make use of the [O II] line luminosity function (LF) reported by Hogg et al. (1998). We adopt the same SIS model for the LRG mass distribution as was used to obtain the $\Delta\theta$ values in Table A.1, and we model the background galaxies as exponential disks with a half-light radius of approximately 3 kpc (fixed to $0''.5$ at $z = 0.5$).

For each system, we explore a range of impact parameters b from 0 to $5''$. At each b -value, we generate a lensed image of the model background galaxy, then convolve it

³As we will see in Chapter 4, *HST*-ACS *broadband* imaging in fact detects the background galaxy *continuum* quite well. The reference to the narrowband filter set is retained here for the historical record.

with a Gaussian point-spread function corresponding to the median seeing reported in the spectroscopic plate header. We then integrate the image over a 3''-diameter circular fiber aperture centered on the model lens. The result is a tabulated function $f(b)$ giving the fraction of the intrinsic flux received by the fiber; that is, if the total galaxy line flux were S in the absence of lensing and limited fiber sampling, the [O II] line flux received by the spectroscopic fiber from a background galaxy with a source-plane offset b would be $S_{\text{fib}} = f(b)S$. In general $f(b)$ may be greater or less than one due to the competing effects of lens magnification and incomplete sampling by the fiber.

Next we adopt the [O II]-emitter LF reported by Hogg et al. (1998) by fitting a Schechter function to their Figure 6. After converting from logarithmic units, the number of [O II] emitters per unit volume in an interval dL at line luminosity L is well approximated by

$$\phi(L) dL \propto L^\alpha \exp(-L/L_\star) dL \quad , \quad (2.15)$$

with $\alpha \simeq -1.3$ and $L_\star \simeq 3.4 \times 10^{42}$ ergs s⁻¹ (the overall normalization is unimportant for our purposes). We make a crude conversion from their assumed $(\Omega_M, \Omega_\Lambda) = (0.3, 0)$ universe to our cosmology by scaling their reported luminosities up by a factor of 1.2: the ratio of squared luminosity distances in our cosmology to theirs ranges from 1.16 at $z = 0.3$ to 1.27 at $z = 1$, and the bulk of galaxies in their study fall within this range. Assuming the form of the LF does not evolve, it corresponds to an intrinsic flux function at any redshift z for the number of galaxies per unit redshift per unit solid angle within some intrinsic flux range dS about S :

$$\psi(z, S) dS = N(S, z) S^\alpha \exp(-S/S_\star) dS \quad , \quad (2.16)$$

with the same α as the LF and $S_\star = L_\star/[4\pi D_L^2(z)]$, where $D_L(z)$ is the luminosity distance to redshift z . $N(S, z)$ is a flux- and redshift-dependent normalization, the form of which will prove unimportant.

We can now derive a joint probability density function (PDF) for the observation of an [O II]-emitting galaxy behind a given LRG at impact parameter b , redshift z , and with line flux S_{fib} in the fiber by setting the differential probability proportional to the corresponding expected differential number count and making use of the known relationship of S_{fib} to intrinsic flux S through $f(b)$:

$$\begin{aligned} p(b, z, S_{\text{fib}}) db dz dS_{\text{fib}} &\propto \psi(z, S) d\Omega dz dS \\ &= \psi[z, S_{\text{fib}}/f(b)] (2\pi b db) dz [dS_{\text{fib}}/f(b)] \quad . \end{aligned} \quad (2.17)$$

The term $d\Omega = 2\pi b db$ represents the solid angle in the source plane of an annulus of radius b and thickness db . The *observed* quantities S_{obs} and z_{obs} for the system are equal to the system's true S_{fib} - and z -values plus some observational noise that is independent of b , so assuming the noise is small relative to the scale on which the joint PDF varies, we may reinterpret the joint PDF as an approximate conditional PDF on b given z_{obs} and S_{obs} :

$$p(b; z_{\text{obs}}, S_{\text{obs}}) db = N'(z_{\text{obs}}, S_{\text{obs}}) b [f(b)]^{-1} \psi[z_{\text{obs}}, S_{\text{obs}}/f(b)] db \quad . \quad (2.18)$$

The normalization $N'(z_{\text{obs}}, S_{\text{obs}})$ need not be derived explicitly, since we can simply compute the right-hand side without it for the relevant range of b -values and normalize afterward. With this PDF in hand, we can finally assign a ‘‘lensing probability’’ to the system as the integrated probability for impact parameters less than the critical value for multiple imaging in the SIS model—the ‘‘Einstein radius’’, equal to one-half the $\Delta\theta$ value given in Table A.1.

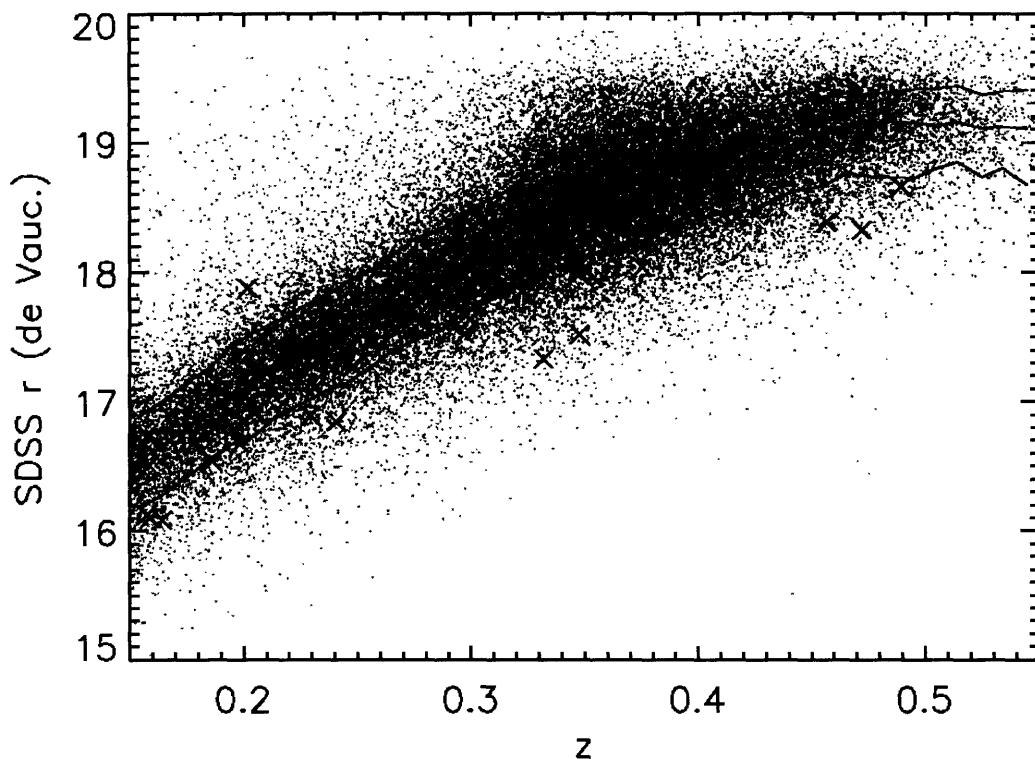


Figure 2-4: Comparison of lens-candidate LRGs (crosses) to full LRG sample (gray dots) in the magnitude-redshift plane. The three black lines show the redshift-dependent median de Vaucouleurs r magnitude of the full sample and the 84th- and 16th-percentile r values.

Summing this probability over all systems gives our quoted estimate of 19 strong lenses out of 49 candidates.

2.5.3 Lens Candidates in Context

We present a comparison between our initial sample of lens-candidate LRGs and the full 51,000 parent LRG sample in Figure 2-4. The lens candidate LRGs seem somewhat skewed toward brighter magnitudes. The conservative interpretation is that the broadband selection properties of fainter LRGs are more easily perturbed by background galaxies, but it may also reflect a lensing signal, with more massive galaxies providing more magnification. If the logarithmic slope of the underlying [O II] LF is steeper than -1 at the luminosities probed by our survey, then magnified lines of sight should show a statistically enhanced number of [O II] emitters (Turner et al. 1984). Hogg et al. (1998) find the logarithmic [O II] LF slope to be steeper than -1 for line luminosities $\gtrsim 10^{42}$ ergs s^{-1} , whereas the median observed [O II] luminosity in our sample is of order 10^{41} ergs s^{-1} . These numbers suggest that magnification bias is not the explanation for the observed brightness of our lens candidates relative to the full LRG sample, but a more definite statement must await spatially resolved follow-up observations.

Most known gravitational lens systems have been selected on the basis of some combination of source properties and lens cross section, whereas the SDSS LRG sample is selected

based on colors and magnitude. It is therefore of interest to compare known early-type lens galaxies to our candidate lenses, although this is difficult since we do not currently have truly comparable observations of the two samples. Figure 2-5 presents our best attempt at such a comparison for lens velocity dispersions and apparent magnitudes as a function of redshift⁴, with *HST* known-lens data taken from Rusin et al. (2003a). The known-lens velocity dispersions are estimated from lensed image separations in the manner described by Kochanek et al. (2000); they may be systematic overestimates if these lenses are superimposed on the “mass sheet” of a high-density environment (Holder and Schechter 2003). Magnitude comparison is made by transforming SDSS *g*- and *r*-band magnitudes to Johnson-Morgan *V*-band using the observed transformation of Smith et al. (2002). We see that our LRG lens candidates are in general of greater velocity dispersion than known lenses, and in the redshift range where the two samples overlap, the LRGs are more luminous. The brightness of the LRGs combined with the relative faintness of the background galaxies in our sample suggests that any confirmed LRG lenses would be well suited to the type of detailed lens stellar-dynamical studies described by KT.

2.6 Conclusions

We have presented a catalog of candidate strong galaxy-galaxy gravitational lens systems detected spectroscopically within the Sloan Digital Sky Survey. These systems have known foreground *and* background redshifts; only the detailed spatial alignment of foreground and background galaxies remains unknown until further observation. We plan to conduct integral-field spectrographic follow-up observations of these systems, which will allow us to resolve the spatial distribution of the background nebular line emission that we have detected. These observations should confirm a substantial number of lenses within our candidate sample, with many lensed galaxies at lower redshift than any other currently known lensed extra-galactic optical sources. Any lenses confirmed within our sample will be of considerable interest for the study of early-type galaxy mass distributions, and could have implications for lens-time-delay H_0 measurements and anomalous quasar-lens flux ratios. Our sample demonstrates the feasibility of the emission-line-based spectroscopic lens search technique within the SDSS and other redshift surveys, and we plan to extend the search to higher source redshifts in the near future. We have also developed and applied a method for abating the influence of night sky emission-line residuals in the 7000–9000-Å range that allows us to detect [O III] and $H\beta$ emission over the redshift range $z \sim 0.4$ – 0.8 without an excess of false-positive detections.

⁴We plot these quantities as a function of redshift to avoid the issue of evolutionary and k corrections.

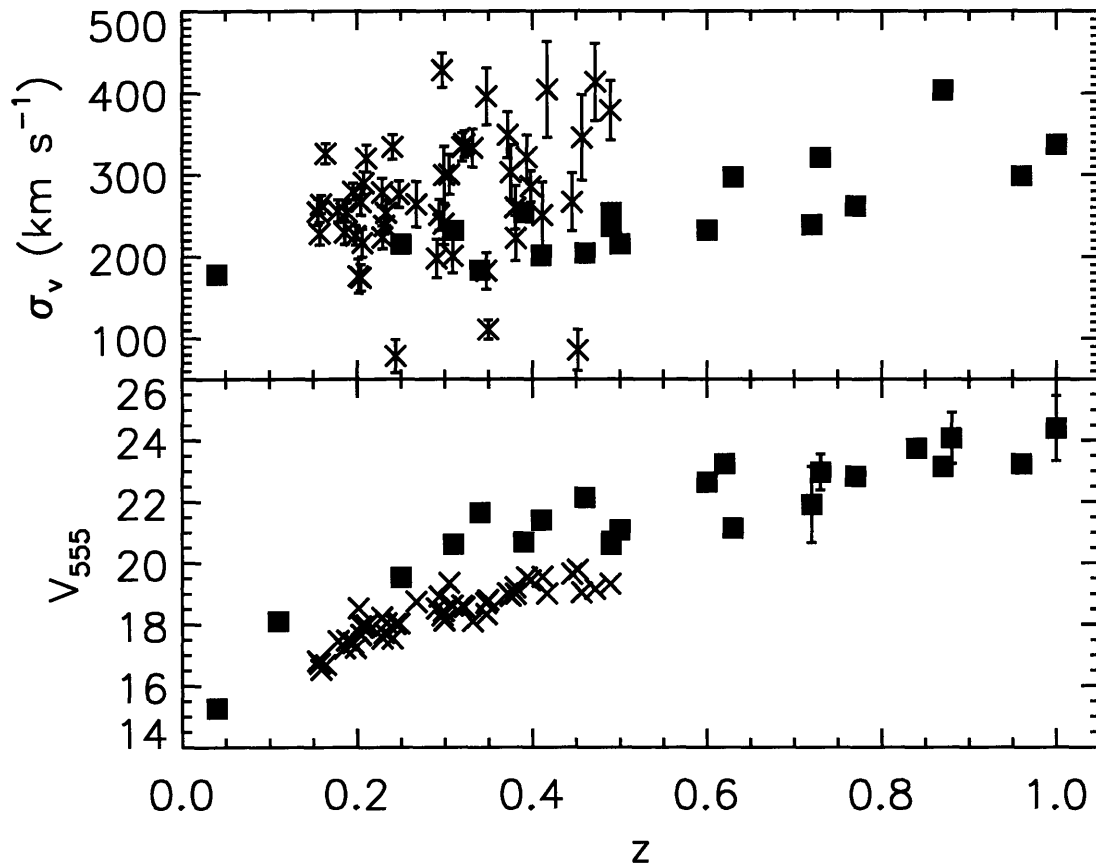


Figure 2-5: Comparison of candidate LRG lens galaxies (crosses) with known early-type lenses with known lens redshifts (filled squares). *Top panel:* comparison of velocity dispersions σ_v measured for LRG lens candidate galaxies and inferred from image separations $\Delta\theta$ in known early-type lens systems with known lens and source redshifts. Image separations are taken from Rusin et al. (2003a), and conversion to velocity dispersion estimates is made via Equation 5 of Kochanek et al. (2000). For visual clarity, we omit error bars on the latter data points; Kochanek et al. (2000) estimate 10% errors in the $\Delta\theta \rightarrow \sigma_v$ conversion. *Bottom panel:* V -band magnitude comparison. SDSS g - and r -band magnitudes are converted to Johnson-Morgan V via the observed transformation of Smith et al. (2002); we have also corrected for an 0.2-magnitude systematic error in the SDSS magnitudes used to generate the figure (Abazajian et al. 2003), which has since been corrected in the SDSS photometric pipeline. Error bars on SDSS photometric quantities are smaller than plotted symbol sizes. Known-lens photometric data taken from Rusin et al. (2003a). All magnitudes have been corrected for galactic extinction using Schlegel et al. (1998) dust maps.

Chapter 3

Integral-Field Spectroscopic Observations of Strong Gravitational Lens Candidates

3.1 Introduction

This chapter presents the results of a gravitational-lens survey conducted using high-spatial-resolution integral-field units (IFUs) on the Gemini-North 8m telescope on Mauna Kea and the Walter Baade (Magellan I) 6.5m telescope at Las Campanas Observatory. The primary aim of the survey is to enlarge the sample of known strong galaxy-galaxy gravitational lenses. The lenses confirmed by these observations are amenable to detailed photometric and spectroscopic observation. We use the combined Einstein radii and velocity dispersions of confirmed lens systems to constraint the shape of the radial density profile in the core of the early-type lensing galaxies. The lens-candidate sample was selected from the Sloan Digital Sky Survey MAIN and Luminous Red Galaxy (LRG) spectroscopic samples by the methods of Bolton et al. (2004) (Chapter 2). A secondary motivation for this study is to explore the technical capabilities of high-resolution IFUs on today's large telescopes, which can collect spatially resolved spectroscopic data across the entire optical band with a single telescope pointing. With the richness and quality of data that they can deliver, these IFUs hold great promise for the study of galaxy-scale strong gravitational lenses. They can simultaneously obtain the spatially resolved redshifts that are necessary to confirm the hypothesis of strong lensing, permit the construction of lens-galaxy-subtracted narrowband images suitable for gravitational-lens modeling, and measure the projected kinematics (rotation and velocity dispersion) of the lens galaxy over an extended field of view. This chapter shows that the first two of these three goals can be achieved even with relatively short IFU exposure sequences ($\lesssim 1$ hr); the third goal should be attainable with somewhat longer integrations.

3.2 Instrumentation

The observations for this work were obtained with with integral-field units built by the University of Durham Astronomical Instrumentation Group for the the Inamori Magellan Areal Camera and Spectrograph (IMACS; Bigelow and Dressler 2003) and the Gemini-North Multi-Object Spectrograph (GMOS-N; Hook et al. 2003). The IMACS IFU (Schmoll et al. 2004) observes two $5'' \times 7''$ fields of view in the focal plane, separated by roughly one

arcminute: one FOV for the object and one from which to estimate the sky background (which should perhaps be called a foreground). The fields are sampled by a close-packed hexagonal array of lenslets which subtend $0''.2$ from side to side, for a total of 2000 lenslets between the two fields. The lenslets feed the light to optical fibers, which reformat the fields via a defined field-mapping into a one-dimensional array of output lenslets (a “pseudo-slit”) for dispersion; see Figure 3-1 for a schematic diagram of the IFU focal-plane to detector-plane mapping. This is accomplished within the space of a narrow cartridge that occupies the width of three adjacent mask slots in the slit-mask server, which inserts and removes the IFU in the same manner as a simple mask. Thus the IFU behaves like a slitmask with two $5'' \times 7''$ slits on the input side and one long slit on the output. The IMACS IFU can be used with either of the two IMACS cameras: $f/4$ (“long”) or $f/2$ (“short”). All data presented was obtained in the $f/2$ mode; some $f/4$ data was obtained under extremely poor observing conditions and is not included in this thesis. In direct imaging mode, the short camera observes a circular field of view with a diameter of $27'$ at a scale of $0''.20$ per pixel, which accommodates the entire IFU pseudo-slit and permits use of both $5'' \times 7''$ IFU fields in their entirety. The full width at half maximum (FWHM) of the IFU fiber point-spread function (PSF) on the detector is about 2.6 pixels in short-camera mode, and adjacent spectra are separated by about 3.5 pixels. The short camera uses gratings for dispersion. The long-camera direct-imaging FOV is $15' \times 15'$ at a scale of $0''.11$ per pixel, and can thus accommodate only 1200 of the 2000 total fibers making up the pseudo-slit: this limits the two IFU fields in the focal plane to contiguous $5'' \times 4''$ regions. The FWHM of the IFU fiber PSF is approximately 3.9 pixels in long-camera mode, and the spectra are separated by about 6.3 pixels. Gratings are used for dispersion in the long camera.

The GMOS-N IFU operates in an identical manner to the IMACS IFU, with a few notable exceptions. First, while the object field is $5'' \times 7''$ (1000 lenslets) as in IMACS, the background field is half this size: $5'' \times 3''.5$ (500 lenslets). Second, the 1500 total fibers are reformatted not into one single pseudo-slit, but rather into two parallel pseudo-slits separated by approximately 3200 pixels on the detector. This design choice is necessitated by the smaller GMOS CCD detector mosaic (as compared to IMACS), and entails two major choices of IFU observation mode. In “one-slit” mode, one of the output pseudo-slits is masked, the object and background fields are reduced to half their full size, and the full wavelength domain is available for the chosen grating setup. In “two-slit” mode, both pseudo-slits are used and the full spatial object and background fields are available, but broad-band filters must be used to limit the wavelength domain of the individual pseudo-slits so as to prevent overlapping of spectra. All GMOS-N IFU observations for this work were obtained in two-slit mode, since maximum spatial coverage was desired in order to capture any possible lensing configuration, but only minimal wavelength coverage was needed to observe specific redshifted emission lines. The GMOS-N direct-imaging pixel scale is $0''.07$ per pixel, and the IFU spectra are separated by approximately 5.7 pixels in cross-dispersion. The FWHM of the IFU fiber PSFs on the GMOS detector is approximately 4.2 pixels, and hence we used a binning factor of 2 in the dispersion direction to increase the signal-to-noise ratio of our GMOS-N IFU observations (by reducing the read-noise contribution).

Table 3.1 lists the various unique spectrograph configurations used in the work reported here, along with their general characteristics. Reference to these configurations hereafter will be made using the short names listed.

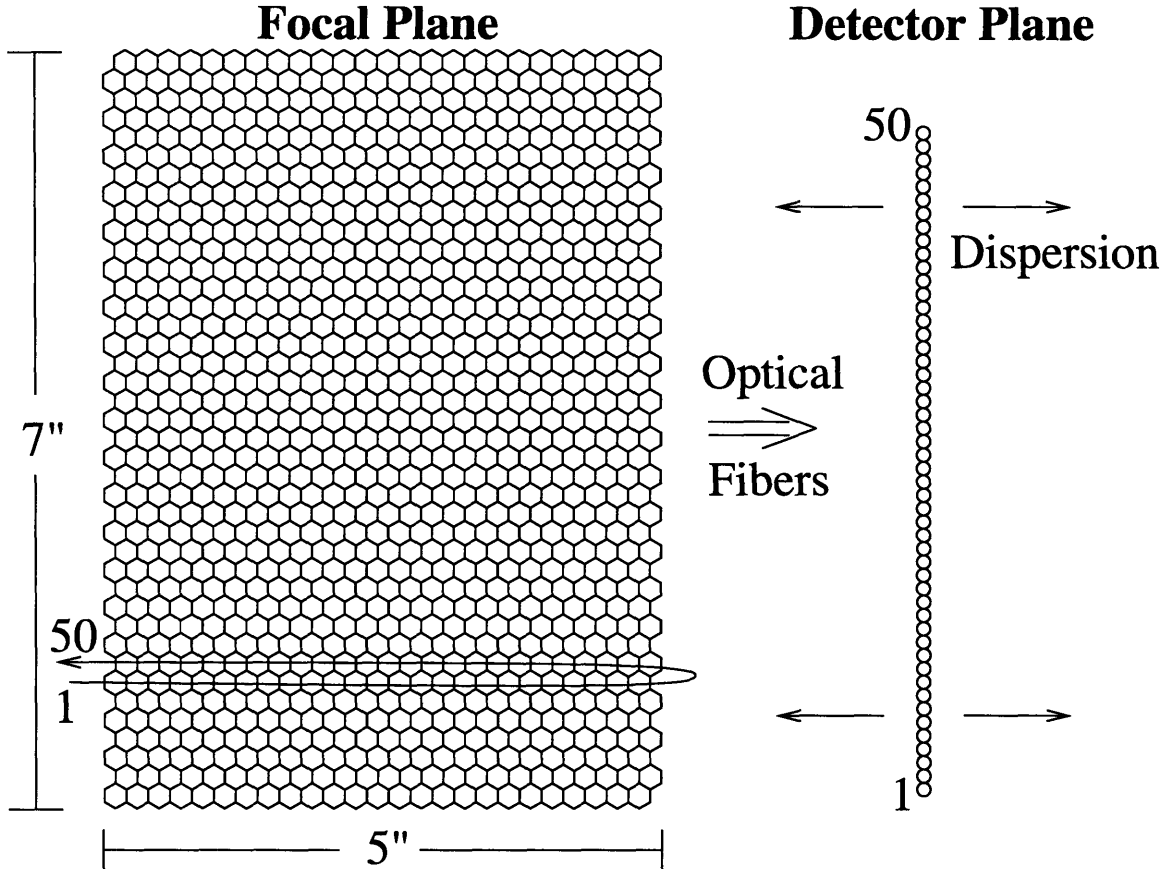


Figure 3-1: Schematic representation of the IFU focal-plane to detector-plane mapping. The $5'' \times 7''$ field of view in the focal plane is fully sampled by 1000 hexagonal lenslets with side-to-side diameter of $0''.2$. The lenslets feed optical fibers, which reformat the lenslet data in blocks of 50 as shown. The blocks are arranged end to end with some inter-block spacing along a “pseudo-slit” and dispersed in wavelength to produce 1000 spectra on the CCD. A separate and similarly sampled field of view is used for sky estimation, and the 50-fiber blocks from this field alternate in sequence with the object-field blocks on the detector.

Setup	Mode	Disperser	Filter	Range	$R = \lambda/\Delta\lambda$
IMACS-2	short camera	300 l/mm grism	none	4000–9000Å	~ 2000
GMOS-g	two-slit	B600 grating	Sloan g'	4000–5500Å	~ 4000
GMOS-r	two-slit	R600 grating	Sloan r'	5500–7000Å	~ 4000
GMOS-i	two-slit	R600 grating	Sloan i'	7000–8500Å	~ 4000

Table 3.1: IFU spectrograph configurations used.

3.3 Calibration and Reduction of IFU Data

The format of the data delivered by the GMOS-N and IMACS IFUs to their respective CCD-mosaic detectors is sufficiently complicated to justify analysis with specially-developed software. We have developed our own set of IFU data-analysis software tools written in the IDL language. We refer to this software as “kungifu” (kung eye eff you), and in this section we describe its function. The kungifu package can be obtained from the author for

use by other investigators.

3.3.1 Bias Subtraction and Data Formatting

The IMACS detector consists of a mosaic of eight 2048×4096 -pixel CCDs. The bias level of raw frames varies between the CCDs, within each CCD, and from one exposure to the next. For any given exposure, the bias is well characterized as the sum of row-overscan and column-overscan terms. Our IMACS bias-subtraction routine first fits a smooth b-spline (de Boor 1977) to the overscan region at the end of each row, for a specified breakpoint spacing. This model is evaluated for all pixels in all rows of the image and subtracted. Occasional abrupt bias-jumps of several to tens of ADU are often seen at a particular row across all eight CCDs; the b-spline-fit domain can be reset at the location of these jumps. Best results are obtained by using column-value to determine a fractional row-value in fitting and evaluation of this first bias model. The IMACS bias level also has significant column-dependence, and a similar b-spline fit to the overscan region at the end of each column is subtracted next. The bias-subtracted and overscan-trimmed individual CCD images are then stored to a single multi-extension FITS (MEF) file.

The detailed GMOS-N bias pattern is more stable than the IMACS bias pattern, but cannot be estimated from the overscan alone. Thus we perform GMOS-N bias subtraction using mean bias images, and also subtract an overall average bias value for each of the three GMOS-N CCDs from the overscan region to account for slight variations from one exposure to another. In two-slit IFU mode, the central CCD records spectra from both pseudo-slits. We break the central CCD into 2 logically separate images to separate these two regions, and store them as separate MEF extensions along with the first and third CCDs, after bias subtraction and overscan trimming.

3.3.2 Flat-field Modeling and Tracing

Relative flux calibration of IMACS and GMOS-N is accomplished using IFU exposures of uniform illumination by (approximately) flat-spectrum lamps. The raw flat images obtained in this manner measure the product of two non-uniform responses: the varying sensitivity of individual CCD pixels relative to one another, and the different throughputs of the fibers relative to one another. In an ideal spectrograph the illumination pattern of the fibers would be fixed relative to the detector, and these two effects would never need to be distinguished. In actuality both GMOS-N and IMACS exhibit limited flexure between successive exposures that causes the IFU fiber spectra to shift their position in CCD coordinates. Thus we attempt a factorization of the pixel-response and fiber-response calibrations by assuming an approximate scale separation between them. Since the IFU fiber spectra (for all data obtained for this work) run approximately along CCD rows, horizontal cross sections through the IFU spectroscopic flat frames follow the smooth variation of the flat-lamp spectrum, modulated by gradual transitions from one fiber to the next. We generate smooth-model spectroscopic flatfield images by fitting b-spline models to these cross sections, with a breakpoint spacing chosen ideally to be smaller than the typical scale of flat-lamp features but greater than the scale of pixel-to-pixel defects. The resulting model-flat images are then an approximation to the fiber response, and the ratio of raw- to model-flat images give the approximate pixel response (“pixel flat”). Figure 3-2 demonstrates this flat-field factorization graphically. We derive a master pixel flat from the median-image of many individual pixel flats in a given spectrograph configuration, for application to all science frames in that

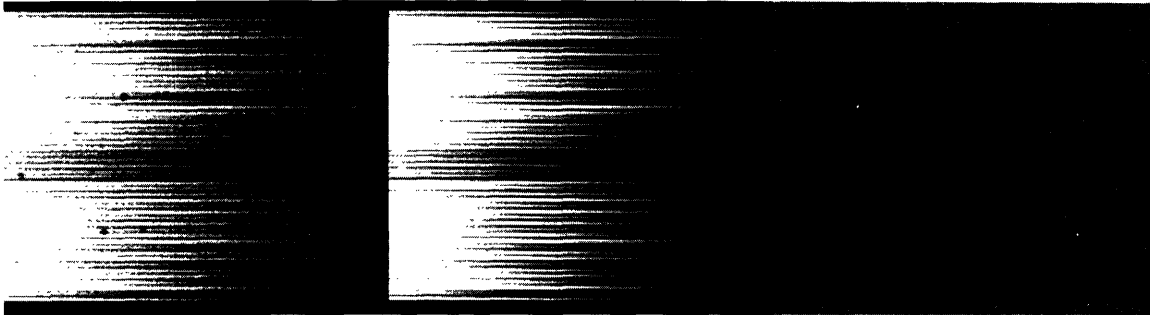


Figure 3-2: Factorization of IFU spectroscopic flat-field image via b-spline modeling. Left: small section of a raw flat-field image for one 50-fiber IMACS-IFU block. Spectra run horizontally; lighter color = higher counts. Center: model flat generated for same section by b-spline fits to each row, showing fiber response. Right: “pixel flat” for this section, given by ratio of raw flat to model flat (left to center) and indicating relative pixel response.

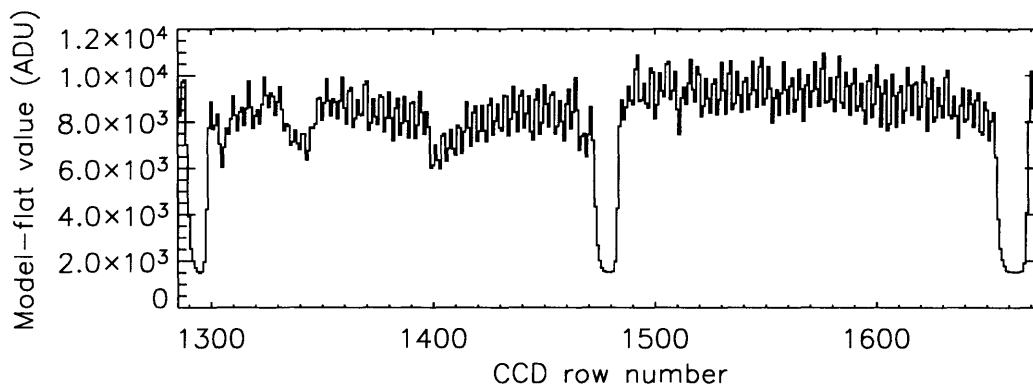


Figure 3-3: Cross section through an IMACS- $f/2$ model flat for two 50-fiber blocks. Note the substantial variation in fiber-to-fiber throughput and the significant overlap of the wings of adjacent fibers. Also note the non-zero level in between blocks, indicating a scattered-light contribution to the count levels.

configuration. We choose not to use imaging flats to calibrate the pixel response, since this calibration can in general be wavelength-dependent. Using pixel flats derived from spectroscopic flat-field frames ensures that the correction is derived with illumination at the appropriate wavelength. We describe our use of the model-flat images for the calibration of fiber response in § 3.3.5 below.

We also use the model-flat images to determine the location of individual fiber traces on the CCD. For both the IMACS and GMOS-N IFUs, fibers along the output pseudo-slit are grouped into blocks of 50, with median inter-fiber spacings on the detector of 3.5, 6.4, and 5.7 pixels respectively for IMACS- $f/2$, IMACS- $f/4$, and GMOS-N. Figure 3-3 shows a cross-section through an IMACS- $f/2$ model flat for two 50-fiber blocks. Fibers are approximately equally-spaced within the blocks, and we use this fact to our advantage to locate and trace all 50 fibers in a block at once. For the purpose of locating block positions relative to one another, our automatic tracing routine also makes use of a table of inter-block separations in units of the approximate local inter-fiber spacing (which will be independent of pixel scale), which is determined once for each IFU by a careful analysis of a model-flat cross section.

The necessary first step in tracing all spectra in the model-flat image is to locate all peaks in a cross section in order to define starting positions for the traces. Our strategy for initial peak location is as follows:

1. Choose a starting column in the image and fit a cubic spline to the cross-section through the model flat along that column. The cross section may be a median cross-section for a small (~ 10 -column) neighborhood about the starting column, and may be modestly smoothed to suppress noise peaks.
2. Solve the spline analytically for all local maxima along the cross section, rejecting peaks at which the spline value is less than some fraction of the median cross-section data value (typically ~ 0.4 : this rejects low-level peaks in the block gaps).
3. Determine the median inter-peak separation in rows, and associate as contiguous blocks any succession of peaks with neighbor-to-neighbor separations between 0.5 and 1.5 times the median inter-peak separation.
4. Working inward from a specified edge of the CCD, locate the first contiguous block of 50 peaks. Determine the identity of this block based on the number of peaks passed over before locating it. (Our implementation of this step assumes that no spurious peaks are counted, and that a contiguous 50-fiber block is found before 50 peaks have been missed. In practice these have been safe assumptions.)
5. Starting from the identified block, use a table of inter-block separations in units of the approximate local inter-fiber spacing to guess the position of the next block, and guess the inter-fiber spacing within this next block to be the same as in the identified block. Explore a grid of possible positions and inter-fiber separations for this next block about the guess values. Define the best position and fiber-separation for the new block in the cross section by maximizing the sum of spline-interpolated values at the 50 peak positions predicted by the given trial block-position and fiber-spacing values.
6. Repeat step 5, working outward on the CCD until all 50-fiber blocks have been located with their positions and inter-fiber separations in the cross section.

To trace the full model-flat images, we take the starting positions and inter-fiber separations for each block in the starting column and proceed to solve for positions and inter-fiber separations in successive columns with the same optimization described in step 5 above. Guess values for a block are taken from the values for that same block in the previously-solved column, and a non-linear optimization (using the IDL `POWELL` procedure) is used instead of a grid search. The tracing process can be made faster by only solving every 10 to 20 columns, since the tilt of the traces relative to the CCD rows is rather slight. The final trace solution is stored as low-order polynomial fits to block-position and fiber-separation as a function of CCD column for each block. To account for slight deviations from equal fiber spacing, we calculate flux-weighted centroids within a small range about the predicted trace positions for all fibers, and define a “tweak” to be added to each fiber-trace position as the median difference between this centroid-trace and the trace position from the 50-fiber solution along the entire spectrum. We note that directly tracing using flux-weighted centroiding is not feasible because the proximity of fiber spectra to one another leads to widespread jumping of traces between fibers. Our method prevents this by tying the centroiding to the more stable 50-fiber solution.

3.3.3 Scattered-Light Subtraction

All IMACS and GMOS-N spectroscopic exposures exhibit a non-negligible scattered-light background not directly associated with the flux through the fibers, as evidenced by non-zero count levels in the inter-block regions where the flux from the fibers drops essentially to zero. For all IFU frames used in this work—arc, flat, and object—we subtract a model of this background after pixel-flat correction. We estimate this scattered-light image from the observed levels between the fiber blocks. We use the flat-field-derived trace solution to define bands in the inter-block regions running parallel to the spectra, with a reasonable buffer to avoid the wings of the fiber cross sections. Each band is fit with a b-spline as a function of column, and this fit is subsequently evaluated for each column. We then interpolate this fit across the fiber blocks by fitting a b-spline in each column, taking the band centers in that column as independent variables and the previous-fit evaluations in that column as dependent variables. The b-spline breakpoint spacing in each fit may be adjusted according to the signal-to-noise in the scattered light levels and the degree of structure that one wishes to model.

3.3.4 Wavelength Calibration

We establish wavelength calibration using exposures of He-Ne-Ar (for IMACS) and Cu-Ar (for GMOS-N) arc lamps. Determination of a single global wavelength solution is not practical, since the 50-fiber blocks that make up the pseudo-slit image have discrete offsets in the dispersion direction relative to one another, and individual fibers within a block often have their own offsets (see Figure 3-4). Therefore, we determine an individual dispersion solution for each fiber on each CCD. We first process arc images by subtracting the bias level, dividing by a pixel flat, and subtracting a scattered-light image model. We then use the traces determined for the most closely-associated (in time) spectroscopic flat, globally shifted slightly if needed for alignment, to perform a boxcar extraction of the arc image. This results in one arc spectrum for each fiber on each CCD. We identify a few bright lines on each CCD which we use to determine an approximate wavelength solution for each fiber, which we then use to predict approximate positions for a set of ~ 10 – 20 reference lines. The centroids of these lines are found in each spectrum by simultaneously fitting fixed-width Gaussian and Gaussian-derivative profiles at the predicted positions in the spectra (weighting by extracted inverse-variance spectra), with the Gaussian-derivative coefficient giving a linear approximation to the necessary profile shift. The determined shifts are applied, and the process is iterated several times. Peaks whose determined positions differ from their initially-predicted positions by a value greater than some reasonable threshold are rejected and masked from dispersion-solution fitting. After the initial peak-finding iteration, the peak positions are held fixed, and a new fit is performed using a Gaussian profile and a profile representing the derivative of that Gaussian with respect to its width. A few iterations of this fit provide a measurement of the variation of extracted line-spread-function widths across the arc image, and allow for a final peak-finding iteration using measured line-profile widths rather than an assumed fixed width. The final set of peak positions is fit with a set of polynomial functions (typically 3rd to 6th order) giving CCD column as a function of wavelength for each fiber. The median line-spread width for each fiber is saved for later use (§ 3.3.6).

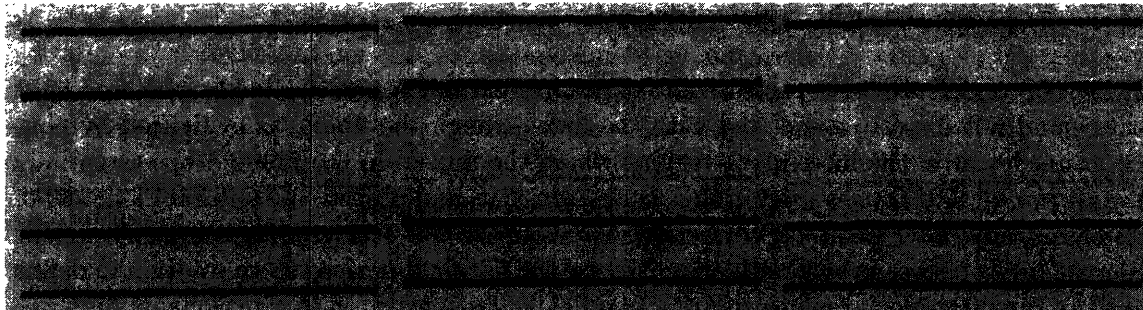


Figure 3-4: IMACS- $f/4$ He-Ne-Ar IFU image subsection, showing discrete offsets between neighboring blocks and individual-fiber offsets within blocks. We show $f/4$ data rather than $f/2$ because of the finer fiber PSF sampling. Image has been rotated to put dispersion in the vertical direction. Darker pixels represent higher counts

3.3.5 Extraction

IMACS and GMOS-N IFU observations distribute the photons from a few dozen square arcseconds of the sky over a few tens of millions of CCD pixels. Thus for all but the brightest objects, low signal-to-noise is a danger. This fact combined with the well-behaved profile of the IFU fibers on the CCD suggests optimal spectrum extraction as a natural approach (e.g. Hewett et al. 1985; Horne 1986). In an optimal extraction, the specific flux of a spectrum at a given wavelength is determined not from a simple sum over pixels within a boxcar aperture, but rather from the amplitude of a maximum-likelihood fit at that wavelength of a model to the observed spatial profile of the spectrum (i.e. the one-dimensional flux density orthogonal to the dispersion axis). This gives the maximum signal-to-noise in the extracted spectrum, and is unbiased to the extent that the model matches the actual profile. The most immediate obstacle to optimal extraction of IMACS and GMOS-N IFU data (aside from the sheer number of spectra) is the significant overlap between neighboring spectra (see Figure 3-3). If we knew the form of the fiber profile, the spectra could be de-blended from their neighbors by simultaneous fitting (through the solution of banded-diagonal linear systems for the fiber spectral intensities within each block), but the correct profile model cannot be readily determined as a consequence of the overlap. Fortunately the situation is less problematic for fiber-fed IFUs such as those of IMACS and GMOS-N than for multi-object multi-fiber spectrographs, since adjacent fibers on the detector are also adjacent on the sky (an explicit design feature). Since the $0''.2$ -diameter IFU lenslets will critically sample all but the very best ground-based seeing, the blending of neighboring fiber spectra on the detector leads to no significant loss of information (Allington-Smith et al. 2002). Nevertheless, even putting aside the problem of deblending, correct modeling of the fiber profile over the entire detector would seem to be a daunting chore (see Viton and Milliard 2003). Happily, the model flats described in § 3.3.2 provide us with a high signal-to-noise determination of the spatial profile for all fibers and at all wavelengths.

We first normalize the model flats by dividing out a crude approximation to the flat-field lamp spectrum. This step is not crucial (particularly if one eventually performs an absolute flux calibration), but it prevents the lamp spectrum from being imprinted on the data before flux calibration. Using the model-flat trace solution, we perform a boxcar extraction of the scattered-light-subtracted model-flat frames. The resulting spectra for each fiber are divided by their individual median values, to correct roughly for varying fiber throughput. We then fit a smooth b-spline model to the set of all normalized spectra, with wavelength as

an independent variable taken from an appropriate arc-frame dispersion solution. We make a single fit for all CCDs on the detector so as to preserve accurate flatfielding across CCDs; we rescale the values for individual CCDs before fitting to account for gain differences. With the crude lamp spectrum in hand, we assign a wavelength to each pixel in the full model-flat image by linearly interpolating the single-fiber dispersion solutions between traces. We then divide each pixel in the model flat by the model lamp-spectrum value at its wavelength. We note that it is not important to use an exceedingly accurate model of the lamp spectrum, but only to divide all pixels with the same wavelength by the same value. Finally, we divide each model-flat image by the median value over all CCDs covering the same wavelength domain.

Following this process, the normalized model flats are suitable for use in extracting spectra from the pixel-flat corrected and scattered-light-subtracted object frames. Before extracting, we shift the model flats perpendicular to the dispersion direction with a flux-conserving damped-sinc kernel¹ so as to maximize the cross-correlation between the model-flat image and the object-frame image. This shifting of the model flat accounts for the slight (typically of order 1 pixel or less) flexure that can occur between the object frames and the flat frames taken immediately following. Our approach to extraction is described mathematically as follows. We define boundaries between fiber spectra by lines exactly half-way between the fiber traces, and in each CCD column i we associate with fiber j all pixels (i.e. rows) k falling between the boundaries on either side. Pixels split by the boundary are associated fractionally (see Figure 3-5). Let $w_k^{(i,j)}$ express this weighting: $w_k^{(i,j)} = 1$ for rows k wholly within the boundaries for fiber j in column i , 0 for rows wholly outside, and between 0 and 1 for rows fractionally included. Let d_{ik} be the data frame to be extracted, σ_{ik}^2 be the statistical variance of d_{ik} , and f_{ik} be the aligned, normalized model flatfield image of the fiber response. The optimally extracted specific flux in fiber j at column i (corresponding to a particular wavelength by the dispersion solution for that fiber), which we denote I_{ij} , will be given by the value that minimizes

$$\chi^2 = \sum_k w_k^{(i,j)} (d_{ik} - I_{ij} f_{ik})^2 / \sigma_{ik}^2 , \quad (3.1)$$

which is

$$I_{ij} = \sum_k w_k^{(i,j)} f_{ik} d_{ik} / \sigma_{ik}^2 \bigg/ \sum_k w_k^{(i,j)} f_{ik}^2 / \sigma_{ik}^2 . \quad (3.2)$$

A simple adjustment of this expression suggests a more succinct conceptual and operational approach:

$$I_{ij} = \sum_k (d_{ik} / f_{ik}) (w_k^{(i,j)} f_{ik}^2 / \sigma_{ik}^2) \bigg/ \sum_k w_k^{(i,j)} f_{ik}^2 / \sigma_{ik}^2 . \quad (3.3)$$

This instructs us to obtain the optimally extracted specific flux by dividing the data image by the model-flat image, then computing a weighted average over the appropriate fiber/column window, with the statistical weight given by the product of the squared model-flat image and the inverse-variance image. We implement the extraction algorithm in this manner. We note that although the absolute extracted flux values are not meaningful unless and until they are flux-calibrated, the flat-fielding procedure produces well-calibrated

¹The damped sinc function is defined as the usual sinc function times an additional Gaussian damping envelope; the image shifting is implemented by the SSHIFT2D function in IDL.

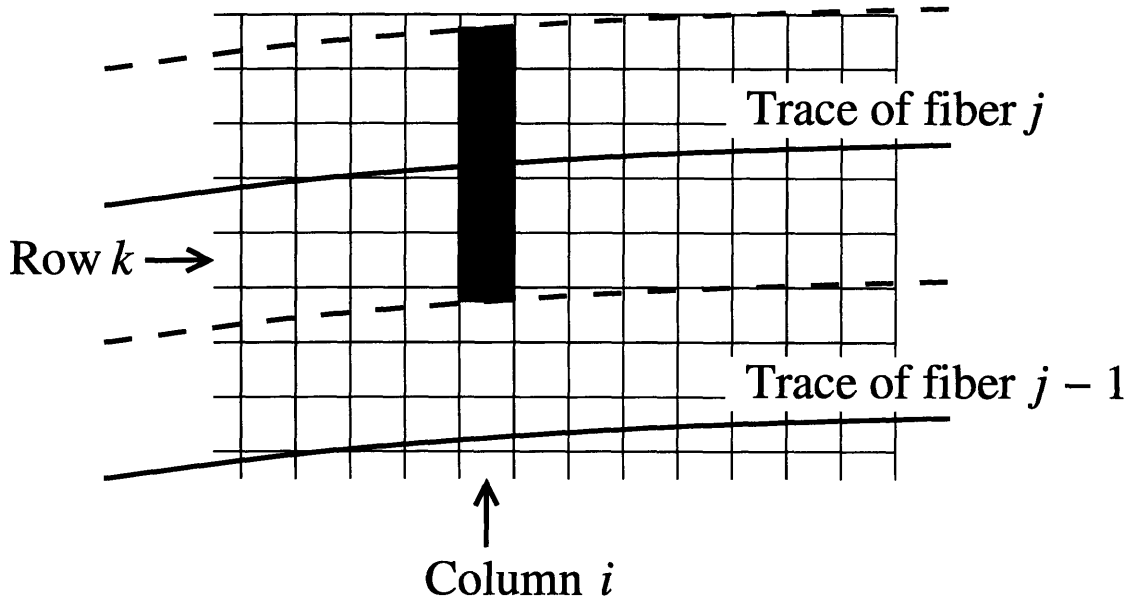


Figure 3-5: Diagram of association of pixels with a specific fiber j in a specific CCD column i , shown in gray. Tilt of traces with respect to CCD pixel grid is exaggerated.

specific flux (flux per unit wavelength) measurements in a relative sense at any given wavelength across the entire spatial field.

The optimal-extraction technique also provides a natural means for rejecting cosmic-ray (CR) hits in single exposures, because cosmic rays generally will not have the same shape as the fiber cross section. We flag pixels with highly statistically significant positive deviations between the data frame and the optimal-extraction model frame as CR pixels and grow the resulting CR mask to laterally-adjacent pixels, then repeat the extraction with CR pixels given zero weight. Figure 3-6 illustrates various elements of the image extraction process for a small subregion of one IMACS CCD.

We store the extracted IFU object spectra for each CCD in the IMACS and GMOS-N mosaics as a separate image extension in a single MEF file for a single exposure. These spectrum images have a horizontal dimension equal to that of the CCD and a vertical dimension equal to the number of fibers with spectra falling on the CCD, and are not rectified in wavelength but rather have a unique wavelength sampling for each spectrum. We note here that storing the data in this two-dimensional spectrum-image form instead of in the “data-cube” form of two spatial dimensions by one spectral dimension affords a distinct advantage even for wavelength-rectified data (§ 3.3.7) in that it preserves the integrity of the detector frame. To determine the best wavelength solution for each object frame, we take the multifiber dispersion solution from an appropriate arc frame, and use night-sky emission lines to determine a slight shift, tilt, and rescaling in CCD coordinates in order to compensate for spectrograph flexure among science frames and between science frames and the calibration-arc frame. We use the resulting dispersion solutions to generate complementary images that give the wavelength of each data pixel in the extracted spectrum images.

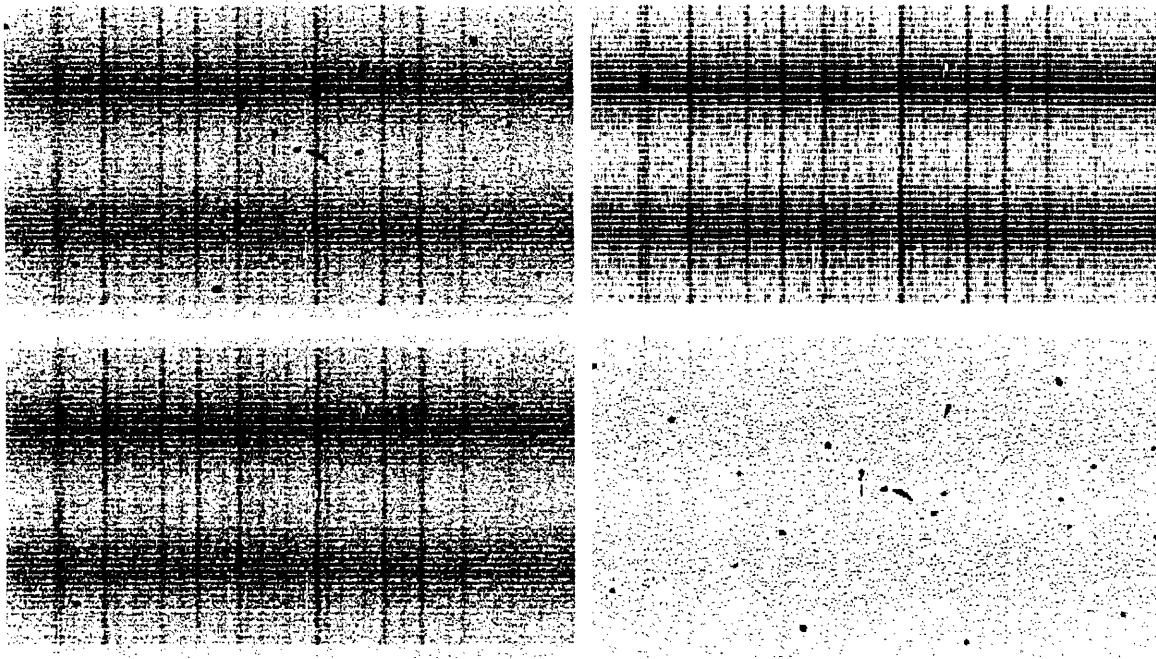


Figure 3-6: Optimal extraction of IMACS-*f*/2 IFU data with a normalized model spectroscopic flat-field image. Darker pixels represent higher counts. Upper left: 50-fiber subsection of a raw IFU spectroscopic observation, covering approximately 400Å. Galaxy-continuum spectra from individual fibers run horizontally, and night-sky emission lines run vertically. Upper right: optimal-extraction image model obtained by fitting normalized spectroscopic model flat to data as described in § 3.3.5. Model image is undetermined in regions heavily affected by cosmic-ray hits. Lower left: data image after model-based cosmic-ray rejection. Cosmic-ray pixel values have been replaced with extraction-model values where possible. Lower right: Residual image (upper right subtracted from upper left.)

3.3.6 Sky Subtraction

There is a distinct advantage in the estimation and subtraction of the night-sky spectrum before performing any rectification in wavelength (e.g. Kelson 2003). The multiple fibers of the IFU fields of view each have a slightly different sampling in pixels on the detector, and hence the discrete line-spread function (LSF) observed for night-sky emission lines depends upon the sub-pixel location of the line’s central wavelength. The native binning of the CCD, when considered for all blank-sky fibers together, provides a finely subsampled observation of the night sky spectrum. We thus fit a b-spline model to this data as a function of the central wavelength of each native spectral pixel, which we then evaluate for all fibers (object and sky) and subtract as our sky model. The extracted one-dimensional LSF of the IMACS and GMOS-N IFUs exhibits some variation due to global distortions and fiber-optic heterogeneity, which we parametrized to leading order as a varying LSF width as measured for each fiber from arc frames as described in § 3.3.4 above. This LSF width is then treated as a second independent variable in the b-spline model, fitted with linear dependence. Results of this sky subtraction method in an *I*-band region of strong OH rotational lines can be seen in Fig. 3-7, for a faint galaxy observed at high airmass.

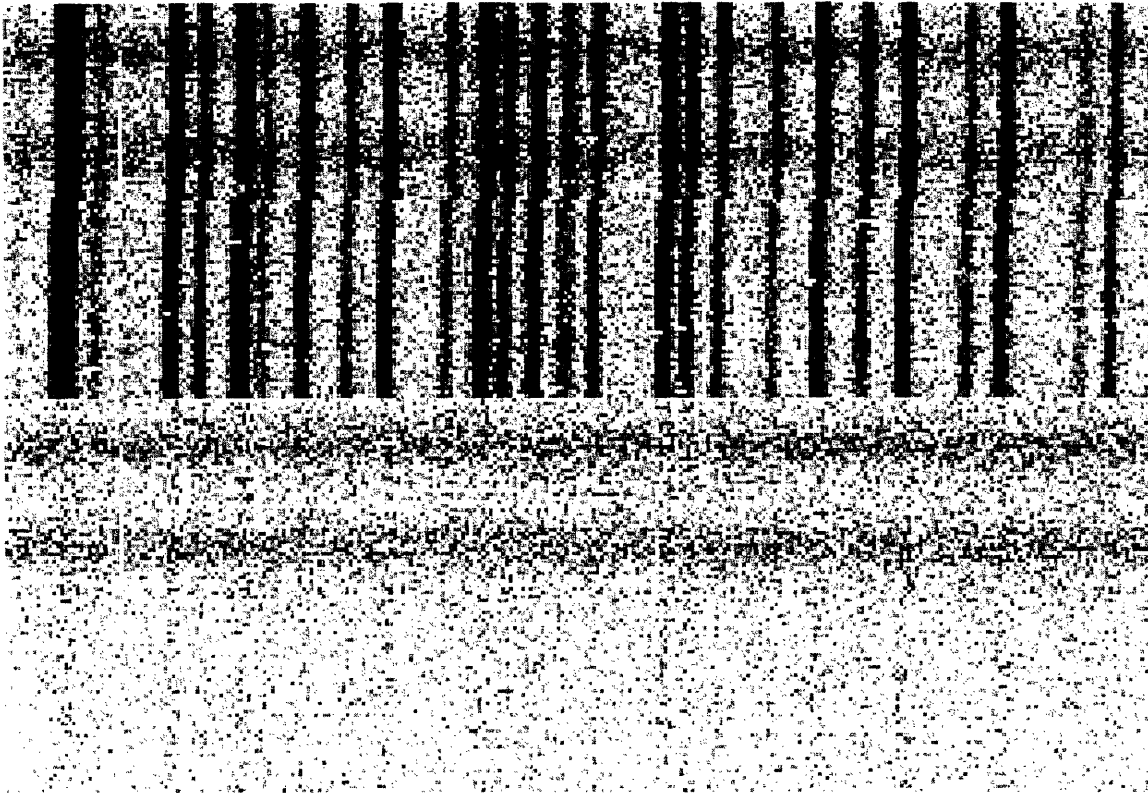


Figure 3-7: 100 extracted fiber spectra (50 object and 50 background) in the range 7795–8075 Å of a faint galaxy observed at high airmass. Spectra are shown before and after sky-model subtraction (top and bottom, respectively). Darker pixels represent higher counts.

3.3.7 Rectification and Combination

To facilitate the combination of multiple exposures (and to make analysis more straightforward), we rebin our sky-subtracted IFU spectra onto a uniform wavelength baseline. We use a constant-wavelength binning across a spectrum, with bin size slightly larger than the largest native pixel-width, so that only nearest-neighbor correlations will be present in the rebinned frames. The wavelength-bin boundaries are specified in heliocentric vacuum wavelengths, corrected with a heliocentric velocity shift appropriate to each observation, converted to air wavelengths, and mapped into the extracted IFU frames using the arc-frame dispersion solution as adjusted based on night-sky emission lines. Multiple exposures are then combined after re-binning, with further cosmic-ray rejection. Finally, the rebinned data from individual CCDs are combined onto a single mosaic image with the orientation of the detector mosaic. As a data product, we prefer this mosaic to a three-dimensional “data cube” (2 spatial plus 1 spectral dimension) because it allows the reduced data to be displayed all at once in the frame of the detector. Data cubes may always be constructed using the fieldmapping. We do not rebin our data spatially, since all observations were made with single undithered telescope pointings.

3.4 Gravitational-Lens Modeling with IFU Data

In this section we describe the analysis techniques that we apply to our lens-candidate IFU data. We construct narrowband images of all systems at the wavelength of background-redshift line emission, and carry out gravitational-lens modeling for systems that show lensing morphology at sufficient signal-to-noise ratio and sufficient spatial resolution.

3.4.1 Narrowband Image Reconstruction

Figure 3-8 shows an excerpt of extracted, sky-subtracted, and wavelength-rectified IFU spectra for SDSSJ0037–0942, one of our newly discovered lens systems. (The full catalog of lenses is presented in § 3.4.3 below.) We wish to use data in this form to reconstruct narrowband images in the focal plane at the wavelength of background-galaxy line emission, to be analyzed for gravitational-lensing morphology. The two main challenges are (1) clean separation of the respective contributions from foreground and background galaxies, and (2) maximization of the signal-to-noise ratio in the resulting narrowband images. We address these issues by adopting a strategy of simultaneous emission-line and continuum fitting. To a very good approximation (and largely as a consequence of our initial selection bias), continuum emission seen in the IFU spectra of our lens candidates can be attributed to the foreground galaxy. Similarly, line emission at the known background redshift is almost certainly from the background galaxy (barring a coincidence in observed wavelength between distinct emission lines in the foreground and background galaxies, which has been controlled in the original candidate selection by avoiding common emission-line wavelengths in the rest frame of the foreground galaxy). We begin our fitting procedure by assuming a Gaussian profile for the emission line with a best-guess width and central wavelength, and by assuming a flat continuum. For these parameters, we generate two spectral basis functions (line and continuum) over a small fitting region in the neighborhood of the emission feature (typically of order 10 to 20 Å wide). We then make a linear fit to the spectrum in each object fiber over the fitting range in wavelength using these basis functions, and calculate a total χ^2 over all object fibers. This linear fit is wrapped within a non-linear fit that minimizes the global χ^2 value by adjusting the emission-line and continuum parameters (line width, line position, and dimensionless continuum slope) used to generate the basis functions. The linear-fitted coefficients of the final basis functions are then our best decomposition of the spectrum into emission-line and foreground components. Figure 3-8 also shows the model fitted to the spectrum in this manner for a subset of the full object-fiber set.

With the emission-line and continuum coefficients from each fiber, we can form narrowband images in the focal plane of the telescope using the known IFU field mapping. Figure 3-10 shows continuum and emission-line narrowband images of SDSSJ0037 at the position of [O III] 5007 emission at the background redshift of 0.6322: this and other lenses are discussed in detail individually in § 3.4.3. We use the narrowband continuum image for flux calibration at our wavelength of interest by summing all lenslets within a 3''-diameter aperture centered on the foreground galaxy and scaling to the calibrated SDSS specific flux for the galaxy, which corresponds to the same approximate aperture.

3.4.2 Lens Modeling

We analyze all candidate lens systems uniformly by fitting a singular isothermal ellipsoid (SIE) mass model to the observed emission-line image configurations. The SIE model is well

motivated, simple, analytic, and able to reproduce all qualitative features of galaxy-scale strong lenses. (A related model, the singular isothermal sphere with external shear, also offers these advantages.) The convergence (scaled surface density) of the SIE model in the frame of its own principal axes is given by

$$\kappa_{\text{SIE}} = \frac{1}{2} \frac{b}{R_q} \quad , \quad (3.4)$$

where

$$R_q = \sqrt{qx^2 + y^2/q} \quad (3.5)$$

and x and y are angular coordinates in the plane of the sky. The dependence of the model on x and y only through R_q means that all isodensity contours are aligned, similar, concentric (but not confocal) ellipses. This symmetry is termed *homoeoidal* since the rings bounded by differentially separated isodensity contours fit the geometric definition of homoeoids. The parameter b expresses the strength of the lens and q gives the minor-to-major axis ratio of the iso-density contours (hence $0 < q \leq 1$ by convention). When $q = 1$, the SIE reduces to the singular isothermal sphere (SIS) and b is equal to the Einstein radius of the model, which is related to the velocity dispersion σ of the lensing distribution through

$$b_{\text{SIS}} = 4\pi \frac{\sigma^2}{c^2} \frac{D_{\text{LS}}}{D_{\text{S}}} \quad . \quad (3.6)$$

(D_{LS} and D_{S} are angular-diameter distances from lens to source and observer to source.) For purposes of comparison between models with differing q values, we adopt the same intermediate-axis normalization as Kormann, Schneider, and Bartelmann (1994), whereby the mass interior to a given iso-density contour at fixed b is constant with changing q . The lensing potential ψ of the SIE may be expressed analytically (Kassiola and Kovner 1993; Kormann et al. 1994), but for our purposes we need only its derivatives, which we adopt in the form given by Keeton and Kochanek (1998) and converted to our normalization:

$$\psi_x = \frac{b}{\sqrt{q^{-1} - q}} \arctan \left[\frac{(\sqrt{q^{-1} - q}) x}{R_q} \right] \quad , \quad (3.7)$$

$$\psi_y = \frac{b}{\sqrt{q^{-1} - q}} \operatorname{arctanh} \left[\frac{(\sqrt{q^{-1} - q}) y}{R_q} \right] \quad . \quad (3.8)$$

These give the (negative) components of the angular deflection that map image-plane coordinates to source-plane coordinates (e.g. Narayan and Bartelmann 1996). One may verify that these expressions satisfy the two-dimensional Poisson equation:

$$\nabla^2 \psi = \frac{\partial}{\partial x} \psi_x + \frac{\partial}{\partial y} \psi_y = 2\kappa_{\text{SIE}} \quad . \quad (3.9)$$

We perform all lens modeling with our own IDL routines. Our precise modeling recipe varies somewhat from system to system and is discussed in more detail in § 3.4.3. As is always the case when fitting gravitational lens models, we must take care not to fit for more parameters than are constrained by the data; fortunately the SIE is generally free from fundamental degeneracies among its parameters with regard to the constraints furnished

by observations of real lenses. To summarize the process, we start with an educated guess for the parameters of the lens model, which we use as a starting point for a nonlinear optimization that seeks to minimize the scatter among the approximate measured image positions as mapped back into the unlensed source plane. The lens parameters and average source-plane position that result from this procedure can then be used as a starting point for routines that handle errors correctly and calculate χ^2 in the image plane. For some lenses, we constrain the center of the lensing potential to be coincident with the center of the lensing galaxy, which we determine by fitting a Sérsic model to the IFU continuum image. For lenses consisting of unresolved images, we fit the images with hexagonally-sampled Gaussians (constrained to have the same width as one another). The image positions and fluxes from these fits are then used to constrain the lens model, which we optimize via nonlinear minimization of χ^2 with respect to the parameters of the lens model (and unlensed source position and flux). Taking image fluxes as lens-model constraints would be a dubious maneuver for quasar lenses, in which the small physical size of the continuum region gives rise to large microlensing effects on the fluxes of lensed images. In this paper we are concerned with lensed narrow-emission-line regions which should be of sufficient physical size to average over these microlensing effects (Drozdovsky et al. 2005), and thus incorporating image fluxes as lens-model constraints is a reasonable approach unless and until we see flux ratio anomalies similar to those seen in quasar lens systems. We note that we are also ignoring any possible effects of differential extinction as a function of position in the lens galaxies, under the assumption that our quiescent early-type lens sample is relatively free of dust. For lenses showing extended emission-line brightness distributions, we fit for lens and source parameters by generating an unlensed source-galaxy image (either Gaussian or Sérsic, with ellipticity if necessary) and viewing it through the potential of the parametrized lens model. This image is then smeared by a Gaussian PSF model (whose width is fit as another free parameter), integrated over the hexagonal IFU lenslets, and used to calculate χ^2 directly relative to the narrowband IFU data. We expect appreciable degeneracies between best-fit model parameters (i.e. between the PSF width and the intrinsic source size), but the parameter of greatest interest to us—the model’s Einstein radius—is largely orthogonal to the others. Quoted errors on the Einstein radius are square-root-diagonal entries from the covariance matrix of the nonlinear fit unless otherwise noted. The non-linear optimization is performed with the Levenberg-Marquardt method as implemented in the MPFIT function in the IDL language, which in turn calls MINPACK-1 software (Moré and Wright 1993).

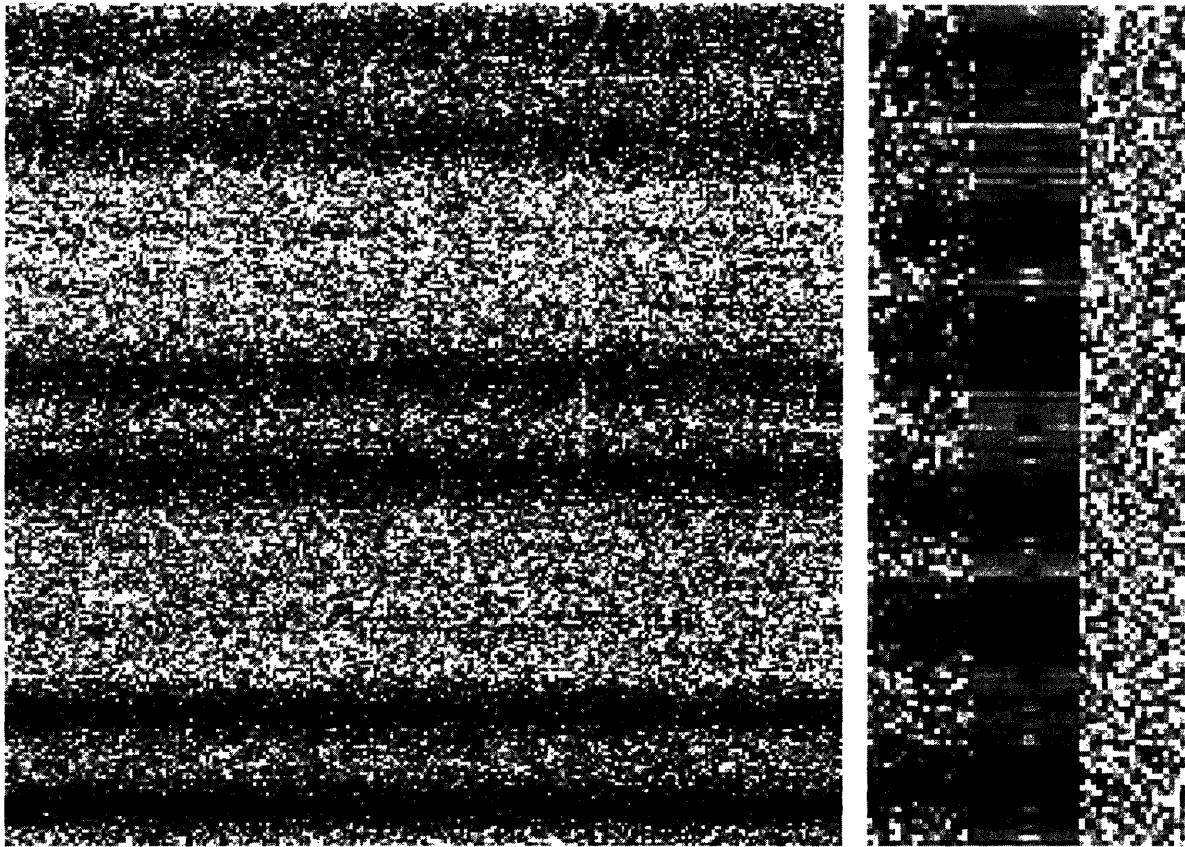


Figure 3-8: Narrowband spectral component modeling. Left: Excerpt of extracted, sky-subtracted, and wavelength-rectified spectral data for SDSSJ0037. Individual rows of pixels correspond to 250 individual fibers (150 object and 100 sky, interspersed in blocks of 50 as on the detector), and columns correspond to unique wavelengths (ranging from 7920Å at left to 8268.6Å at right). Prominent spots are redshifted [O III] 4959 and [O III] 5007 emission. Right: 150 object-fiber spectra from data at left in a 27-Å window centered on redshifted [O III] 5007 emission. Shown from left to right are data, model fitted to data using continuum and emission-line basis functions in each fiber, and residuals (data – model). Darker pixels represent higher counts.

3.4.3 The Lenses

SDSSJ0037–0942

SDSSJ0037–0942 was observed on the night of UT 2004 September 18 with 2×1200 s in the IMACS-2 configuration. The $1\text{-}\sigma$ line threshold at 8174 \AA was approximately $1.2 \times 10^{-17} \text{ erg cm}^{-2} \text{ s}^{-1} \text{ arcsec}^{-2}$. Figure 3-10 shows continuum and emission-line narrowband images of SDSSJ0037 at the position of [O III] 5007 emission at the background redshift of 0.6322. The spatial separation between these two spectral components now becomes obvious, and we identify the system as a double gravitational lens (we address the question of alternative explanations to gravitational lensing in § 3.5 below). We confirm the background redshift by summing spectra in small ($\sim 1''.2$ -diameter) apertures about the emission-line image centers to give the spectrum shown in Fig. 3-9, revealing [O III] 4959 and $H\beta$. Vertical lines show the narrow wavelength window used to fit for the emission-line and continuum coefficients displayed in Fig. 3-10. Also shown is the [O II] 3727 doublet, which is detected at high significance.

For this unresolved double-image lens, we have six constraints: the RA, Dec, and flux for each image. Three unavoidably free parameters are the unlensed Ra, Dec, and flux of the source. The Einstein radius of the SIE model is another free parameter, as is the ellipticity of the lensing potential (our data are not sufficient to constrain the deconvolved ellipticity of the lensing galaxy, and in any event this ellipticity need not be the same as that of the total lensing mass distribution, i.e. luminous plus dark matter). We also fit for the position angle of the lensing distribution. We adopt the lens-galaxy centroid as a fixed center for the lensing potential, since the lens-model will otherwise be underconstrained. Thus in this case the number of free parameters in the lensing model is exactly equal to the number of constraints, and the best-fit model is able to reproduce the image positions and fluxes exactly. However, we note that the nonlinear nature of strong gravitational lensing implies that not all image configurations can necessarily be fit by a given model even if the numbers of constraints and free parameters are equal. The lens has a best-fit Einstein radius of $b = 1''.50 \pm 0''.01$. We also find significant alignment between the lens-galaxy isophotal major axis (position angle $(7 \pm 3)^\circ$ E of N) and the fitted lens-model major axis (position angle $(9 \pm 2)^\circ$ E of N); this supports our lensing interpretation and buttresses our choice of the SIE model, whose quadrupole moment is provided by intrinsic ellipticity rather than by external shear.

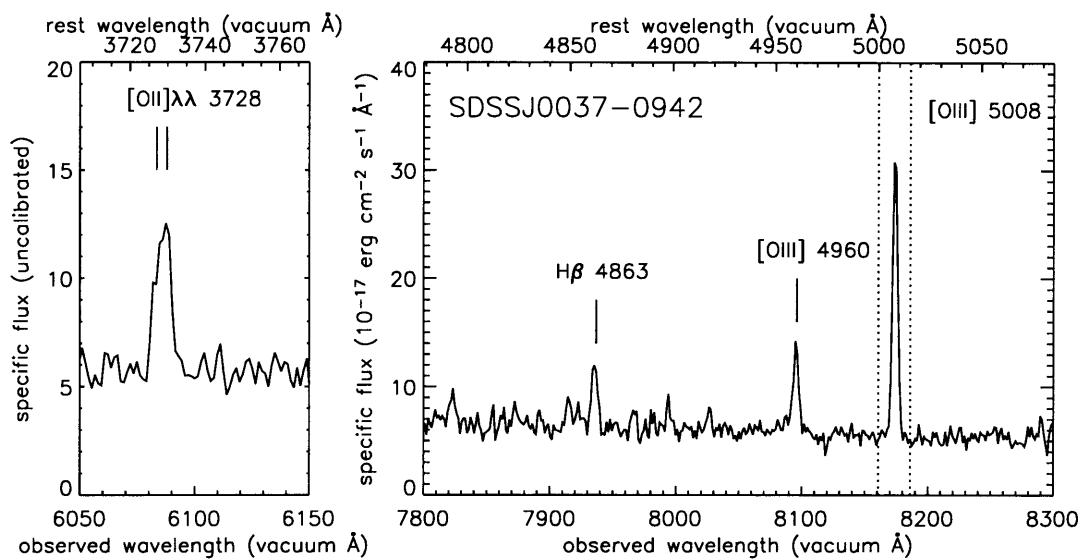


Figure 3-9: Summed spectra of SDSSJ0037 for fibers with significant background-redshift [O III] 5007 emission-line flux as seen in Fig. 3-10. Flux calibration is applied at the wavelength of redshifted [O III] 5007. The identity of the emission line as [O III] 5007 at redshift $z = 0.6322$ is confirmed by the clear detection of [O III] 4959 and $H\beta$, as indicated. Also shown with dashed lines is the wavelength range used to form the continuum and emission-line images of Fig. 3-10, and the blended [O II] 3727 doublet.

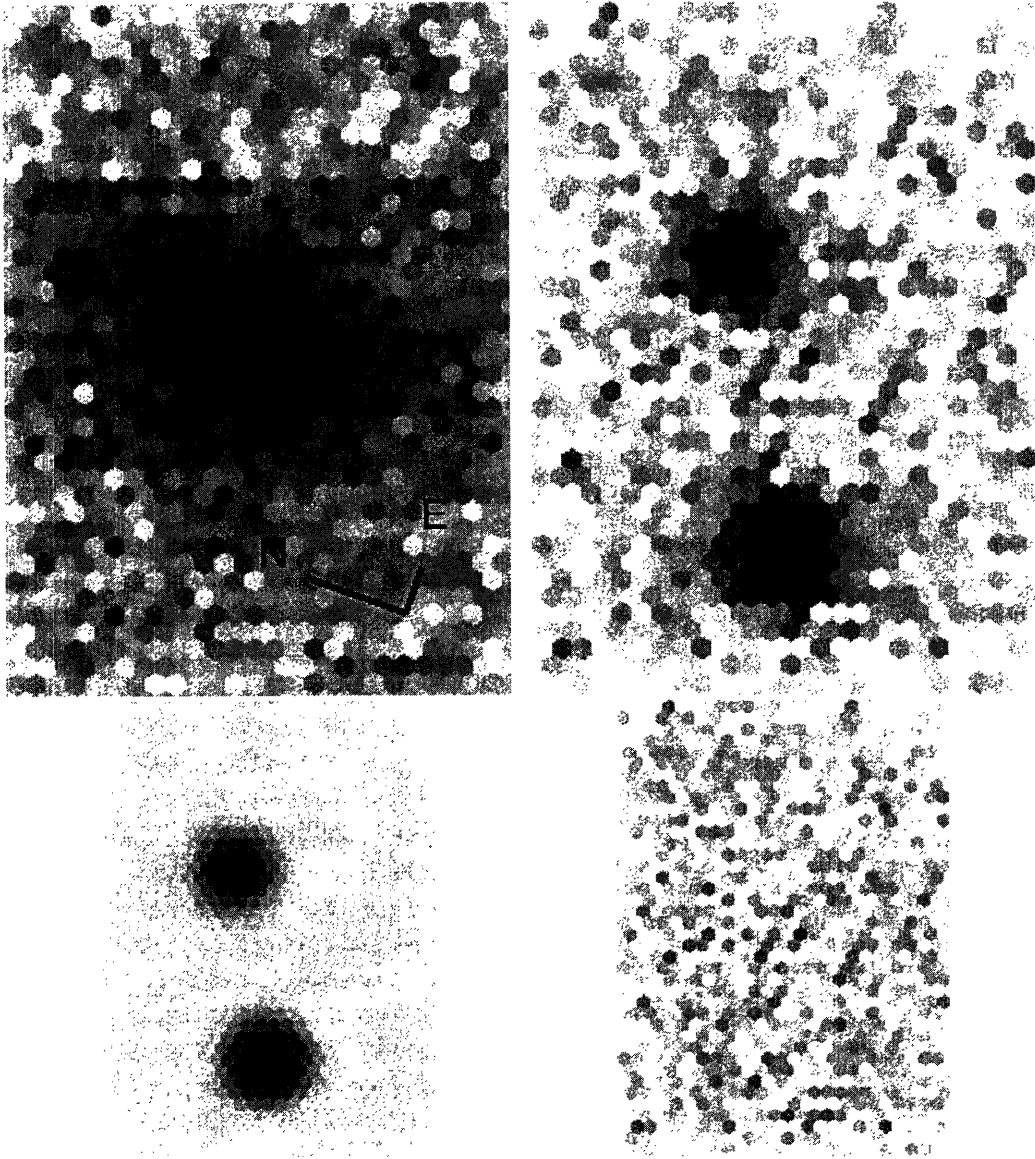


Figure 3-10: IMACS-2 IFU narrowband imaging of SDSSJ0037 at 8174 \AA , corresponding to redshifted $[\text{O III}] \ 5007$. Upper left panel shows reconstructed foreground-galaxy continuum image, with white-to-black scaling from -1 to $3 \times 10^{-18} \text{ erg cm}^{-2} \text{ s}^{-1} \text{ \AA}^{-1}$ per IFU lenslet. Upper right panel shows reconstructed emission-line image, with scaling from -1 to $4 \times 10^{-17} \text{ erg cm}^{-2} \text{ s}^{-1}$ per IFU lenslet. Lower left panel shows lenslet-integrated Gaussian image models used to determine image positions and fluxes for gravitational-lens modeling, and lower right panel shows residual image of upper right minus lower left.

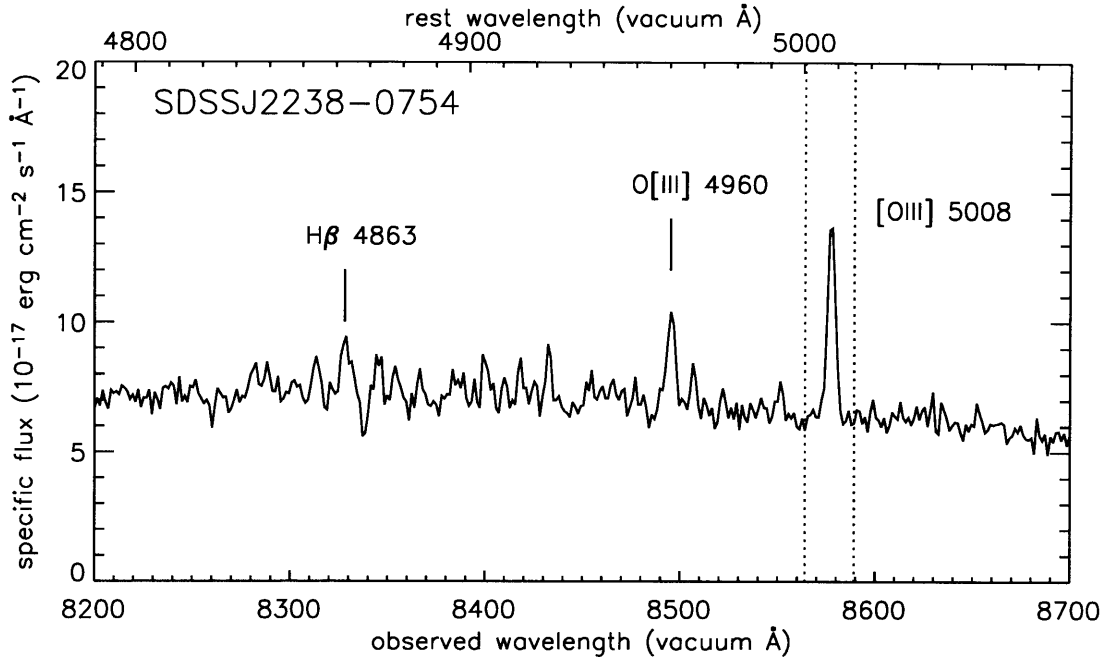


Figure 3-11: Summed spectra of SDSSJ2238 in $\sim 1''.2$ -diameter apertures about the emission-line image flux peaks seen in Figure 3-12

SDSSJ2238–0754

SDSSJ2238–0754 was observed on the night of UT 2004 September 18 in the IMACS-2 configuration with an exposure time of 3×1200 s. The target galaxy is at a redshift of $z = 0.1371 \pm 0.0001$, and the [O III] 5007 and [O II] 3727 doublets were both detected at high significance in the SDSS spectrum at a redshift of $z_{\text{BG}} = 0.7126$. These background emission-line detections were confirmed in the IFU data as seen in Fig. 3-11 for the [O III] 5007 doublet. The median total depth of the observations at 8577 \AA (the wavelength of redshifted [O III] 5007) over the IFU field of view gives a 1σ line flux in a 5-\AA window of approximately $8.4 \times 10^{-18} \text{ erg cm}^{-2} \text{ s}^{-1} \text{ arcsec}^{-2}$. Decomposing continuum and emission-line fluxes in the manner of § 3.4.1 reveals two tangentially stretched emission-line images surrounding the foreground galaxy, which we interpret as a strong-lens configuration. The brighter and more elongated of the images is slightly closer in angular position to the center of the foreground galaxy as would be the case for three merging images in a so-called “short-axis quad” (Saha and Williams 2003), which necessitates a quadrupole in the lensing distribution. The elongation seen in both images suggests modeling the system as a lensed extended brightness distribution. After finding an approximate solution through source-plane optimization as described above, we fit a model by parameterizing the lens as an SIE, the source (in the unlensed source plane) as a circular Gaussian, and the observational PSF as a Gaussian of unknown width. Our best-fit model has an Einstein radius of $b = 1''.24 \pm 0''.02$ and an axis ratio of $q = 0.74 \pm 0.03$.

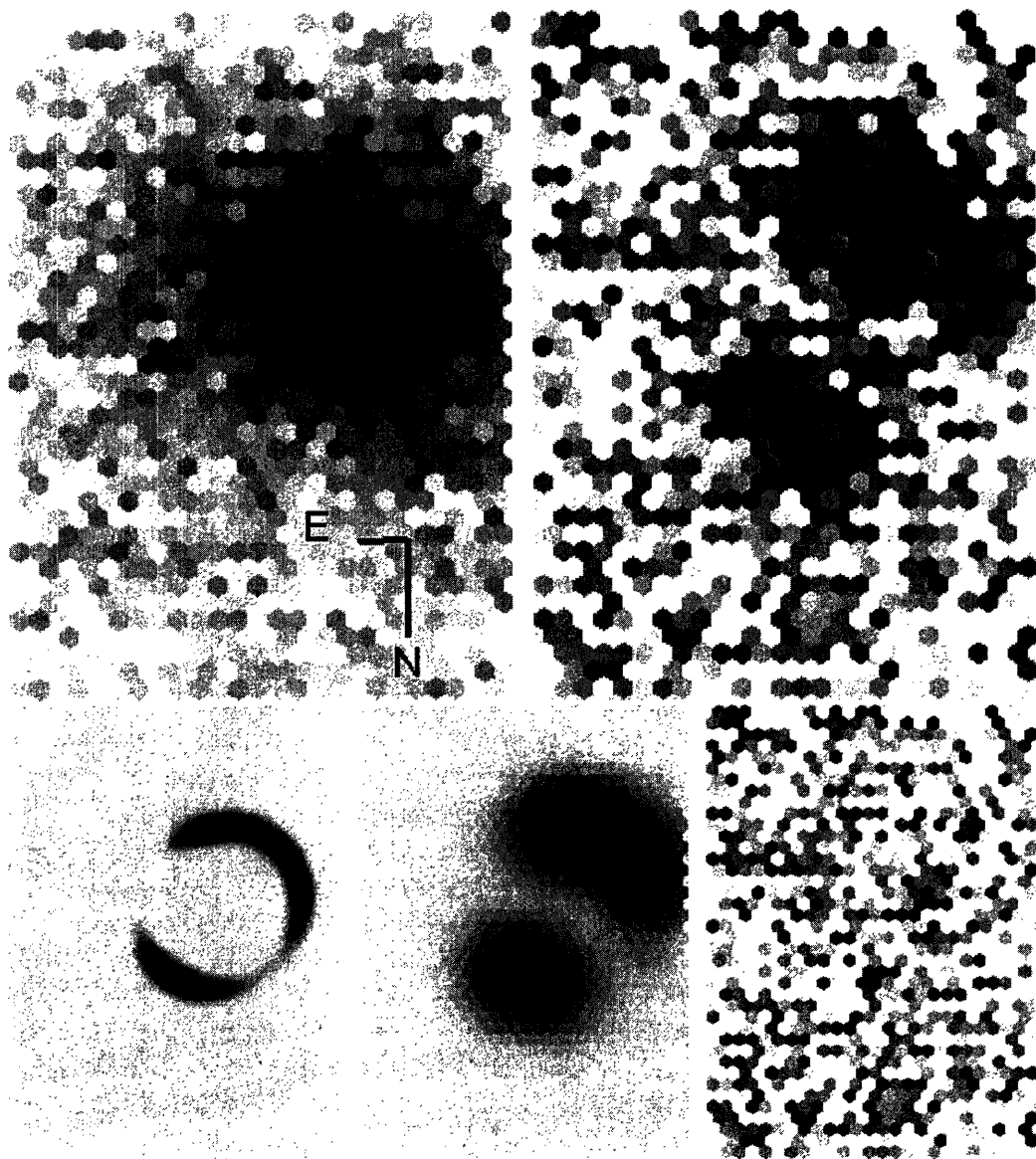


Figure 3-12: IMACS-2 IFU narrowband imaging of SDSSJ2238 at 8577 \AA , corresponding to redshifted $[\text{O III}] 5007$. Top left: continuum image. Top right: emission-line image. Bottom left: best-fit model gravitationally lensed emission-line image. Bottom center: model lensed image, suitably smoothed and sampled to match IFU data. Bottom right: residual emission-line image (top right minus bottom center). For continuum image, white-to-black scaling is from -5 to $25 \times 10^{-19} \text{ erg cm}^{-2} \text{ s}^{-1} \text{ \AA}^{-1}$ per IFU lenslet. For emission-line images, scaling is from -2 to $8 \times 10^{-18} \text{ erg cm}^{-2} \text{ s}^{-1}$ per IFU lenslet.

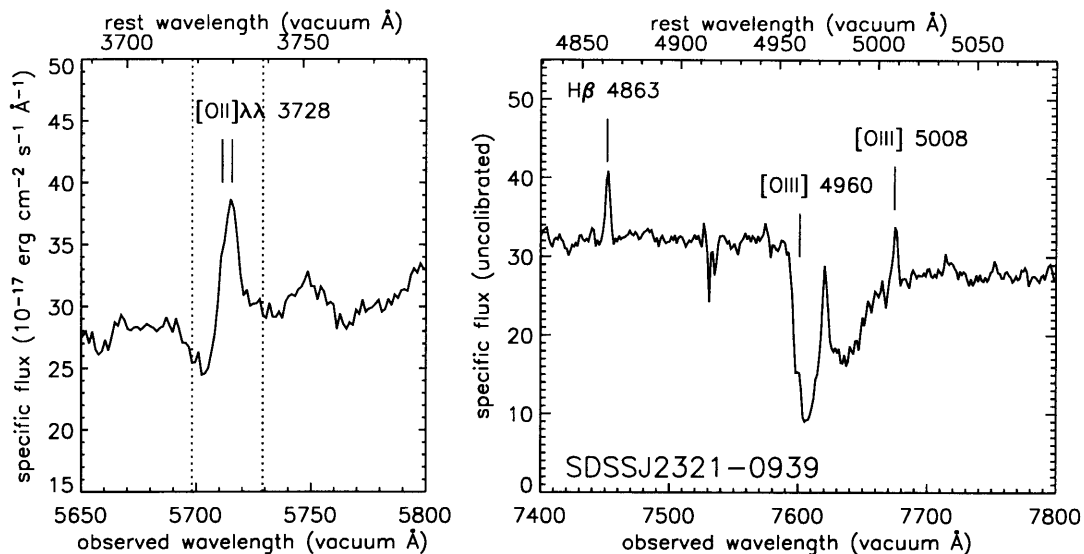


Figure 3-13: Summed spectra of SDSSJ2321 for fibers with significant [O II] 3727 emission-line flux as seen in Figure 3-14. Flux calibration is applied at the position of redshifted [O II] 3727 emission. The absorption feature at the position of [O III] 4959 is due to the telluric band of atmospheric O₂ absorption between 7590 and 7700 Å.

SDSSJ2321–0939

SDSSJ2321–0939 was observed on the night of UT 2004 September 18 in the IMACS-2 configuration with an exposure time of 2×1500 s. The [O II] 3727 doublet, H β , and [O III] 5007 are all detected in both the SDSS and IFU spectra (see Figure 3-13); [O III] 4959 falls deep within the A-band of atmospheric absorption and is not significantly detected. We construct narrowband and continuum images at the position of the redshifted [O II] 3727 doublet, which we parameterize as a double Gaussian with appropriate peak separation. The narrowband emission shows a clear ring structure which we may interpret as an Einstein ring image of the background galaxy. Figure 3-14 shows the narrowband IFU imaging for this system, along with the best-fit gravitational lens model and residuals. Our lens model is again based on an extended distribution, and we also allow for an intrinsic ellipticity and position angle of the background galaxy given the higher signal-to-noise ratio as compared with the SDSSJ2238 data. Our best-fit SIE model has an Einstein radius of $1''.52 \pm 0''.04$.

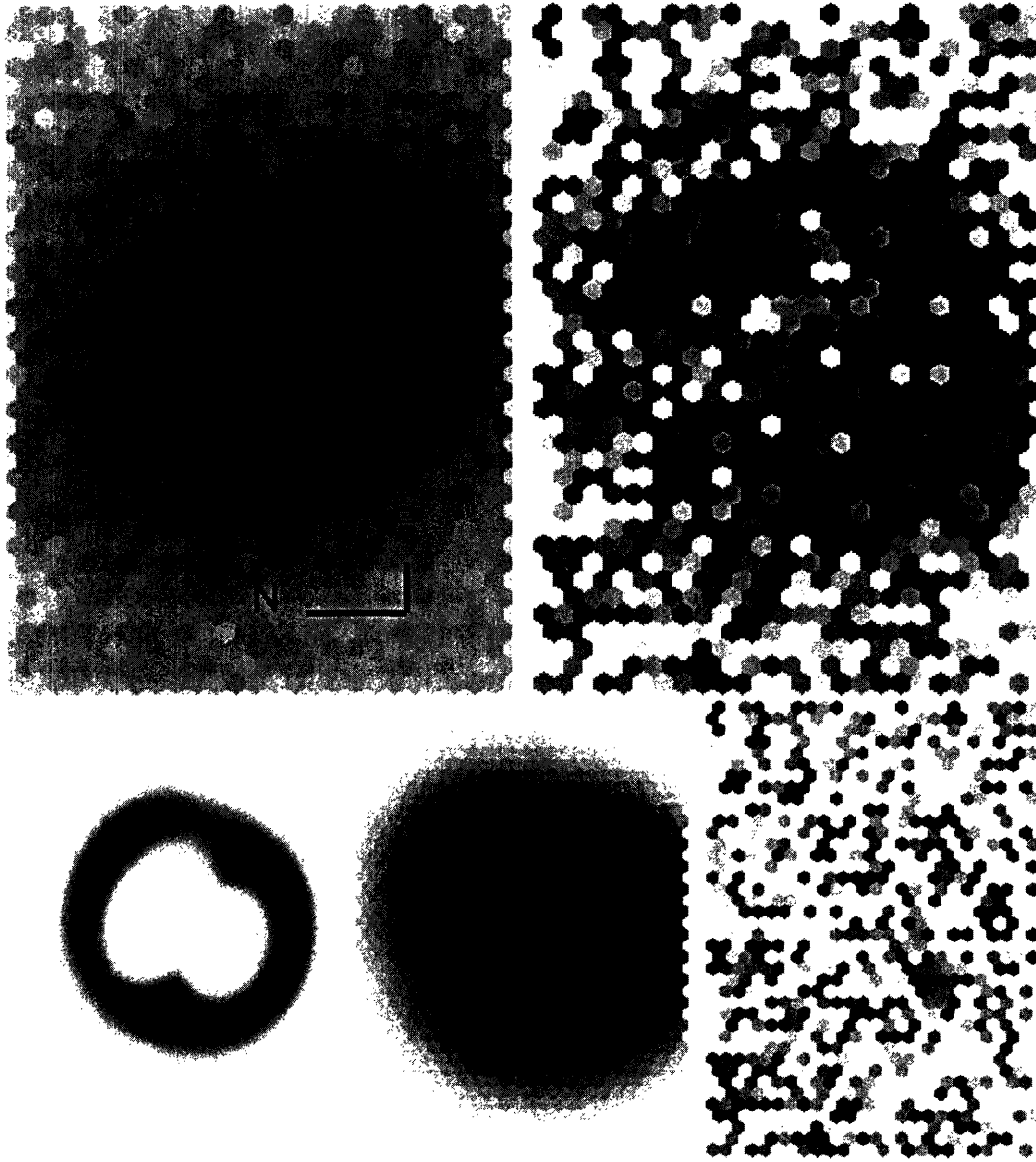


Figure 3-14: IMACS-2 IFU narrowband imaging of SDSSJ2321 at 5713 Å, corresponding to redshifted [O II] 3727. Individual panels are as in Figure 3-12. For continuum image, white-to-black scaling is from -1 to $7 \times 10^{-18} \text{ erg cm}^{-2} \text{ s}^{-1} \text{ \AA}^{-1}$ per IFU lenslet. For emission-line images, scaling is from -1 to $7 \times 10^{-18} \text{ erg cm}^{-2} \text{ s}^{-1}$ per IFU lenslet. (Bottom left image has been scaled by a factor of 0.4 relative to the other emission-line images.)

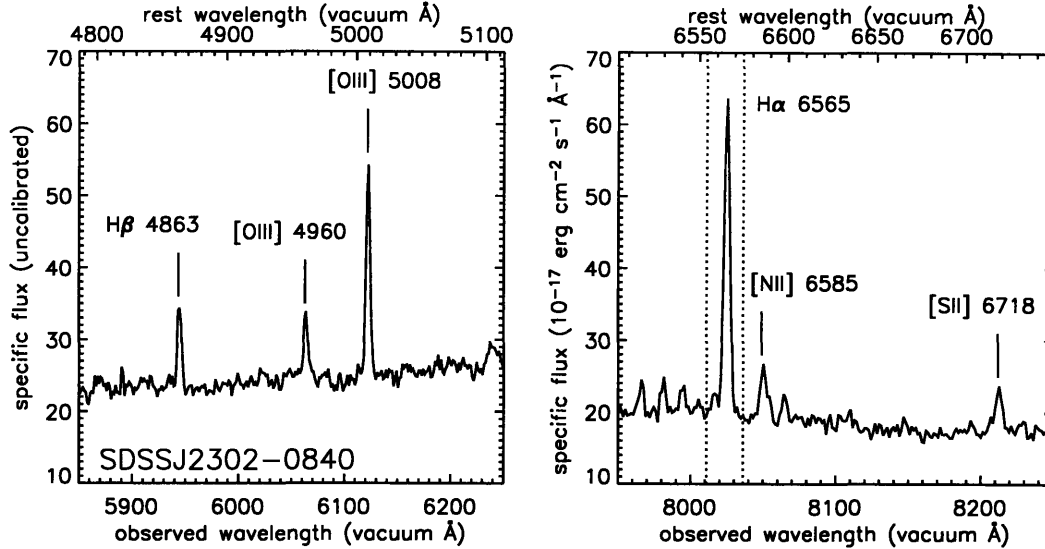


Figure 3-15: Summed spectra of SDSSJ2302 for fibers with significant background-redshift $H\alpha$ emission-line flux as seen in Figure 3-16. Flux calibration is applied at the wavelength of redshifted $H\alpha$.

SDSSJ2302–0840

SDSSJ2302–0840 was observed on the night of UT 2004 September 19 in the IMACS-2 configuration with an exposure time of 3×900 s. The redshift of the background galaxy is low enough for the $H\alpha$ line to be detected at an observed wavelength of approximately 8024 \AA , where the $1\text{-}\sigma$ line flux of the exposure sequence was approximately $1 \times 10^{-17} \text{ erg cm}^{-2} \text{ s}^{-1}$. $[\text{O III}] 5007$, $[\text{O III}] 4959$, $H\beta$, and $[\text{O II}] 3727$ are all detected in the SDSS and IFU spectra at high significance; Figure 3-15 presents sub-ranges of the IFU spectra for fibers with significant emission-line flux. We construct emission-line and continuum images at the wavelength of redshifted $H\alpha$ as shown in Figure 3-16. The emission-line image shows evidence of a quadruple-image lens configuration with an extended ring. Our best-fit SIE model has an Einstein radius of $1''.11 \pm 0''.01$. The model fits poorly unless the centroid of the lens potential is left free to move away from the measured foreground-galaxy centroid; the final displacement between the lens-model potential center and the foreground-galaxy centroid is $0''.23$ (about one IFU lenslet). The residual emission-line image also shows significant under-subtracted flux at the brightest point in the image; this may be attributable to a milli- or micro-lensing perturbation of a compact source component that our model does not incorporate. Our measured Einstein radius for SDSSJ2302 should nevertheless be quite robust.

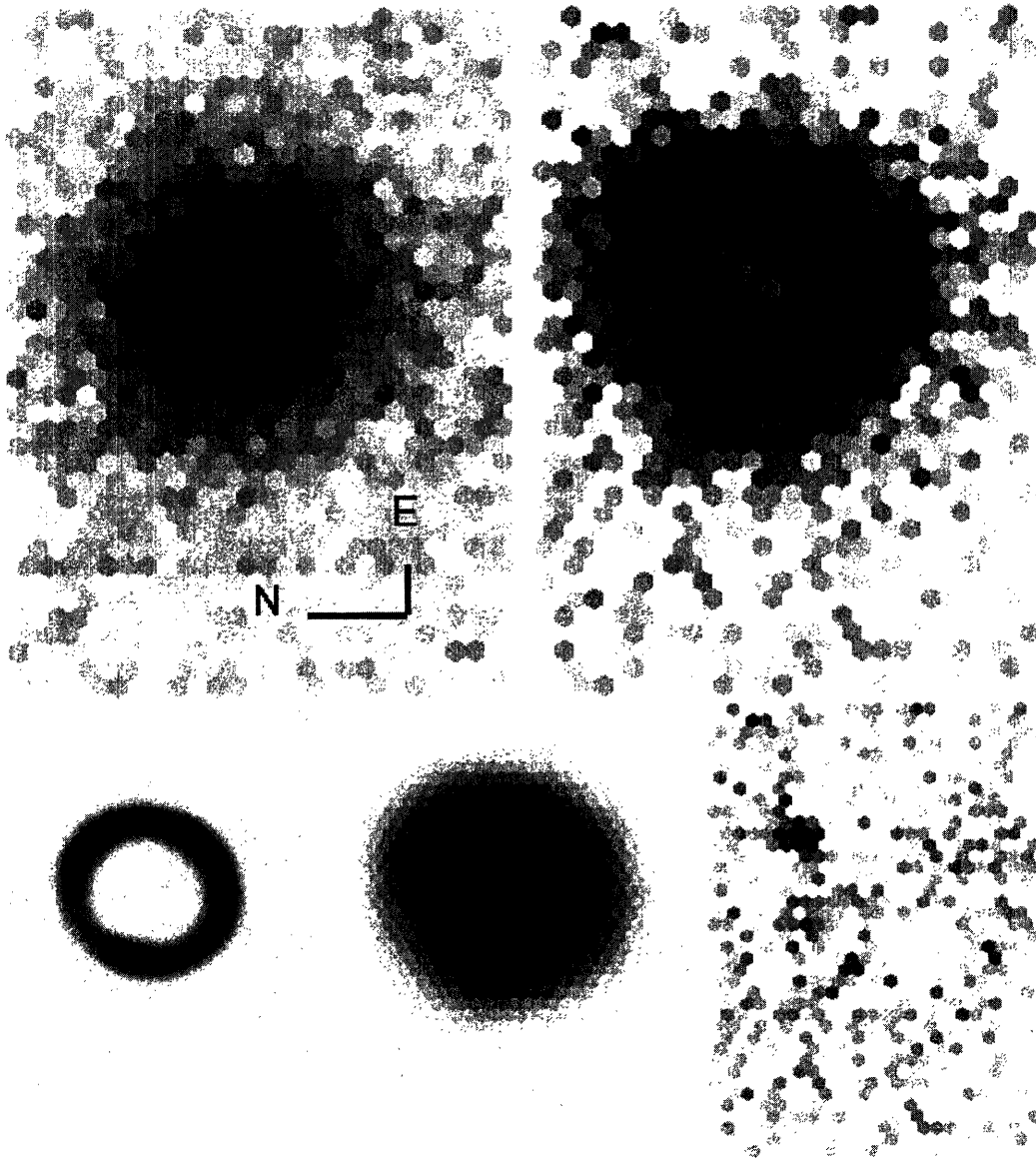


Figure 3-16: IMACS-2 IFU narrowband imaging of SDSSJ2302 at 8024 \AA , corresponding to redshifted $H\alpha$. Individual panels are as in Figure 3-12. For continuum image, white-to-black scaling is from -1 to $7 \times 10^{-18} \text{ erg cm}^{-2} \text{ s}^{-1} \text{ \AA}^{-1}$ per IFU lenslet. For emission-line images, scaling is from -5 to $25 \times 10^{-18} \text{ erg cm}^{-2} \text{ s}^{-1}$ per IFU lenslet. (Bottom left image has been scaled by a factor of 0.35 relative to the other emission-line images.)

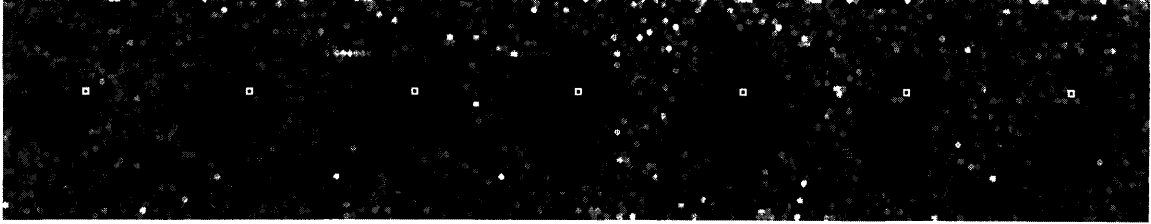


Figure 3-17: Iso-wavelength slices through the redshifted $H\alpha$ emission line of the lensed background galaxy in SDSSJ0044. The continuum contribution has been subtracted off; white squares indicate the fitted center of the best-fit SIS gravitational-lens model. Note that both images rotate in the same sense (counterclockwise in this figure) about the potential center, as is to be expected for a strong gravitational lens. Orientation and parity on the sky is as in Figure 3-19.

SDSSJ0044+0113

Summed IFU emission-line spectra and reconstructed narrowband images of the gravitational lens SDSSJ0044+0113 can be seen in Figures 3-18 and 3-19 respectively. The exposure time was 2×900 s and the $1\text{-}\sigma$ line flux at the wavelength of redshifted background $H\alpha$ emission (7855 \AA) was approximately $1.1 \times 10^{-17} \text{ erg cm}^{-2} \text{ s}^{-1}$. The background emission lines show slight spatial variation in their peak wavelengths, indicating rotation of the background galaxy. The total velocity shifts are comparable to the instrumental resolution, and can be measured by including an extra Gaussian-derivative basis function when fitting for narrowband image coefficients in the manner described in § 3.4.1. As seen in Figure 3-17, the emission-line velocity field has the parity expected for a double-image gravitational lens, although we do not use the velocity information in our lens modeling. Precise centroiding of the foreground galaxy in the continuum image is complicated by the presence of a significant continuum contribution from the background galaxy. We therefore fit the lens with an SIS model (no ellipticity) and leave the potential center as a free parameter; the fitted center is nevertheless quite near to the brightness peak in the continuum image (see Figure 3-19). Parameterizing the source galaxy as a Gaussian leaves appreciable systematic residuals in the radial profile of the brighter image, thus we also fit for a Sérsic index in the lensed galaxy. The best-fit SIS Einstein radius for the system is $b = 0''.772 \pm 0''.017$.

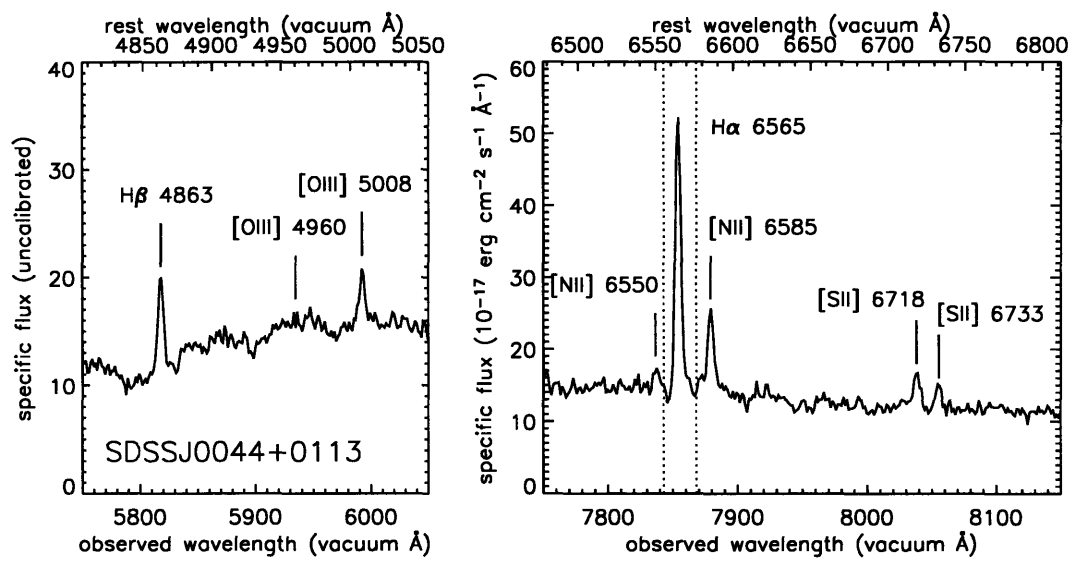


Figure 3-18: Summed spectra of SDSSJ0044 for fibers with significant background-redshift H α emission-line flux as seen in Figure 3-19. Flux calibration is applied at the wavelength of redshifted H α .

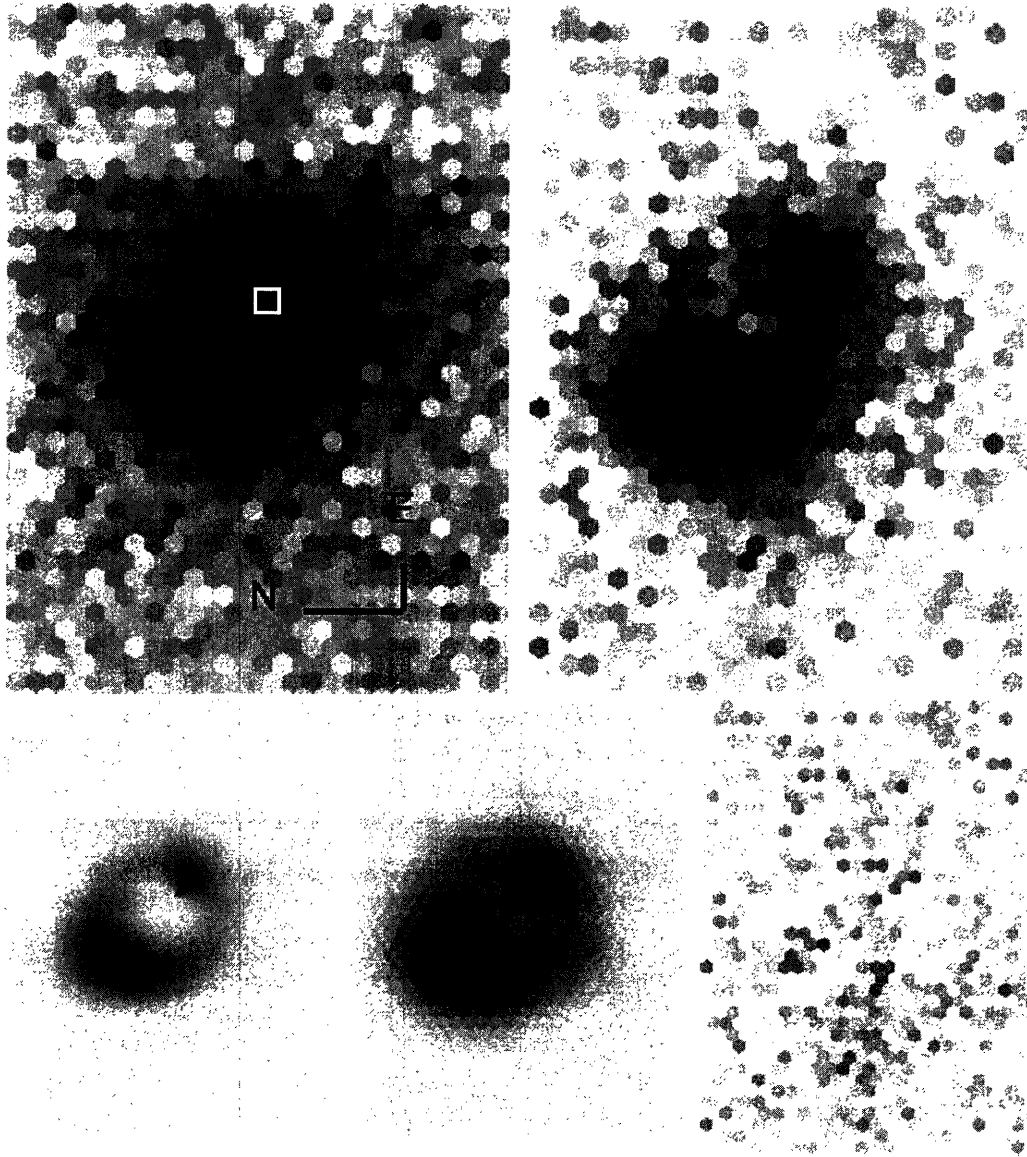


Figure 3-19: IMACS-2 IFU narrowband imaging of SDSSJ0044 at 7855 \AA , corresponding to redshifted $\text{H}\alpha$. Individual panels are as in Figure 3-12. White square in the continuum image is centered on the fitted SIS lens-potential center. For continuum image, white-to-black scaling is from -1 to $4 \times 10^{-18} \text{ erg cm}^{-2} \text{ s}^{-1} \text{ \AA}^{-1}$ per IFU lenslet. For emission-line images, scaling is from -1 to $5.5 \times 10^{-17} \text{ erg cm}^{-2} \text{ s}^{-1}$ per IFU lenslet. (Bottom left image has been scaled by a factor of 0.5 relative to the other emission-line images.)

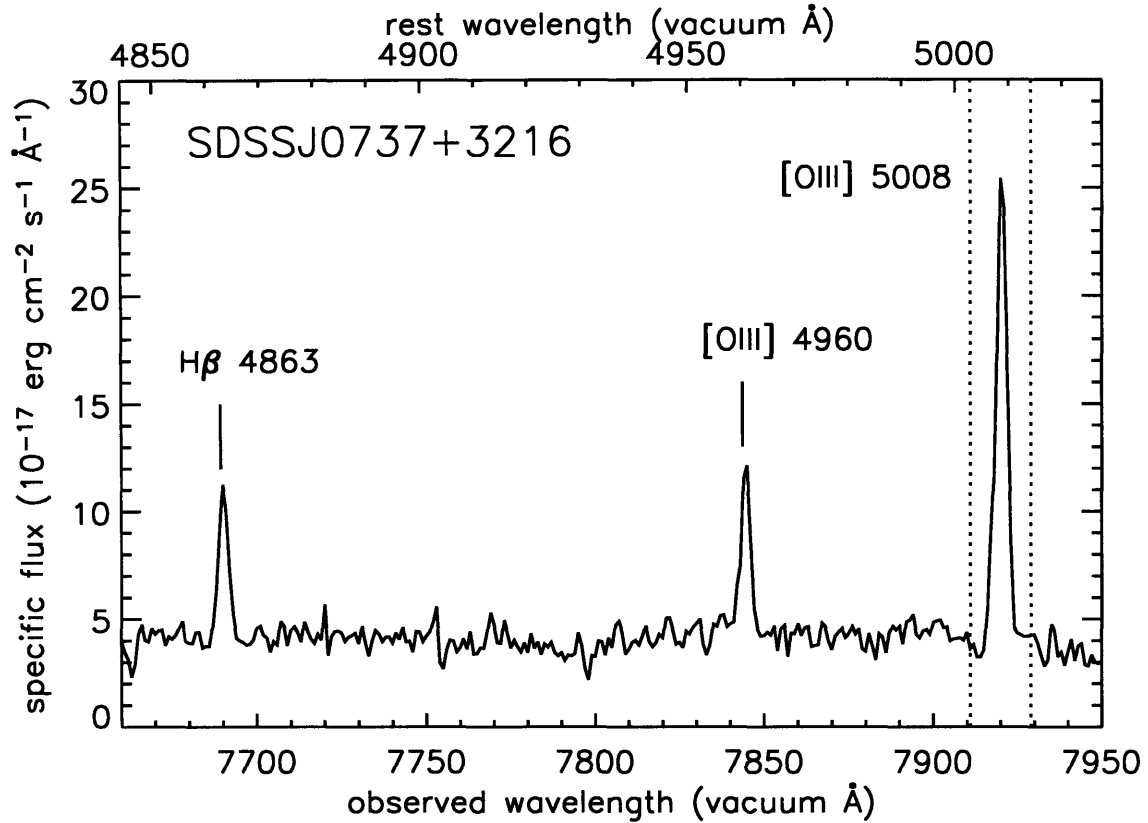


Figure 3-20: Summed spectra of SDSSJ0737 for fibers with significant background-redshift [O III] 5007 emission-line flux as seen in Figure 3-21. Flux calibration is applied at the wavelength of redshifted [O III] 5007.

SDSSJ0737+3216

SDSSJ0737+3216 was observed for 3×900 s in the GMOS-i configuration. The exposure time gives a $1\text{-}\sigma$ line flux of 4.3×10^{-18} erg cm $^{-2}$ s $^{-1}$ at 7920 Å, the wavelength of redshifted [O III] 5007. Narrowband image shows clear strong-lensing morphology with an extended arc image and counterimage. The bright, elongated arc image is closer to the lens-galaxy center than is the counterimage, indicating a short-axis-quad configuration. The system is modeled successfully by an SIE model with a fitted Einstein radius is $1''.00 \pm 0''.01$.

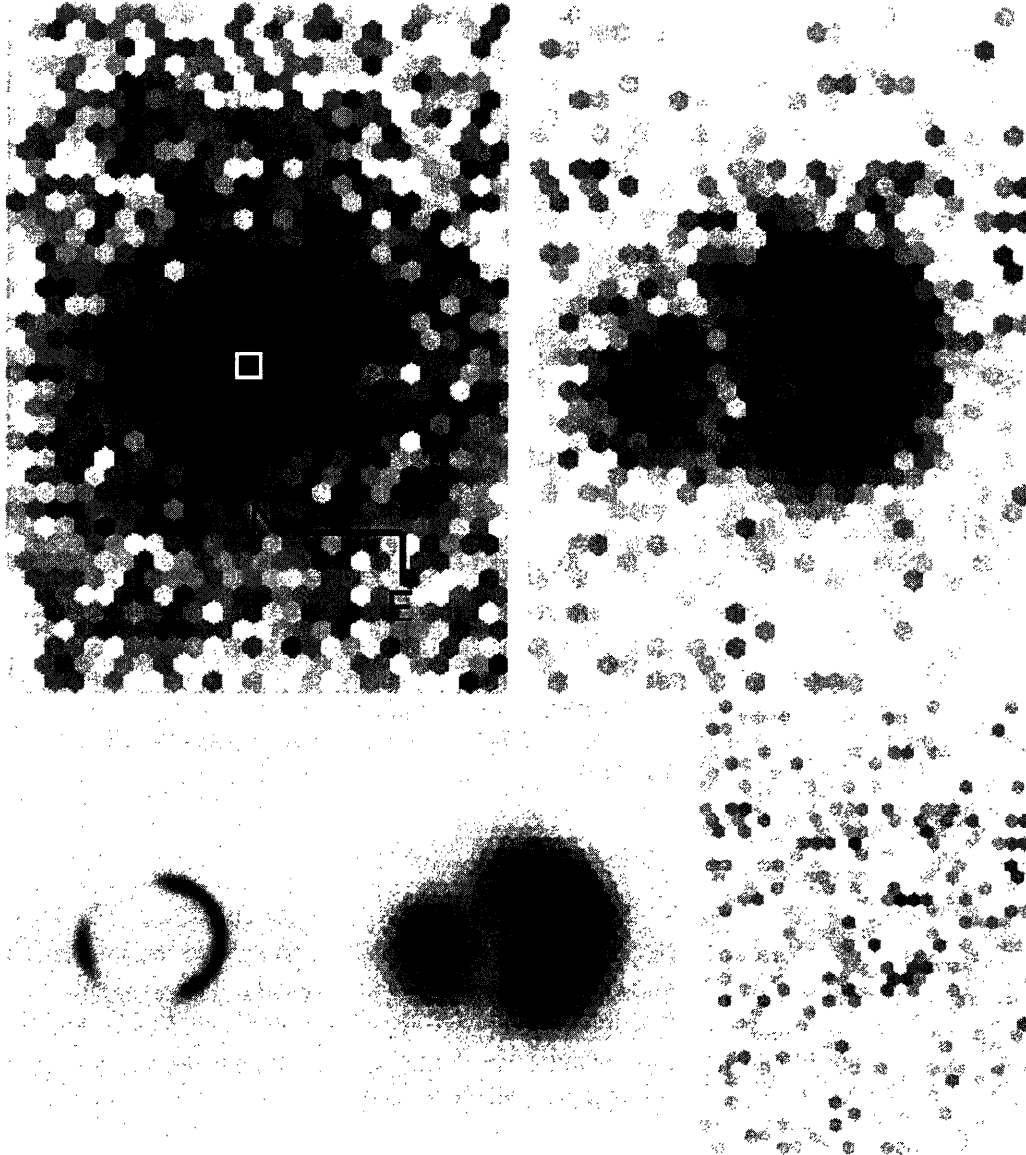


Figure 3-21: GMOS-*i* IFU narrowband imaging of SDSSJ0737 at 7920 Å, corresponding to redshifted [O III] 5007. Individual panels are as in Figure 3-12. For continuum image, white-to-black scaling is from -2.5 to $10 \times 10^{-19} \text{ erg cm}^{-2} \text{ s}^{-1} \text{ \AA}^{-1}$ per IFU lenslet. For emission-line images, scaling is from -2.5 to $15 \times 10^{-18} \text{ erg cm}^{-2} \text{ s}^{-1}$ per IFU lenslet. (Bottom left image has been scaled by a factor of 0.15 relative to the other emission-line images.)

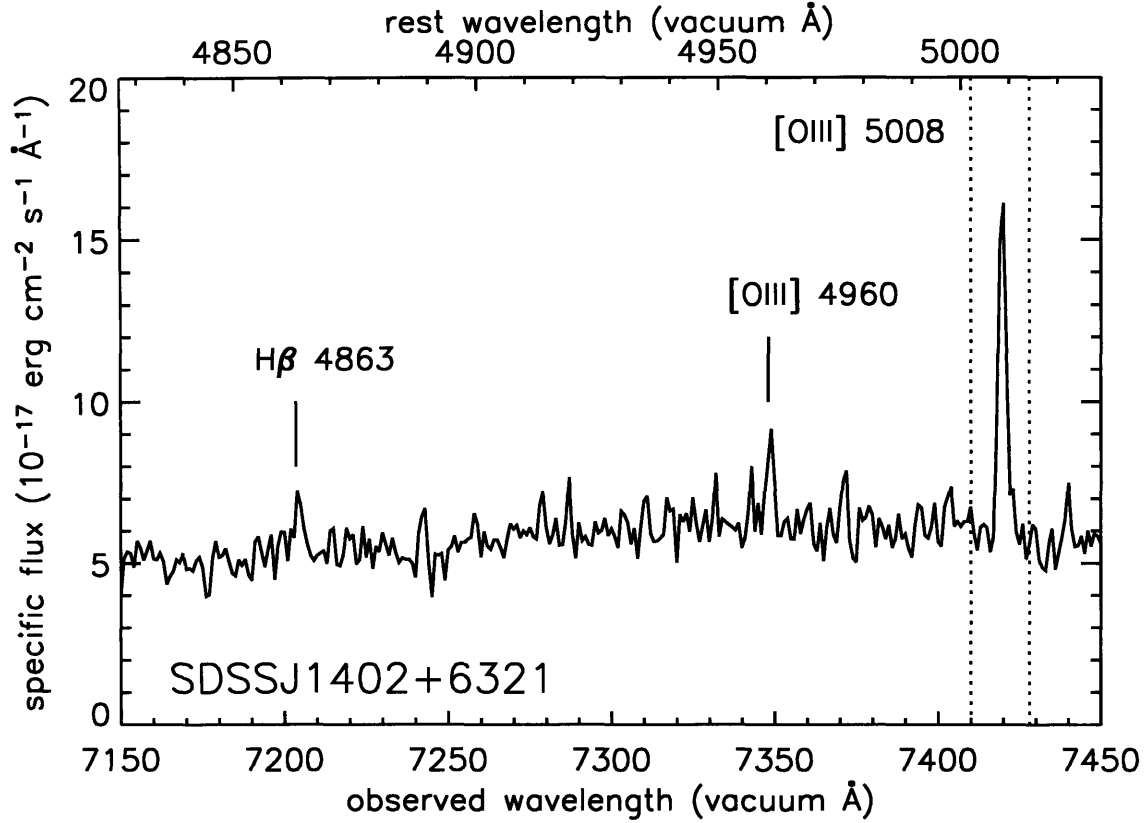


Figure 3-22: Summed spectra of SDSSJ1402 for fibers with significant background-redshift [O III] 5007 emission-line flux as seen in Figure 3-23. Flux calibration is applied at the wavelength of redshifted [O III] 5007.

SDSSJ1402+6321

SDSSJ1402+6321 was observed for 3×900 s with the GMOS-i configuration, giving a $1\text{-}\sigma$ line flux of $3.8 \times 10^{-18} \text{ erg cm}^{-2} \text{ s}^{-1}$ at 7419 \AA , the wavelength of redshifted [O III] 5007. The emission-line image shows quadruple-image lens morphology, and can be modeled with four circular Gaussian images of equal width. The system is successfully modeled as an quadruple-image SIE lens with an Einstein radius of $1''.41 \pm 0''.02$ by taking the Gaussian image model positions and fluxes as constraints to the lens model.

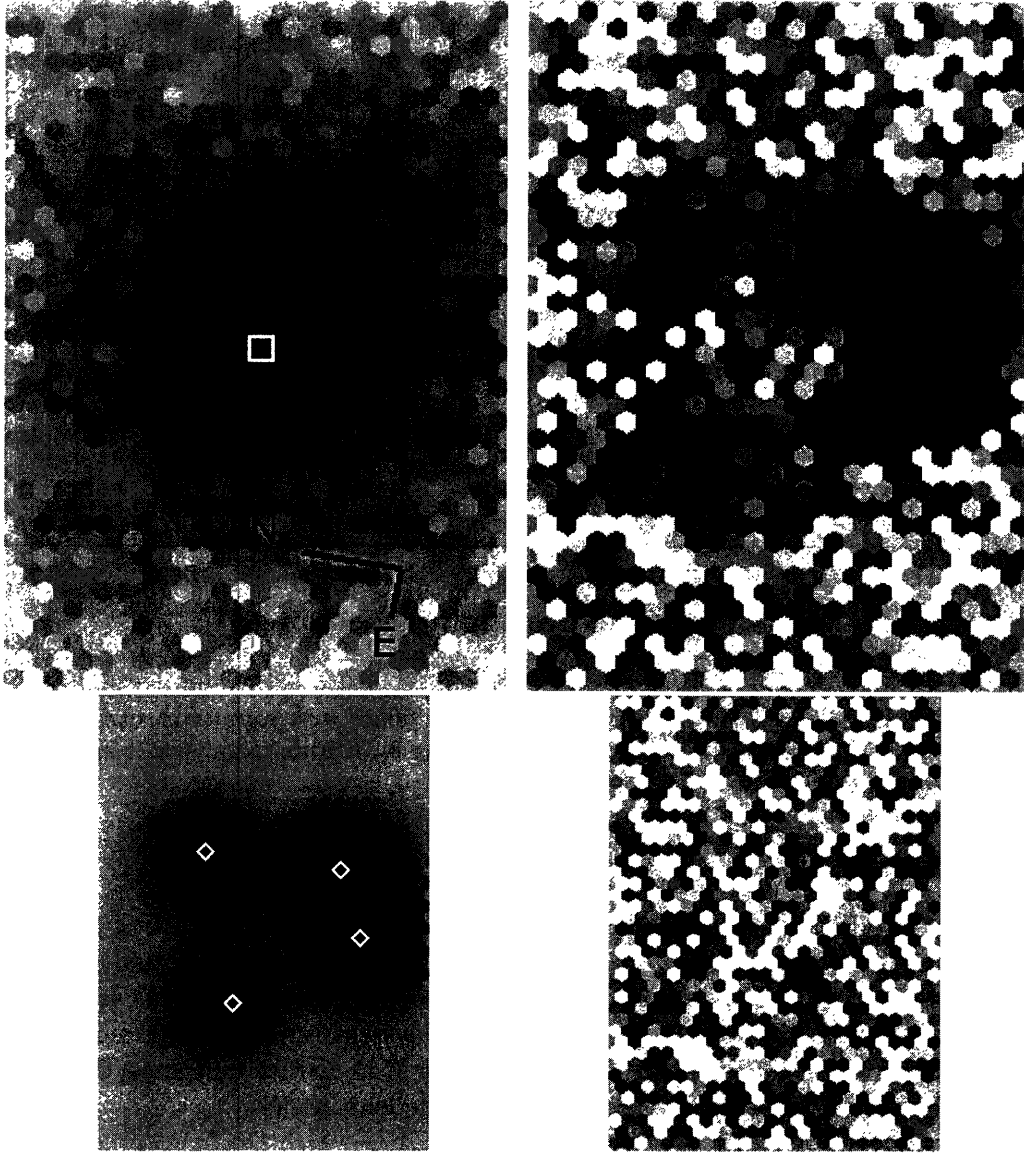


Figure 3-23: GMOS-*i* IFU narrowband imaging of SDSSJ1402 at 7419 Å, corresponding to redshifted [O III] 5007. Individual panels are as in Figure 3-10. White square in the continuum image is centered on the fitted SIS lens-potential center, and white diamonds in model lensed image show image positions of the best-fit SIE lens model. For continuum image, white-to-black scaling is from -5 to $18 \times 10^{-19} \text{ erg cm}^{-2} \text{ s}^{-1} \text{ \AA}^{-1}$ per IFU lenslet. For emission-line images, scaling is from -1 to $3 \times 10^{-18} \text{ erg cm}^{-2} \text{ s}^{-1}$ per IFU lenslet.

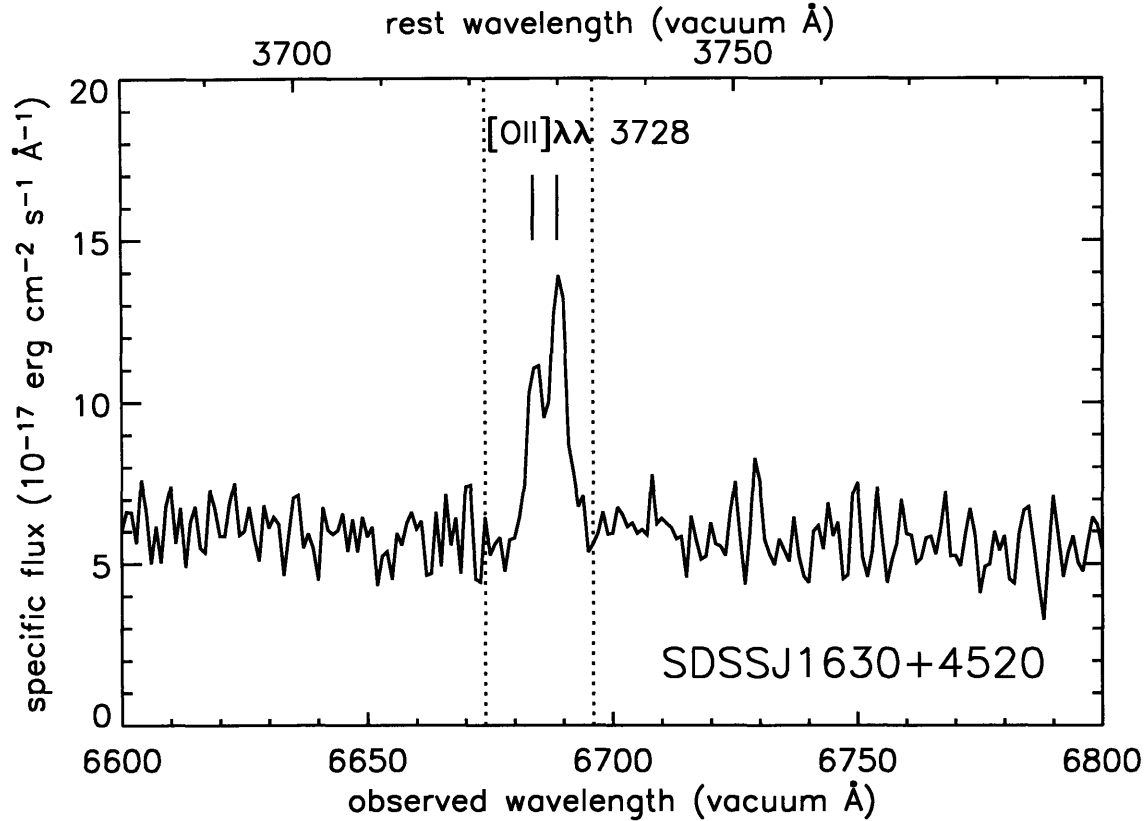


Figure 3-24: Summed spectra of SDSSJ1630 for fibers with significant background-redshift [O II] 3727 emission-line flux as seen in Figure 3-25. Flux calibration is applied at the wavelength of redshifted [O II] 3727.

SDSSJ1630+4520

SDSSJ1630+4520 was observed for 3×900 s in the GMOS-r configuration, giving a $1\text{-}\sigma$ line flux of $5.1 \times 10^{-18} \text{ erg cm}^{-2} \text{ s}^{-1}$ at 6685 \AA , the wavelength of redshifted [O II] 3727. The emission-line image shows partial Einstein-ring morphology, with an added compact component. Summed IFU spectra in the spatial regions of detected line emission confirms the identification as [O II] 3727 through the splitting of both components of the doublet with the expected separation in wavelength (Figure 3-24). We are unable to successfully fit a simple parameterized lens model to this system in the manner used for others systems. We nevertheless interpret the ring morphology as a sign of strong lensing, and we make a rough measurement of the ring radius by averaging radial positions over the ring as shown in Figure 3-25. This gives a ring radius of $1''.73$, for which we assume an error of $0''.10$ (one-half IFU lenslet). We also note the possible hint of a central image in Figure 3-25, although at very low significance.

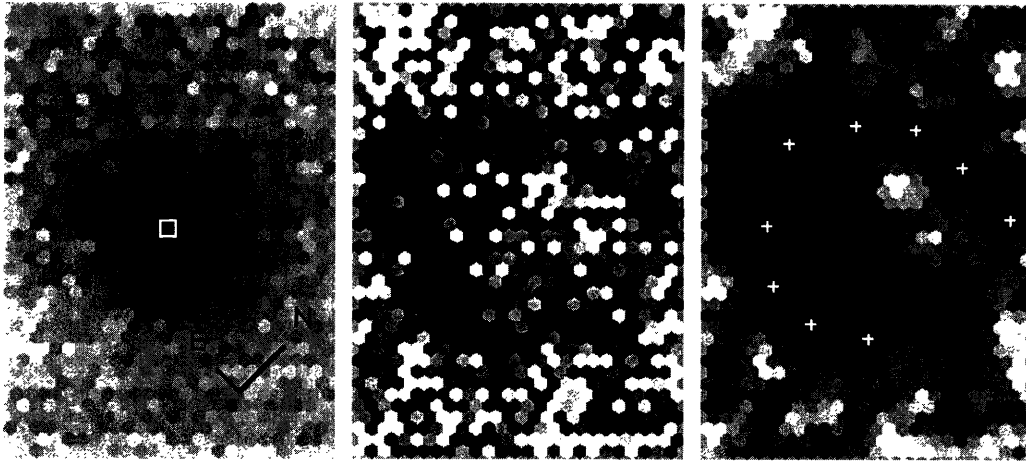


Figure 3-25: GMOS-*r* IFU narrowband imaging of SDSSJ1630 at 6685 Å, corresponding to redshifted [O II] 3727. Left panel shows continuum image with white-to-black scaling is from -5 to $18 \times 10^{-19} \text{ erg cm}^{-2} \text{ s}^{-1} \text{ \AA}^{-1}$ per IFU lenslet and white square showing fitted center of continuum image. Center panel shows emission-line image with scaling from -1 to $3 \times 10^{-18} \text{ erg cm}^{-2} \text{ s}^{-1}$ per IFU lenslet. Right panel shows emission-line image smoothed with a 7-lenslet hexagonal kernel. White crosses show positions used in averaging for ring radius, and scaling is as in center panel.

Other Systems

Appendix D presents the catalog of IFU-observed lens-candidate systems that either

1. show non-strongly lensed (i.e. no multiple imaging) background line emission,
2. show evidence of strong lensing but for which the IFU data do not permit lens-modeling/Einstein-ring measurement because of either insufficient spatial resolution or a low signal-to-noise ratio, or
3. are not detected with sufficient spatial resolution and/or signal-to-noise to make even a tentative judgement as to their status as lenses, non-lenses, or non-detections.

Although these systems do not yield any direct constraints on the structure of their foreground galaxies, they provide a valuable measure of both the limits of the IFU for high-resolution study of faint lensed emission-line galaxies and of the diversity of systems discovered by our spectroscopic selection technique. These data can also prove useful in the interpretation of high-resolution *Hubble Space Telescope* imaging data obtained for an overlapping sample of galaxies by an ongoing Snapshot Survey program (Bolton et al. 2005), which is described in Chapter 4. The IFU data, though insufficient to establish the incidence of strong lensing in their own right, can support or refute a lensing interpretation of the *HST* data by revealing whether or not the background-redshift line emission is coincident with the putative lensed images seen by *HST*.

3.5 Initial Conclusions

Several immediate conclusions can be drawn from the lens-modeling results of our IFU survey. First, we have demonstrated the feasibility of using high-resolution integral-field spectroscopy to reconstruct narrowband images of gravitationally lensed emission-line galaxies that are of a quality sufficient to permit rather robust gravitational lens modeling. The closest image separation that we have succeeded in modeling is the $\approx 1''.5$ splitting between the images of SDSSJ0044. We targeted a number of lens candidates with smaller expected separations in our GMOS survey (for which the queue observing constraints were set to require an image quality of $0''.8$ FWHM or better), and the data can be seen in Appendix D. We have confirmed the background-redshift line emission for nearly all of these systems, but were unable to construct lens models due to the limited spatial resolution. The system SDSSJ1029+6115 (Figures D-5 and D-6) provides an illustrative example. The expected lensed image splitting for this system (twice the Einstein radius for the known z_{FG} , z_{BG} , and σ_v assuming an SIS model) is $\approx 1''.1$, and this seems to be the approximate scale of separation between the features in the iso-wavelength emission-line image sequence of Figure D-6. At higher spatial resolution (and assuming we are indeed seeing a strong lens), this system could provide detailed lensing constraints on the radial and angular mass structure of the foreground galaxy, since the background-galaxy rotation curve effectively provides multiple lensed images across the source plane. At the delivered resolution of our data, meaningful lens modeling unfortunately does not seem possible.

With the exception of the undersubtracted image flux in SDSSJ2302 and the apparently complicated source distribution in SDSSJ1613, the SIE model is quite successful in fitting our gravitational-lens images both in position and in flux levels. Without exploring the degeneracies between the radial and angular structure of simple lens models as constrained

by our data, we cannot take this success in itself as an indication of an isothermal radial profile. The success of our simple model does however suggest that the angular structure of our lenses must be fairly simple. If known quasar lens galaxies can be compared to our lenses, the fact that we do not see the same extreme image flux ratio anomalies as are seen between simple quasar lens data and models suggests that micro/millilensing (Mao and Schneider 1998; Metcalf and Madau 2001; Chiba 2002; Dalal and Kochanek 2002; Witt et al. 1995; Schechter and Wambsganss 2002) must be responsible for nearly all of the quasar flux-ratio effects, and not significant higher-order macroscopic angular structure as suggested by some authors (Evans and Witt 2003; Möller et al. 2003).

Since all of our lenses have well-measured stellar velocity dispersions from the SDSS, we can measure the dynamical normalization between the stellar dispersion and the isothermal lens-model velocity dispersion. Figure 3-26 presents this comparison. We correct lens-model velocity dispersions for environmental effects in the manner described in § 3.6.2 below (typically a few-percent correction), and correct the SDSS aperture velocity dispersions σ_v to a uniform $R_e/8$ aperture using the empirical factor of Jorgensen et al. (1995). Following Kochanek et al. (2000), we compute the normalization factor $f = \sigma_{\text{SIE}}/\sigma_e 8$. We find that $f = 0.95 \pm 0.03$ (68% confidence) for our sample of 8 lenses. This normalization is close to value of unity expected by Kochanek (1994) for galaxies within isothermal dark-matter halos.

Finally, we briefly address the question of whether or not these systems could in fact be unlensed projections of multiple background objects, rather than strong lenses. We consider this an unlikely explanation for two principal reasons. First, all systems show image morphologies that are well-fit by simple lens models (with the exception of SDSSJ1630, which shows ring morphology centered on the foreground galaxy). If we were observing unlensed projected background galaxies, surely some would have image configurations unexplainable by lensing. Second, and perhaps more succinctly, we have every reason to expect that when one galaxy is placed far behind another, massive galaxy at small impact parameter, it will be strongly lensed. The near-unity dynamical normalization that we find between stars and lensing mass further supports the consistency of the lensing interpretation in this respect. Thus we regard strong lensing as the most plausible explanation of the features that we observe.

3.6 Constraining the Density Profile with Aperture Masses and Velocity Dispersions

Our new strong-lensing galaxies are particularly powerful probes of galaxy structure in that they permit accurate photometry and spectroscopy without significant contamination by the light of the lensed source. Indeed, the SDSS provides a well-calibrated stellar velocity-dispersion measurement integrated over its 3''-diameter spectroscopic fiber that we may use along with the SDSS effective radii and IFU lensing constraints to distinguish between various possible total (luminous+dark) mass profiles using a more sophisticated method than the simple comparison of velocities shown in Figure 3-26.

3.6.1 Mass, Light, and Velocity

In order to make model-based predictions for the observed SDSS stellar velocity dispersion we will make several simplifying assumptions. Since triaxial pressure-supported dynam-

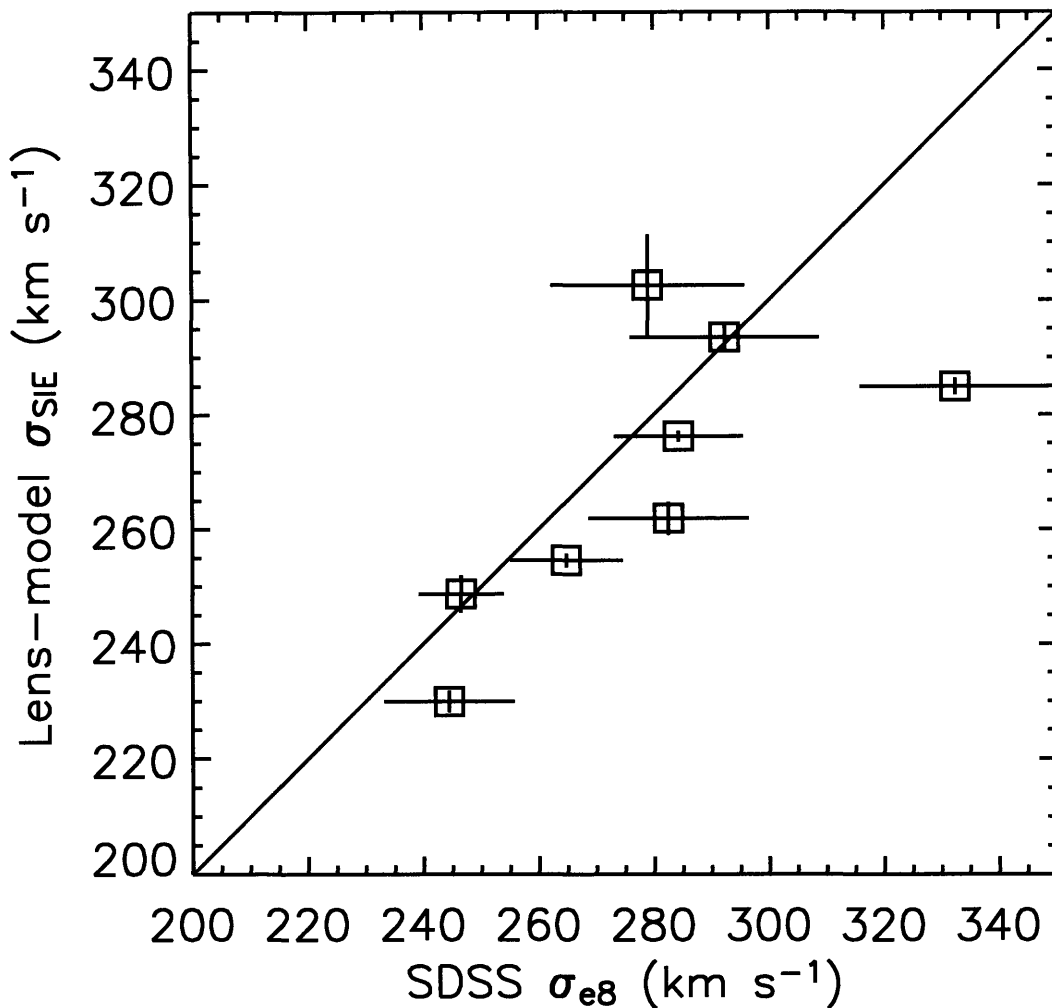


Figure 3-26: Comparison of SDSS stellar velocity dispersion to SIE lens-model velocity dispersion for eight IFU lenses.

ical models are much more complicated than spherical models, and in any event would be severely underconstrained by our current data, our first assumption will be that of a spherical galaxy+halo model. This will obviously incur some error as our lenses generally have non-zero ellipticity. Following Kochanek (1994), we attempt to minimize these errors by adopting azimuthally averaged values. We evaluate effective radii at the intermediate axis (the geometric mean of the major and minor axes), we use Einstein radii from elliptical models normalized to the intermediate axis, and we use SDSS velocity dispersions computed from circular-aperture data. We also assume that any rotation speed v_R in our galaxies is negligible compared to their velocity dispersions σ_v . Kochanek (1994) finds that when angular-average quantities are employed, the fractional error between actual velocity dispersions and the dispersions computed under the simplifying assumptions are of the

order

$$\frac{e}{12} - \frac{1}{4} \left(\frac{v_R}{\sigma} \right)_{\max}^2, \quad (3.10)$$

where e is the projected ellipticity of the galaxy.

For spherical systems, the radial velocity dispersion σ_r of a stellar distribution with luminosity density $\nu(r)$ is related to the total mass profile through the spherical Jeans equation:

$$\frac{1}{\nu} \frac{d(\nu\sigma_r^2)}{dr} + \frac{2\beta\sigma_r^2}{r} = -\frac{GM(r)}{r^2}. \quad (3.11)$$

Here $\beta = 1 - \sigma_\theta^2/\sigma_r^2$ expresses the anisotropy of the velocity-dispersion tensor and $M(r)$ is the total mass interior to the three-dimensional radial coordinate r . If we simplify further and consider only models of constant β , the spherical Jeans equation has an integrating factor and its solution can be expressed as a quadrature (Binney 1980):

$$\nu\sigma_r^2 = r^{-2\beta} \int_r^\infty GM(r)\nu r^{(2\beta+2)} dr. \quad (3.12)$$

In the absence of high-resolution imaging data, we assume that our lens galaxies are well fit by a de Vaucouleurs profile

$$I(R) = I_e \exp\{-k_{1/4}[(R/R_e)^{1/4} - 1]\} \quad (3.13)$$

($k_{1/4} = 7.66925001$) and use the effective (half-light) radii R_e measured by the SDSS to constrain the galaxy size. Since the Jeans equation is formulated in three dimensions but our data are projected along the line of sight, we must contend with various projection and deprojection calculations in our analysis. The first necessary deprojection is that of the de Vaucouleurs surface-brightness law from two dimensions into three. Under our spherical assumption, any three-dimensional density $\nu(r)$ is related to its two-dimensional projection $I(R)$ through the Abel integrals

$$I(R) = 2 \int_R^\infty \frac{\nu r dr}{\sqrt{r^2 - R^2}}, \quad (3.14)$$

$$\nu(r) = -\frac{1}{\pi} \int_r^\infty \frac{dI}{dR} \frac{dR}{\sqrt{R^2 - r^2}} \quad (3.15)$$

(e.g. Binney and Tremaine 1987). The de Vaucouleurs law does not have a simple analytic deprojected form, but we may solve Equation 3.15 numerically for the three-dimensional de Vaucouleurs law. Since the numerical solution of Equation 3.12 requires formal integration out to ∞ , it is of interest to seek an accurate analytic approximation to the deprojected de Vaucouleurs law. Mellier and Mathez (1987) present an analytic approximation of the form $\nu(r) \propto r^{-0.855} \exp[-k_{1/4}(r/R_e)^{1/4}]$ which is accurate to within 1% of the true deprojected density over the range $0.1 < r/R_e < 100$. We desire even greater accuracy to ensure that our approximation contributes negligibly to our error budget over a wide range of radial scales, so we derive an improved approximation in the following manner. We take the natural logarithm of the numerically deprojected and tabulated 3D de Vaucouleurs profile and subtract from it the expression $-k_{1/4}[(r/R_e)^{1/4} - 1]$. We then perform a least-squares fit to the residual function with a cubic polynomial in $\ln(r/R_e)$, with equal weight per logarithmic radial interval over the range $10^{-5} < r/R_e < 10^5$. The resulting approximation for $\nu(r)$ is within 0.2% of the numerically deprojected value over the range $10^{-4} < r/R_e < 10^4$. Our

approximation takes the analytic form

$$\nu(r) = (I_e/R_e) \exp \left\{ -k_{1/4}[(r/R_e)^{1/4} - 1] + \sum_{m=0}^3 c_m [\ln(r/R_e)]^m \right\} , \quad (3.16)$$

with the c_m 's given by

$$\begin{aligned} c_0 &= -0.70021079 \\ c_1 &= -0.85007013 \\ c_2 &= -2.3120817 \times 10^{-3} \\ c_3 &= 7.8293738 \times 10^{-5} . \end{aligned} \quad (3.17)$$

Note that the constant c_0 controls the normalization of the profile, and the value of c_1 would be the -0.855 of Mellier and Mathez (1987) if we did not fit for the higher-order coefficients c_2 and c_3 .

The logarithmic slope of the central three-dimensional galaxy density profile is of great empirical and theoretical interest, and our lensing and velocity-dispersion data give us the power to constrain this parameter in our lensing galaxies. We model the total lens-galaxy mass profile as a power-law function of the form

$$\rho(r) = \frac{(3 - \gamma)M_e}{4\pi R_e^3} \left(\frac{r}{R_e} \right)^{-\gamma} . \quad (3.18)$$

We scale all radii to the *two-dimensional* galaxy half-light (effective) radius R_e , since power-law density profiles are by definition scale free. The normalization is such that the mass enclosed within a sphere of radius r in three dimensions is

$$M(r) = M_e \left(\frac{r}{R_e} \right)^{3-\gamma} \quad (3.19)$$

and M_e is the mass interior to R_e in 3D for all γ . Our strategy for constraining the parameter γ in our lens galaxies is to take the mass enclosed by the Einstein radius as determined from our strong-lensing observations to fix the mass normalizations M_e of a grid of power-law models spanning a range in γ , compute the predicted radial velocity-dispersion profile for each model by solving Equation 3.12 for a correctly-sized de Vaucouleurs model embedded in that mass model, project these solutions numerically along the line of sight via the relation

$$I(R)\sigma_{\text{l.o.s.}}^2 = 2 \int_R^\infty \left(1 - \beta \frac{R^2}{r^2} \right) \frac{\nu \sigma_r^2 r dr}{\sqrt{r^2 - R^2}} \quad (3.20)$$

(Binney and Tremaine 1987), and integrate the resulting luminosity-weighted squared-dispersion profile over the seeing-smearred SDSS spectroscopic aperture. We will compute our constraints for several values of the parameter β corresponding to radial, isotropic, and tangential orbital anisotropies.

3.6.2 Mass Normalization from Lensing

In order to apply the mass constraints derived from strong lensing to the power-law dynamical models discussed above, we must first address several subtle complications. Specifically,

these are the effects of environmental overdensity, two-dimensional versus three-dimensional enclosed masses, and the model dependence of the measured Einstein radius in asymmetric lens systems (e.g. doubles); we address these concerns in that order.

Correction for Environmental Effects

The Einstein radius of a strong gravitational lens provides a robust measurement of the mass enclosed by the lensed images, which in the neighborhood of the lens corresponds to the mass within a cylindrical volume along the line of sight. If we ignore possible projected contributions from an overdense environment, we will overestimate the mass of the lens galaxy. To make an approximate correction for environmental effects to our lensing mass measurements, we employ a strategy suggested by the work of Keeton and Zabludoff (2004). For each of our lenses, we identify as neighbors those galaxies detected by the SDSS within a physical radius of 500 kpc and with SDSS $g-r$ and $r-i$ colors within ± 0.15 . This simple photometric redshift technique should very effectively select neighboring early-type galaxies, which will be the most effective tracers of the local overdensity around our lens galaxies. We then model the surface-density contributions of these neighbors with isothermal spheres in the following manner. Let b_0 be the isothermal Einstein-radius parameter of the lens galaxy, related to its velocity dispersion σ_0 through Equation 3.6, and let L_0 be its luminosity in some specified waveband. Similarly, let $\{b_i\}$, σ_i , and $\{L_i\}$ (with i ranging from 1 to N_{gal}) be the Einstein-radius parameters, velocity dispersions, and luminosities of the identified neighbor galaxies. Also let $\{R_i\}$ be the angular offsets of the neighbors from the center of the lens. The isothermal galaxy model then implies

$$\frac{b_i}{b_0} = \left(\frac{\sigma_i}{\sigma_0}\right)^2 . \quad (3.21)$$

With few exceptions, we do not have velocity-dispersion measurements for the neighboring galaxies. Thus we adopt a Faber-Jackson scaling of the form $L \propto \sigma^4$ to obtain

$$\frac{b_i}{b_0} = \left(\frac{L_i}{L_0}\right)^{1/2} . \quad (3.22)$$

(This is equivalent to Equation 3 of Keeton and Zabludoff 2004.) The ratio of b parameters between the lens and its neighbors can now be estimated from SDSS photometric data. From Equation 3.4, we approximate the total convergence at the position of the lens as

$$\begin{aligned} \kappa &= \frac{1}{2} \frac{b_0}{R_q} + \sum_{i=1}^{N_{\text{gal}}} \frac{1}{2} \frac{b_i}{R_i} \\ &= \frac{1}{2} \frac{b_0}{R_q} + b_0 \sum_{i=1}^{N_{\text{gal}}} \frac{1}{2R_i} \left(\frac{L_i}{L_0}\right)^{1/2} \\ &= \frac{1}{2} \frac{b_0}{R_q} + \kappa_{\text{env}} . \end{aligned} \quad (3.23)$$

The SDSS photometry and astrometry thus yield a direct estimate of the environmental convergence κ_{env} which scales linearly with b_0 , the true Einstein-radius parameter of the lens galaxy in the absence of environmental convergence. Next we use the well-known scaling

between fitted and true lens strengths in the presence of an unmodeled mass sheet,

$$b_0 = (1 - \kappa_{\text{env}})b_{\text{fitted}} \quad (3.24)$$

(Gorenstein et al. 1988; Saha 2000; Keeton and Zabludoff 2004). (This relation can be derived easily for the circularly symmetric case from the fact that the average convergence within the *observed* Einstein radius is always unity.) Substituting for κ_{env} from Equation 3.23, we may solve for b_0 in terms of the observable quantities b_{fitted} , L_i/L_0 , and R_i :

$$b_0 = \left[\frac{1}{b_{\text{fitted}}} + \sum_{i=1}^{N_{\text{gal}}} \frac{1}{2R_i} \left(\frac{L_i}{L_0} \right)^{1/2} \right]^{-1} . \quad (3.25)$$

We note that environmental corrections in low-redshift lenses such as ours will in general be smaller than for high-redshift lenses, since the images form at smaller physical radii and hence higher physical densities within the lens galaxy, lessening the relative effect of a given superposed environmental surface density. Note also that although we adopt Faber-Jackson scaling, the velocity dispersions of the neighbors are *not* set using a typical Faber-Jackson constant of proportionality. Rather, the constant is set by local self-consistency, so that the contributions of the lens galaxy and all neighbors at the position of the lens reproduce the observed image splitting. Thus associating all the mass of the environment with individual galaxies will not prevent us from modeling the effect of a single massive group/cluster halo, provided the halo mass distribution is traced by the galaxy distribution.

Deprojecting the Mass Constraint

Assuming we have an accurate measurement of the Einstein radius of a lens system corrected for extra environmental convergence, we must translate the cylindrical enclosed-mass constraint of the Einstein radius into a spherical enclosed-mass constraint on the 3D mass model under consideration with which to scale our Jeans-equation solution. For power-law density profiles this is easily done. If the three-dimensional density and enclosed mass are given by Equations 3.18 and 3.19, then projection of the density via Equation 3.14 and a subsequent integration of the two-dimensional density out to the radius of interest shows that the two-dimensional (cylindrical) enclosed mass is given by

$$M_{\text{cyl}}(R) = C_\gamma M_e (R/R_e)^{3-\gamma} , \quad (3.26)$$

with

$$C_\gamma = \int_0^\infty (1 + u^2)^{-\gamma/2} du . \quad (3.27)$$

We compute C_γ once for each power-law model under consideration, and use it to correct the projected mass M_{Ein} within the observed Einstein radius R_{Ein} to the mass enclosed by a sphere of radius R_e , which is simply

$$M_e = \frac{M_{\text{Ein}}}{C_\gamma} \left(\frac{R_e}{R_{\text{Ein}}} \right)^{3-\gamma} . \quad (3.28)$$

The Einstein Radius in Asymmetric Image Configurations

In attempting to constrain the logarithmic slope of power-law galaxy mass models, we must remember that our lensing constraints were derived by fitting an isothermal model to the data. For quadruple lenses and ring lenses, the mass enclosed within the Einstein radius is essentially model-independent, and is robustly measured for all mass models by fitting any single lens model. As discussed by Rusin et al. (2003b), double lenses require somewhat more care in their interpretation. In the context of circularly symmetric lens models, the observational mass constraint provided by a double-image strong lens is

$$\frac{M(R_1)}{R_1} + \frac{M(R_2)}{R_2} = \pi \Sigma_c (R_1 + R_2) . \quad (3.29)$$

For the symmetric case, setting R equal to the Einstein radius gives $M(R_{\text{Ein}}) = \pi \Sigma_c R_{\text{Ein}}^2$. We wish to answer the following question: how is the Einstein radius of a circular power-law lens model with an asymmetric image configuration related to the Einstein radius of an isothermal lens model fitted to the same data? We express the enclosed-mass function of the power-law model as

$$M(R) = \pi \Sigma_c R_{\text{Ein}}^2 (R/R_{\text{Ein}})^{1+\delta} \quad (3.30)$$

(i.e. $\delta = 2 - \gamma$ in the notation used above). For isothermal models $\delta = 0$, while $\delta < 0$ models have steeper profiles than isothermal and $\delta > 0$ models have shallower profiles. The data are the image radii R_1 and R_2 , and for the isothermal model we see from Equation 3.29 that $R_{\text{Ein,iso}} = R_1 + R_2$. Substituting the power-law $M(R)$ relation into Equation 3.29 and rearranging a bit, we find that

$$\frac{R_{\text{Ein,pow}}}{R_{\text{Ein,iso}}} = 2 \left[\frac{(1 + R_1/R_2)^\delta}{1 + (R_1/R_2)^\delta} \right]^{\frac{1}{1-\delta}} \quad (3.31)$$

(a nearly identical derivation is given by Kochanek 2004a). This correction is generally small but significant. For $R_1/R_2 = 3$, we have $R_{\text{Ein,pow}}/R_{\text{Ein,iso}} \simeq 1.07$ for $\delta = 0.5$ (corresponding to a 3D profile with $\rho \propto r^{-1.5}$), and $R_{\text{Ein,pow}}/R_{\text{Ein,iso}} \simeq 0.93$ for $\delta = -0.5$ ($\rho \propto r^{-2.5}$). We will use the correction factor from Equation 3.31 to determine approximately correct Einstein radii (and hence aperture-mass constraints) for generalized power-law models given the fitted isothermal Einstein radii. We note however that we are still susceptible to any systematic bias that might arise from our failure to consider the role of lens ellipticity in this correction.

3.6.3 Observational Power-Law Index Constraints

We are now equipped to calculate the constraints placed upon the logarithmic density slope γ in our strong-lens galaxies by the lensing mass constraints and aperture velocity-dispersion constraints. For each system, we compute the expected radial velocity-dispersion profile along the line of sight for a grid of power-law models ranging from $1 \leq \gamma \leq 3$. The mass profiles are scaled to respect the lensing mass constraints as derived from the SIE fitting (or ring-radius measurement, for the case of SDSSJ1630) and corrected for the effects of environment, deprojection, and lens-configuration asymmetry as described in § 3.6.2. The luminosity-weighted squared-dispersion profile for each value of γ is then integrated over the SDSS aperture, represented by a spherical top-hat convolved with a Gaussian PSF specified by the SDSS reduction pipeline. The derived value for γ is given by the value that predicts

the observed SDSS velocity dispersion σ_v . To estimate our confidence limits on γ for each system, we assume that our observational errors in Einstein radius R_{Ein} , de Vaucouleurs half-light radius R_e , and velocity dispersion σ_v are uncorrelated with one another (a fairly safe assumption) and characterized by a Gaussian distribution about the best value with a width given by our error estimates (an assumption perhaps more dubious but still sensible). We solve for γ for a grid of R_{Ein} , R_e , and σ_v ranging ± 4 standard deviations about the best value for each observational parameter, and weight the likelihood of the resulting γ by the differential probability of the input observational parameter set. The gridded solutions and likelihoods are then sorted, summed, and normalized to derive the cumulative and differential likelihood function for the parameter γ given the observed galaxy data and its errors. Figure 3-27 shows the derived likelihood curves for each of our 8 systems, under the assumptions of isotropic orbits ($\beta = 0$), slightly radial orbits ($\beta = 0.3$), and slightly tangential orbits ($\beta = -0.3$). Note the especially tight constraints on SDSSJ2302: this is a consequence of its apparently small effective radius ($\approx 0''.5$) as compared to the other lenses. Such a small value is somewhat worrisome (and in fact the SDSS photometric pipeline assigns a higher likelihood to an exponential surface-brightness model than to a de Vaucouleurs model). For the present we take the de Vaucouleurs R_e at face value for SDSSJ2302. The tight constraints are then a consequence of having an Einstein radius that is significantly different than the radius from which most of the velocity-dispersion weight is observed.

An immediate first question to consider is whether or not our eight systems are consistent with a universal single value of the power-law index γ . We can make a χ^2 test of this hypothesis by approximating the γ -likelihood functions of the individual lenses (which we index with i) as Gaussians. The variance σ_i^2 for each Gaussian is set to the square of one half the width of its two-sided 68% confidence interval. We calculate the best value for a hypothetical single γ as the sample mean of the individual maximum-likelihood (ML) values $\{\gamma_i\}$, with inverse-variance weighting. We then calculate the total χ^2 for the sample in the standard manner. For $\beta = (0.0, 0.3, -0.3)$ we find $\chi^2 = (24.4, 21.9, 27.4)$ for 7 degrees of freedom, giving reduced values of $\chi_r^2 = (3.5, 3.1, 3.9)$. Thus for the range of β considered, the universal γ hypothesis is ruled out at $> 99.7\%$ confidence (within the context of a normal-error approximation).

Given the apparent inconsistency of the data with a single γ value for all galaxies, we next solve for the parameters $\bar{\gamma}$ and σ_γ^2 of a ML Gaussian distribution for the intrinsic γ values:

$$P_\gamma(\gamma|\bar{\gamma}, \sigma_\gamma^2) d\gamma = \frac{1}{\sqrt{2\pi\sigma_\gamma^2}} \exp\left[-\frac{1}{2} \frac{(\gamma - \bar{\gamma})^2}{\sigma_\gamma^2}\right] d\gamma . \quad (3.32)$$

To permit analytic convolution of the intrinsic and observational scatter in γ , we again make a normal-error approximation via the $\{\sigma_i^2\}$ as defined above. The likelihood function to maximize is then

$$\mathcal{L}(\bar{\gamma}, \sigma_\gamma^2|\{\gamma_i, \sigma_i^2\}) = \prod_i P_\gamma(\gamma_i|\bar{\gamma}, \sigma_\gamma^2 + \sigma_i^2) . \quad (3.33)$$

We compute this likelihood function over a uniform 1000×1000 grid with $1 < \bar{\gamma} < 3$ and $0 < \sigma_\gamma < 1$. The function has a single smooth peak and drops to negligible values at all grid boundaries except at $\sigma_\gamma = 0$ near the peak. We normalize the function and determine the curve of constant likelihood enclosing 68% of the total likelihood. Table 3.2 gives the ML $\bar{\gamma}$ and σ_γ^2 values along with the projections of the 68% contour onto their respective axes for three values of the anisotropy parameter β . As one would expect, the

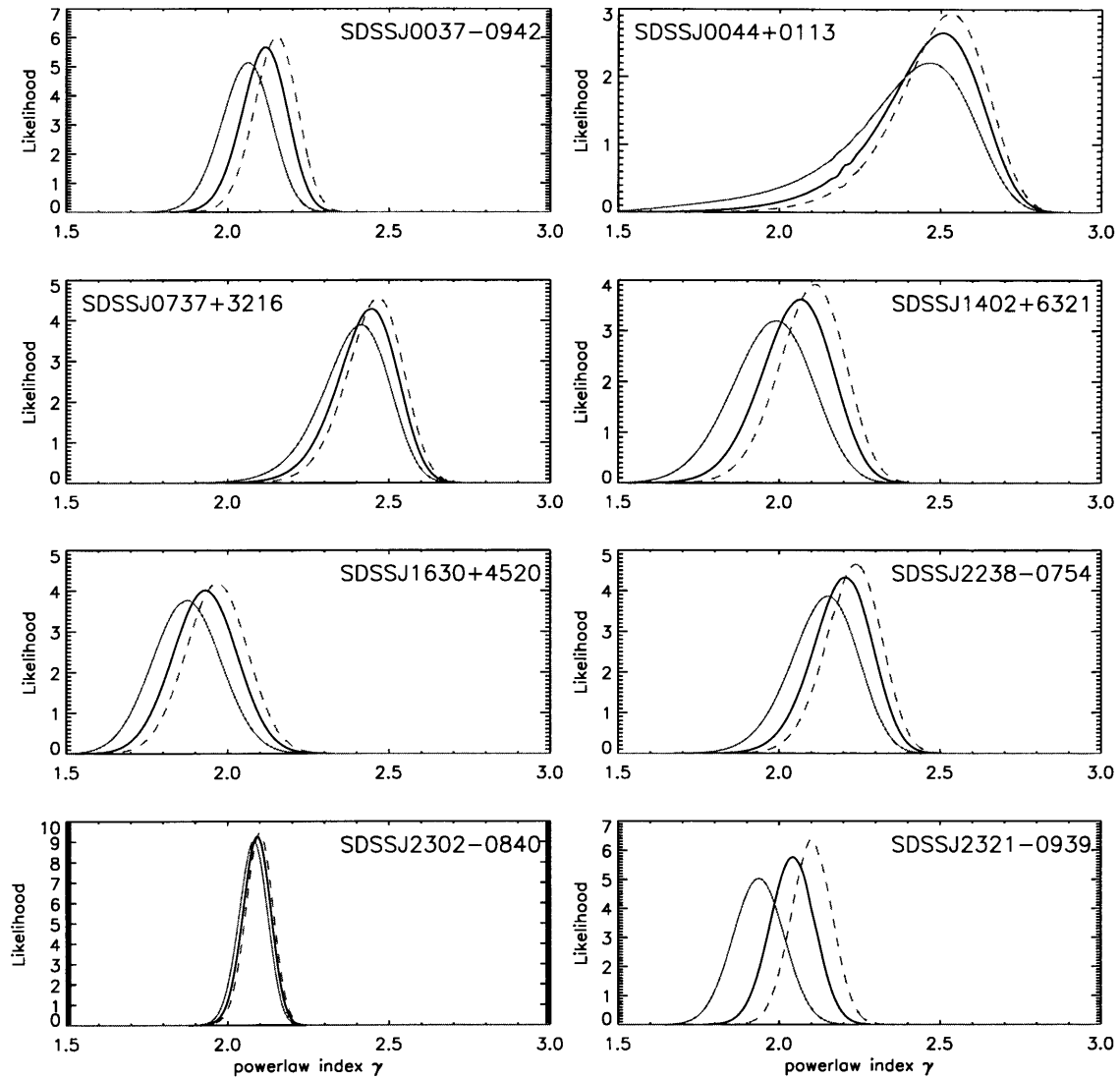


Figure 3-27: Power-law mass model likelihood constraints from IFU lensing and SDSS velocity-dispersion measurements. Solid black lines show likelihood curves for $\beta = 0$ (isotropic) models, solid gray lines show curves for $\beta = 0.3$ (radial) models, and dashed gray lines show curves for $\beta = -0.3$ (tangential) models.

principal axes of the likelihood contours are closely aligned with the $\bar{\gamma}$ and σ_γ^2 axes (i.e. $\bar{\gamma}$ and σ_γ^2 are essentially orthogonal model parameters). We see that the data favors a slightly steeper-than-isothermal profile with a modest but uncertain scatter of $\Delta\gamma \approx 0.1-0.2$. In the following chapters we will see the constraints of this nature that can be obtained when high-resolution imaging from the *Hubble Space Telescope* is available.

β	$\bar{\gamma}$	σ_{γ}
0	$2.15^{+0.12}_{-0.10}$	$0.13^{+0.13}_{-0.08}$
0.3	$2.09^{+0.12}_{-0.11}$	$0.13^{+0.14}_{-0.10}$
-0.3	$2.19^{+0.11}_{-0.11}$	$0.14^{+0.13}_{-0.08}$

Table 3.2: IFU lens sample constraints on the mean and standard deviation of a model Gaussian intrinsic power-law index distribution. Results are shown for several assumed values of the orbital anisotropy parameter β . Quoted errors are projections of the 68% confidence likelihood contour.

Chapter 4

The Sloan Lens ACS Survey: Hubble Space Telescope Imaging of Spectroscopic Gravitational-Lens Candidates

4.1 Introduction

This chapter presents the observational results of an efficient *Hubble Space Telescope (HST)* Snapshot imaging survey (program #10174) for new strong galaxy-galaxy gravitational lenses using the Advanced Camera for Surveys (ACS). We refer to this survey as the Sloan Lens ACS (SLACS) Survey. The targeted lens candidates are selected spectroscopically from within the Sloan Digital Sky Survey (SDSS) database for having nebular line emission at a redshift significantly higher than that of the SDSS target galaxy, as described in Chapter 2. The SLACS survey is optimized to detect bright early-type lens galaxies with faint lensed sources, in order to increase the sample of known gravitational lenses suitable for detailed lensing, photometric, and dynamical modeling. We present a catalog of 19 newly discovered gravitational lenses, 5 possible lenses, and 4 non-lenses/non-detections, implying a survey efficiency between 68% and 86%. The lensed features in these systems are revealed in great detail through a novel method for the effective subtraction of foreground galaxy images to reveal faint background features. The lens systems that we present here all show extended morphology in their lensed images, which can be used to derive detailed constraints on the gravitational potential of the lens galaxy. For several lenses, Gemini 8m and Magellan 6.5m integral-field spectroscopic data further support the lensing interpretation. The high efficiency of the SLACS survey appears to benefit from a magnification bias whereby faint but highly magnified background galaxies are selected with greater frequency than bright, unlensed projections, implying a steeply falling source-galaxy emission-line luminosity function. We show that the SLACS lens galaxies have photometric properties that are fairly typical of the spectroscopic parent sample from which they are drawn. Hence our sample represents the first statistically significant and homogeneously selected sample of bright early-type lens galaxies, furnishing a powerful probe of the structure of early-type galaxies within the half-light radius. The success of the SLACS survey in discovering a large number of new lenses suggests consideration of spectroscopic lens surveys as an explicit science goal of future redshift surveys.

4.2 The Survey

4.2.1 Candidate Selection

The method by which we select our lens candidates is essentially that described Chapter 2 (also Bolton et al. 2004). Briefly, we subtract best-fit PCA templates (a byproduct of the redshift pipeline) from the observed SDSS target-galaxy spectra. We require the SDSS continuum to be well-fit by the template, which effectively yields a parent sample of galaxies with well-behaved absorption-dominated spectra and very secure redshifts z_{FG} . The residual spectra are then scanned for nebular line emission at redshifts greater than z_{FG} . Spectra in which such emission is significantly detected for at least three separate common atomic transitions at a single background redshift z_{BG} are taken as lens candidates for having emission at two different redshifts along the same line of sight as sampled by the 3''-diameter SDSS spectroscopic fiber. Taking z_{FG} , z_{BG} , and the measured stellar velocity dispersion σ_v from SDSS allows us to calculate an approximate strong-lensing cross section for each system using a singular isothermal sphere (SIS) model as $\pi\theta_E^2$, with the Einstein radius given by $\theta_E = 4\pi(\sigma_v^2/c^2)(D_{LS}/D_S)$. To maximize the number of strong lenses in our survey, we formed our Cycle 13 *HST* target list from the candidates with the highest predicted lensing cross section. Thus our *HST* target sample is velocity-selected to leading order, with an additional selection bias in favor of systems with larger angular-diameter distance ratios D_{LS}/D_S (a function of the redshifts z_{BG} and z_{FG}). We take 20 of our targets from the list of lens candidates published in Bolton et al. (2004), which were selected from within the luminous red galaxy spectroscopic sample of the SDSS (LRG, Eisenstein et al. 2001). The LRG sample is defined by photometric selection cuts that very efficiently select massive early-type galaxies in the redshift range $0.15 < z_{\text{FG}} \lesssim 0.5$, as confirmed by SDSS spectroscopy. These galaxies are very homogeneous in their spectral, photometric, and morphological properties, and we place no further requirements on our LRG-sample lens candidates beyond their photometric selection as described in Eisenstein et al. (2001) and subsequent spectroscopic confirmation as galaxies with redshifts $z > 0.15$. The remaining 29 targets on our Snapshot list are selected with the same spectroscopic algorithm from within the MAIN sample of the SDSS (Strauss et al. 2002). The MAIN sample is much more heterogeneous, and we impose an absorption-dominated spectral criterion by requiring our lens candidates to have rest-frame equivalent widths in $\text{H}\alpha$ of $EW_{\text{H}\alpha} < 1.5 \text{ \AA}$ (with a few exceptions). It should be noted that although most of the systems we target do indeed exhibit early-type morphology, the candidate selection is purely spectroscopic aside from the initial targeting by SDSS based on imaging detection.

4.2.2 ACS Image Processing

Our ACS Snapshot observing strategy is discussed in Bolton et al. (2005), and consists of one 420s Wide-Field Channel (WFC) exposure through each of the two filters F435W and F814W. The SLACS lens candidates are selected to yield bright lenses with faint background sources. This facilitates the photometric, morphological, and kinematic study of the lens galaxy, but can also make the relatively faint lensed features difficult to detect and even more difficult to use in lens modeling. The key to success is effective subtraction of the image of the lens galaxy by fitting a smooth model to the image data (e.g. Peng et al. 2002). Given the extremely regular isophotal structure of most early-type galaxies, this is a reasonable proposition. The most common parametrized model for early-type brightness

distributions is the generalized de Vaucouleurs or Sérsic law (Sersic 1968):

$$I(R) = I_e \exp\{-b_n[(R/R_e)^{1/n} - 1]\} . \quad (4.1)$$

By convention, the effective radius R_e for any n is the radius enclosing half of the model's total luminosity. Accordingly, the constant b_n is given implicitly in terms of the incomplete and complete gamma functions by the relation

$$2\gamma(b_n, 2n) = \Gamma(2n) \quad (4.2)$$

(Ciotti 1991), with $b_4 = k_{1/4}$ in Equation 3.13. We experimented with elliptical Sérsic model-fitting and subtraction in our analysis, but generally found that the systematic residuals of the fit were large compared to the surface-brightness levels of the lensed features that we hope to use to constrain gravitational-lens models. The shortcomings of the Sérsic model led us to implement a more generalized galaxy-model fitting procedure involving a b-spline fit to the radial profile with a low-order multipole dependence to fit the angular structure.

The b-spline technique is a well-known method for fitting a piecewise-defined polynomial of arbitrary order to the dependence of a series of data values upon an independent variable (de Boor 1977). The coefficients of the polynomial change at breakpoints in the independent-variable domain, whose spacing may be chosen to allow more or less freedom depending upon the level of detail to be fit. A b-spline of order n (where by convention $n = 1$ is piecewise constant, $n = 2$ is linear, $n = 3$ is quadratic, $n = 4$ is cubic, and so on) has continuous derivatives to order $n - 2$ across the breakpoints. Here we will use bsplines of order $n = 4$, which have continuous 0th, 1st, and 2nd derivatives. The coefficients of the b-spline are determined by fitting to the data in a least-squares sense, and by the breakpoint spacing and derivative-continuity conditions. A b-spline model may be reinterpreted in terms of a number of localized basis functions within the domain whose shapes are set by the order of the b-spline and by the breakpoint spacing and whose amplitudes are determined by the fit to the data. The fit itself is entirely linear, and the localized influence of each basis function within the domain implies that only a banded-diagonal matrix need be inverted in the solution for the coefficients.

The radial b-spline technique for galaxy images permits smooth fitting of arbitrary radial brightness profiles. Since we do not have multiple dithered exposures to combine, we perform our b-spline galaxy-model fitting in the native ACS pixel coordinates of the images. We account for the distortion in the ACS by using the solution provided in the image headers to compute relative tangent-plane RA and Dec values for all pixels in the image, which are taken as the independent variables for the fit. We fit for surface brightness as a function of position using cosmic-ray-masked flat-fielded images (i.e. calibrated by the CALACS software pipeline¹ to measure surface brightness rather than counts-per-pixel), so our fits are not biased by slight variations in pixel area across the images. The one non-linear step in our b-spline galaxy-model fitting is the determination of the center of the lensing galaxy; we describe our centering method further below. The model-fitting procedure is carried out using the adopted center for the lens galaxy within a suitable subsection of the ACS field (typically $12'' \times 12''$), along with an error image, a mask specifying cosmic-ray and other zero-weight pixels, and a mask corresponding to stars, neighboring galaxies, and any apparent background-galaxy features. For each pixel in the subimage, the radial offset R

¹(see <http://www.stsci.edu/hst/acs/>)

from the galaxy center (in arcseconds) and the azimuthal angle θ relative to a fixed position angle are computed. A set of breakpoints in R is chosen for the fit, typically every $0''.2$ – $0''.3$ in the central $1''$ to $2''$, with increased spacing further out. For the case of complete Einstein rings, breakpoints at the ring radius can be removed to allow smoother interpolation of the lens-galaxy model over the ring region. A multipole angular dependence is incorporated into the fit as follows. If the purely one-dimensional b-spline fit is represented as

$$I(R) = \sum_k a_k f_k(R) \quad , \quad (4.3)$$

where the $f_k(R)$ are the localized basis functions that are only non-zero over a small range of breakpoints and the a_k are their amplitudes, then the two-dimensional fit is represented by

$$I(R, \theta) = \sum_{m,k} [b_{mk} \cos(m\theta) + c_{mk} \sin(m\theta)] f_k(R) \quad . \quad (4.4)$$

The number of multipole orders to be fit is chosen individually for each galaxy, with $m = 0$ (monopole) and $m = 2$ (quadrupole) always present and higher-order terms added if necessitated by systematic angular structure in the residual images. With the occasional exception of an $m = 1$ (dipole) term to capture slightly disturbed morphologies or mild mis-centering in the central regions, only even multipole orders are used. This form of angular dependence is ideal for fitting early-type galaxies: the fit remains linear, the global symmetries seen in early-type galaxies are naturally reflected in the low-order terms, and effects such as isophotal twists, varying ellipticity with radius, and diskiness/boxyness can be captured with minimal effort (with only the last of these effects requiring multipole orders beyond the quadrupole). As an example, we describe the fit to the sky-subtracted image of the E3 lens galaxy SDSSJ0912+0029 to give the F814 residual image shown in Figure E-1, which uses breakpoints spaced every $0''.3$ in R and multipole terms of order 0, 2, and 4 (monopole, quadrupole, and octopole). The ratio of the $m = 2$ amplitudes (defined as $\sqrt{b_{2k}^2 + c_{2k}^2}$) to the $m = 0$ amplitudes rises from ≈ 0.25 in the center to ≈ 0.4 at the effective radius (about $3''$), and the ratio of the $m = 4$ to the $m = 0$ amplitudes rises from ≈ 0 to ≈ 0.1 over the same range. Some of this increase in angular structure with radius is due to our fitting directly to the PSF-blurred data. We note also that the monopole term can automatically include a fit to the sky background.

Following the completion of the initial b-spline model-fitting step (which for our $12'' \times 12''$, 240×240 -pixel images generally takes 2–3 seconds on a 2.53GHz Pentium 4 Linux PC), we examine the residual (data–model) image for faint features not associated with the smooth galaxy model and not initially masked, and perform a second fit with an updated mask, also adding multipole orders as needed. Since at this stage we are principally concerned with generating high-quality residual images and not with the measurement of lens-galaxy parameters, we fit directly to the images without convolving the b-spline model with the HST point-spread function. The resulting residual images of our new lenses are presented in § 4.3.

The centering necessary for the b-spline galaxy fit is accomplished by first fitting with respect to a best-guess center with monopole, dipole, and quadrupole terms. This fit is then evaluated in a ring and used to determine a flux centroid, which is adopted as a new best-guess center for another iteration of the same procedure. Within a few iterations this process—which amounts to minimizing the dipole term—converges to a position that we

adopt as the constrained center for the final model fit.

4.3 Observed Systems and New Lenses

Here we describe the catalog of candidate lens systems observed by the SLACS survey up until 2005 March 22. Photometric and spectroscopic parameters for the sample as measured by SDSS are given in Table A.1. Figure B-2 presents the SDSS discovery spectra of all targeted systems, focused on the background-redshift line emission. Based on their spectroscopic detections (i.e. two redshifts in one SDSS fiber spectrum), imaging colors and morphology, and on their ability to be fit by simple singular isothermal ellipsoid (SIE) lens models (Koopmans et al. 2005, in preparation), we classify these systems as definite lenses, possible lenses, and non-lenses/non-detections, and we display their ACS images in Figures E-1, E-2, and E-3 respectively. The classification presented here represents the consensus of the five SLACS collaborators. All systems classified as lenses here have been successfully fitted with SIE gravitational lens models using the method of Warren and Dye (2003) as implemented by Koopmans et al. (2005, in preparation). This technique uses the residual *HST*-ACS image data following the subtraction of a smooth galaxy model as described in § 4.2.2. For an assumed set of SIE model parameters, a linear least-squares solution is found for the pixellated source-plane brightness distribution that best fits the observed images when viewed through the potential of the lens model and convolved with the *HST* PSF. The best-fit lens model is then found by wrapping this linear fit within a nonlinear optimization of the SIE parameters. For systems with low signal-to-noise, the source-plane brightness distribution is regularized using a term in the linear χ^2 that penalizes curvature. The SIE Einstein-radius parameters derived from this fitting will be used in Chapter 5.

For cases where the images in Figures E-1—E-3 are not self-explanatory, we provide the following brief remarks:

SDSSJ0216–0813: A faint but definite counterimage is seen to the NE in both bands in this system, opposite the more obvious extended arc.

SDSSJ0912+0029: This system shows a faint extended counterarc to the S in the F814W band, opposite the more prominent Northern arc. Both images are only marginally detected in the *F435W* band.

SDSSJ0956+5100: This system includes a small round red companion to the N of the lens galaxy, not to be confused with the prominent lensed images.

SDSSJ1251–0208: This galaxy has extended spiral structure in addition to the lensing bulge.

SDSSJ1330–0148: This system is judged to be a lens on the basis of the compact counterimage detected at high significance in both bands.

SDSSJ1402+6321: This lens, with faint quadruple images, was the first system observed by the SLACS survey and is the subject of Bolton et al. (2005).

SDSSJ1618+4353: The angular resolution of *HST* reveals this system to be a pair of foreground galaxies. The pair lenses a compact background source into a 3+1 quad configuration. The extra compact image to the west of the counterimage is more blue in color than the lensed images and thus does not pertain to the lensed configuration.

SDSSJ1718+6424: A second nearby galaxy contributes significantly to the lensing potential in this system.

We note that all five systems considered possible but not definite lenses (shown in Figure E-2) show a faint candidate counterimage near the center of the foreground galaxy

opposite a more prominent image at larger radius. If these features were all due to residual error in the foreground galaxy subtraction, this configuration would not be expected. Indeed, the most asymmetric double lenses will in general have faint counterimages at small angular offset from the lens center, and will be the most difficult lenses to confirm. Their status as lenses or non-lenses has a significant impact on statistical inferences based on the lens sample as will be shown in § 4.4.1. Integral-field spectroscopy provides the best chance to associate background-redshift line emission with the faint putative core images and thereby confirm or reject a strong-lensing hypothesis.

Many of the lens galaxies shown in Figure E-1 show such striking features in their residual images that their interpretation as strong lenses is nearly certain when considered in combination with the SDSS spectroscopic detection and the success of fitted SIE lens models as described above (and Koopmans et al. 2005, in preparation). For putative lenses with less dramatic morphology, further evidence as to their status may be obtained with integral-field spectroscopy, which can confirm or deny the spatial coincidence between the high-redshift line emission and the candidate lensed features seen with *HST*. For several of our SLACS target galaxies, we have obtained spatially resolved spectroscopy with integral-field units (IFUs) on the 6.5m Walter Baade (Magellan I) telescope at Las Campanas Observatory and the 8m Gemini-North telescope at Mauna Kea; this data can be seen in § 3.4.3 and in Appendix D. In all cases, the IFU emission-line images are coincident with the ACS residual-image morphology, supporting the strong-lensing interpretation. As an example, Figure 4-1 presents this comparison for the lens system SDSSJ1402+6321 in a single figure with equal image size, alignment, and rotation between *HST* and IFU data.

4.4 Statistics

The statistics of strong gravitational lensing are the subject of a great body of literature (e.g. Turner et al. 1984 and many others), most of it dealing with the lensing of quasars by galaxies. The rigorous statistics of the SLACS survey, though involving similar considerations, would be sufficiently distinct to require their own detailed treatment: our original sample is formed from potential lensing objects rather than from potentially lensed sources, and we must consider the effects of an extended source image and finite fiber sampling. A full lens-statistical analysis is beyond the scope of the current paper, but we do address two particular statistical questions related to the distribution of lensing configurations and the distribution of lens-galaxy observables.

4.4.1 Magnification Bias

One of the greatest uncertainties at the outset of our survey was of course the fraction of strong lenses within the candidate list. One can attempt to calculate the lensing probabilities of the candidates given z_{FG} , z_{BG} , σ_v , assuming a model for the SDSS spectroscopic observations, and assuming a luminosity function (LF) and size/shape for the background emission-line galaxies, as was done in § 2.5.2, but the large number of uncertain ingredients makes for a somewhat dubious calculation. To put it simply, we did not know before carrying out our survey whether or not the majority of our targets would owe their high-redshift line emission to the PSF-smearred wings of bright unlensed galaxies at large impact parameter rather than to Einstein-ring images of faint galaxies closely aligned with the SDSS target galaxy. The high ratios of lenses to non-lenses and quads/rings to doubles that we now see are suggestive of a magnification bias in our selection, with highly magnified faint

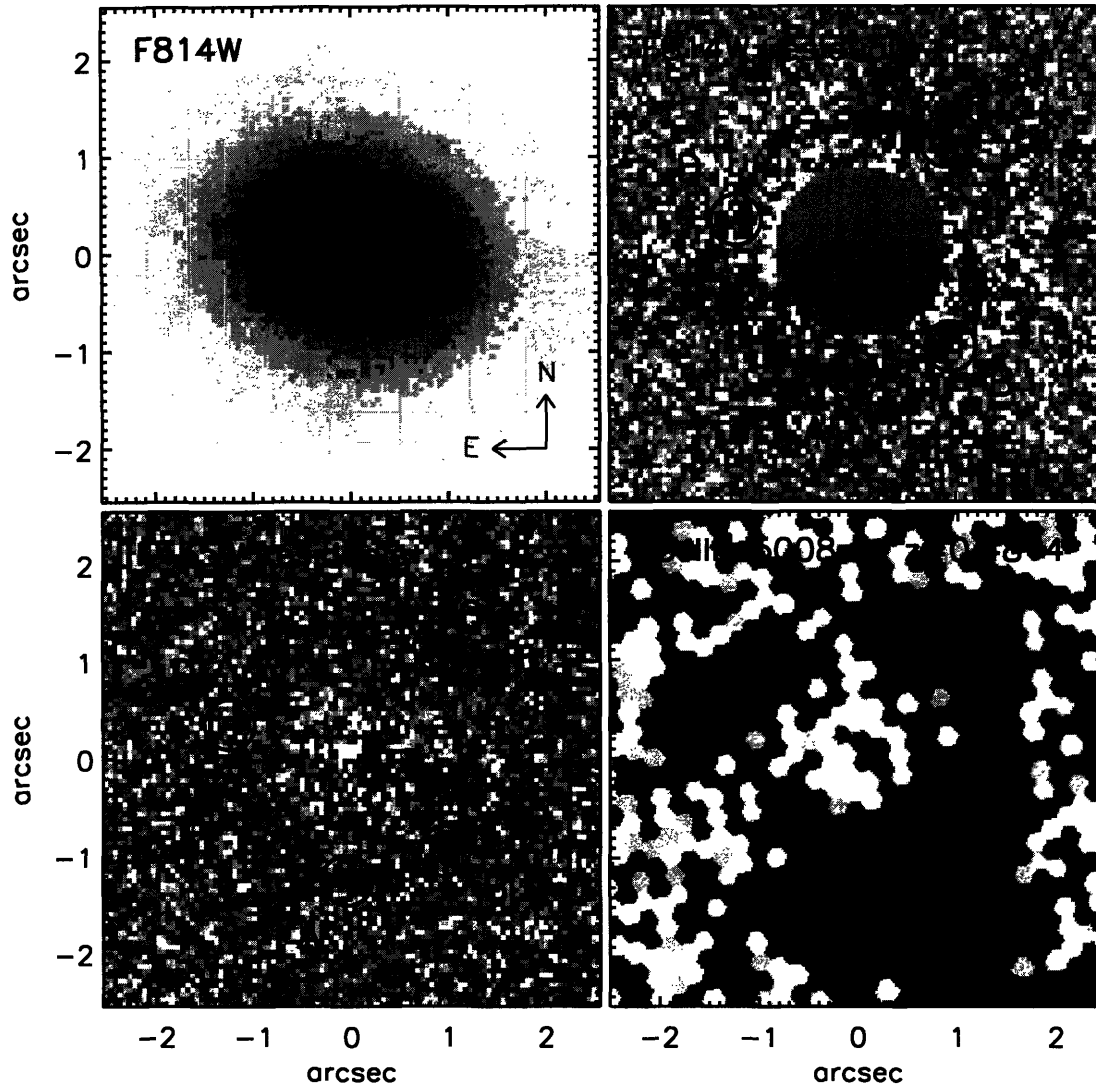


Figure 4-1: *HST* and IFU image comparison for SDSSJ1402+6321. Upper left: *HST*-ACS F814W direct image of SDSSJ1402+6321 with N up, E left. Upper right and lower left: Sérsic-subtracted F814W and F435W residual images showing four putative lensed features, labeled A–D. Lower right: IFU continuum-subtracted emission-line image of [O III] 5007 emission at a redshift higher than that of the foreground galaxy. Note coincidence of IFU emission-line image features with putative lensed images in *HST* data, supporting the strong lensing hypothesis and ruling out an interpretation of the features as spiral structure in the foreground galaxy. IFU emission-line image gray-scale has been histogram-equalized. See Figure 3-22 for summed IFU spectra confirming the identity of the IFU line emission as [O III] 5007. Figure is reproduced from Bolton et al. (2005). Figure-generation script written by Leonidas A. Moustakas.

lensed galaxies detected with greater frequency than less magnified lensed galaxies or unlensed projections. In the simplest circumstance of flux-limited surveys for point sources such as quasars, magnified lines of sight will be over-represented if the logarithmic slope of the source LF, $d \log N(> L)/d \log L$, is steeper than -1 (Narayan 1989; Borgeest et al.

1991). In the context of a power-law luminosity function for which the number of galaxies per unit volume per unit luminosity is proportional to $L^{-\alpha}$, this magnification bias will hold if $\alpha > 2$. Although we defer the full statistical analysis of the SLACS sample to future work, it is informative to examine a simplified treatment of the rough constraint on the LF of emission-line galaxies at redshift ~ 0.5 afforded by the incidence of lensing within the SLACS survey.

For our toy model, we assume that all the SLACS lenses are isothermal spheres with an Einstein radius of $1''.2$ (an approximate median value from Koopmans et al., in preparation), and that we can estimate the source-plane impact parameter of the background galaxy in units of the Einstein radius from the asymmetry of the lensed image configuration as $x = (R_1 - R_2)/(R_1 + R_2)$. Here R_1 and R_2 are the distances of the outermost and innermost opposing images from the lens center, which we estimate directly from the residual images. The scaled impact parameter x is a proxy for the magnification μ (and for the quad/ring versus double distinction, in some sense), with smaller x giving larger μ . We calculate the overall delivered magnification function $\mu(x)$ by assuming $1''.3$ seeing (the median SDSS spectroscopic seeing for our targets) and integrating over the $3''$ -diameter SDSS fiber. We model the source galaxies as exponential disks with a disk scale length of $0''.2$, and compute their lensed images as a function of impact parameter for the assumed SIS lens model. The resulting function $\mu(x)$ peaks at ≈ 7 for $x = 0$, falls to ≈ 1.9 at $x = 0.5$, and to ≈ 0.27 at $x = 1$. To verify that our circular approximation is not unreasonable, we also compute $\mu(x)$ along the minor and major axes of an elliptical lens model with isodensity axis ratio $q = 0.8$, and find it to be within 10% of the value computed for a circular model out to $x = 1.5$. We approximate the LF of emission-line galaxies as a scale-free power law, with the number of galaxies per unit volume per unit luminosity L proportional to $L^{-\alpha}$. This gives a number of galaxies per unit area on the sky down to some limiting line flux S_{lim} of

$$N(> S_{\text{lim}}) \propto S_{\text{lim}}^{1-\alpha} . \quad (4.5)$$

The differential source-plane cross section per unit scaled impact parameter is simply $d\sigma/dx \propto x$ (since $d\sigma = 2\pi x dx$). For a fixed value of α , the differential probability of detecting a background galaxy with a given impact parameter is then given by

$$\begin{aligned} p(x|\alpha) dx &\propto N(> S_{\text{lim}}/\mu) \left(\frac{d\sigma}{dx} \right) dx \\ &\propto [\mu(x)]^{\alpha-1} x dx . \end{aligned} \quad (4.6)$$

Note that for the power-law LF the limiting flux S_{lim} is absorbed into the overall normalization factor. We may then regard $p(x|\alpha)$ as a likelihood function for α given our observed impact parameters $\{x_i\}$:

$$\mathcal{L}(\alpha|\{x_i\}) = \prod_i p(x_i|\alpha) , \quad (4.7)$$

and find the maximum-likelihood (ML) value for α .

The derived α value is quite sensitive to the inclusion or exclusion of the possible lenses presented in Figure E-2. If we use only the definite lenses Figure E-1, we find an ML value of $\alpha \simeq 4.0$, while if we include the five systems from Figure E-2 with their estimated x values we find $\alpha \simeq 3.4$. Including the Figure E-2 systems all with fiducial values of $x = 1$ gives $\alpha \simeq 2.2$. The range in α is large, but the values support the naïve conclusion of $\alpha > 2$ based on the apparent bias of the sample toward highly magnified systems. Including a

typical magnification factor of ~ 4 and assuming a nominal source redshift of $z_{\text{BG}} = 0.5$, our typical source galaxy has an [O II] 3727 luminosity $L_{[\text{OII}]}$ of order $10^{41} \text{ erg s}^{-1}$ (Bolton et al. 2004). For continuum-selected galaxies over the range $0 < z < 1.5$, Hogg et al. (1998) find an [O II] 3727 LF steep enough to cause a magnification bias for $L_{[\text{OII}]} \gtrsim 10^{42}$. Thus our apparent magnification bias may be indicative of a fading of the LF break luminosity to the slightly lower redshifts probed by our survey and a consequent steepening of the LF at fixed L .

4.4.2 Are Our Lenses Special?

A large and homogeneous sample of gravitational lenses such as we present here holds great promise for the study of early-type galaxy structure *if* our lenses are a fair sampling of the early-type galaxy population of the universe. The velocity and redshift dependence of our HST target selection should not in itself present any complication in the comparison of our lenses to other galaxies with similar velocity dispersions and redshifts. However, before using our new strong lenses to make deductions about the structure of early-type galaxies in general, we must verify that our lens selection has not somehow produced a sample of atypical galaxies. The question can be framed between two alternatives: do we select simply for back-lighting through a chance foreground-background coincidence, or is there some significant bias by which galaxies with atypical properties are more likely to be selected as lens candidates based on their SDSS spectra? To test this possibility we exploit the huge parent-sample size of the SDSS (Early Data Release through Data Release 3). For each lens we construct a control sample of SDSS galaxies with nearly the same redshift and velocity dispersion—quantities for which we explicitly select—and test whether the lens galaxy is typical of galaxies in the control sample in terms of its magnitude, color, and effective radius—quantities for which we do not explicitly select. Although this is not a definitive test of the representative nature of our lenses (it will not uncover any “hidden variable” bias that does not correlate with photometric observables), it is straightforward, robust, and informative. By forming control samples at the redshift of the lenses, we avoid the necessity of applying evolution- and k -corrections to the broadband magnitudes. We may perform our comparison sensibly for galaxies with velocity dispersions well-measured by SDSS. We exclude the lens SDSSJ1251–0208 from the analysis, both because its spectral signal-to-noise ratio is too low for a confident velocity-dispersion measurement and because its $\text{H}\alpha$ equivalent width exceeds our absorption-dominated threshold. The double-lens galaxies SDSSJ1618+4353 and SDSSJ1718+6424 are also excluded for obvious reasons. This leaves a well-defined sample of 16 single early-type lenses. The comparison sample for each lens consists of unique galaxies from the SDSS database with redshifts within ± 0.005 of the lens redshift, velocity dispersions within $\pm 15 \text{ km s}^{-1}$ (approximately the median velocity-dispersion error of the sample) of the lens galaxy, and median signal-to-noise per spectral pixel greater than 8. For LRG-sample targets, we also require the comparison sample to pass the photometric LRG cuts, and for the MAIN-sample lenses, we require a rest-frame $EW_{\text{H}\alpha} < 1.5 \text{ \AA}$. We make a luminosity-distance correction to the broadband magnitudes and an angular-diameter-distance correction to the effective radii within the redshift slice to place all galaxies closer to the exact redshift of the lens. The resulting individual comparison samples have as few as 17 and as many as 1793 galaxies, with a mean of 451 and a median of 337 control galaxies per lens galaxy. Smaller control samples limit the statistical significance of an outlying lens in that its rank is at least $1/N_{\text{gal}}$ and at most $1 - 1/N_{\text{gal}}$, where N_{gal} is the number of galaxies in its control sample.

We would like to answer the question of whether our lenses have observables (luminosities, colors, and effective radii) consistent with having been drawn from the distribution of those observables seen in the control samples. Since we only have one lens at each redshift, a straightforward Kolmogorov-Smirnov (K-S) test of the lens sample against the control samples is not possible: even under the null hypothesis, each individual lens has a different parent distribution. We may however put all these parent distributions on common footing by using the fact that the K-S test is invariant under a monotonic rescaling of the variable under consideration. Specifically, for each individual lens's control sample, there exists a transformation of the observable of interest that converts the control distribution into a uniform distribution between the minimum and maximum values. The correspondingly transformed lens observable is simply equal to the normalized rank (between 0 and 1) of the lens quantity within the cumulative distribution of the control sample in that quantity. Thus we may perform a one-dimensional K-S test of the distribution of lens-observable ranks against a uniform distribution over the interval 0 to 1. This test is in some sense like a rank-correlation test within the K-S formalism: does ranking as a lens correlate with ranking in luminosity, color, or size? Figure 4-2 shows the cumulative distributions of lens rankings in r (magnitude), $g - r$ (color), and R_e (effective radius) within their control samples. From these distributions we compute the statistic D_{KS} , equal to the maximum difference between the cumulative rank distribution and the null-hypothesis distribution. Since the parent distribution under the null hypothesis is known exactly by construction (uniform probability for any rank between 0 and 1), and since the total number of control galaxies is much larger than the number of lenses, we compute the significance of D_{KS} for a distribution of 16 values against a known parent distribution (e.g. Press et al. 1992). The resulting probabilities of the lens sample having been drawn at random from the control-sample distributions in r , $g - r$, and R_e are 0.195, 0.426, and 0.233 respectively: none of these probabilities are especially unlikely. Although the statistical significance is not great, we do note that none of our lenses fall within the largest quartile of their control samples in effective radius, which is somewhat suggestive of the effect that less centrally condensed objects are less efficient gravitational lenses (e.g. Li and Ostriker 2002). Overall, when judged by their photometric properties, our lenses appear to be a fair sampling of galaxies with similar redshifts and velocity dispersions.

4.5 Discussion and Conclusions

The success of the SLACS survey in discovering a large number of gravitational lenses convincingly demonstrates the technical feasibility of carrying out spectroscopic surveys for strong gravitational lenses. The results are even more striking when one considers that this type of lens survey was never one of the explicit science or design goals of the SDSS. The positive results of our survey are thus a testament to the performance of the SDSS telescope and spectrograph, and to the optimal quality of the SDSS spectroscopic data pipeline. With the clarity of hindsight, we may identify those particular features of the SDSS that were beneficial to the spectroscopic lens survey project and those that could conceivably be improved in any future survey to increase the yield of spectroscopically selected strong lenses suitable for specified science goals.

The obvious and overwhelming advantage afforded by the SDSS for this project or any other rare object survey is in the massive number of galaxies observed. Empirically, we have found that spectroscopic lenses and lens candidates appear with a frequency on the

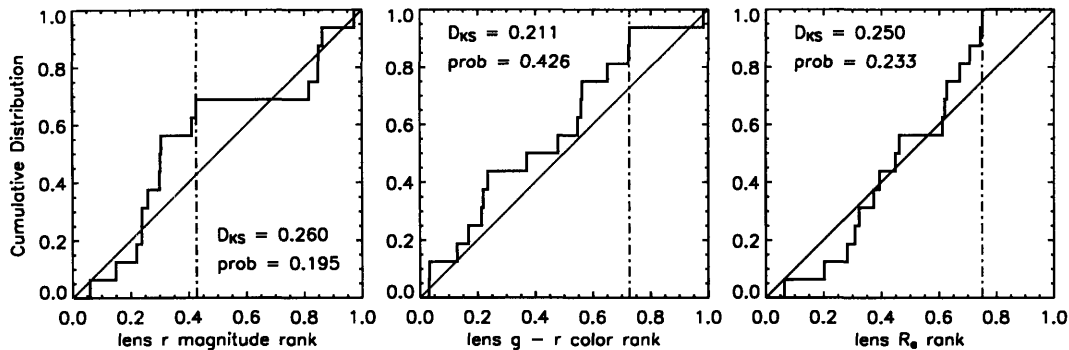


Figure 4-2: Kolmogorov-Smirnov tests of the rank of lens-galaxy observables within the cumulative distributions of those observables in control galaxy samples with similar redshifts and velocity dispersions. From left to right are the distributions for r -band magnitude, $g - r$ color, and effective (half-light) radius R_e (all as measured from SDSS imaging data for a de Vaucouleurs galaxy model). Solid black lines show the cumulative distribution in rank, solid gray lines show the null hypothesis for this distribution, and vertical dash-dot lines show the location of the maximum difference between the two distributions.

order of one in a thousand in the SDSS: starting with $\sim 10^5$ galaxies is therefore one key to success. At the same time, the large number of highly magnified galaxies that we have found close to the spectroscopic detection limit (note the generally low emission-line signal-to-noise ratio in the discovery spectra of Figure B-2) suggests that we may only be seeing the tip of the iceberg. Even for a conservative power-law LF exponent of $\alpha = 2$, an increase in the spectroscopic depth by a given factor should yield an increase by the same factor in the number of detected lenses (see Equation 4.5). We conclude that (1) a spectroscopic lens survey will always be at an advantage if it can “piggy back” on a more broadly conceived spectroscopic survey that does not have lenses as its sole scientific goal, and (2) future spectroscopic surveys that go significantly deeper than the SDSS should, all other factors being equal, discover a significantly larger number of gravitational lenses.

One might suspect that a significant factor in the success of the SLACS survey is the large ($3''$ -diameter) aperture of the SDSS spectroscopic fibers, which should capture a significantly larger fraction of the lensed flux from lenses with $\sim 2''$ splittings (i.e. $\sim 1''$ Einstein radii) than would a smaller fiber. If we reduce the model fiber size to $2''$ in diameter in the calculations of § 4.4.1 we find the delivered flux suppressed by a factor of 0.4–0.5 depending on impact parameter. This is essentially the factor of $(1/1.5)^2 \simeq 0.44$ corresponding to the diminished aperture size. Thus for lenses of the angular size typical of SLACS lenses, the advantage of a large fiber is just the simple advantage of a large aperture due to the smearing effects of seeing; a smaller fiber would not have lost a disproportionate amount of line flux due to lensing geometry. However, for lenses with larger image splittings (which would occur for higher redshift sources behind the same foreground galaxies), a small fiber would likely be a qualitative disadvantage to a spectroscopic lens survey.

For two principal reasons, our spectroscopic survey owes much success to having targeted lens candidates with background redshifts confirmed by multiple emission lines. First, the incidence of false-positive spectroscopic detections and emission-line mis-identifications is negligible. Second, to fixed line-flux limits, intermediate-redshift emission from [O II] 3727, [O III] 5007, and the hydrogen Balmer series is more common than Lyman- α emission at high redshift (Hippelein et al. 2003; Maier et al. 2003), and thus we see an abundance of

oxygen/Balmer lenses. However, for optical surveys, this survey strategy limits the background redshifts to $z_{\text{BG}} \lesssim 0.8$, beyond which $\text{H}\beta$ and $[\text{O III}] 5007$ move out of the observable band. There is a definite incentive to discover significant numbers of lenses with higher lens and source redshifts, both to probe evolution in the lens population and to observe lensed images at larger physical radii within the lens galaxy in order to obtain greater leverage on dark-matter halos. Therefore in designing future surveys to discover gravitationally lensed emission-line galaxies at higher redshift, two obvious considerations are increased survey depth to detect a fainter population, and increased spectroscopic resolution beyond the $\lambda/\Delta\lambda \approx 1800$ resolution of the SDSS in order to split the $[\text{O II}] 3727$ doublet and resolve the characteristic asymmetric profile of Lyman- α emission (thus permitting more secure single-line redshifts).

The SLACS lens sample provides a statistically significant and homogeneously selected sample of mostly early-type gravitational lens galaxies, the largest such sample assembled to date. The lensed images provide an aperture mass constraint within a typical scale of $\sim R_e/2$. The SLACS lens galaxies are all vastly brighter than their lensed background galaxies, and are thus ideally suited to detailed photometric measurement as with the current ACS data. They are also excellent candidates for spatially resolved spectroscopy to constrain dynamical galaxy models in combination with the mass constraints from strong lensing. In fact, nearly all of the SLACS galaxies already have well-measured luminosity-weighted velocity dispersions inside the $3''$ SDSS fiber (see Table A.1), and thus we have already increased the number of known gravitational lenses with known stellar velocity dispersions by an appreciable factor. Hence this lens sample represents a unique resource for the detailed measurement of the mass profile of early type galaxies within the effective radius.

Chapter 5

Mass Profile Constraints from HST Lensing and Photometry

5.1 Why HST?

The full potential of strong galaxy-galaxy lensing to constrain the gravitational potentials of lens galaxies can only be realized with high-resolution imaging data such as is provided by the *Hubble Space Telescope* (*HST*). High-resolution imaging allows for detailed photometry and astrometry of the lensed images, which in turn can constrain detailed models of the lensing potential. When the lensed sources are extended galaxies such as in our lens sample (see Figure E-1), the relative distortions and magnifications between multiple lensed images can furnish constraints on the slope of the lensing potential. Similar constraints are generally unavailable in quasar lenses, both because the quasar images sample only single positions in the source plane and because the flux ratios of quasar images are strongly altered by the effects of local substructure in the lens. High-resolution imaging also permits detailed measurement of the surface-brightness distribution of the lens galaxy and hence tightly constrains the shape of the stellar contribution to the lens potential. In this chapter we exploit our high-resolution *HST* data to derive several results on the radial density profile of the gravitational lenses presented in Chapter 4.

5.2 Aperture Masses and Velocity Dispersions, Revisited

In § 3.6 we derived the constraints that can be obtained by combining measurements of lens-galaxy mass within the aperture of the Einstein radius with lens-galaxy velocity dispersions within the aperture of the SDSS spectroscopic fiber. Here we revisit that calculation with our expanded sample of lenses observed with *HST*-ACS and presented in Chapter 4.

5.2.1 The Stellar Distribution

The effective radius of the lensing galaxy is a key ingredient in our calculation, and the exquisite angular resolution of *HST* allows for a much more accurate measurement of this quantity than can be obtained from ground-based data. We make this measurement by fitting an elliptical de Vaucouleurs surface brightness model (Equation 3.13) directly to the F814W band ACS data in the native frame over a $24'' \times 24''$ region centered on the target galaxy. The fit is weighted by the inverse statistical variances in each pixel, and pixels

affected by cosmic rays are given zero weight. We also mask regions of the image affected by stars, neighboring galaxies, and lensed features. We account for the distortion in the ACS by using the astrometric solution supplied in the image header to compute the RA and Dec of each native pixel relative to the image center. The model surface brightness distribution is then evaluated at these positions and compared to the flat-fielded image pixel values (which represent surface-brightness measurements). Figure 5-1 shows the comparison between de Vaucouleurs effective radii as measured by *HST* and SDSS for the same 26 galaxies (all galaxies shown in Figures E-1–E-3, excluding the double systems SDSSJ1618+4353 and SDSSJ1718+6424). Under the assumption that the *HST* measurements give the true R_e values to within their statistical errors (which are less than 1%), this figure gives an indication of the accuracy of the SDSS values and error estimates that were used in § 3.6, and shows the improvement provided by *HST*. Although we used SDSS r -band effective radii in § 3.6, we use i -band values here in order to make the fairest comparison to *HST*-ACS F814W¹. The agreement between *HST* and SDSS values is generally good for $R_e < 3''$, but the few systems with $R_e > 3''$ as measured with *HST* have systematically lower values from SDSS. This is likely due to a systematic bias arising from the respective choices of regions over which to fit: the SDSS pipeline fits de Vaucouleurs profiles out to $R = 7R_e$, whereas our *HST* fits are over a fixed $24'' \times 24''$ region. Since we are most concerned here with obtaining an accurate profile at the small radii probed by strong lensing, we choose not to enlarge the area of the fitting region for the few $R_e \gtrsim 3''$ galaxies in our sample.

5.2.2 Lensing Aperture-Mass Constraints

As seen in Figure E-1, our *HST*-ACS strong lens sample shows a great richness of lensing configurations that can provide detailed constraints on the projected potential of the lensing galaxies. The type of constraints provided, the classes of models appropriate, and the associated degeneracies between the resulting model parameters will in general vary greatly according to the details of each system. In § 5.3 below we will explore the radial mass profile constraints that may be derived for one of our lenses with a particularly favorable image configuration. As a first step, we may analyze all the lenses homogeneously in terms of the SIE model as in § 3.4, to measure the SIE-model Einstein radii and derive the associated aperture-mass constraints. Here we will use the SIE-model Einstein radii of Koopmans et al. (2005, in preparation), for which we assume uniform 0'01 errors. These Einstein radii have been measured by fitting SIE models to the residual *HST*-ACS imaging data as described in § 4.3. For the five lenses that overlap with the IFU lens sample from § 3.4, we may compare the Einstein radii from IFU and *HST* data as a cross-check of the two methods. This comparison is shown in Table 5.1. For the four model-fitted IFU systems, the Einstein radii agree with the *HST*-measured values to within 0'05. This level of agreement bodes well for ground-based IFU strong lensing studies, although the disagreement somewhat exceeds the quoted statistical uncertainties in the IFU Einstein radii ($\chi_r^2 \simeq 2.4$ for the sample of five).

¹The median fractional difference between SDSS r - and i -band R_e values for our sample is 7% (i.e. r values are slightly greater), which may indicate a mild radial color gradient or may simply reflect systematic bias in the SDSS model fitting.

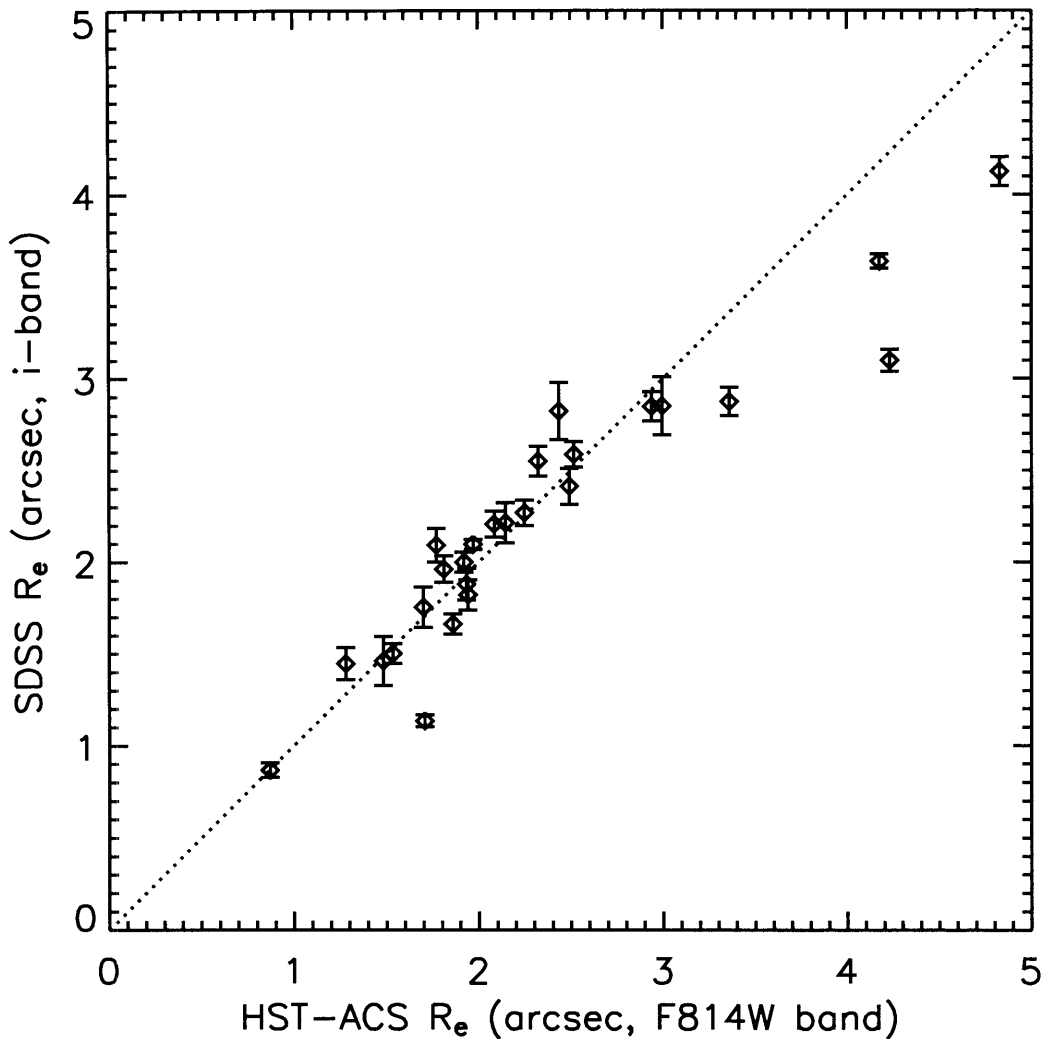


Figure 5-1: Comparison of de Vaucouleurs effective radius measurements from SDSS and *HST*-ACS data. Fractional statistical errors on the *HST* measurements are less than 1% in all cases, with a median value of 0.5%.

5.2.3 Power-Law Constraints from SDSS Velocity Dispersions

We now compute the constraints on power-law models for the lens-galaxy density profiles as in § 3.6. From the SDSS spectroscopic detections, we already know lens and source redshifts, and thus we know the correct scaling between angular and physical quantities in each lens system (under our assumed cosmology). Given the high quality of our ACS imaging data, we assume that the less-than-1% statistical errors on our measured effective radii contribute negligibly to the error budget. For computational simplicity, we will also propagate our assumed errors in the Einstein radii b through the scaling $b \propto \sigma_v^2$ (Equation 3.6) and recast them as additional errors on the observed velocity dispersion (although this scaling strictly holds only for isothermal profiles). We compute environmental, deprojection, and

System Name	IFU θ_E	<i>HST</i> θ_E
SDSSJ0037-0942	$1''.50 \pm 0''.01$	$1''.47 \pm 0''.01$
SDSSJ0737+3216	$1''.00 \pm 0''.01$	$1''.03 \pm 0''.01$
SDSSJ1402+6321	$1''.41 \pm 0''.02$	$1''.39 \pm 0''.01$
SDSSJ1630+4520	$1''.73 \pm 0''.10$	$1''.81 \pm 0''.01$
SDSSJ2321-0939	$1''.52 \pm 0''.04$	$1''.57 \pm 0''.01$

Table 5.1: Comparison of Einstein radii of SIE gravitational-lens models fitted to IFU and *HST* data. Errors on *HST* Einstein radii are estimated. IFU Einstein radius of SDSSJ1630+4520 has been estimated directly from average ring radius, without SIE model fitting.

image-asymmetry corrections as described in § 3.6.2. We also perform the analysis with two different version outputs of the SDSS velocity dispersions from the `specBS` pipeline, to gauge the effect of any systematic error in the measured velocity dispersions upon our results. With our assumed Gaussian errors in velocity dispersion (including the mass-error contribution), we compute likelihood curves for the power-law slope γ , from which we determine maximum-likelihood (ML) values and confidence limits. Figure 5-2 shows the determined ML values of γ for each of the 16 simple lens galaxies with well-measured stellar velocity dispersions (those with spectral signal-to-noise per pixel greater than 8). Values for γ are plotted as a function of σ_{e8} , the SDSS $R = 1''.5$ -aperture velocity dispersions corrected to an aperture of $R = R_e/8$ using the empirical correction of Jorgensen et al. (1995). We see no obvious linear trend in γ with σ_{e8} , although there is a slight indication of an increase in γ to either side of $\sigma_{e8} \approx 280 \text{ km s}^{-1}$. Although the extremely small sample sizes at both the low- and high-velocity ends obviously preclude any strong statements, we may divide the sample into three bins in velocity dispersion and compute an average value in each bin in order to quantify the trend. We partition at 235 km s^{-1} and 335 km s^{-1} , which gives 3, 9, and 4 galaxies respectively in the low-, medium-, and high-velocity bins; this partitioning is also summarized in Table 5.2. There will almost certainly be intrinsic scatter in γ within these bins, but in the absence of a larger sample we content ourselves with determining a single ML γ value within each bin. We compute an overall likelihood function of γ in each bin as the normalized product of the individual likelihood functions in the bin, which we then use to determine the ML values and confidence limits within the bin. The resulting likelihood functions are well-approximated by Gaussians, and thus we use Gaussian fits to establish ML values and 68% confidence limits. The resulting ML γ values are given in Table 5.3, as calculated for a variety of assumptions. Taking the first line of Table 5.3 as our best estimate, we see that within the context of a model that neglects intrinsic scatter, we detect an increase in γ of $\simeq 0.15$ over $60\text{--}70 \text{ km s}^{-1}$ to either side of the minimum at $\sigma_{e8} \approx 290$. Adding errors between adjacent bins in quadrature, we would characterize this as a “two-to-three-sigma” detection on either side of the minimum. We are limited in our ability to measure the trend in γ as a function of velocity dispersion (which may be considered a dynamical proxy for mass) by the fact that the SLACS Survey has explicitly selected high- σ_v lenses in order to maximize lensing cross section and lens confirmation rate. The natural selection of lenses in other surveys is also weighted by lensing cross section, and thus strong lenses are typically massive galaxies. During HST Cycle 14, we will extend our survey to galaxies of lower mass in order to use strong lensing and stellar dynamics to

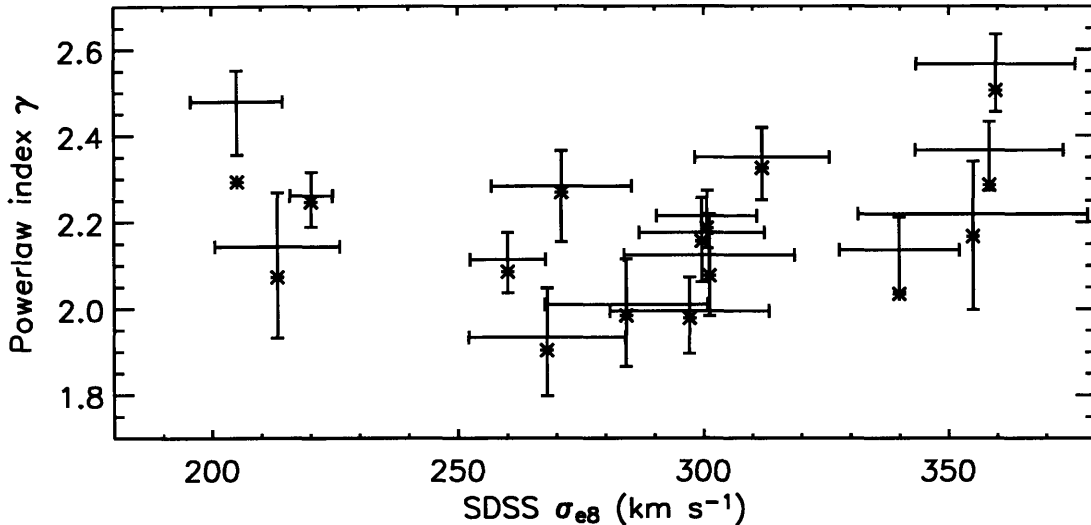


Figure 5-2: Power-law index γ versus stellar velocity dispersion from SDSS, corrected to an aperture of $R_e/8$ using the empirical relation of Jorgensen et al. (1995). Error crosses are centered on the maximum-likelihood values obtained by accounting for the effects of extra environmental convergence; stars indicate the values that are obtained when environmental effects are ignored. We note that the horizontal and vertical errors are almost entirely correlated (neglecting the contribution of the lensing-mass uncertainty to the error budget), in the sense that higher velocity dispersions will translate into higher γ values.

	Low- σ	Medium- σ	High- σ
N_{galaxies}	3	9	4
Defining range (km s^{-1})	$\sigma_{e8} < 235$	$235 \leq \sigma_{e8} < 325$	$\sigma_{e8} \geq 325$
Mean σ_{e8} (km s^{-1})	213	288	353

Table 5.2: Partition of *HST*-ACS lens sample into velocity-dispersion bins

measure the mass dependence of early-type galaxy structure and mass-to-light ratio².

Table 5.3 also illustrates the impact of various possible sources of systematic error upon our power-law density-profile results. We see that neglecting the contribution of environmental overdensity to the convergence at the lens position leads to an underestimate of the average γ by 0.02 to 0.1, with the greatest effect occurring for the highest velocity-dispersion galaxies. The possible effects of systematic error in the velocity-dispersion values can be seen in the decrease in the ML γ values by 0.06–0.13 when dispersions from a previous version of the *specBS* pipeline are used. We also see that changes of +0.3 (–0.3) in the assumed velocity anisotropy parameter β lead to changes in the derived γ of ≈ -0.06 ($\approx +0.04$).

All of our lenses probe the mass distribution in the lens galaxy on scales less than the half-light radius, and the median ratio of Einstein radius to effective radius within the sample

²These lower-mass galaxies will have lower lensing cross sections and hence should have a lower lensing rate, although a magnification bias may again skew the distribution of candidates in favor of lenses over non-lenses.

Environmental Correction?	Anisotropy Parameter β	specBS Version	γ for Low σ	γ for Medium σ	γ for High σ
yes	0.0	new	2.28 ± 0.05	2.13 ± 0.03	2.29 ± 0.05
no	0.0	new	2.23 ± 0.05	2.11 ± 0.03	2.19 ± 0.05
yes	0.0	old	2.22 ± 0.05	2.04 ± 0.03	2.16 ± 0.06
yes	+0.3	new	2.24 ± 0.05	2.07 ± 0.03	2.23 ± 0.06
yes	-0.3	new	2.31 ± 0.05	2.17 ± 0.03	2.32 ± 0.05

Table 5.3: Maximum-likelihood power-law indices versus velocity dispersion for varying assumptions

is 0.55. At these scales the contribution from stellar mass may be expected to dominate over the dark component, so it is of great interest to examine the relationship between the mass slope (derived from the Jeans equation as constrained by the Einstein radius, de Vaucouleurs half-light radius, and SDSS velocity dispersion) and the slope of the light profile that we may measure directly from the ACS data. If our lenses have nearly constant mass-to-light ratios as a function of R within the Einstein radius, then the mass and light slopes should be nearly equal. The most unambiguous way to test the constant mass-to-light hypothesis would be to fit lens models based on the light distribution as observed by *HST*. Given the detail of our ACS data, these lens models will in general be more complicated than the simple parametrized SIE model considered to this point, and will involve more expensive numerical integrations. We defer the study of such lens models to future work. In order to make the best comparison to the singular power-law mass models that we have so far considered, we attempted to fit singular elliptical power-law luminosity profiles to the ACS images of our lenses within a $2''$ radius about the lens center, roughly the scale probed by our measurements. These fits were generally poor, with a median χ^2 per degree of freedom of $\chi_r^2 = 4.1$. In all cases the systematic failure of the singular-model fit was an over-fitting of the data inside $\sim 0''.2$ and an underfitting immediately outside this region. The addition of a core-radius parameter R_c ,

$$I(R) \propto R^{-\eta} \longrightarrow I(R) \propto (R^2 + R_c^2)^{\eta/2} \quad , \quad (5.1)$$

increased the fit quality dramatically in all cases (giving a median $\chi_r^2 = 1.5$). Furthermore, the fitted core radii were in all cases quite small, with a median fitted core radius of $R_c = 0''.08$ and a maximum value of $R_c = 0''.15$. These values are close to the imaging resolution limit of *HST*: at some level they may not represent physical core radii within the galaxy, but simply serve to suppress the sensitivity to the surface-brightness spike of the singular model that can give a bad fit. Nevertheless, addition of the core removes a non-negligible amount of light from the model's center and thus effectively makes the light profile less steep at fixed η .

Figure 5-3 shows the comparison between mass and light power-law indices, for both cored and singular power-law light models. In adopting the power-law index from the cored model for comparison to that of the singular models considered in the Jeans equation solution, we provide the following relation for the logarithmic slope of the 2D profile of the

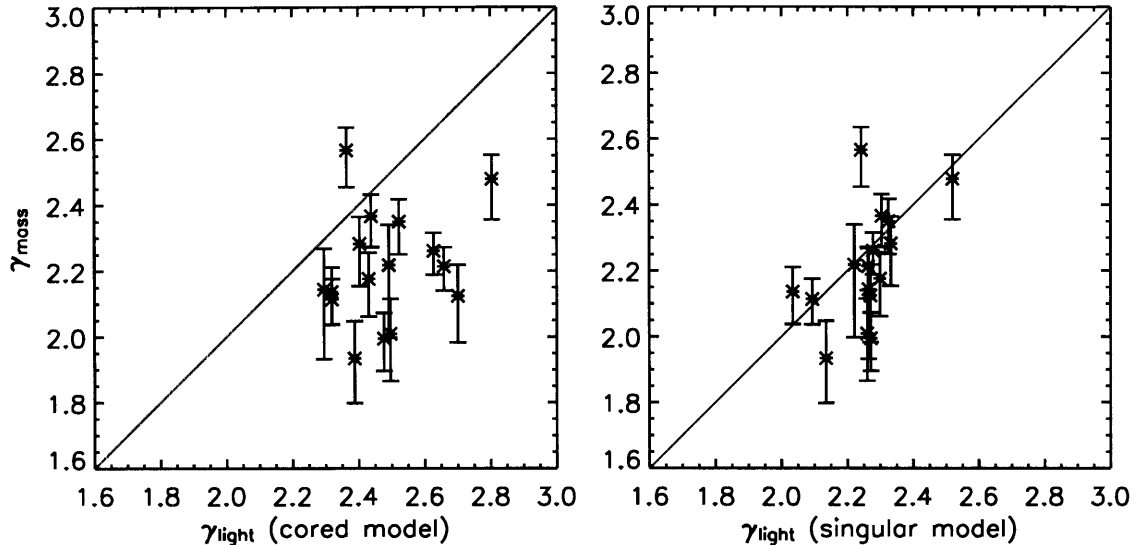


Figure 5-3: Mass power-law index versus light power-law index for *HST*-ACS lenses. Results are shown for a cored power-law ellipsoid light model (left) and a singular power-law ellipsoid light model, both fitted to the data inside a $2''$ radius. Fitted core radii are of order $0''.1$ for all lenses, whereas Einstein radii are of order $1''$. Error bars show 68% confidence limits of γ_{mass} ; statistical errors on γ_{light} are negligible.

cored model, which may be derived easily:

$$\frac{d \ln I}{d \ln R} = -\eta \left(1 + \frac{R_c^2}{R^2 + R_c^2} \right) . \quad (5.2)$$

The ML mass power-law indices are significantly shallower than the light power-law indices derived from the cored models, with a median difference of $\Delta\gamma = -0.27$. Taken at face value, this indicates an increasing mass-to-light ratio with radius, which would represent a significant detection of dark matter within $R_e/2$ in our sample. The interpretation is complicated by our neglecting the fitted core radii, which although small do imply somewhat shallower light profiles than the singular power-law models with equivalent indices. Note also that all systematic uncertainties considered in Table 5.3 favor even shallower mass profiles, with the exception of tangentially anisotropic orbits ($\beta < 0$), which are disfavored based on observations of local-universe galaxies (Kronawitter et al. 2000). We see that the difference between mass and light indices is much less significant for the singular power-law models fitted to the data (median $\Delta\gamma = -0.05$), although the generally poor fit of these models makes this comparison even harder to interpret. We also note (although this is not plotted) that the ML mass power-law index does not correlate significantly with the ratio of fitted SIE Einstein radius to de Vaucouleurs effective radius.

We may compute for our *HST* lens sample the same overall mean and width of the distribution of galaxies with respect to γ , as was done in Chapter 3 for the IFU lens sample and presented in Table 3.2. For the sample of 16 *HST* lenses with well-measured σ_v , our ML parameters for a Gaussian intrinsic distribution in γ are shown in Table 5.4. A similar χ^2 test as described in Chapter 3 rules out the hypothesis of a single universal γ value at $> 99.996\%$ confidence. We also show the projections of the two-parameter likelihood

β	$\bar{\gamma}$	σ_γ
0	$2.22^{+0.07}_{-0.07}$	$0.13^{+0.07}_{-0.05}$
0.3	$2.17^{+0.08}_{-0.08}$	$0.16^{+0.08}_{-0.06}$
-0.3	$2.25^{+0.06}_{-0.07}$	$0.12^{+0.07}_{-0.05}$

Table 5.4: *HST* lens sample constraints on the mean and standard deviation of a model Gaussian intrinsic power-law index distribution. Results are shown for several assumed values of the orbital anisotropy parameter β . Quoted errors are projections of the 68% confidence likelihood contour. Compare to IFU results of Table 3.2.

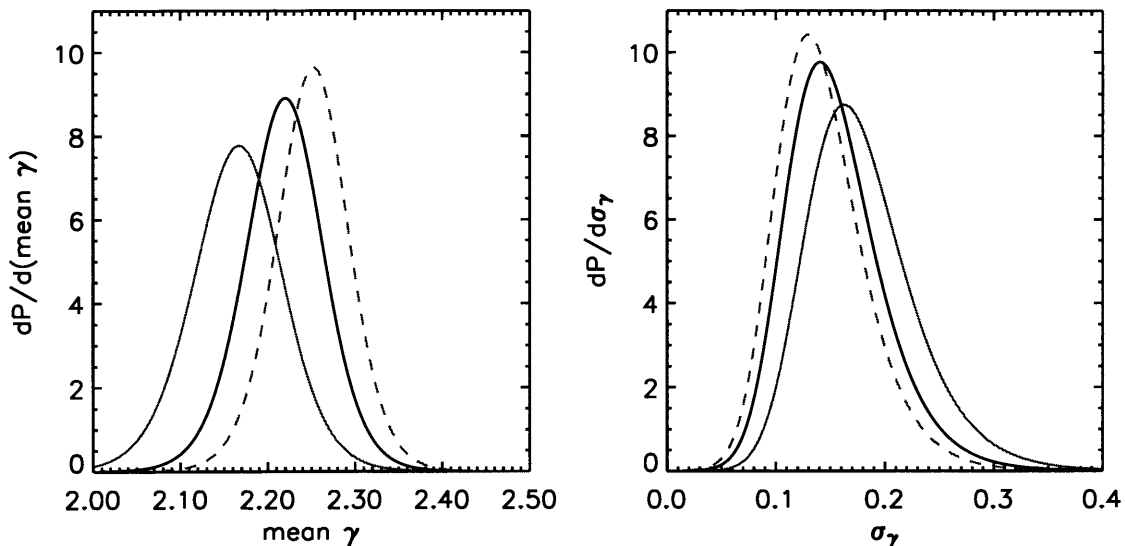


Figure 5-4: Projected likelihood of Gaussian power-law index distribution parameters $\bar{\gamma}$ (mean γ) and σ_γ . Solid black curves are for $\beta = 0$, solid gray are for $\beta = 0.3$, and dashed gray are for $\beta = -0.3$.

function onto the $\bar{\gamma}$ and σ_γ axes in Figure 5-4. Note in particular that although the 68% uncertainty in the parameter σ_γ is comparable to its magnitude, $\sigma_\gamma = 0$ (i.e. universal γ) is ruled out at high significance by the data. The ML parameter values that we find here are in agreement with the results of Chapter 3 within the quoted error ranges. To be fair, 5 lenses overlap between the two samples. Nevertheless, this agreement is reassuring and suggests that our analysis is consistent. We also see that when we are restricted to using SDSS velocity dispersions in both cases, IFU lens-modeling plus SDSS effective radii are in fact competitive with *HST*-ACS lens modeling and effective radii for constraining the distribution of galactic γ values. The full power of the *HST* data can be realized by obtaining higher-quality velocity dispersions at a range of projected radii within the lens galaxies.

5.3 Mass Profile Constraints from Lensing Alone

In § 3.4.2 we considered the SIE as an appropriate choice of lens model given the data. Our *HST*-ACS lens data are sufficiently rich that we may now explore possible departures from isothermality in our lens models in order to derive constraints on lens-galaxy radial mass profiles from lensing data alone. The most natural one-more-parameter generalization of the SIE is the singular power-law ellipsoid (SPLE). A competing generalization would be a softened isothermal ellipsoid with a finite core radius. We choose the SPLE because both theoretical and observational evidence favors a cuspy central density profile. The convergence of the SPLE may be expressed as

$$\kappa_{\text{SPLE}} = \left(1 - \frac{\eta}{2}\right) \left(\frac{b}{r_q}\right)^\eta, \quad (5.3)$$

where η is a power-law index with $\eta = 1$ corresponding to the SIE model. The normalizing factor is taken so that the parameter b gives the Einstein ring radius for $q = 1$ at all η values, and r_q is as defined in Equation 3.5. When $q = 1$ the deflection angle of the SPLE may be computed analytically as

$$\alpha = b \left(\frac{b}{r}\right)^{\eta-1}. \quad (5.4)$$

For $q \neq 1$ the SPLE potential and its gradients can not be expressed analytically, but as with all homoeoidal lensing distributions they may be computed from one-dimensional quadratures over the distribution elliptically interior to the point of interest (Schramm 1990). To implement the SPLE potential gradient numerically, we use the general result of Schramm (1990) as expressed in closed form by Barkana (1998) and adapted to our notation and normalization conventions. We also make a change of integration variables in Equation 13 of Barkana (1998) to remove the singularity of the integrand at the lower limit, facilitating numerical integration. Rather than use the series approximation of Barkana (1998), we take advantage of the scale-free nature of the SPLE to reduce our computational expense in fitting SPLE lens models to the data. As one might expect from the $q = 1$ result of Equation 5.4, and as one can easily verify from the relations in Schramm (1990) and Barkana (1998), the two-dimensional angular deflection vector $\vec{\alpha}$ of the SPLE for any value of q obeys the relation

$$\vec{\alpha}(c\vec{x}) = c^{1-\eta}\vec{\alpha}(\vec{x}), \quad (5.5)$$

where \vec{x} is the angular vector from the potential center to the point of interest in the image plane and c is a numerical constant. When modeling lenses with extended sources, each iteration in the optimization process (with fixed lens parameters) requires the value of the angular deflection vector at all significant pixels in the image plane in order to assign the correct source-plane surface-brightness value to each pixel. An ACS $5'' \times 5''$ strong-lens image region with $0''.05$ per pixel contains 10^4 pixels and thus requires 10^4 deflection values. However, we only need to know the deflection as a function of azimuth at one value of r_q . Hence we may integrate for and tabulate the components of the deflection vector at fixed r_q over one quadrant in azimuth (the other three quadrants are obtained trivially through the symmetry of the potential), interpolate at the azimuthal positions of our data pixels, and scale for the correct deflections using Equation 5.5. This reduces the necessary numerical quadratures from 10^4 (for example) per model iteration to 10^2 , which when combined with

cubic spline interpolation gives the deflection components to an accuracy of one part in 10^9 for $q = 0.75$.

In the absence of multiple sources at multiple redshifts, strong-lens systems suffer from the well-known “mass sheet degeneracy” (Gorenstein et al. 1988; Saha 2000) whereby the convergence κ of a lens model may be transformed according to

$$\kappa \rightarrow (1 - f)\kappa + f \quad (5.6)$$

for any constant f provided the convergence remains everywhere positive, with all observables except time delays unaltered. The physical interpretation giving rise to the terminology is that any lens model can be scaled up or down and supplemented by a constant sheet of mass while preserving the observed image configuration. We nevertheless see that self-similar power-law mass profiles may in principle be uniquely constrained by strong lensing irrespective of any mass sheet, since the rescaled model will have the same logarithmic density slope. To successfully derive constraints on power-law lens models, we require lensed images across a range of radii: Einstein-ring images tightly constrain the mass interior to the ring but tell nothing of its distribution with respect to radius. Double-image lenses typically probe a larger range of radii than rings or quads, and in principle can be used to measure the density slope of circular lens models if the relative magnifications of their images can be taken as constraints to the macroscopic lens model. Unfortunately the density slope is degenerate with the underconstrained angular structure once the unrealistic assumption of perfect circular symmetry is relaxed. Our ACS lens sample includes one particular lens, SDSSJ0912+0029, which is uniquely suited to deriving simultaneous constraints on the lens ellipticity and the best-fit power-law lensing mass profile. This system consists of an arc and opposing counterarc at smaller radius, each of which themselves trace a significant range of radii within the lens galaxy. Furthermore, the regular structure of the lensed galaxy suggests that a simple parametrized model for its surface brightness distribution can yield satisfactory results.

To fit a power-law lens model to SDSSJ0912, we first determine a centroid and orientation for the lens potential by fitting an elliptical Sérsic model to the ACS data in the native frame, convolving with a PSF model generated by the Tiny Tim software. We initially model the system with an SIE lens model and an exponential-disk lensed-galaxy surface brightness model. We initiate the non-linear fitting procedure with judiciously chosen parameters that produce a reasonable approximation to the observed image configuration. The model is optimized using the Levenberg-Marquardt algorithm as implemented by the IDL function MPFIT. At each iteration, each pixel in the image plane is mapped into the source plane by the parametrized lens model, and assigned the surface brightness of the parametrized source model at that position. The entire image is then convolved with the PSF, and the χ^2 merit statistic is computed with respect to the data. After converging to the best-fitting SIE+exponential-disk model, we allow the lensing power-law index and the source Sérsic index to be free, and further optimize the model. To avoid getting stuck in a local minimum resulting from the original choice of an isothermal profile, we initialize the power-law fit with 30 different stochastically generated parameter sets in the neighborhood of the best isothermal fit. The parameter perturbations are normally distributed on the scale of the square-root diagonal entries of the covariance matrix. We take the overall minimum- χ^2 fitted parameter set as the best fit.

With the lens center and position angle fixed to those values measured by Sérsic fitting to the lens-galaxy isophotes, we find a best-fit value for the power-law index of $\gamma = 2.28 \pm 0.05$,

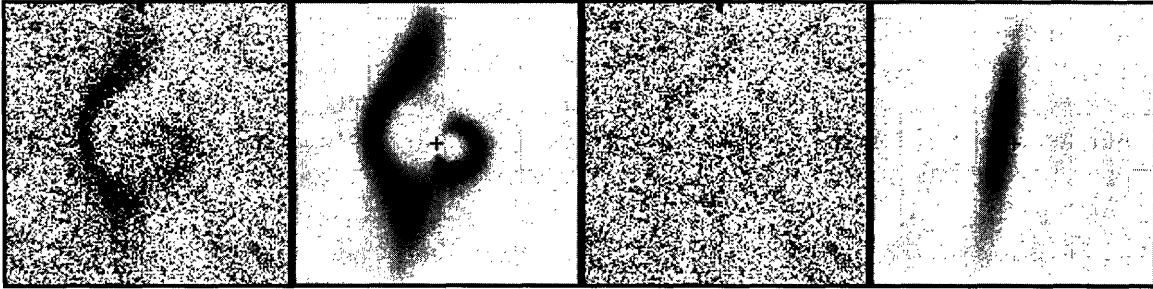


Figure 5-5: *HST*-ACS gravitational-lens modeling of SDSSJ0912+0029, for lens center and position angle fixed to the measured lens-galaxy values. First panel shows F814W data with lens-galaxy model subtracted (as in Figure E-1). Second panel shows best-fit parametrized model lensed image, third panel shows data-minus-model residual image, and fourth panel shows model lensed galaxy in the unlensed source plane (i.e. as it would appear with no intervening lens.) Images are $8'' \times 8''$, and lens-galaxy centroid is marked with a cross. See Figure E-1 for an un-subtracted image of the lens galaxy.

with the confidence limit giving the approximate range for $\Delta\chi^2 = 1$ when marginalizing over all other free parameters. Figure 5-5 shows the resulting gravitational lens model for SDSSJ0912. The lensed background galaxy is seen as a thin, edge-on disk when the parametrized model is evaluated in the unlensed source plane. One possible source of concern is that the lens-model ellipticity determined by the modeling procedure is a rather flattened $q_{\text{mass}} = 0.432 \pm 0.017$ (with the confidence limit taken from the diagonal of the covariance matrix of the fit), as compared with the Sérsic-model ellipticity of the lens galaxy, $q_{\text{light}} = 0.668 \pm 0.001$. In general, more centrally condensed (i.e. high- γ) mass distributions will require more flattened axis ratios to produce comparable gravitational quadrupole effects at a given radius, so the low value of q_{mass} may warn of an overestimate of γ . (We may also be seeing a consequence of our neglecting possible sources of external shear to the lens potential.) Allowing the position angle of the lens potential to be a free parameter in the fit leads to a very slight rotation (0.004°), but further flattens the potential to $q_{\text{mass}} = 0.405$ and steepens the radial profile to $\gamma = 2.32$. To quantify the effect of lens-mass flattening on our derived γ value, we also fit a lens model with q_{mass} fixed to the measured value of q_{light} (and with a free position angle). This gives $\gamma = 2.08 \pm 0.01$ (again with the confidence limit given for $\Delta\chi^2 = 1$ marginalizing over all other free parameters). The model lensed (and unlensed) images from the fixed- q_{mass} fit are qualitatively similar to those seen in Figure 5-5. Both models have a χ^2 per degree of freedom of $\chi_r^2 \simeq 1.06$, with the total χ^2 of the free- q_{mass} fit lower by 57. For comparison, the power-law index derived for SDSSJ0912 by the method of § 5.2.3 is $\gamma = 2.14_{-0.10}^{+0.08}$ (68% confidence, for $\beta = 0$), which is consistent with the range that we find here.

For lenses like ours that show extended structure in the lensed object, modeling of the lens-plane mass distribution is inextricably linked with modeling of the source-plane light distribution. Many of the lenses shown in Figure E-1 have much less regular structure in the lensed galaxy than does SDSSJ0912. For these systems, parameterized models of the source galaxy will be more difficult to construct. One solution is to adopt a non-parametric pixelized source-plane model and perform the type of semi-linear lens modeling described by Warren and Dye (2003); this is the method used by Koopmans et al. (2005, in preparation) to measure the SIE Einstein radii used in this chapter. This technique is somewhat complicated by the need for a regularization scheme to impose smoothness

on the resulting source-plane distribution. In future work, we plan to pursue source-plane galaxy modeling with a b-spline technique similar to the method presented in § 4.2.2 for the subtraction of lens-galaxy images. Like the Warren and Dye (2003) technique, this method would be linear in the source-plane distribution and could fit arbitrarily complicated galaxy shapes, but smoothness would be enforced directly by the parameterization in terms of smooth localized b-spline basis functions. In addition, the breakpoint spacing in the source plane could be adjusted automatically as a function of the magnification predicted by the lens model.

5.4 Conclusions and Future Work

In this chapter we have combined *HST*-ACS measurements of the SIE Einstein radius and de Vaucouleurs effective radius (R_e) with measurements of the luminosity-weighted stellar velocity dispersion from SDSS to constrain the distribution of logarithmic total density slopes γ within $\sim R_e/2$ for a sample of 16 newly discovered early-type gravitational lens galaxies. We find that a universal γ value is ruled out at high confidence by the data. The intrinsic γ distribution, when parametrized as Gaussian, has a mean that is slightly steeper than isothermal and a modest amount of intrinsic scatter. This result, which corresponds to a gently falling but nearly flat rotation curve within the effective radius, is consistent with results from dynamical models fitted to spatially resolved absorption-line profile shapes of local elliptical galaxies (Romanowsky and Kochanek 2001; Gerhard et al. 2001). Future work on this new lens sample will explore the prospects for obtaining tighter constraints on the radial density profile from spatially resolved observations of the line-of-sight velocity-dispersion profile. Follow-up spectroscopic measurements of the lens-galaxy velocity dispersions will also allow us to gauge the systematic accuracy of the SDSS velocity dispersions.

We have also seen that in systems with favorable image geometry, strong-lensing data alone can constrain the parameter γ of a singular power-law ellipsoid lens model. These constraints are enabled by the extended surface-brightness distributions of the lensed objects in our sample. Future work will explore the constraints placed by the strong-lensing data upon empirical constant mass-to-light lens models, and more generally upon empirical lens models with parametrized radial mass-to-light ratio gradients (Napolitano et al. 2005). We note that including shallower-than-isothermal inner slopes in lensing mass models based upon observed luminosity profiles would need to respect constraints from the absence of odd-numbered lensed images in the core (Rusin and Ma 2001). However, Keeton (2003) demonstrates that constant mass-to-light models based on empirical early-type light profiles generally will not produce bright core images.

We have seen that the overdensity of lens-galaxy environments imposes a significant bias upon the derived density-profile parameters if not taken into account. In order to control this effect more accurately, we will pursue deeper multi-color imaging of the fields surrounding our lenses. This imaging will allow us to photometrically identify all lens-galaxy neighbors down to flux limits fainter than currently possible with SDSS imaging. This data will also permit a more sophisticated consideration of the role of environmental shear in generating the observed lensing geometry.

Finally, we have seen that our current lens sample is weighted heavily toward high-mass (i.e. high- σ_v) lens galaxies as a consequence of the candidate selection process. We are conducting a further *HST*-ACS Snapshot program in Cycle 14 (program #10587) to

target 118 lens candidates across a range of σ_v values as measured by SDSS. If a significant low-mass lens sample is confirmed by this new survey, it will permit the first strong-lensing measurement of galaxy structure as a function of mass.

Appendix A

SDSS Lens-Candidate Parameters

Table A.1 in this appendix gives SDSS photometric and spectroscopic parameters for 80 lenses and lens candidates from the survey described in this thesis. All systems are included that were either (1) published as candidates in the original survey candidate paper (Bolton et al. 2004), (2) included in the target list of the *HST* Cycle 13 Snapshot Survey (program number 10174), or (3) observed with the IFU and reported in the thesis. These three categories are largely but not completely overlapping.

System Name	Plate-MJD-Fiber	de Vaucouleurs Model g, r, i	deVauc. R_e (")	ML	SNR /pix	z_{FG}	z_{BG}	σ_v (km s $^{-1}$)	$\Delta\theta$ (")	[O II] flux	Obs. key
SDSSJ002431.96+003123.2	0390-51900-589	20.39,18.49,17.91	1.86 ± 0.18	dV	7.5	0.3979	0.5953	286 ± 19	1.39	15 ± 2	ab
SDSSJ003524.13+002400.2	0689-52262-632	19.16,17.88,17.46	1.95 ± 0.10	dV	11.0	0.2017	0.2710	176 ± 21	0.43	15 ± 2	ab
SDSSJ003753.21-094220.1	0655-52162-392	18.16,16.93,16.47	2.16 ± 0.06	dV	21.5	0.1955	0.6322	279 ± 10	2.94	20 ± 2	abcde
SDSSJ004402.89+011312.6	0393-51794-456	17.26,16.30,15.86	2.32 ± 0.04	dV	22.4	0.1196	0.1965	266 ± 13	1.56	93 ± 4	c
SDSSJ010933.72+150032.5	0422-51811-508	20.03,18.37,17.88	1.68 ± 0.14	dV	7.2	0.2939	0.5249	251 ± 19	1.47	12 ± 2	ab
SDSSJ011123.50+000012.8	0694-52209-076	20.89,19.40,18.75	0.97 ± 0.18	dV	4.0	0.4516	0.5013	86 ± 25	0.04	18 ± 2	a
SDSSJ021652.54-081345.3	0668-52162-428	19.25,17.58,17.00	3.05 ± 0.13	dV	8.5	0.3317	0.5235	333 ± 23	2.13	16 ± 3	abcde
SDSSJ032454.50-011029.1	0414-51869-244	21.15,19.03,18.45	2.61 ± 0.64	dV	3.4	0.4453	0.6240	267 ± 35	1.03	23 ± 2	ab
SDSSJ073728.45+321618.5	0541-51959-145	19.56,17.97,17.25	2.16 ± 0.13	dV	13.2	0.3223	0.5812	338 ± 16	2.67	47 ± 2	a cde
SDSSJ080240.81+450452.7	0436-51883-633	17.94,16.79,16.40	2.82 ± 0.09	dV	19.6	0.1423	0.4523	244 ± 11	2.26	26 ± 3	d
SDSSJ080358.21+453655.6	0439-51877-333	18.60,17.43,16.89	1.26 ± 0.04	dV	15.4	0.1313	0.2938	228 ± 12	1.60	15 ± 2	d
SDSSJ080532.29+303712.6	0860-52319-452	19.59,18.21,17.63	1.39 ± 0.06	dV	11.3	0.3200	0.3810	334 ± 17	0.94	34 ± 2	a c
SDSSJ081323.37+451809.4	0439-51877-589	18.79,17.59,17.04	2.08 ± 0.09	dV	13.2	0.1834	0.6436	256 ± 15	2.57	11 ± 2	d
SDSSJ081931.92+453444.8	0441-51868-108	18.82,17.64,17.17	2.32 ± 0.13	dV	10.4	0.1943	0.4463	225 ± 15	1.56	36 ± 3	de
SDSSJ085038.70+020155.2	0468-51912-362	20.55,18.89,18.21	1.76 ± 0.37	dV	3.8	0.4114	0.5677	251 ± 41	0.89	7 ± 3	a
SDSSJ091205.30+002901.1	0472-51955-429	17.45,16.31,15.85	3.36 ± 0.05	dV	20.1	0.1642	0.3239	326 ± 12	2.90	17 ± 3	a de
SDSSJ092857.33+440059.1	0870-52325-465	19.50,18.05,17.41	1.37 ± 0.05	dV	8.8	0.2908	0.4538	198 ± 24	0.75	19 ± 3	a c
SDSSJ093543.93-000334.8	0476-52314-177	19.30,17.62,17.01	3.53 ± 0.19	dV	7.3	0.3475	0.4670	396 ± 35	2.10	9 ± 2	a d
SDSSJ094839.59+041653.7	0570-52266-621	18.12,16.94,16.47	1.92 ± 0.04	dV	14.7	0.1585	0.2558	293 ± 17	1.80	25 ± 4	d
SDSSJ095320.42+520543.7	0902-52409-577	18.62,17.62,17.27	1.77 ± 0.09	dV	13.8	0.1315	0.4670	229 ± 19	2.09	14 ± 3	de

Table A.1: SDSS lens-candidate photometric and spectroscopic parameters. System names give truncated J2000 RA and Dec as HHMMSS.ss±DDMMSS.s. Plate-MJD-Fiber (MJD = modified Julian date - 2400000.5) in combination constitute a unique identifier to an SDSS spectrum. De Vaucouleurs model magnitude errors are all of order 0.01. De Vaucouleurs effective (half-light) radii are as measured in the r band, and are given as intermediate-axis values (converted from SDSS major-axis values using measured axis ratios). The dV/Ex classification given in the “ML” column indicates which of the two models—de Vaucouleurs or exponential disk—had greater likelihood given the SDSS imaging data. Signal-to-noise ratio (SNR/pix) is median value per spectral pixel. Redshift errors are of order 0.0001. Velocity dispersions σ_v are dubious for SNR $\lesssim 10$, for $\sigma_v \lesssim 100$ km s $^{-1}$, or for $\sigma_v \gtrsim 420$ km s $^{-1}$. Image splittings $\Delta\theta$ are twice the Einstein radius of an SIS model with SDSS redshifts and velocity dispersion. Line fluxes for [O II] λ 3727 are in units of 10^{-17} erg cm $^{-2}$ s $^{-1}$. “Obs. key” indicates systems that are included in: (a) the original candidate paper Bolton et al. (2004), (b) the MagIC target sample discussed in § 2.5.2, (c) the IFU target sample described in this thesis, (d) the Cycle 13 *HST* Snapshot target list, and (e) the subset of the Cycle 13 *HST* targets observed as of 2005 March 22 and presented in Figures E-1–E-3.

System Name	Plate-MJD-Fiber	de Vaucouleurs Model g, r, i	deVauc. R_e (")	ML	SNR /pix	z_{FG}	z_{BG}	σ_v (km s $^{-1}$)	$\Delta\theta$ (")	[O II] flux	Obs. key
SDSSJ095629.77+510006.6	0902-52409-068	18.47,17.20,16.72	2.33 ± 0.09	dV	14.1	0.2405	0.4700	334 ± 15	2.94	38 ± 3	a cde
SDSSJ095944.07+041017.0	0572-52289-495	18.62,17.56,17.09	1.21 ± 0.04	Ex	17.1	0.1260	0.5351	197 ± 13	1.66	17 ± 3	de
SDSSJ101051.51+060432.6	0996-52641-106	19.95,18.31,17.75	1.88 ± 0.13	dV	5.7	0.3475	0.4801	183 ± 22	0.48	20 ± 3	a
SDSSJ102551.31-003517.4	0272-51941-151	17.34,16.21,15.71	4.05 ± 0.08	dV	20.5	0.1589	0.2764	264 ± 11	1.64	14 ± 3	a de
SDSSJ102927.53+611505.2	0772-52375-140	17.55,16.51,16.09	2.45 ± 0.05	dV	17.4	0.1574	0.2512	228 ± 14	1.08	28 ± 5	a c
SDSSJ110102.15+073622.1	1002-52646-504	18.81,17.55,17.07	2.73 ± 0.12	dV	8.9	0.2058	0.5810	217 ± 17	1.65	37 ± 5	a
SDSSJ111739.60+053413.9	0835-52326-571	19.00,17.73,17.27	2.49 ± 0.11	dV	9.9	0.2285	0.8235	277 ± 19	2.99	22 ± 2	de
SDSSJ112837.76+583527.1	0951-52398-036	20.04,18.33,17.86	2.12 ± 0.18	dV	4.7	0.3809	0.5466	223 ± 28	0.78	27 ± 4	a c
SDSSJ113629.47-022304.0	0328-52282-350	20.43,18.91,18.22	1.31 ± 0.15	dV	4.5	0.3936	0.4645	321 ± 27	0.81	6 ± 2	a
SDSSJ115107.03+645540.5	0598-52316-477	20.27,18.49,17.81	1.63 ± 0.12	dV	5.3	0.3804	0.5437	260 ± 27	1.05	13 ± 3	a c
SDSSJ115510.06+623722.4	0777-52320-501	20.08,18.28,17.72	3.12 ± 0.35	dV	4.2	0.3751	0.6690	303 ± 34	2.08	9 ± 2	a cd
SDSSJ120444.07+035806.3	0842-52376-208	18.57,17.44,16.95	1.50 ± 0.05	dV	12.8	0.1644	0.6307	267 ± 17	2.91	36 ± 3	d
SDSSJ120540.43+491029.3	0969-52442-134	18.53,17.29,16.67	2.30 ± 0.10	dV	13.9	0.2150	0.4808	281 ± 13	2.37	38 ± 3	de
SDSSJ123851.61+670928.3	0494-51915-074	18.61,17.43,16.95	2.47 ± 0.11	dV	17.5	0.2312	0.4446	238 ± 10	1.47	13 ± 2	a
SDSSJ124645.61+044025.0	0847-52426-190	18.72,17.58,17.15	1.13 ± 0.06	dV	13.8	0.1686	0.4644	208 ± 14	1.52	54 ± 3	d
SDSSJ125028.25+052349.0	0847-52426-549	18.54,17.36,16.83	1.76 ± 0.07	dV	13.1	0.2318	0.7946	252 ± 14	2.41	46 ± 3	de
SDSSJ125050.52-013531.6	0337-51997-460	16.57,15.67,15.25	3.08 ± 0.04	dV	28.2	0.0871	0.3526	246 ± 9	2.56	53 ± 4	d
SDSSJ125135.70-020805.1	0337-51997-480	18.68,17.65,17.29	3.64 ± 0.19	dV	7.2	0.2243	0.7844	233 ± 23	2.09	25 ± 2	de
SDSSJ125919.05+613408.6	0783-52325-279	18.87,17.50,16.98	1.94 ± 0.07	dV	13.8	0.2334	0.4488	253 ± 16	1.67	17 ± 3	a cde
SDSSJ130035.90+652236.2	0602-52072-332	20.37,18.70,18.06	1.00 ± 0.08	dV	6.5	0.3050	0.3300	300 ± 24	0.36	2 ± 0.5	a
SDSSJ130613.65+060022.1	0849-52439-615	18.47,17.35,16.88	2.14 ± 0.07	dV	12.0	0.1730	0.4721	237 ± 17	1.96	20 ± 3	d
SDSSJ131047.95+621154.9	0784-52327-350	17.41,16.50,16.12	5.12 ± 0.13	dV	15.1	0.1984	0.5142	226 ± 12	1.71	10 ± 3	a c
SDSSJ133045.53-014841.6	0910-52377-503	18.51,17.57,17.16	0.84 ± 0.04	dV	18.4	0.0808	0.7115	185 ± 9	1.70	16 ± 2	de
SDSSJ133332.70-005533.6	0298-51955-212	17.98,16.89,16.42	2.68 ± 0.06	dV	18.2	0.1419	0.5972	216 ± 11	1.98	11 ± 3	d
SDSSJ133828.80-004915.2	0298-51955-001	19.86,18.28,17.39	2.21 ± 0.17	dV	4.4	0.3496	0.4431	111 ± 12	0.14	9 ± 2	a
SDSSJ140228.21+632133.5	0605-52353-503	18.33,17.01,16.51	2.67 ± 0.08	dV	13.7	0.2046	0.4814	267 ± 17	2.23	10 ± 3	a cde
SDSSJ140910.05+610511.7	0606-52365-315	19.20,17.75,17.19	1.25 ± 0.05	Ex	13.4	0.2971	0.3556	428 ± 21	1.60	18 ± 3	a c
SDSSJ141622.34+513630.4	1045-52725-464	19.37,18.14,17.65	1.71 ± 0.11	dV	7.1	0.2987	0.8120	240 ± 25	1.92	31 ± 2	a cd
SDSSJ142015.85+601914.8	0788-52338-605	16.46,15.60,15.22	2.17 ± 0.03	dV	45.8	0.0629	0.5352	205 ± 4	2.10	56 ± 5	de
SDSSJ143213.33+631703.7	0499-51988-005	16.73,15.77,15.36	5.82 ± 0.11	dV	26.4	0.1230	0.6643	199 ± 8	1.79	65 ± 3	d

Table A.1: (continued)

System Name	Plate-MJD-		de Vaucouleurs		de Vauc.		ML	SNR	z _{FG}	z _{BG}	σ_v (km s ⁻¹)	$\Delta\theta$ (")	[O II] flux	Obs. key
	Fiber	Fiber	Model g, r, i	Model g, r, i	R_e (")	R_e (")								
SDSSJ144210.51-002754.1	0307-51663-065	0307-51663-065	19.82,18.43,17.84	19.82,18.43,17.84	1.34 ± 0.09	1.34 ± 0.09	dV	6.8	0.3717	0.4404	349 ± 28	0.99	33 ± 2	a
SDSSJ144319.62+030408.2	0587-52026-205	0587-52026-205	18.62,17.59,17.16	18.62,17.59,17.16	1.17 ± 0.04	1.17 ± 0.04	dV	18.9	0.1338	0.4187	209 ± 11	1.66	18 ± 2	d
SDSSJ145128.19-023936.4	0921-52380-293	0921-52380-293	17.92,16.75,16.25	17.92,16.75,16.25	2.48 ± 0.07	2.48 ± 0.07	dV	16.9	0.1254	0.5204	223 ± 14	2.10	57 ± 4	d
SDSSJ152123.84+580550.8	0615-52347-311	0615-52347-311	18.68,17.44,17.02	18.68,17.44,17.02	2.06 ± 0.08	2.06 ± 0.08	dV	12.1	0.2042	0.4857	174 ± 16	0.96	24 ± 3	a c
SDSSJ153530.38-003852.2	0315-51663-259	0315-51663-259	18.44,17.35,16.83	18.44,17.35,16.83	1.46 ± 0.04	1.46 ± 0.04	dV	14.2	0.1613	0.6586	254 ± 15	2.69	40 ± 3	d
SDSSJ154049.17-003342.4	0315-51663-143	0315-51663-143	19.58,18.08,17.55	19.58,18.08,17.55	2.94 ± 0.22	2.94 ± 0.22	dV	6.2	0.2992	0.4318	300 ± 35	1.46	16 ± 2	a
SDSSJ154731.22+572000.0	0617-52072-561	0617-52072-561	18.03,16.89,16.48	18.03,16.89,16.48	2.56 ± 0.06	2.56 ± 0.06	dV	18.1	0.1883	0.3958	254 ± 12	1.85	15 ± 3	a cde
SDSSJ155030.75+521705.3	0618-52049-123	0618-52049-123	20.82,19.33,18.51	20.82,19.33,18.51	1.14 ± 0.15	1.14 ± 0.15	dV	4.4	0.4564	0.5384	345 ± 52	0.92	9 ± 2	a c
SDSSJ161843.10+435327.4	0815-52374-337	0815-52374-337	18.85,17.65,17.15	18.85,17.65,17.15	1.34 ± 0.05	1.34 ± 0.05	Ex	12.7	0.1989	0.6656	292 ± 29	3.26	8 ± 3	de
SDSSJ162746.44-005357.5	0364-52000-084	0364-52000-084	18.93,17.58,17.10	18.93,17.58,17.10	2.08 ± 0.08	2.08 ± 0.08	dV	15.6	0.2076	0.5243	290 ± 14	2.76	32 ± 3	a de
SDSSJ163028.15+452036.2	0626-52057-518	0626-52057-518	18.85,17.43,16.95	18.85,17.43,16.95	2.02 ± 0.07	2.02 ± 0.07	dV	10.4	0.2479	0.7934	276 ± 16	2.81	18 ± 3	a cde
SDSSJ163602.61+470729.5	0627-52144-464	0627-52144-464	19.01,17.75,17.24	19.01,17.75,17.24	1.48 ± 0.05	1.48 ± 0.05	dV	12.6	0.2282	0.6746	231 ± 15	1.90	9 ± 2	de
SDSSJ170216.76+332044.7	0973-52426-464	0973-52426-464	18.10,16.98,16.45	18.10,16.98,16.45	2.80 ± 0.07	2.80 ± 0.07	dV	15.2	0.1785	0.4357	256 ± 14	2.12	12 ± 3	a cde
SDSSJ170955.44+582348.1	0353-51703-121	0353-51703-121	20.22,18.67,17.97	20.22,18.67,17.97	1.18 ± 0.10	1.18 ± 0.10	dV	8.6	0.2437	0.3776	78 ± 20	0.12	7 ± 2	a
SDSSJ171837.39+642452.2	0352-51789-563	0352-51789-563	16.98,16.06,15.62	16.98,16.06,15.62	3.67 ± 0.07	3.67 ± 0.07	dV	20.7	0.0899	0.7370	273 ± 16	3.68	39 ± 4	de
SDSSJ204249.75-062631.7	0635-52145-290	0635-52145-290	19.70,18.31,17.57	19.70,18.31,17.57	1.55 ± 0.12	1.55 ± 0.12	dV	7.6	0.2677	0.6676	264 ± 28	2.23	9 ± 3	a
SDSSJ205222.58+000111.1	0982-52466-602	0982-52466-602	18.98,17.70,17.16	18.98,17.70,17.16	2.14 ± 0.09	2.14 ± 0.09	dV	11.4	0.2107	0.4638	320 ± 17	3.05	9 ± 2	ab d
SDSSJ213426.44+104313.1	0731-52460-165	0731-52460-165	18.58,17.07,16.56	18.58,17.07,16.56	3.14 ± 0.10	3.14 ± 0.10	dV	13.5	0.2290	0.3964	224 ± 14	1.14	8 ± 2	a
SDSSJ213720.86-080809.5	0641-52199-021	0641-52199-021	19.56,18.13,17.57	19.56,18.13,17.57	1.85 ± 0.14	1.85 ± 0.14	dV	6.6	0.3090	0.6306	201 ± 21	1.08	12 ± 3	ab
SDSSJ214747.04-003227.7	0371-52078-307	0371-52078-307	20.48,18.95,18.15	20.48,18.95,18.15	2.04 ± 0.29	2.04 ± 0.29	dV	4.1	0.4892	0.6030	379 ± 36	1.36	8 ± 2	ab
SDSSJ220218.32-084648.0	0717-52468-165	0717-52468-165	18.87,17.82,17.32	18.87,17.82,17.32	1.05 ± 0.05	1.05 ± 0.05	dV	13.3	0.1613	0.5011	231 ± 12	2.00	11 ± 3	d
SDSSJ223840.19-075456.0	0722-52224-442	0722-52224-442	18.01,16.93,16.40	18.01,16.93,16.40	2.20 ± 0.07	2.20 ± 0.07	dV	18.2	0.1371	0.7126	198 ± 11	1.75	34 ± 3	cd
SDSSJ225125.87-092635.8	0724-52254-277	0724-52254-277	20.28,18.58,17.73	20.28,18.58,17.73	2.03 ± 0.19	2.03 ± 0.19	dV	5.1	0.4719	0.6238	414 ± 47	2.09	11 ± 2	abcd
SDSSJ230053.14+002237.9	0677-52606-520	0677-52606-520	19.19,17.79,17.27	19.19,17.79,17.27	1.76 ± 0.10	1.76 ± 0.10	dV	12.2	0.2285	0.4637	279 ± 17	2.13	18 ± 2	ab de
SDSSJ230220.17-084049.4	0725-52258-463	0725-52258-463	17.72,17.04,16.73	17.72,17.04,16.73	0.48 ± 0.01	0.48 ± 0.01	Ex	29.7	0.0901	0.2224	237 ± 8	1.89	175 ± 4	c
SDSSJ230321.72+142217.9	0743-52262-304	0743-52262-304	18.32,16.93,16.35	18.32,16.93,16.35	3.02 ± 0.09	3.02 ± 0.09	dV	13.3	0.1553	0.5170	255 ± 16	2.51	9 ± 3	ab de
SDSSJ232120.93-093910.2	0645-52203-517	0645-52203-517	16.19,15.29,14.88	16.19,15.29,14.88	3.92 ± 0.05	3.92 ± 0.05	dV	31.5	0.0819	0.5324	249 ± 8	2.97	56 ± 6	cde
SDSSJ234339.73+002527.7	0385-51877-596	0385-51877-596	18.14,16.87,16.33	18.14,16.87,16.33	2.57 ± 0.07	2.57 ± 0.07	dV	22.4	0.1858	0.2719	229 ± 14	0.92	55 ± 3	ab
SDSSJ234358.86-003022.4	0385-51877-076	0385-51877-076	18.43,17.27,16.67	18.43,17.27,16.67	1.88 ± 0.07	1.88 ± 0.07	dV	18.2	0.1807	0.4628	269 ± 11	2.41	35 ± 3	d
SDSSJ234728.08-000521.2	0684-52523-311	0684-52523-311	19.99,18.61,18.03	19.99,18.61,18.03	1.78 ± 0.28	1.78 ± 0.28	dV	4.6	0.4169	0.7152	404 ± 59	3.48	38 ± 3	ab de

Table A.1: (continued)

Appendix B

SDSS Lens-Candidate Spectra

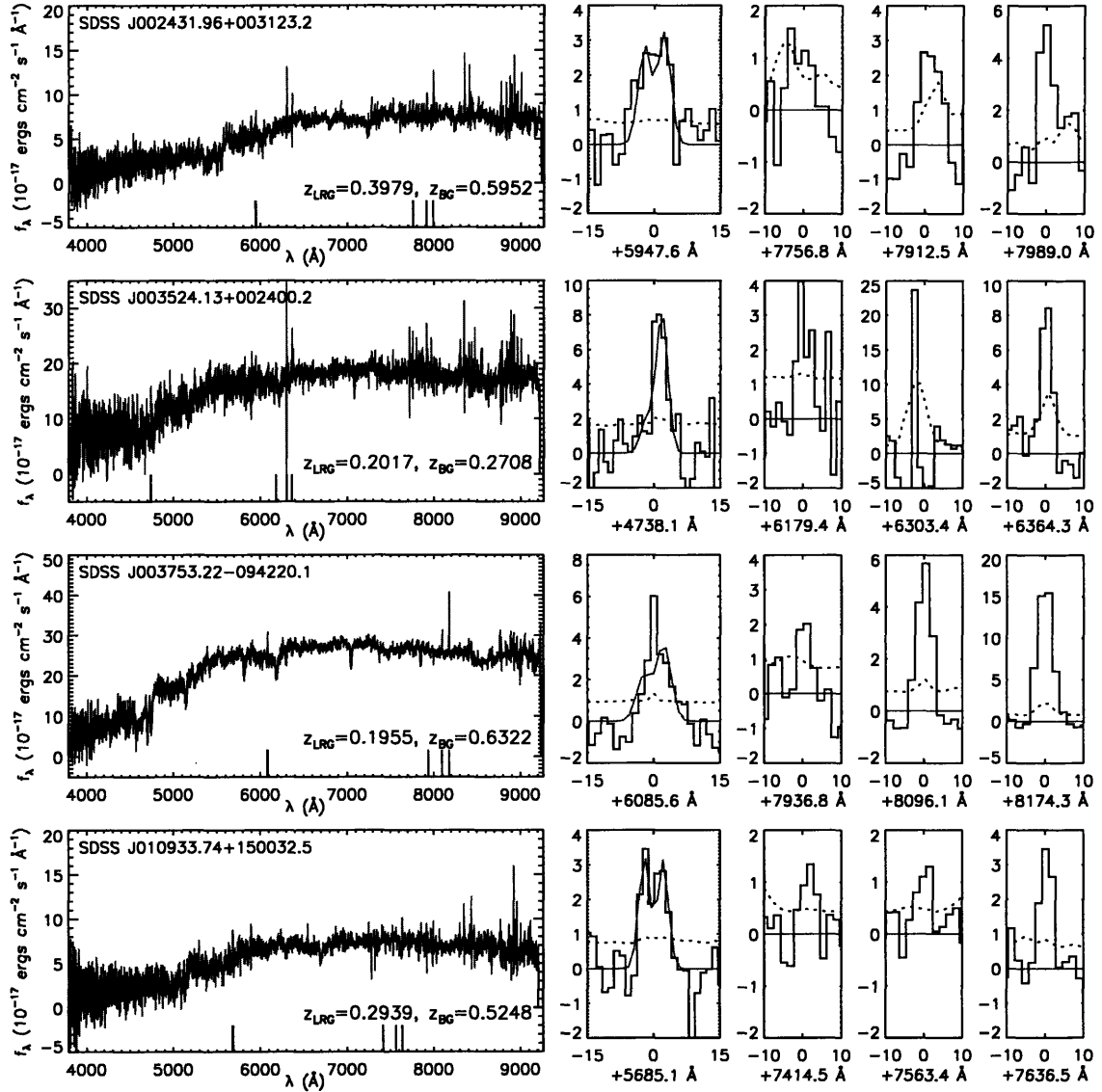


Figure B-1: SDSS LRG spectra with confirmed background-galaxy emission features. In the full-spectrum plots, gray lines show data, black lines show best-fit model spectrum, and long ticks along bottom margin indicate the position of redshifted [O II] 3727, H β , [O III] 4959, and [O III] 5007 background emission. Smaller windows show zooms of the residual (data – model) spectra at the positions of these same redshifted emission lines. Dashed lines in the smaller windows show the 1- σ noise level, rescaled as described in Appendix 2.4. Gray lines in the [O II] 3727 zoom show the double-Gaussian fit; the zero-flux line is drawn in the other three zooms. The spectroscopic resolution is $\lambda/\Delta\lambda \approx 1800$. Note the changing vertical scales.

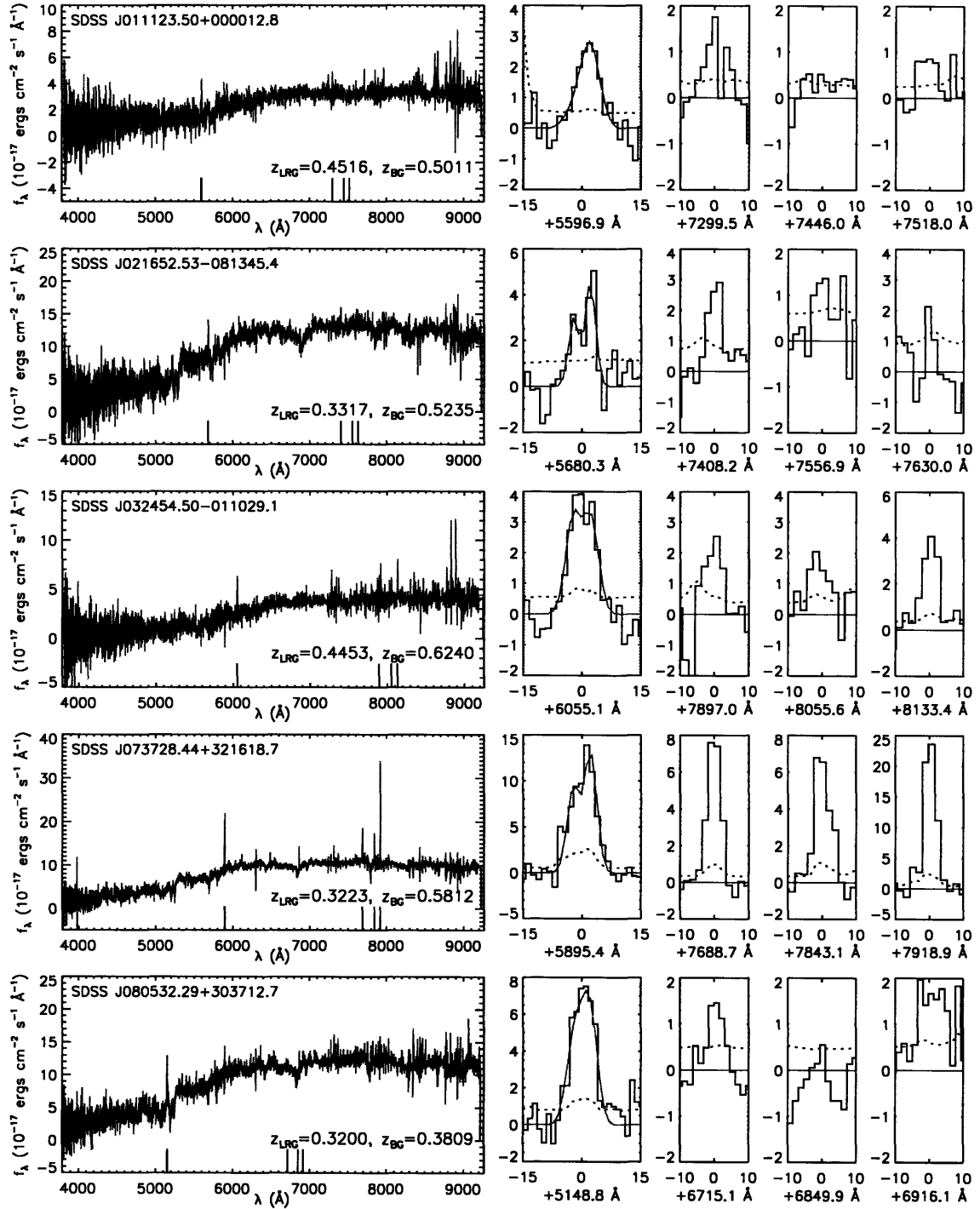


Figure B-1: (continued)

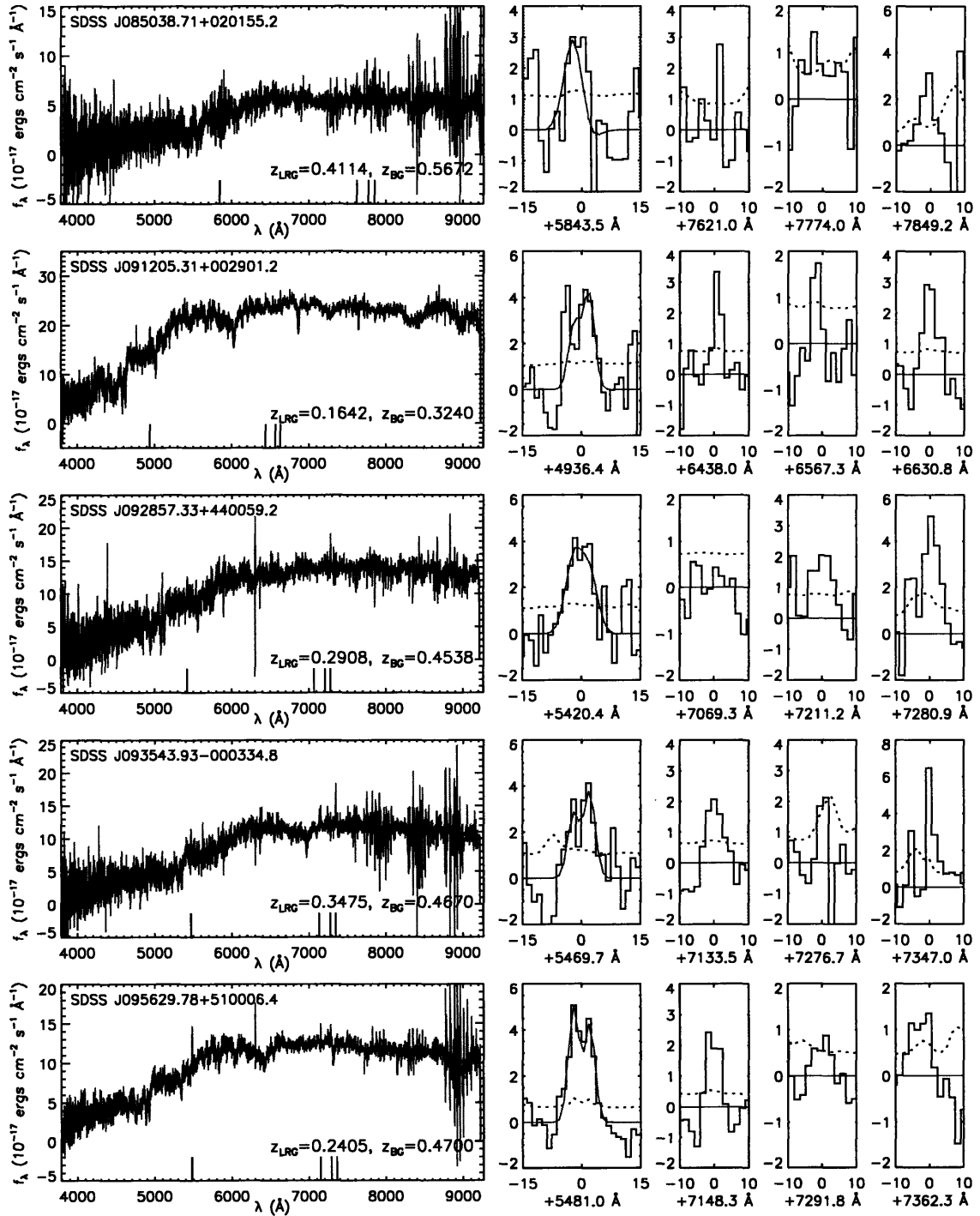


Figure B-1: (continued)

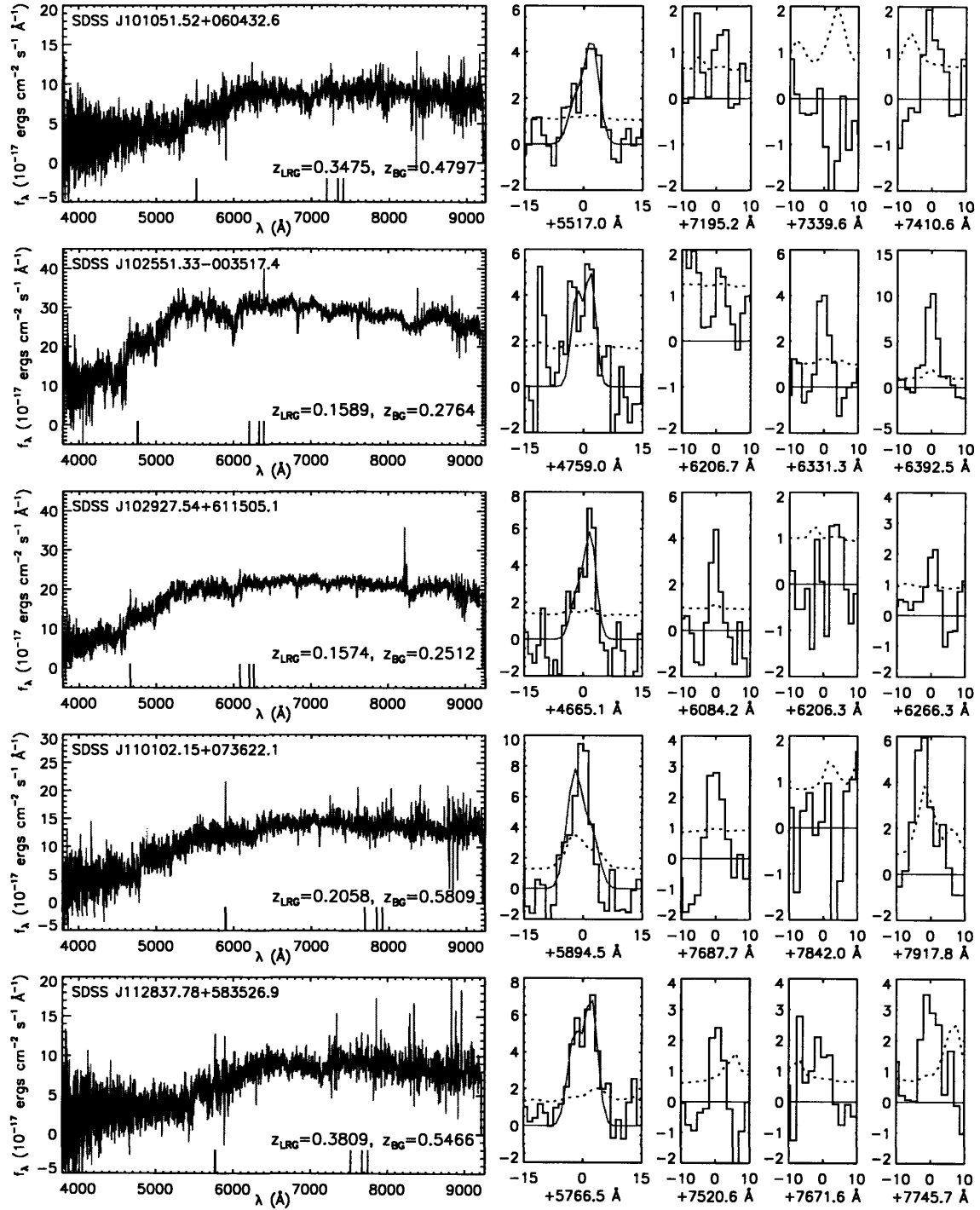


Figure B-1: (continued)

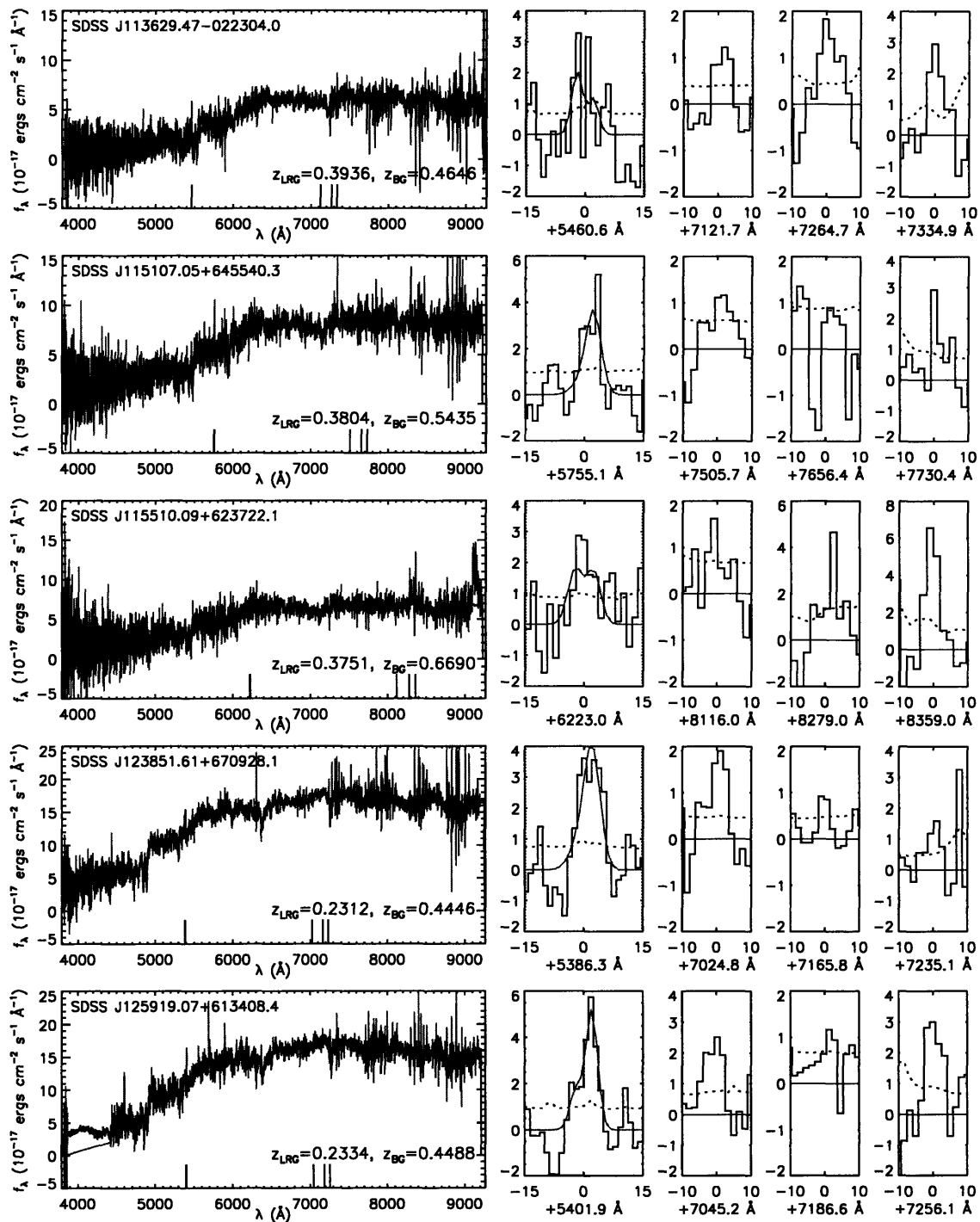


Figure B-1: (continued)

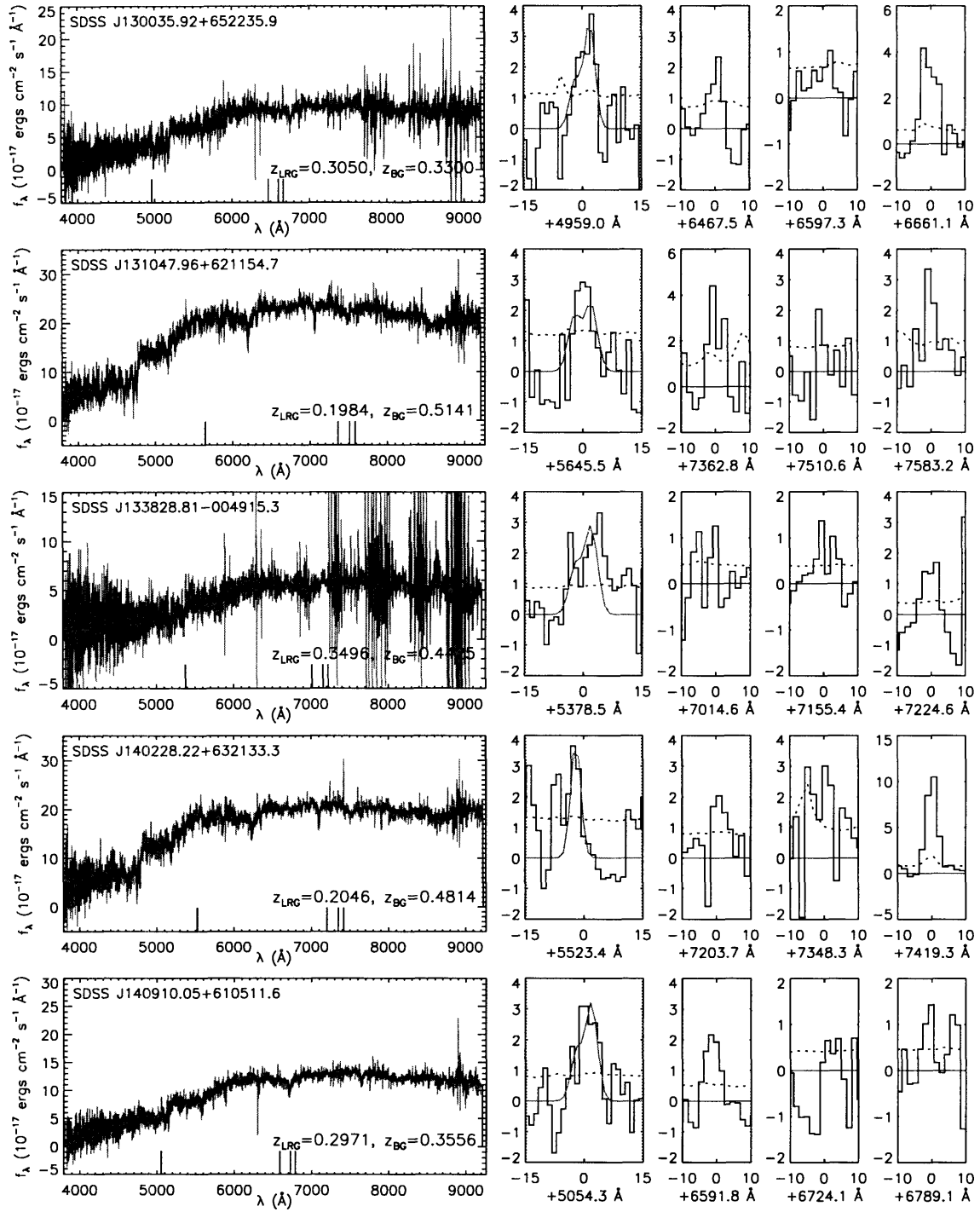


Figure B-1: (continued)

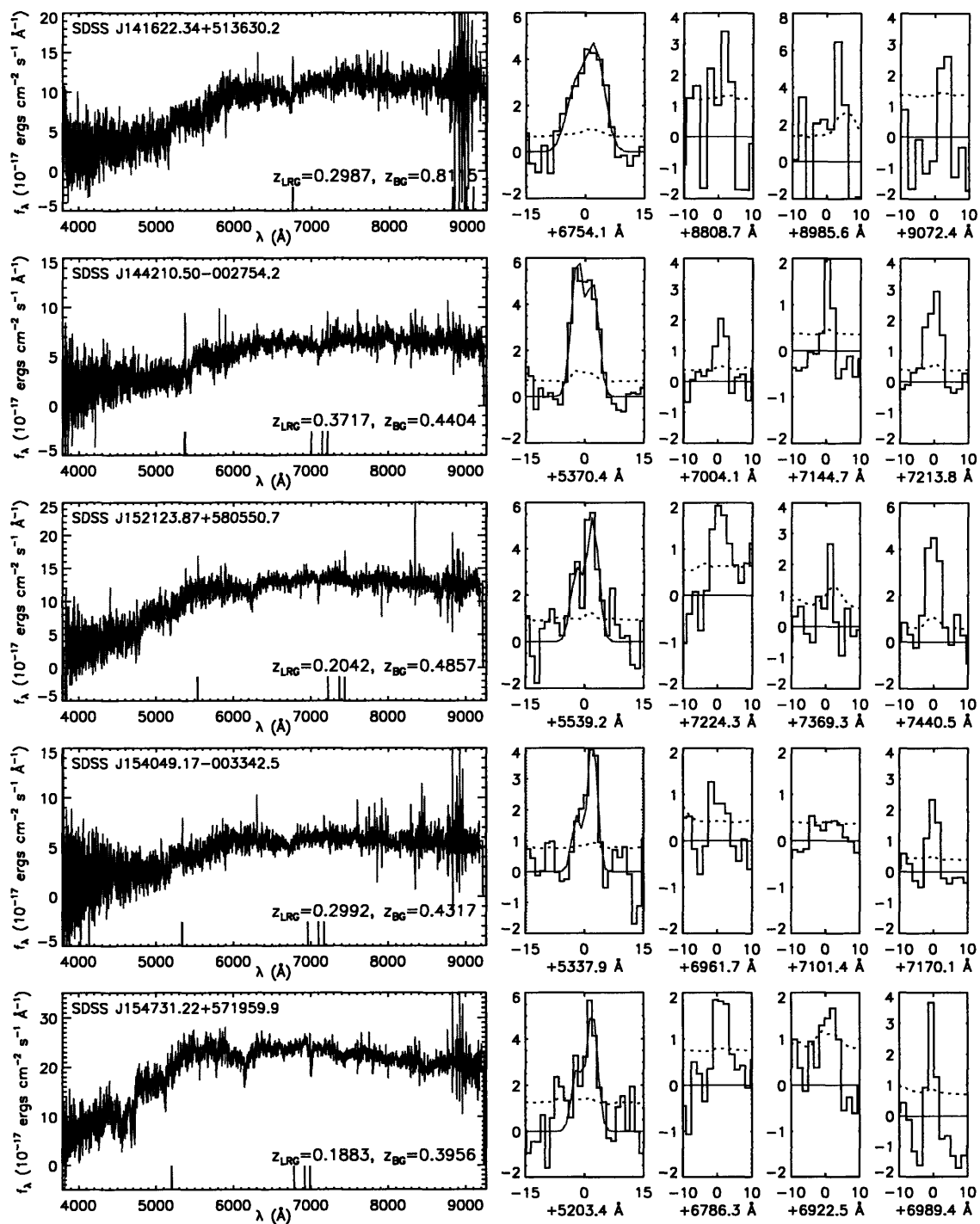


Figure B-1: (continued)

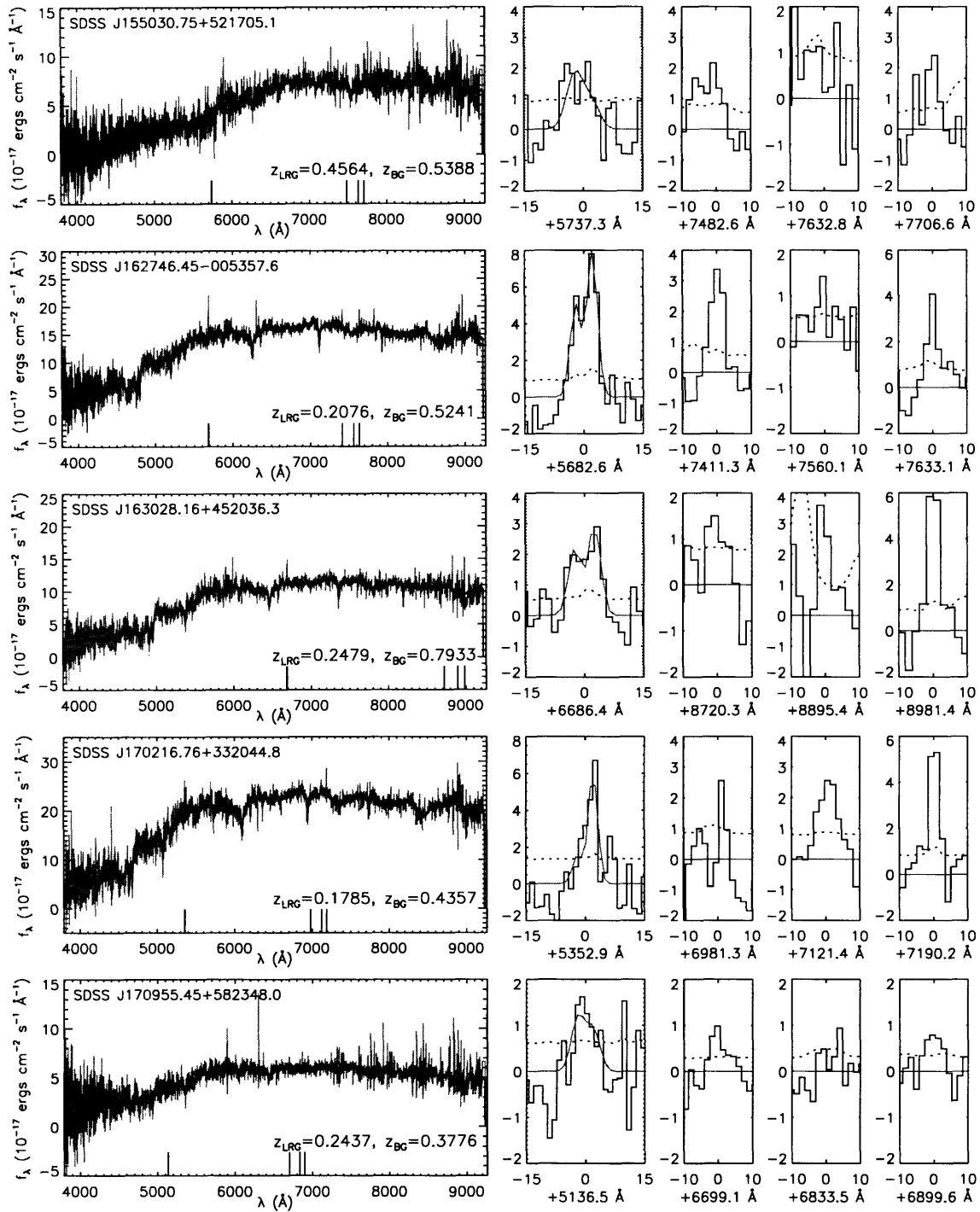


Figure B-1: (continued)

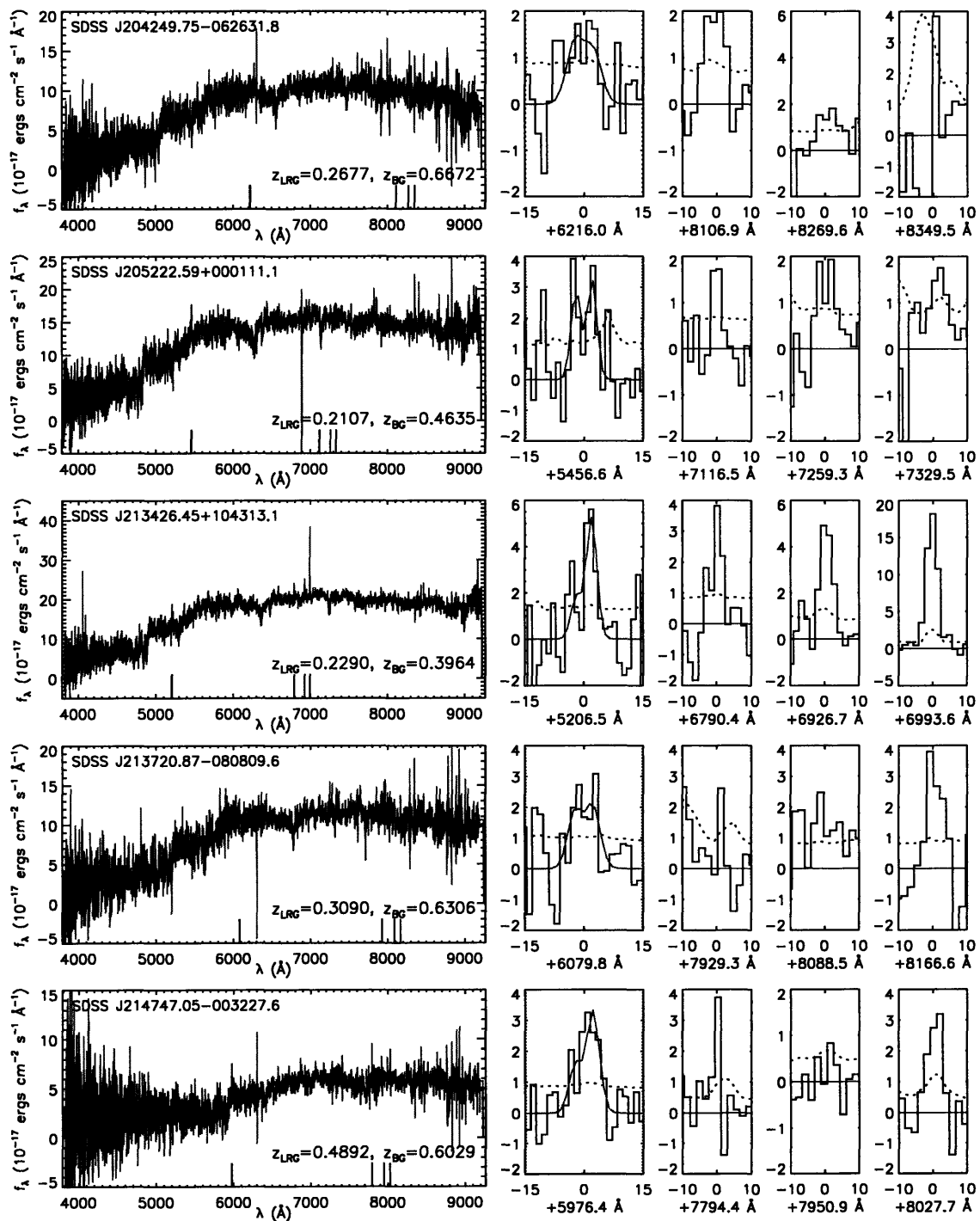


Figure B-1: (continued)

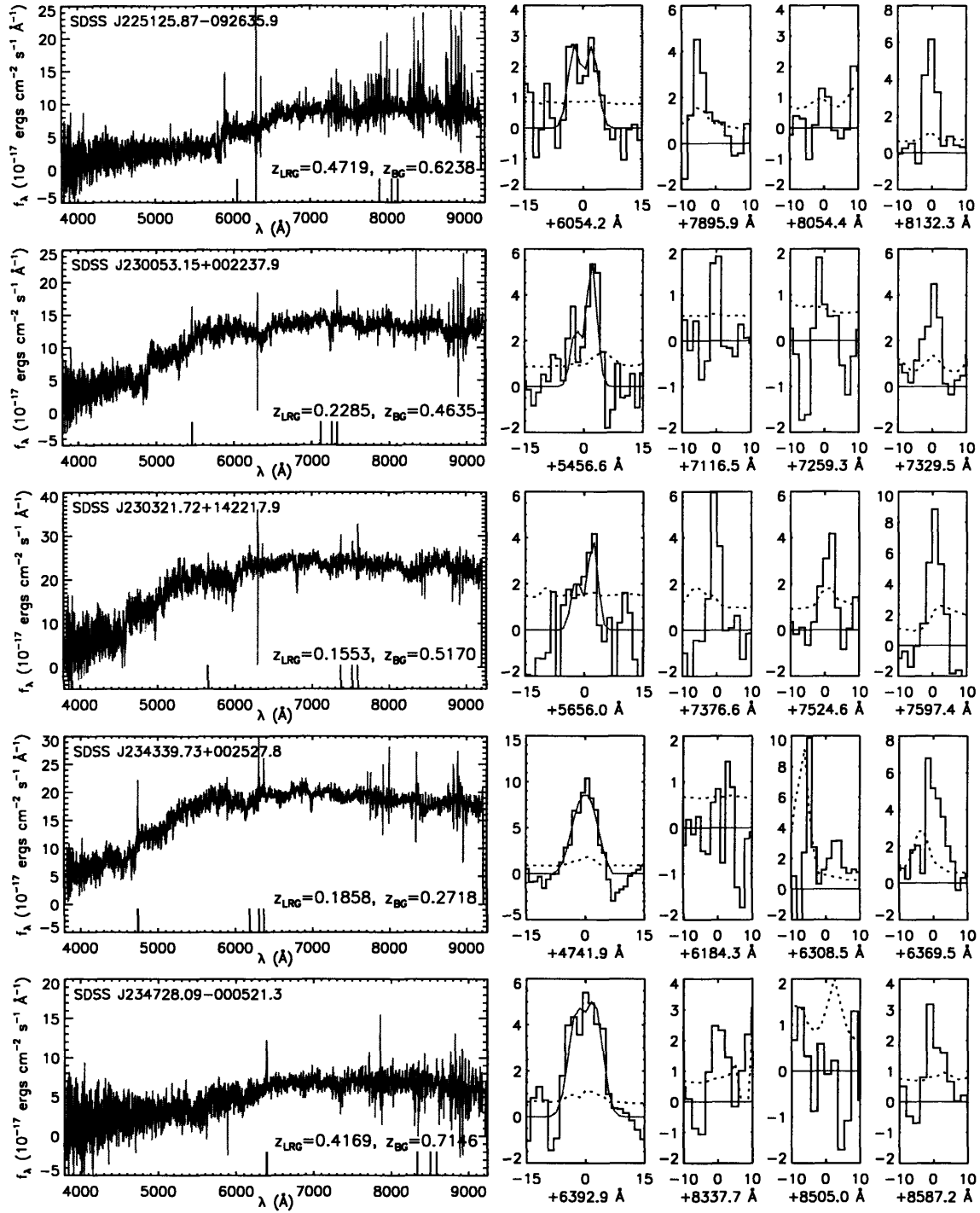


Figure B-1: (continued)

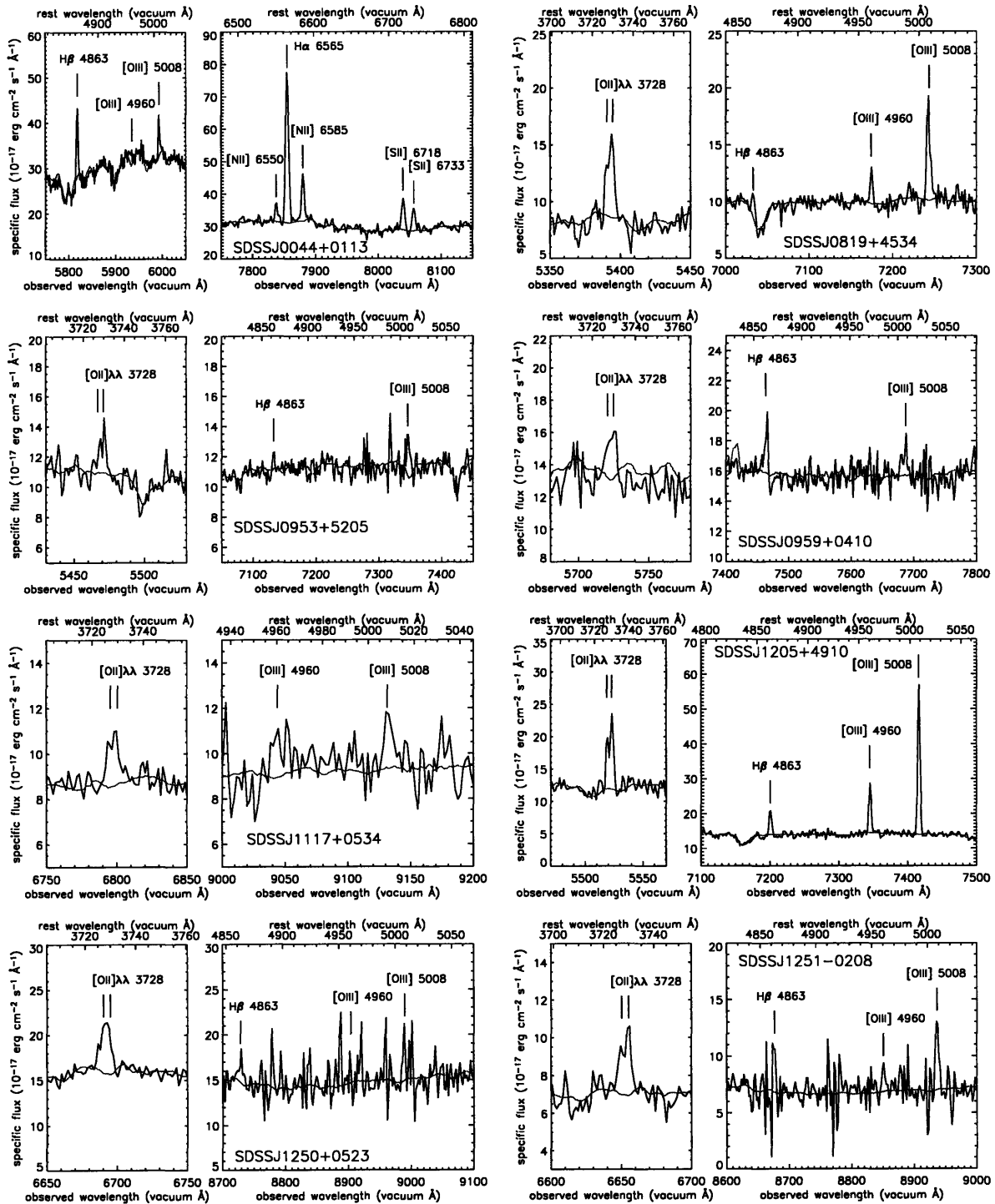


Figure B-2: SDSS spectroscopy showing background line emission in lens-candidate systems observed with *HST*-ACS or IFU, and not shown in Figure B-1. Gray line shows SDSS template fitted to the continuum of the foreground galaxy.

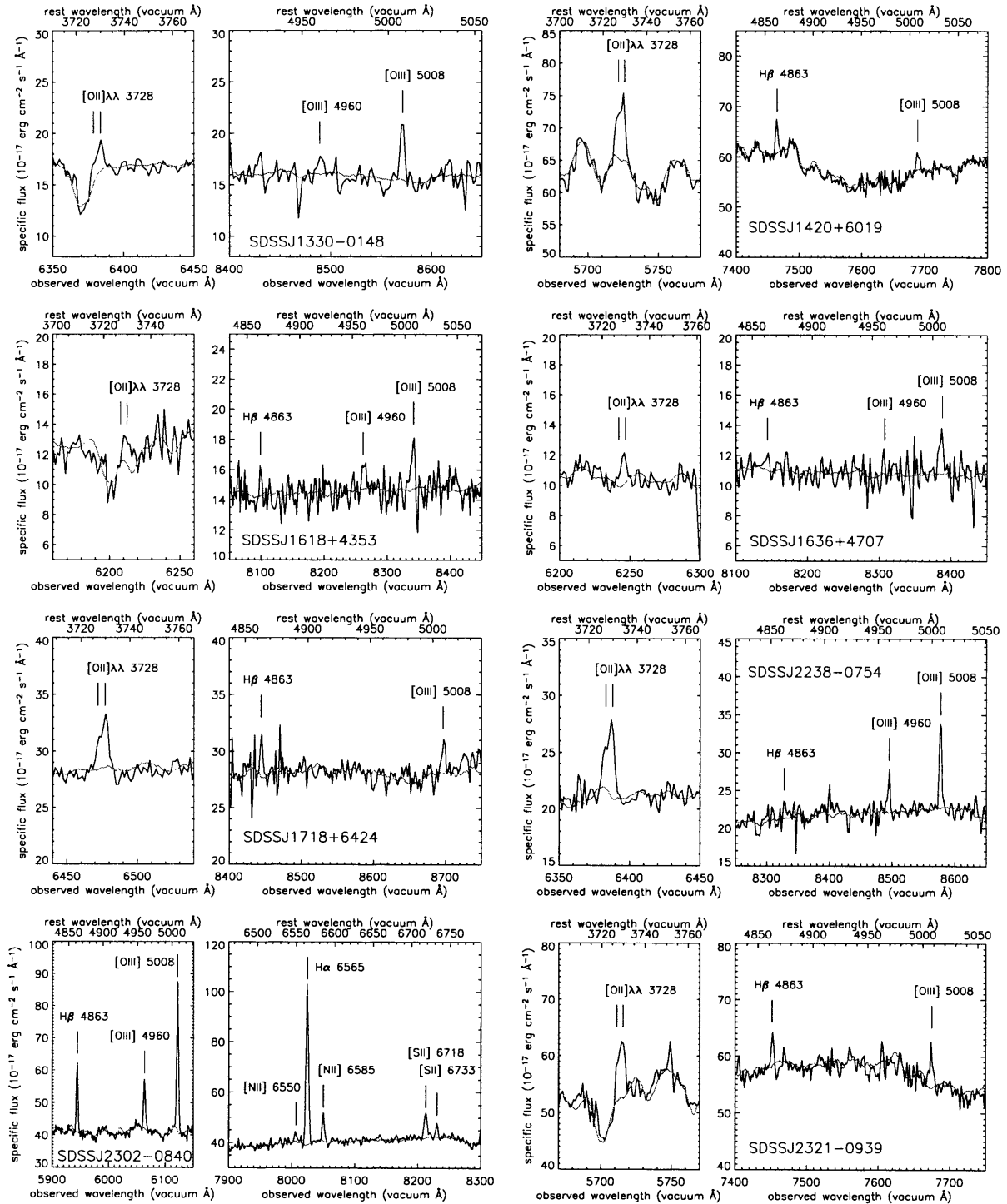


Figure B-2: (continued)

Appendix C

SDSS Lens-Candidate Imaging

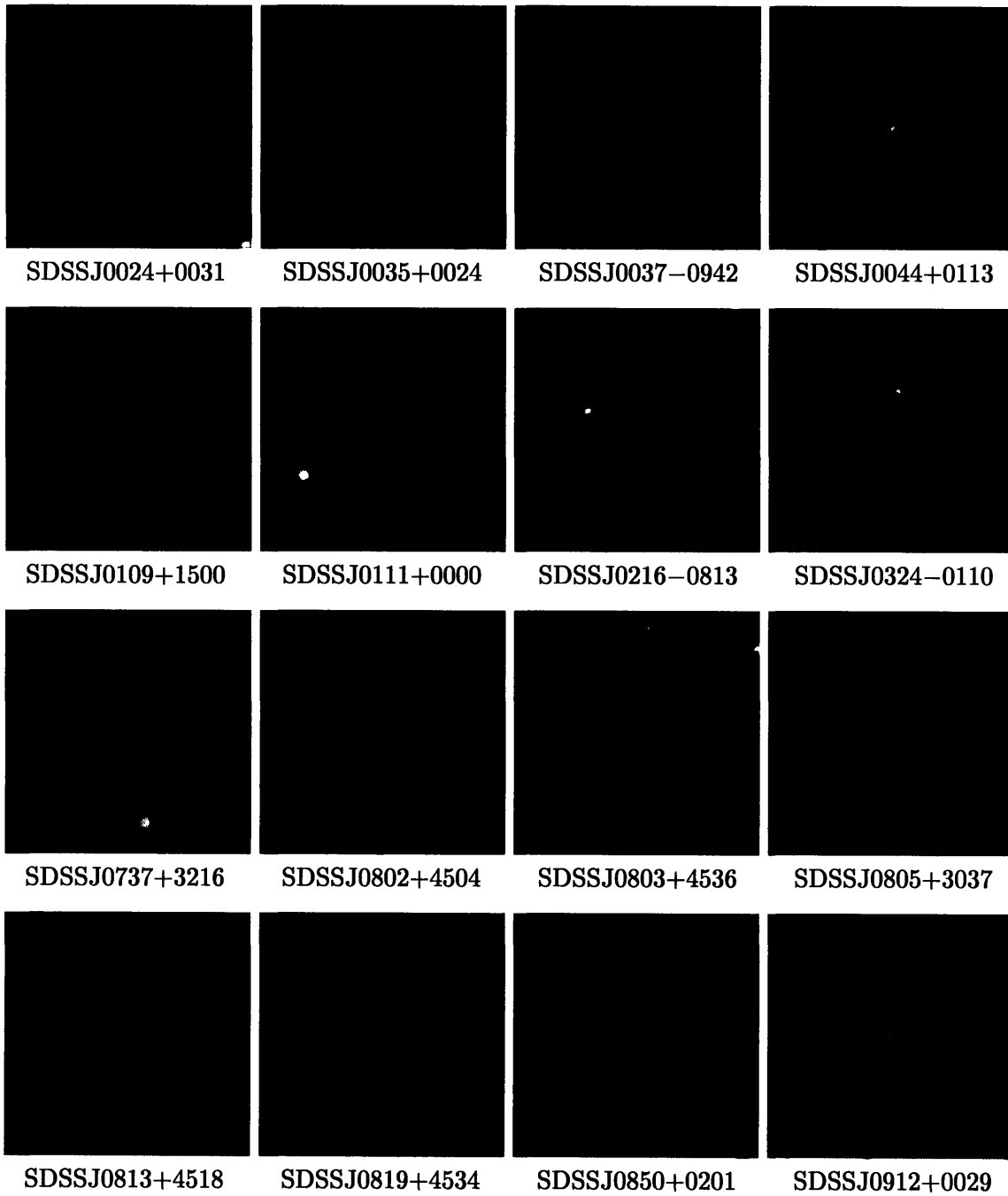


Figure C-1: SDSS color ($g-r-i$) images of lenses and lens candidates. Images are $1' \times 1'$ centered on our systems, with North up and East left.

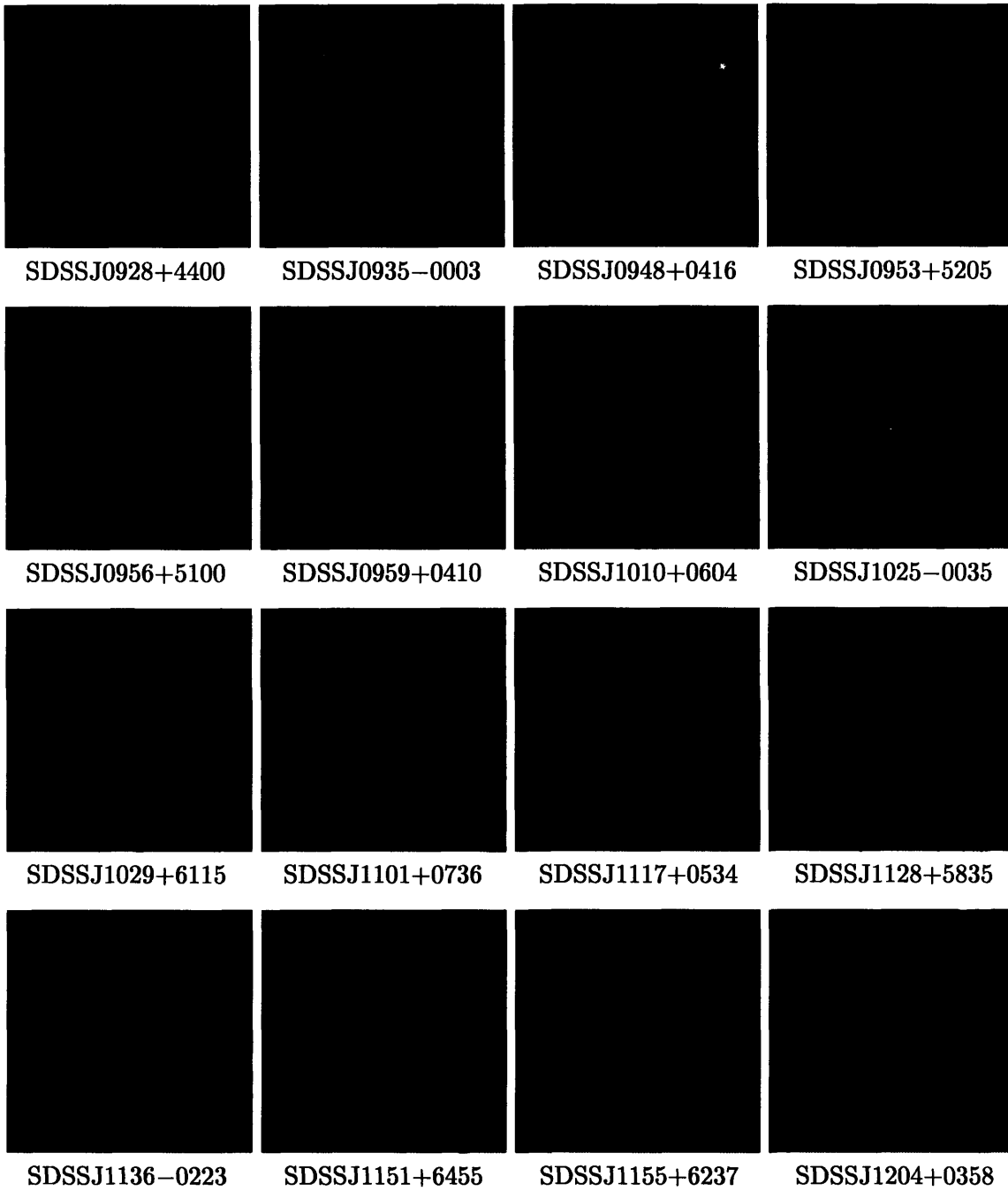


Figure C-1: (continued)

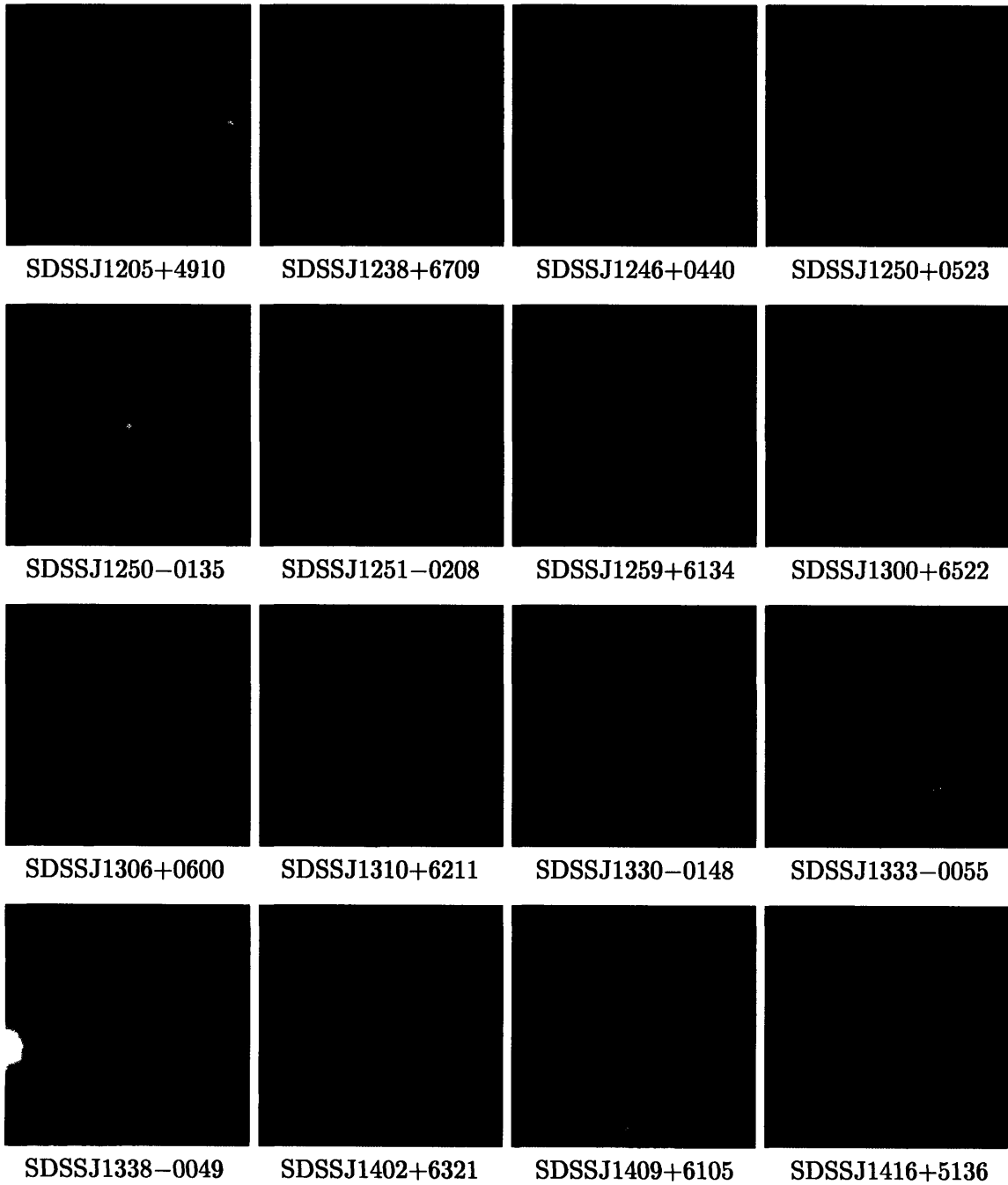


Figure C-1: (continued)

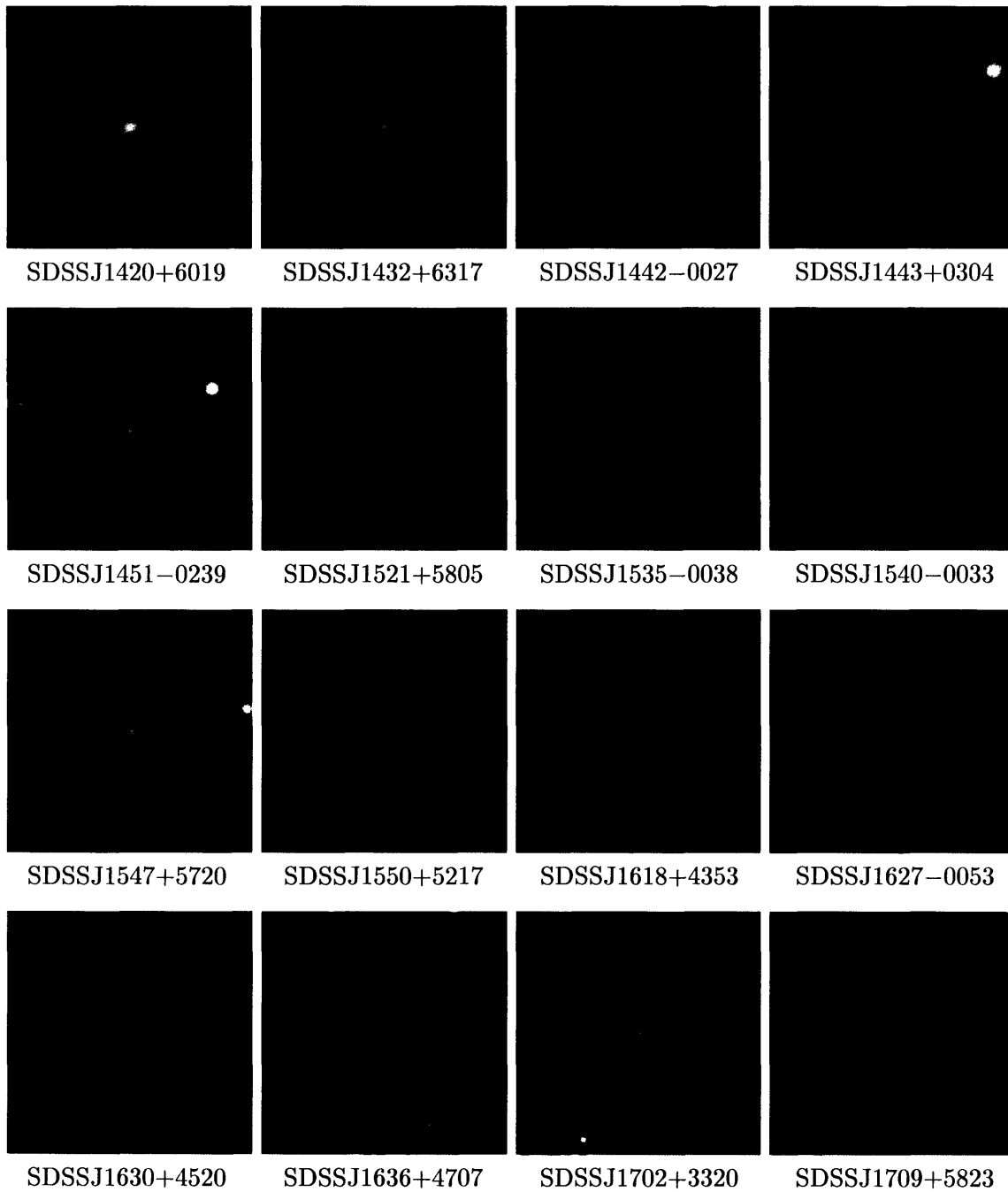


Figure C-1: (continued)

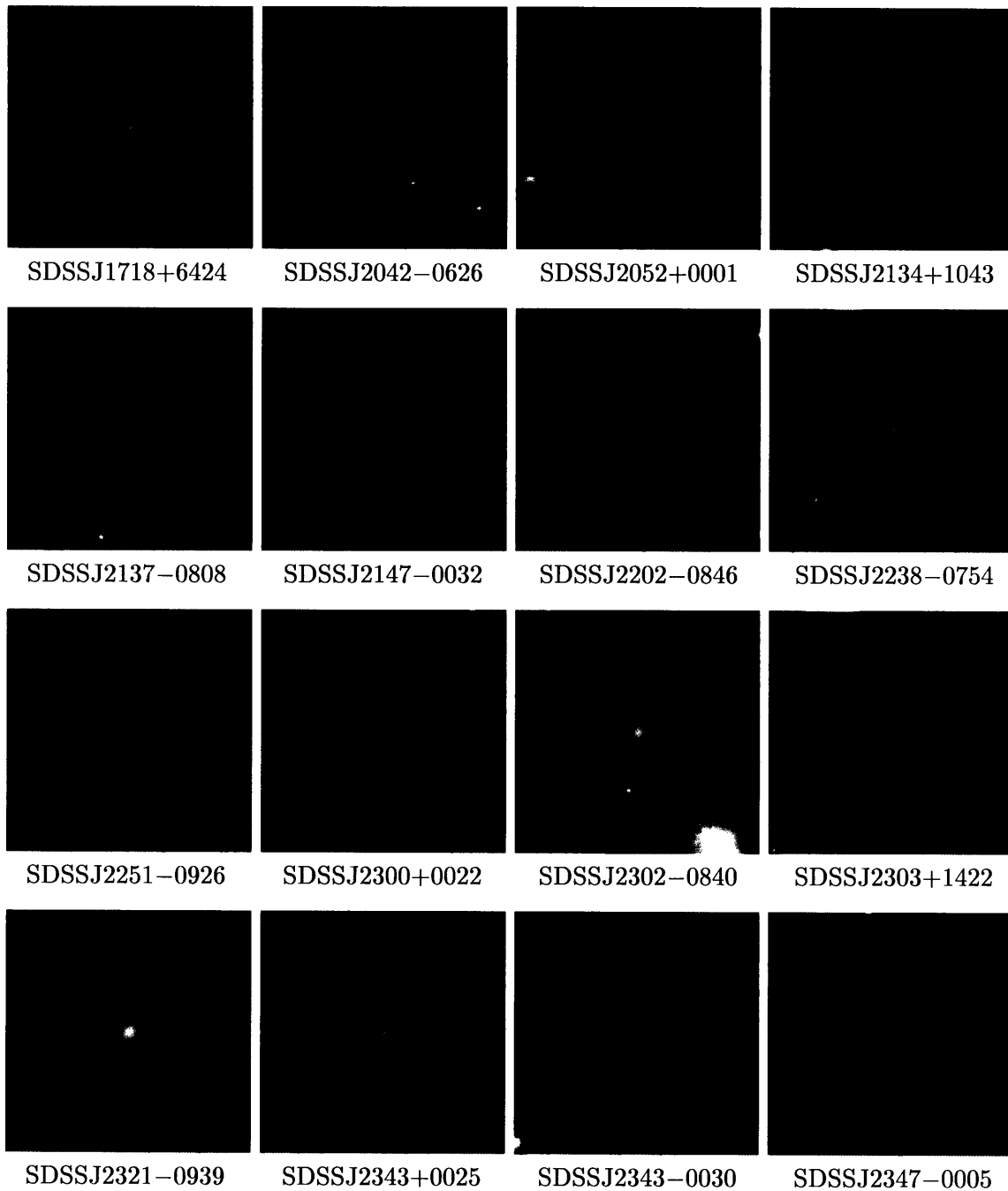


Figure C-1: (continued)

Appendix D

IFU Lens-Candidate Data Catalog

This appendix presents the balance of IFU data, originally referenced in § 3.4.3, from which the incidence of strong lensing could not be established and/or interpreted. Table D.1 gives relevant information for the interpretation of the figures presented in this section. Unless otherwise noted, all figures show (from left to right) summed IFU spectra of fibers with significant background-galaxy line emission, reconstructed IFU continuum image, reconstructed IFU emission-line image, and hex-smoothed emission-line image. Narrowband IFU images are created as described in § 3.4.1.

In addition to the systems for which we present IFU data figures, the following two systems were observed with the GMOS-N IFU, but lacked significant emission-line flux detection: SDSSJ1151+6455, SDSSJ1310+6211.

System Name	UT		Exp. Time (s)	IFU Mode	Target Line	λ_{obs} (Å)	1σ		Image Display Limits			
	Observation Date	Date					Line	Thresh.	Continuum Min	Continuum Max	Emission-Line Min	Emission-Line Max
SDSSJ2251-0926	2004-11-02	2004-11-02	3x1800	IMACS-2	[O III] 5007	8132	0.565	0.08	-0.02	0.08	-0.20	0.40
SDSSJ0216-0813	2004-11-02	2004-11-02	3x1800	IMACS-2	[O II] 3727	5680	0.472	0.09	-0.02	0.09	-0.20	0.30
SDSSJ0805+3037	2004-04-21	2004-04-21	3x900	GMOS-g	[O II] 3727	5149	0.684	0.04	-0.01	0.04	-0.10	0.30
SDSSJ0928+4400	2004-03-20	2004-03-20	3x900	GMOS-i	[O III] 5007	7281	0.351	0.10	-0.03	0.10	-0.10	0.20
SDSSJ0956+5100	2004-05-09	2004-05-09	3x900	GMOS-i	H β	7149	0.491	0.25	-0.08	0.25	-0.10	0.20
SDSSJ1029+6115	2004-05-11	2004-05-11	3x900	GMOS-i	H α	8214	0.444	0.30	-0.10	0.30	-0.10	0.20
SDSSJ1128+5835	2004-05-09	2004-05-09	3x900	GMOS-r	[O II] 3727	5766	1.744	0.10	-0.10	0.10	-0.50	1.00
SDSSJ1151+6455	2004-05-11	2004-05-11	3x900	GMOS-r	[O II] 3727	5754	1.244	-	-	-	-	-
SDSSJ1155+6237	2004-05-08	2004-05-08	2x900	GMOS-i	[O III] 5007	8359	0.546	0.08	-0.04	0.08	-1.00	3.50
SDSSJ1259+6134	2004-05-09	2004-05-09	3x900	GMOS-i	[O III] 5007	7256	0.403	0.25	-0.08	0.25	-0.08	0.15
SDSSJ1310+6211	2004-05-10	2004-05-10	3x900	GMOS-i	[O III] 5007	7583	0.362	-	-	-	-	-
SDSSJ1409+6105	2004-04-28	2004-04-28	3x900	GMOS-g	[O II] 3727	5059	0.919	0.08	-0.04	0.08	-0.10	0.30
SDSSJ1416+5136	2004-05-14	2004-05-14	3x900	GMOS-r	[O II] 3727	6755	1.017	0.08	-0.04	0.08	-0.20	0.50
SDSSJ1521+5805	2004-05-14	2004-05-14	3x900	GMOS-i	[O III] 5007	7440	0.626	0.20	-0.08	0.20	-0.10	0.30
SDSSJ1547+5719	2004-05-14	2004-05-14	3x900	GMOS-g	[O II] 3727	5203	0.607	0.25	-0.08	0.25	-0.10	0.20
SDSSJ1550+5217	2004-05-11	2004-05-11	2x900	GMOS-r	[O II] 3727	5737	0.000	-	-	-	-	-
SDSSJ1702+3320	2004-05-23	2004-05-23	3x900	GMOS-i	[O III] 5007	7190	0.523	0.25	-0.08	0.25	-0.10	0.25

Table D.1: Other IFU observations. IFU modes are described in Table 3.1. Redshifted wavelengths of target background emission lines used to construct emission-line images are given as λ_{obs} . Line threshold values are in units of 10^{-17} erg cm $^{-2}$ s $^{-1}$ for an aperture of one square arcsecond in space and 5Å in wavelength. Image display minimum (white) and maximum (black) values are given in units of 10^{-17} erg cm $^{-2}$ s $^{-1}$ per IFU lenslet, per Å for continuum images and integrated in wavelength for emission-line images.

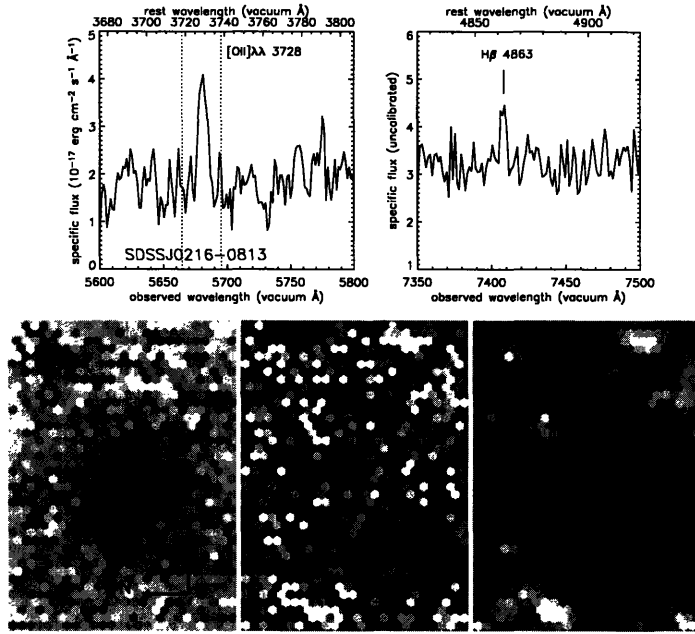


Figure D-1: IMACS-2 IFU spectrum and narrowband imaging of SDSSJ0216–0813. Blended [O II] 3727 emission is detected, as is weak H β , but the [O III] 5007 doublet is lost within the A band of atmospheric absorption. The emission-line imaging morphology is in agreement with the *HST*-ACS residual image of the system seen in Figure E-1, including a very faint detection at the position of the putative counterimage near the center of the lens galaxy.

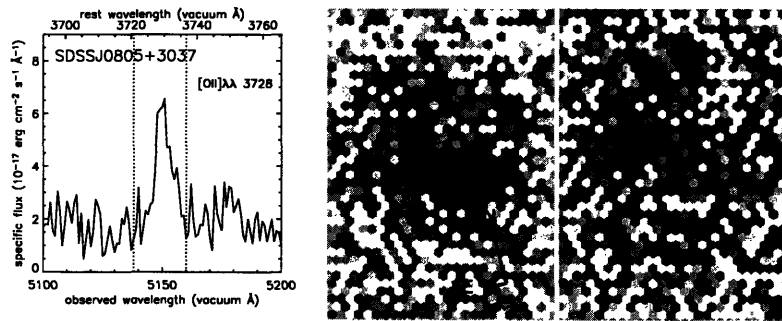


Figure D-2: GMOS-*g* IFU spectrum and narrowband imaging of SDSSJ0805+3037. [O II] 3727 detection is confirmed. Emission-line image is more extended than continuum, but neither is of very good quality. (Smoothed emission-line image not shown.)

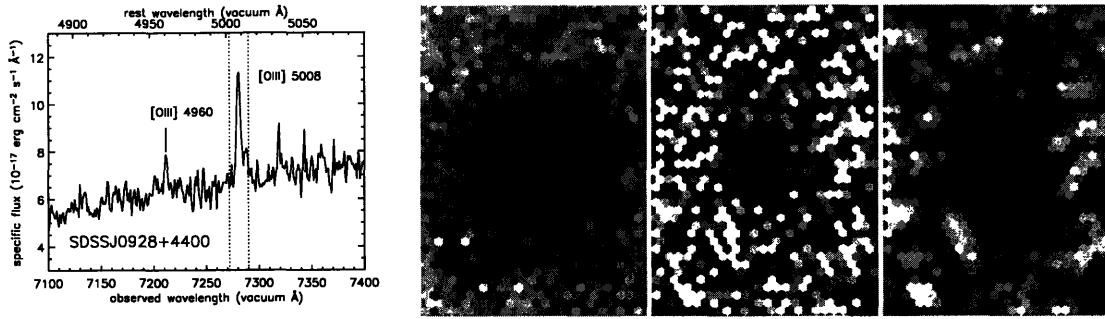


Figure D-3: GMOS-*i* IFU spectrum and narrowband imaging of SDSSJ0928+4400. Emission-line and continuum images appear superposed; could be an unresolved lens. [O III] 4959 detected in addition to [O III] 5007.

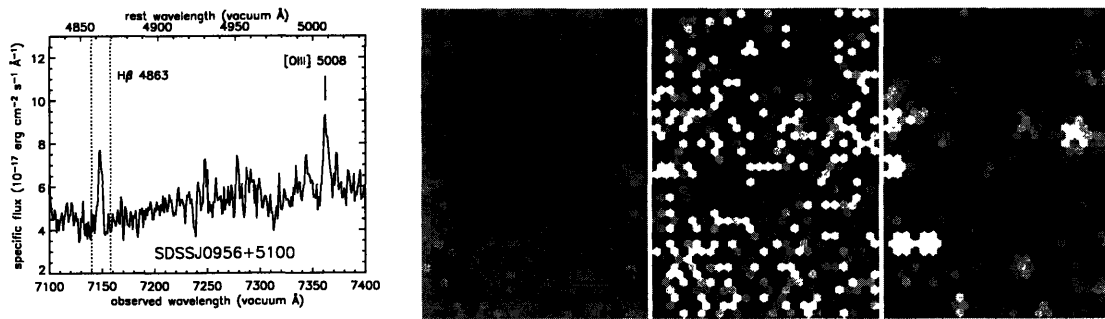


Figure D-4: GMOS-*i* IFU spectrum and narrowband imaging of SDSSJ0956+5100. [O III] 5007 and H β are detected. Emission-line image shows two tangentially elongated, opposing features. Looks like lensing morphology, but S/N too low for conclusive judgement or modeling.



Figure D-5: GMOS-*i* IFU spectrum and narrowband imaging of SDSSJ1029+6115. Left panel shows summed spectra of background emission-line galaxy. Middle panel shows a subset of the extracted and rectified spectra around the H α line of the background galaxy in the frame of the detector, showing evidence of rotation (total, continuum-model, and continuum-subtracted spectra are shown). Right panel shows reconstructed continuum image.

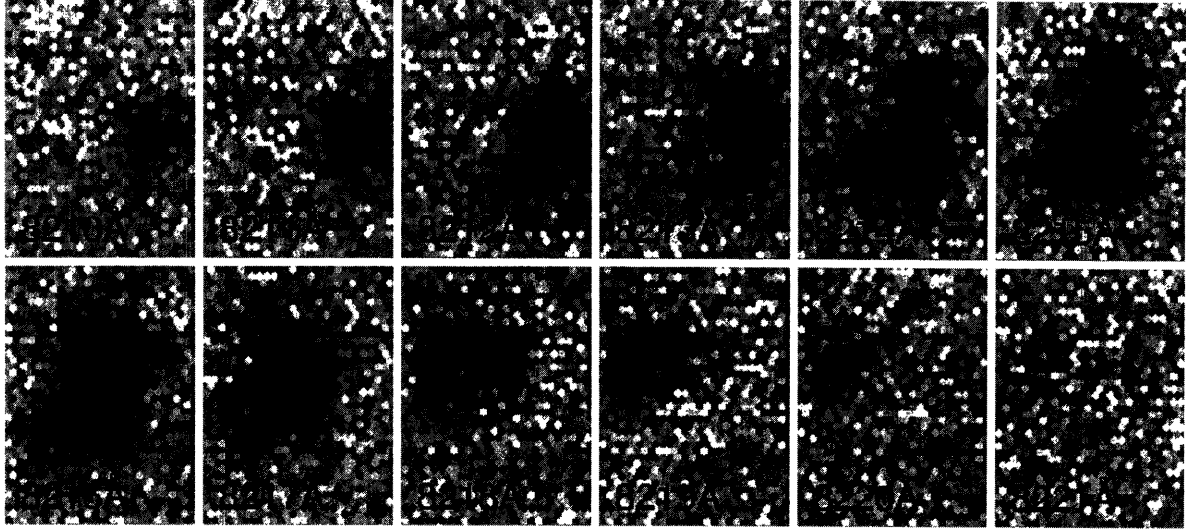


Figure D-6: GMOS-*i* IFU rotation-curve image sequence of SDSSJ1029+6115. Figure shows reconstructed continuum-subtracted 1-Å-wide slices through the H α line of the background galaxy. Data at higher spatial resolution would allow for lens modeling with independent constraints from each source-plane velocity point.

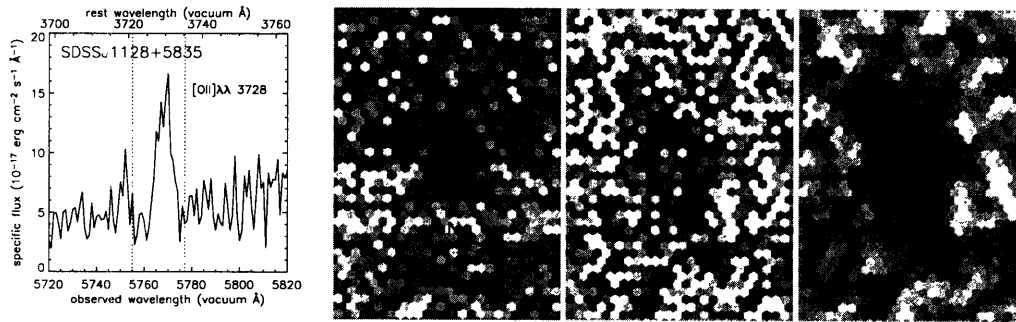


Figure D-7: GMOS-*r* IFU spectrum and narrowband imaging of SDSSJ1128+5835. [O II] 3727 doublet is confirmed at expected position, but emission-line image has low S/N . Smoothed emission-line image shows some evidence of a ring with plausible radius and centered on continuum position.

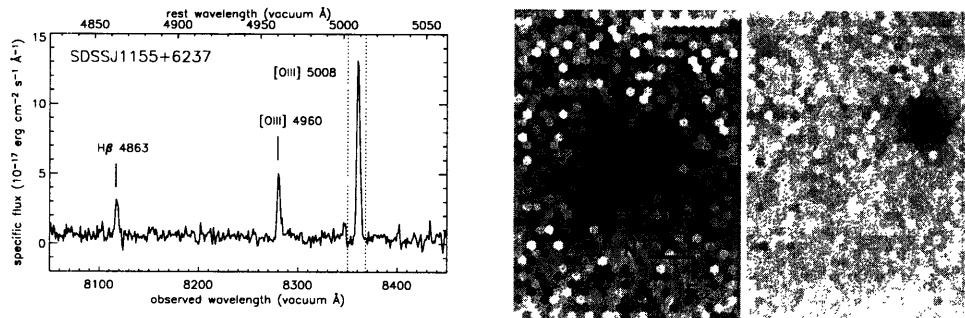


Figure D-8: GMOS-*i* IFU spectrum and narrowband imaging of SDSSJ1155+6237. [O III] 5007 is detected strongly, and confirmed by [O III] 4959 and H β . System is not a lens, but rather an unlensed projection offset by approximately $1''.74$ from the LRG continuum centroid. (Smoothed emission-line image not shown.)

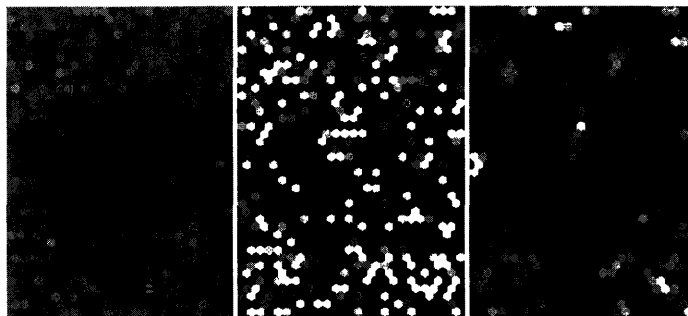


Figure D-9: GMOS-*i* IFU narrowband imaging of SDSSJ1259+6134. Emission-line image shows a slight detection of [O III] 5007. [O III] 4959 is not detected significantly, and $H\beta$ falls into the spectral overlap zone for one of the CCDs. Emission-line image does seem to be double to the extent that the morphology can be distinguished. Lines up roughly with the dubious-but-possible HST residual-image features seen in Figure E-2. (Summed spectrum is not shown since no other lines are detected.)

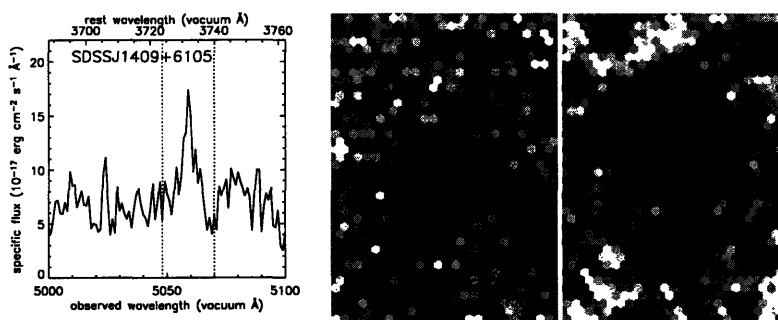


Figure D-10: GMOS-*g* IFU spectrum and narrowband imaging of SDSSJ1409+6105. Shows extended, low- S/N line emission. Only smoothed emission-line image is shown. IFU data has possible wavelength-calibration problems, as the emission line is off by $\approx 5\text{\AA}$ to the red of the position expected from SDSS. (GMOS *g*-band IFU data lacks significant sky-lines with which to fix the dispersion solution, and some science frames exhibit significant flexure with respect to their nearest baseline calibration arcs. The author recommends arcs at altitude immediately following science frames and flats for future GMOS spectroscopic programs, although they are charged to the time allocation.)

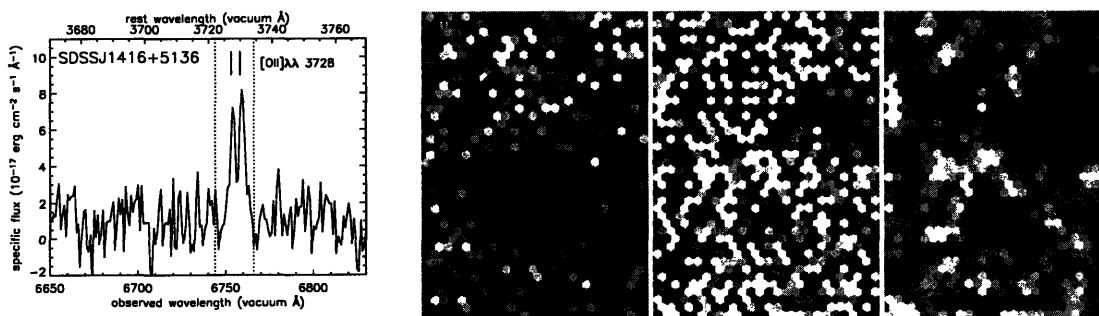


Figure D-11: GMOS-*r* IFU spectrum and narrowband imaging of SDSSJ1416+5136. [O II] 3727 detection is confirmed, but at redshift 0.0004 greater than the value from SDSS spectroscopy, indicating a possible reduction error. Continuum image shows possible hints of neighboring continuum sources. Emission line image looks like double lens, with bright image and faint counterimage. S/N deemed too low to do lens modeling on this system.

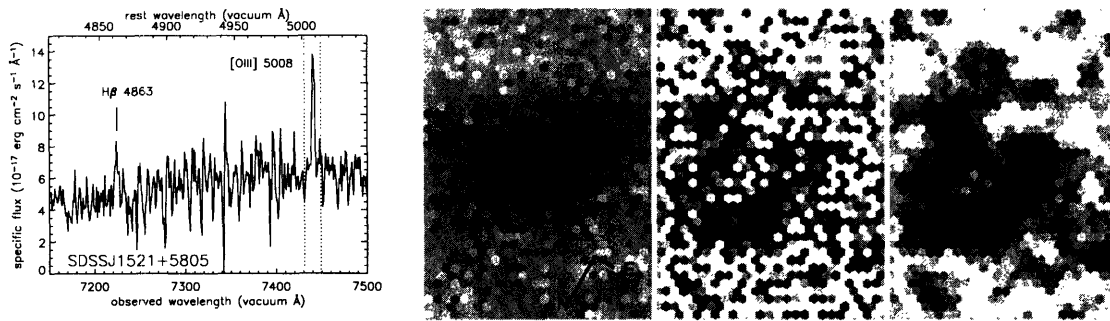


Figure D-12: GMOS-*i* IFU spectrum and narrowband imaging of SDSSJ1521+5805. [O III] 5007 is rather prominent although not exceedingly bright. [O III] 4959 is lost in the noise; H β shows up weak but significant in the summed spectra. Emission-line image is difficult to interpret.

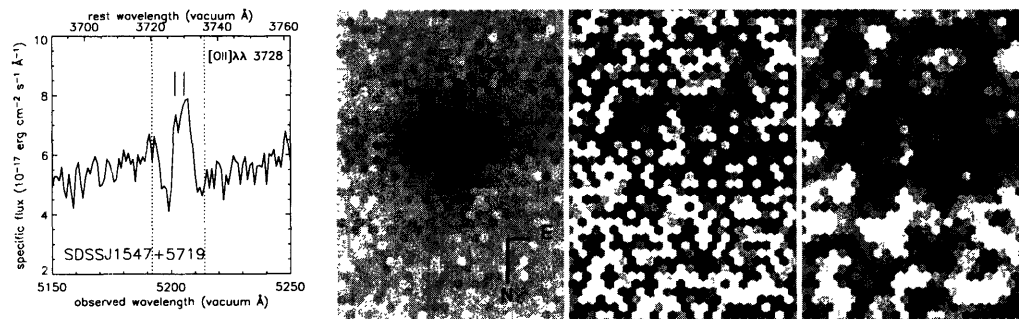


Figure D-13: GMOS-*g* IFU spectrum and narrowband imaging of SDSSJ1547+5719. [O II] 3727 is detected, but emission-line image is low quality, low S/N , and hard to interpret.

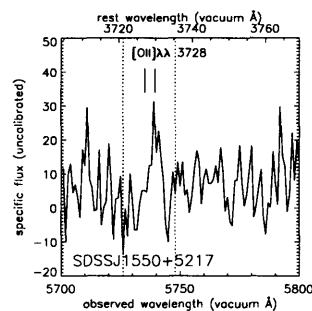


Figure D-14: GMOS-*r* IFU spectrum of SDSSJ1550+5217. [O II] 3727 seen very faintly at expected position in summed spectra, but emission-line image is entirely uninformative and is not reproduced here.

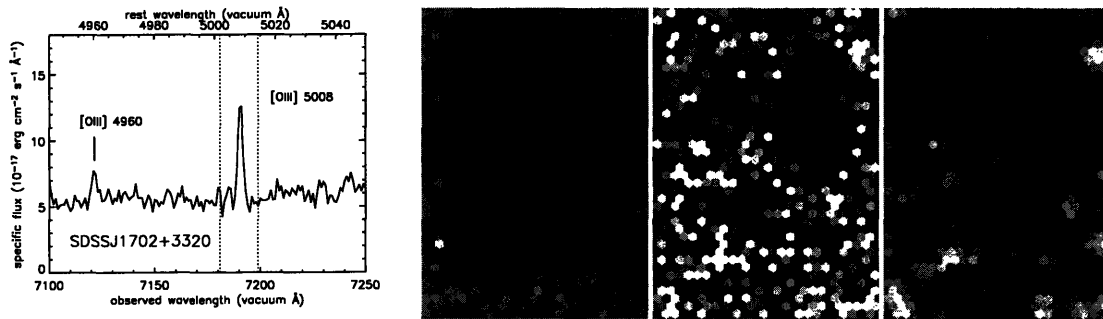


Figure D-15: GMOS-*i* IFU spectrum and narrowband imaging of SDSSJ1702+3320. [O III] 5007 and [O III] 4959 are detected; emission-line image looks like quad lens morphology with two bright merging images, but S/N is too low.

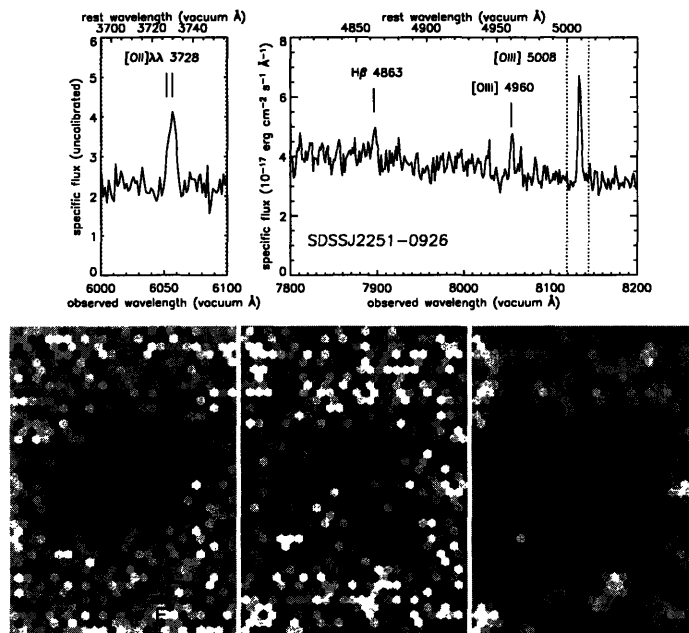


Figure D-16: IMACS-2 IFU spectrum and narrowband imaging of SDSSJ2251-0926. Looks like elongated or double in continuum. Apparent multiple imaging in narrowband, but at low S/N

Appendix E

HST-ACS Lens-Candidate Imaging

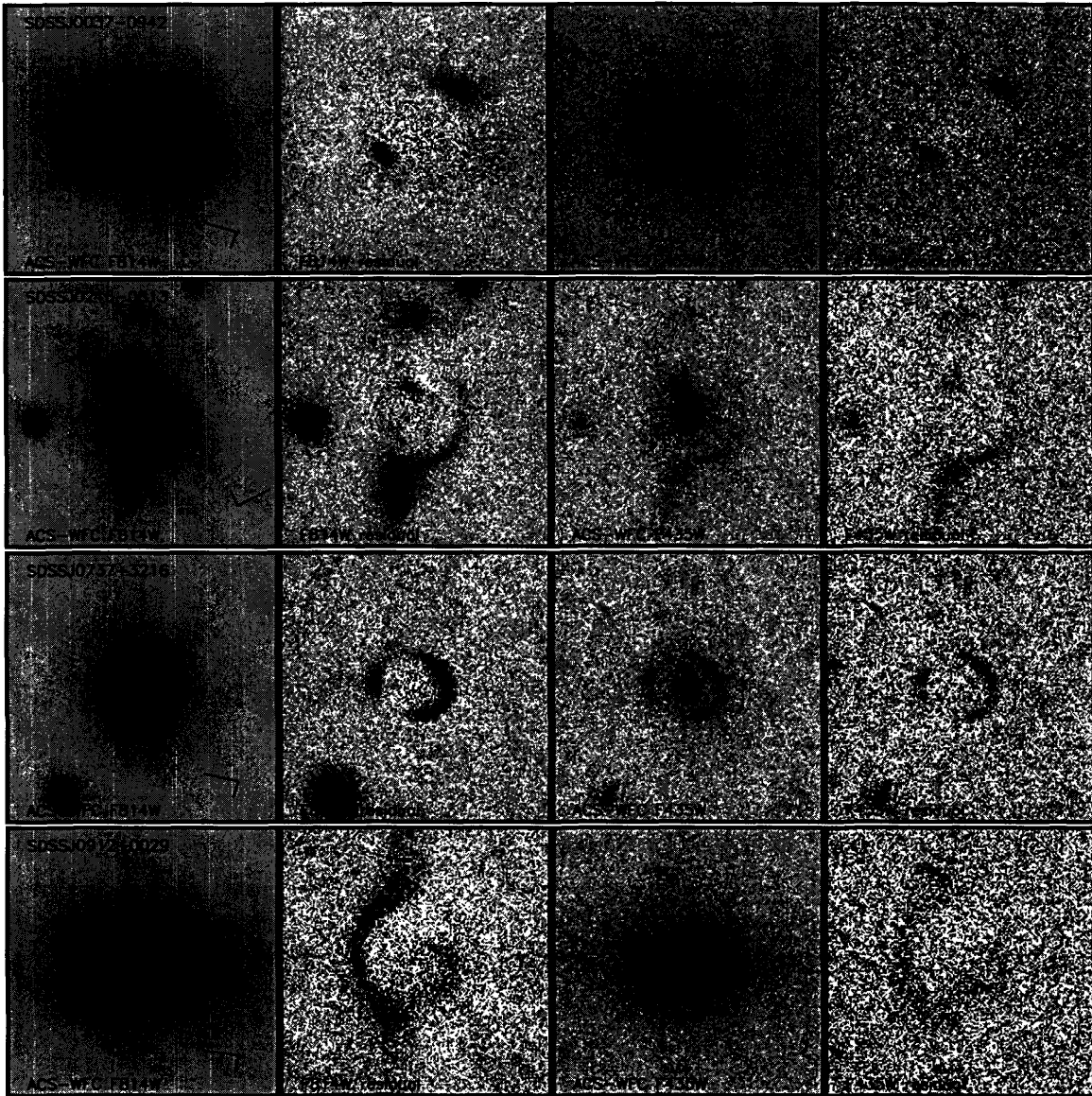


Figure E-1: HST ACS-WFC F814W and F435W imaging of new gravitational lenses from the SLACS survey. Also shown are residual images with smooth b-spline lens-galaxy models subtracted, revealing lensed features more clearly. Images are formed from flat-fielded single-image native ACS data. Cosmic-ray and other zero-weight pixels are replaced with values from a median-smoothed residual image, with the b-spline model galaxy values added for the direct images. Images are $8'' \times 8''$; cardinal directions are slightly non-orthogonal due to distortion in the ACS.

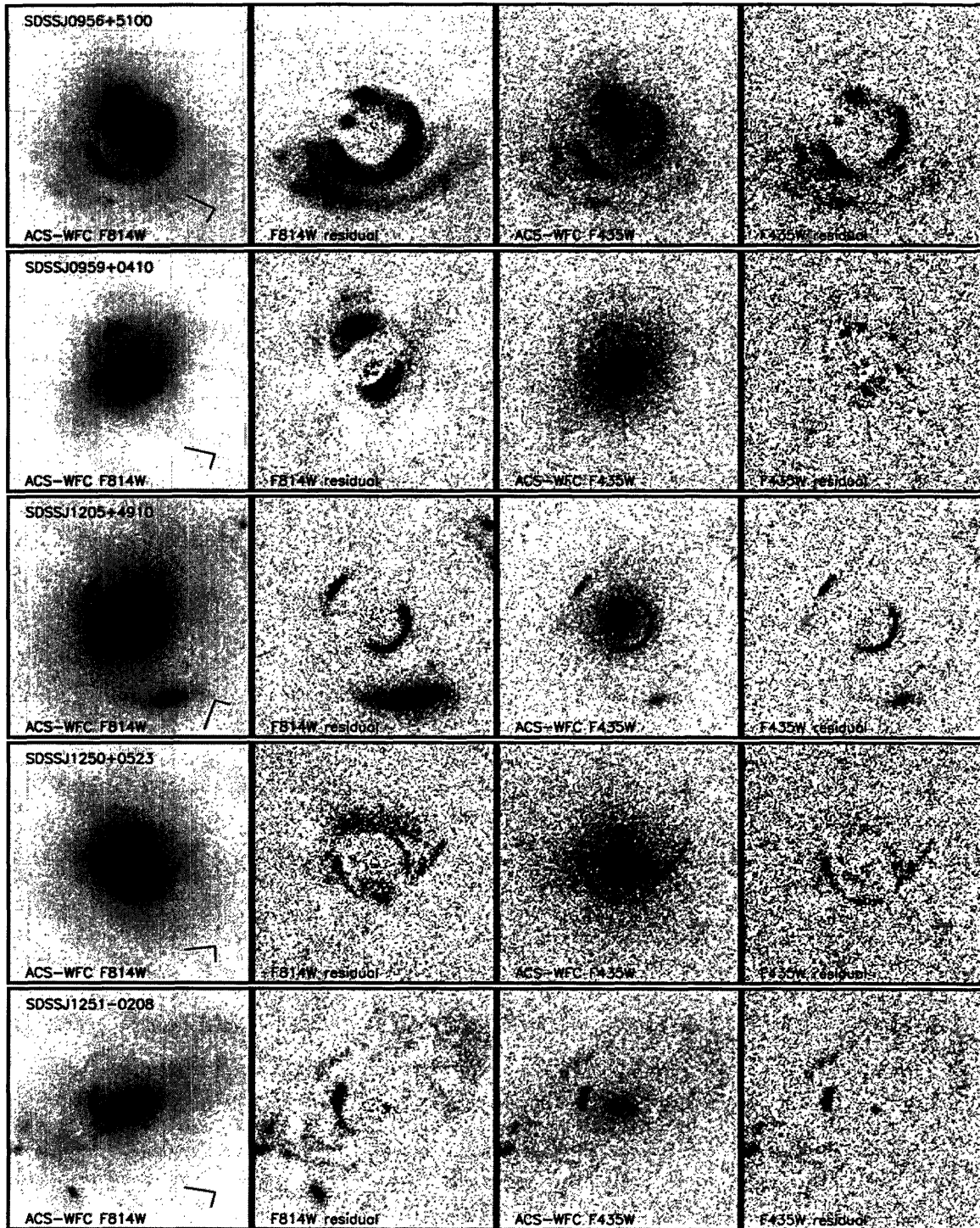


Figure E-1: (continued)

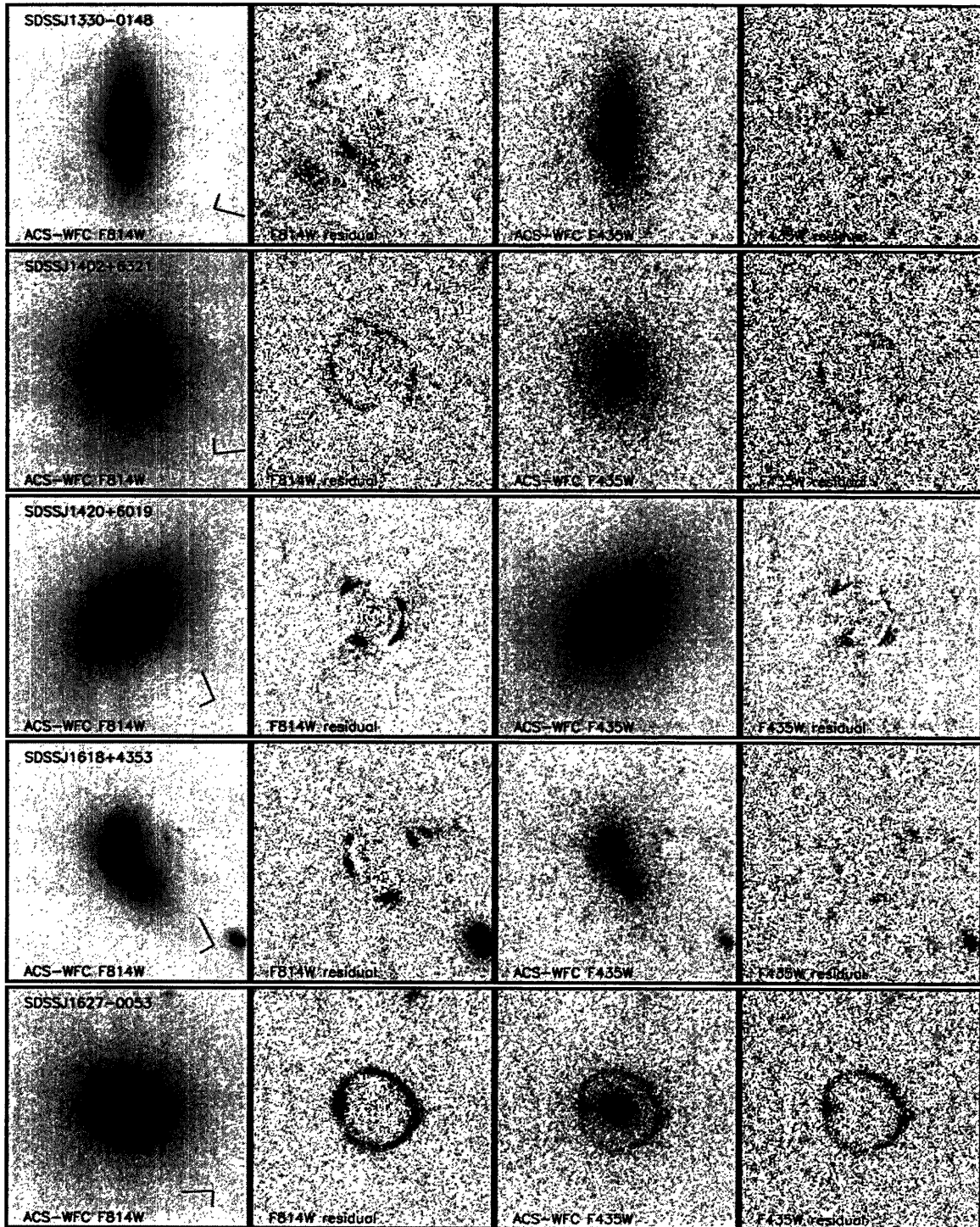


Figure E-1: (continued)

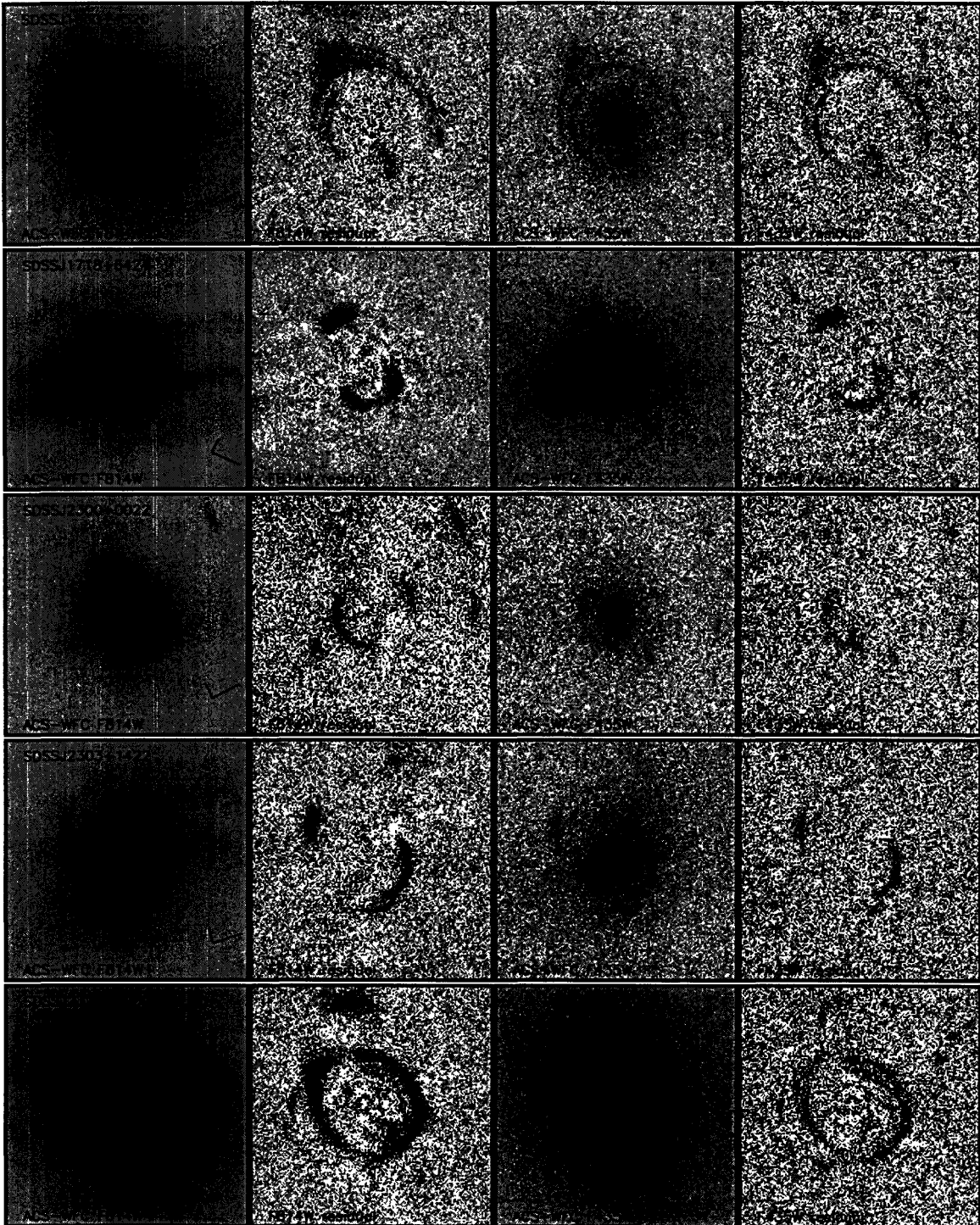


Figure E-1: (continued)

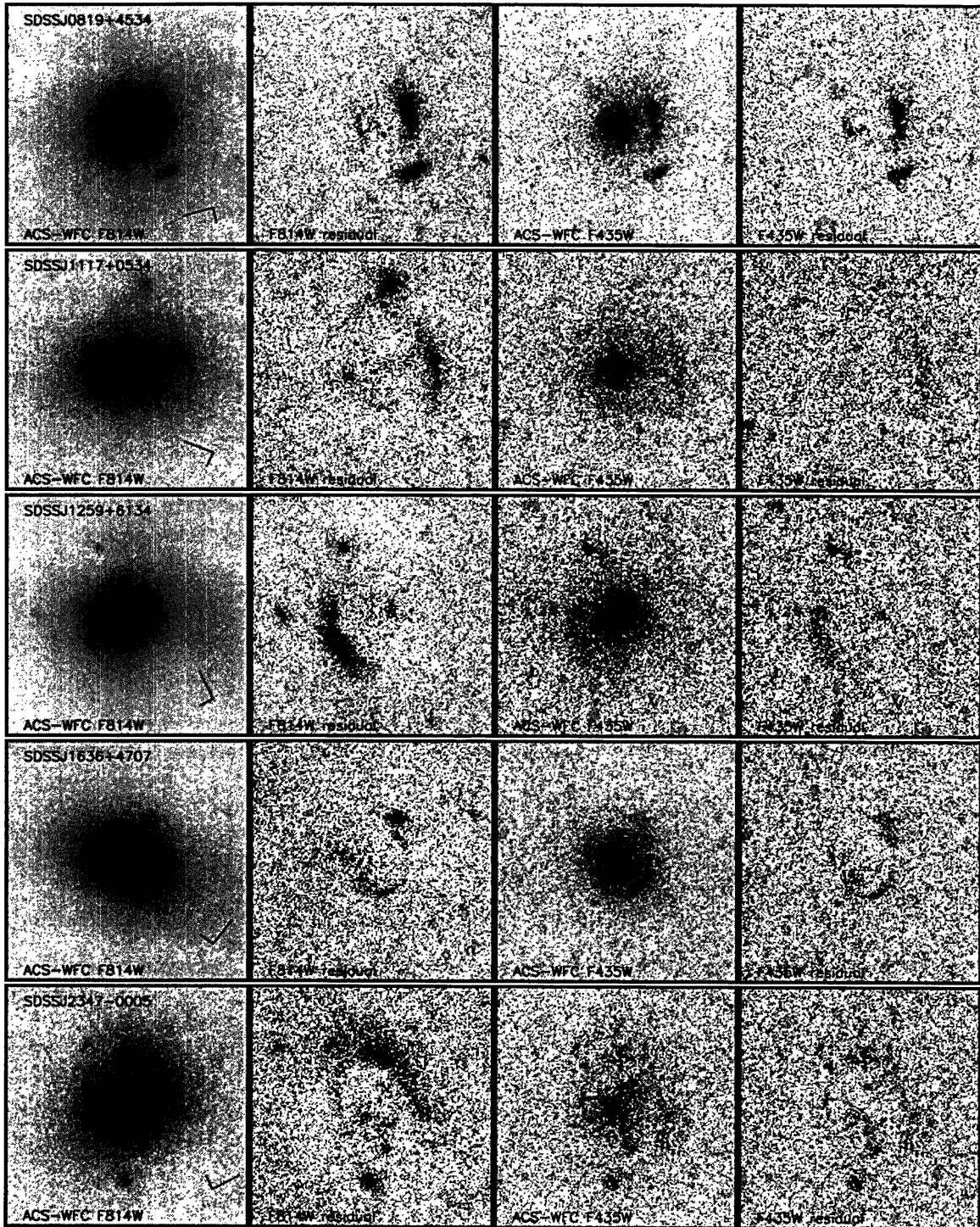


Figure E-2: *HST* ACS-WFC imaging of questionable gravitational lenses from the SLACS survey. Images are as in Figure E-1.

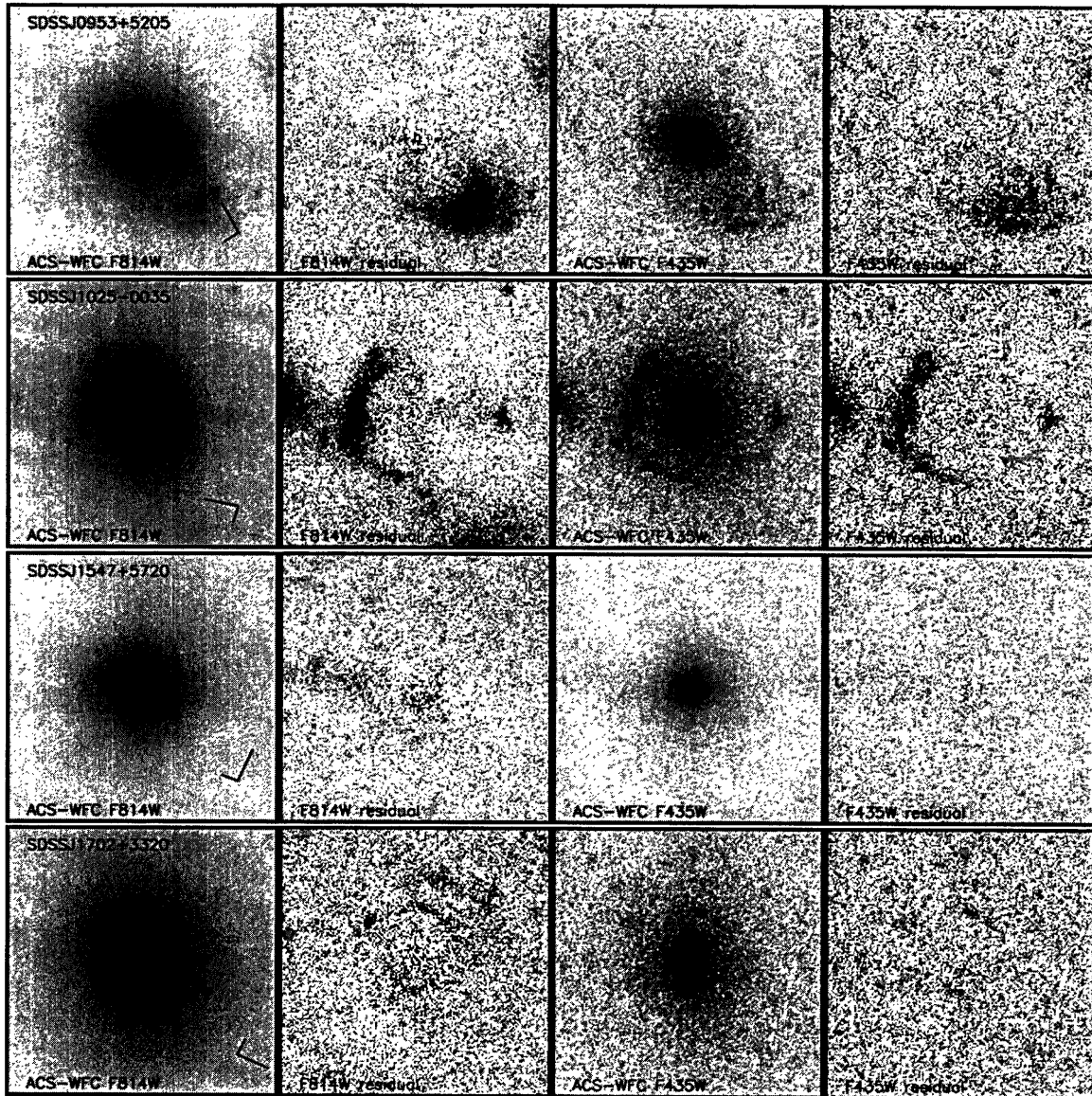


Figure E-3: *HST* ACS-WFC imaging of non-lenses and non-detections from the SLACS survey. Images are as in Figure E-1.

Bibliography

- K. Abazajian et al. The First Data Release of the Sloan Digital Sky Survey. *AJ*, 126: 2081–2086, October 2003.
- J. Allington-Smith et al. Integral Field Spectroscopy with the Gemini Multiobject Spectrograph. I. Design, Construction, and Testing. *PASP*, 114:892–912, August 2002.
- R. Barkana. Fast Calculation of a Family of Elliptical Mass Gravitational Lens Models. *ApJ*, 502:531, August 1998.
- C. M. Baugh, S. Cole, and C. S. Frenk. Evolution of the Hubble sequence in hierarchical models for galaxy formation. *MNRAS*, 283:1361–1378, December 1996.
- M. Bernardi et al. Early-Type Galaxies in the Sloan Digital Sky Survey. III. The Fundamental Plane. *AJ*, 125:1866–1881, April 2003.
- B. C. Bigelow and A. M. Dressler. IMACS, the multiobject spectrograph and imager for Magellan: a status report. In *Instrument Design and Performance for Optical/Infrared Ground-based Telescopes*. Edited by Iye, Masanori; Moorwood, Alan F. M. *Proceedings of the SPIE, Volume 4841*, pp. 1727–1738 (2003)., pages 1727–1738, March 2003.
- J. Binney. The radius-dependence of velocity dispersion in elliptical galaxies. *MNRAS*, 190: 873–880, March 1980.
- J. Binney and S. Tremaine. *Galactic dynamics*. Princeton, NJ, Princeton University Press, 1987, 747 p., 1987.
- M. R. Blanton, H. Lin, R. H. Lupton, F. M. Maley, N. Young, I. Zehavi, and J. Loveday. An Efficient Targeting Strategy for Multiobject Spectrograph Surveys: the Sloan Digital Sky Survey “Tiling” Algorithm. *AJ*, 125:2276–2286, April 2003.
- G. R. Blumenthal, S. M. Faber, R. Flores, and J. R. Primack. Contraction of dark matter galactic halos due to baryonic infall. *ApJ*, 301:27–34, February 1986.
- A. S. Bolton, S. Burles, L. V. E. Koopmans, T. Treu, and L. A. Moustakas. SDSS J140228.22+632133.3: A new spectroscopically selected gravitational lens. *ApJ*, 624: L21–L24, 2005.
- A. S. Bolton, S. Burles, D. J. Schlegel, D. J. Eisenstein, and J. Brinkmann. Sloan Digital Sky Survey Spectroscopic Lens Search. I. Discovery of Intermediate-Redshift Star-forming Galaxies behind Foreground Luminous Red Galaxies. *AJ*, 127:1860–1882, April 2004.
- U. Borgeest, J. von Linde, and S. Refsdal. The double magnification bias by gravitational lensing. *A&A*, 251:L35–L38, November 1991.

- I. W. A. Browne et al. The Cosmic Lens All-Sky Survey - II. Gravitational lens candidate selection and follow-up. *MNRAS*, 341:13–32, May 2003.
- S. Burles, D. J. Eisenstein, P. B. Hall, D. J. Schlegel, and SDSS Collaboration. Serendipitous Emission Lines in the Sloan Digital Sky Survey. *Bulletin of the American Astronomical Society*, 32:1423, December 2000.
- M. Chiba. Probing Dark Matter Substructure in Lens Galaxies. *ApJ*, 565:17–23, January 2002.
- L. Ciotti. Stellar systems following the $R \propto 1/m$ luminosity law. *A&A*, 249:99–106, September 1991.
- D. Crampton, D. Schade, F. Hammer, A. Matzkin, S. J. Lilly, and O. Le Fèvre. The Gravitational Lens CFRS 03.1077. *ApJ*, 570:86–91, May 2002.
- N. Dalal and C. S. Kochanek. Direct Detection of Cold Dark Matter Substructure. *ApJ*, 572:25–33, June 2002.
- C. de Boor. Package for calculating with B-splines. *SIAM Journal on Numerical Analysis*, 14(3):441–472, June 1977.
- S. Djorgovski and M. Davis. Fundamental properties of elliptical galaxies. *ApJ*, 313:59–68, February 1987.
- A. Dressler, D. Lynden-Bell, D. Burstein, R. L. Davies, S. M. Faber, R. Terlevich, and G. Wegner. Spectroscopy and photometry of elliptical galaxies. I - A new distance estimator. *ApJ*, 313:42–58, February 1987.
- I. Drozdovsky et al. The HST/ACS Grism Parallel Survey: II. First Results and a Catalog of Faint Emission-Line Galaxies at $z < 1.6$. *AJ*, in press (*astro-ph/0503592*), 2005.
- S. Dye and S. J. Warren. Decomposition of the Visible and Dark Matter in the Einstein Ring 0047-2808 by Semilinear Inversion. *ApJ*, 623:31–41, April 2005.
- D. J. Eisenstein et al. Spectroscopic Target Selection for the Sloan Digital Sky Survey: The Luminous Red Galaxy Sample. *AJ*, 122:2267–2280, November 2001.
- D. J. Eisenstein et al. Average Spectra of Massive Galaxies in the Sloan Digital Sky Survey. *ApJ*, 585:694–713, March 2003.
- N. W. Evans and H. J. Witt. Fitting gravitational lenses: truth or delusion. *MNRAS*, 345:1351–1364, November 2003.
- C. D. Fassnacht, L. A. Moustakas, S. Casertano, H. C. Ferguson, R. A. Lucas, and Y. Park. Strong Gravitational Lens Candidates in the GOODS ACS Fields. *ApJ*, 600:L155–L158, January 2004.
- M. Fukugita, T. Ichikawa, J. E. Gunn, M. Doi, K. Shimasaku, and D. P. Schneider. The Sloan Digital Sky Survey Photometric System. *AJ*, 111:1748, April 1996.
- O. Gerhard, A. Kronawitter, R. P. Saglia, and R. Bender. Dynamical Family Properties and Dark Halo Scaling Relations of Giant Elliptical Galaxies. *AJ*, 121:1936–1951, April 2001.

- M. V. Gorenstein, I. I. Shapiro, and E. E. Falco. Degeneracies in parameter estimates for models of gravitational lens systems. *ApJ*, 327:693–711, April 1988.
- J. E. Gunn et al. The Sloan Digital Sky Survey Photometric Camera. *AJ*, 116:3040–3081, December 1998.
- P. B. Hall, H. K. C. Yee, H. Lin, S. L. Morris, M. D. Gladders, R. G. Carlberg, D. R. Patton, M. Sawicki, C. W. Shepherd, and G. D. Wirth. Spectroscopic Gravitational Lens Candidates in the CNOC2 Field Galaxy Redshift Survey. *AJ*, 120:1660–1667, October 2000.
- P. C. Hewett, M. J. Irwin, P. Bunclark, M. T. Bridgeland, E. J. Kibblewhite, X. T. He, and M. G. Smith. Automated analysis of objective-prism spectra. I - Quasar detection. *MNRAS*, 213:971–989, April 1985.
- P. C. Hewett, S. J. Warren, J. P. Willis, J. Bland-Hawthorn, and G. F. Lewis. High-Redshift Gravitationally Lensed Galaxies and Tunable Filter Imaging. In *ASP Conf. Ser. 195: Imaging the Universe in Three Dimensions*, page 94, 2000.
- H. Hippelein, C. Maier, K. Meisenheimer, C. Wolf, J. W. Fried, B. von Kuhlmann, M. Kümmel, S. Phleps, and H.-J. Röser. Star forming rates between $z = 0.25$ and $z = 1.2$ from the CADIS emission line survey. *A&A*, 402:65–78, April 2003.
- H. Hoekstra, H. K. C. Yee, and M. D. Gladders. Properties of Galaxy Dark Matter Halos from Weak Lensing. *ApJ*, 606:67–77, May 2004.
- D. W. Hogg, J. G. Cohen, R. Blandford, and M. A. Pahre. The O II Luminosity Density of the Universe. *ApJ*, 504:622, September 1998.
- D. W. Hogg, D. P. Finkbeiner, D. J. Schlegel, and J. E. Gunn. A Photometricity and Extinction Monitor at the Apache Point Observatory. *AJ*, 122:2129–2138, October 2001.
- G. P. Holder and P. L. Schechter. External Shear in Quadruply Imaged Lens Systems. *ApJ*, 589:688–692, June 2003.
- I. Hook et al. Gemini-north multiobject spectrograph integration, test, and commissioning. In *Instrument Design and Performance for Optical/Infrared Ground-based Telescopes. Edited by Iye, Masanori; Moorwood, Alan F. M. Proceedings of the SPIE, Volume 4841, pp. 1645-1656 (2003).*, pages 1645–1656, March 2003.
- K. Horne. An optimal extraction algorithm for CCD spectroscopy. *PASP*, 98:609–617, June 1986.
- J. Huchra, M. Gorenstein, S. Kent, I. Shapiro, G. Smith, E. Horine, and R. Perley. 2237 + 0305 - A new and unusual gravitational lens. *AJ*, 90:691–696, May 1985.
- D. E. Johnston et al. SDSS J090334.92+502819.2: A New Gravitational Lens. *AJ*, 126: 2281–2290, November 2003.
- I. Jorgensen, M. Franx, and P. Kjaergaard. Spectroscopy for E and S0 galaxies in nine clusters. *MNRAS*, 276:1341–1364, October 1995.
- A. Kassiola and I. Kovner. Elliptic Mass Distributions versus Elliptic Potentials in Gravitational Lenses. *ApJ*, 417:450, November 1993.

- G. Kauffmann, S. D. M. White, and B. Guiderdoni. The Formation and Evolution of Galaxies Within Merging Dark Matter Haloes. *MNRAS*, 264:201, September 1993.
- C. R. Keeton. Lensing and the Centers of Distant Early-Type Galaxies. *ApJ*, 582:17–29, January 2003.
- C. R. Keeton and C. S. Kochanek. Gravitational Lensing by Spiral Galaxies. *ApJ*, 495:157, March 1998.
- C. R. Keeton and A. I. Zabludoff. The Importance of Lens Galaxy Environments. *ApJ*, 612:660–678, September 2004.
- D. D. Kelson. Optimal Techniques in Two-dimensional Spectroscopy: Background Subtraction for the 21st Century. *PASP*, 115:688–699, June 2003.
- C. S. Kochanek. Gravitational lenses in redshift surveys. *ApJ*, 397:381–389, October 1992.
- C. S. Kochanek. The dynamics of luminous galaxies in isothermal halos. *ApJ*, 436:56–66, November 1994.
- C. S. Kochanek. Gravitational Lens Time Delays in Cold Dark Matter. *ApJ*, 583:49–57, January 2003.
- C. S. Kochanek. The Saas Fee Lectures on Strong Gravitational Lensing. In *Kochanek, C.S., Schneider, P., Wambsganss, J., 2004, Part 2 of Gravitational Lensing: Strong, Weak & Micro, Proceedings of the 33rd Saas-Fee Advanced Course, G. Meylan, P. Jetzer & P. North, eds. (Springer-Verlag: Berlin), 2004a.*
- C. S. Kochanek. Where Does The Dark Matter Begin? In *The Impact of Gravitational Lensing on Cosmology (IAU 225), Y. Mellier and G. Meylan, eds. (astro-ph/0412089), 2004b.*
- C. S. Kochanek, R. D. Blandford, C. R. Lawrence, and R. Narayan. The ring cycle - an iterative lens reconstruction technique applied to MG1131+0456. *MNRAS*, 238:43–56, May 1989.
- C. S. Kochanek et al. The Fundamental Plane of Gravitational Lens Galaxies and The Evolution of Early-Type Galaxies in Low-Density Environments. *ApJ*, 543:131–148, November 2000.
- C. S. Kochanek, C. R. Keeton, and B. A. McLeod. The Importance of Einstein Rings. *ApJ*, 547:50–59, January 2001.
- C. S. Kochanek and R. Narayan. LensClean - an algorithm for inverting extended, gravitationally lensed images with application to the radio ring lens PKS 1830-211. *ApJ*, 401:461–473, December 1992.
- L. V. E. Koopmans and T. Treu. The Stellar Velocity Dispersion of the Lens Galaxy in MG 2016+112 at $z=1.004$. *ApJ*, 568:L5–L8, March 2002.
- L. V. E. Koopmans and T. Treu. The Structure and Dynamics of Luminous and Dark Matter in the Early-Type Lens Galaxy of 0047-281 at $z = 0.485$. *ApJ*, 583:606–615, February 2003.

- R. Kormann, P. Schneider, and M. Bartelmann. Isothermal elliptical gravitational lens models. *A&A*, 284:285–299, April 1994.
- S. Kotz, T. J. Kozubowski, and K. Podgórski. *The Laplace Distribution and Generalizations: A Revisit with Applications to Communications, Economics, Engineering, and Finance*. Boston: Birkhäuser, 2001.
- A. Kronawitter, R. P. Saglia, O. Gerhard, and R. Bender. Orbital structure and mass distribution in elliptical galaxies. *A&AS*, 144:53–84, May 2000.
- G. I. Langston, S. R. Conner, J. Lehar, B. F. Burke, and K. W. Weiler. Galaxy mass deduced from the structure of Einstein ring MG1654 + 1346. *Nature*, 344:43–45, March 1990.
- L. Li and J. P. Ostriker. Semianalytical Models for Lensing by Dark Halos. I. Splitting Angles. *ApJ*, 566:652–666, February 2002.
- M. Loewenstein and R. E. White. Prevalence and Properties of Dark Matter in Elliptical Galaxies. *ApJ*, 518:50–63, June 1999.
- R. H. Lupton, J. E. Gunn, Z. Ivezić, G. R. Knapp, S. Kent, and N. Yasuda. The SDSS Imaging Pipelines. In *ASP Conf. Ser. 238: Astronomical Data Analysis Software and Systems X*, page 269, 2001.
- O. Möller, P. Hewett, and A. W. Blain. Discs in early-type lensing galaxies: effects on magnification ratios and measurements of H_0 . *MNRAS*, 345:1–15, October 2003.
- C. Maier, K. Meisenheimer, E. Thommes, H. Hippelein, H. J. Röser, J. Fried, B. von Kuhlmann, S. Phleps, and C. Wolf. Constraints to the evolution of Ly-alpha bright galaxies between $z = 3$ and $z = 6$. *A&A*, 402:79–85, April 2003.
- S. Mao and P. Schneider. Evidence for substructure in lens galaxies? *MNRAS*, 295:587, April 1998.
- Y. Mellier and G. Mathez. Deprojection of the de Vaucouleurs $R \exp 1/4$ brightness profile. *A&A*, 175:1–2, March 1987.
- R. B. Metcalf and P. Madau. Compound Gravitational Lensing as a Probe of Dark Matter Substructure within Galaxy Halos. *ApJ*, 563:9–20, December 2001.
- J. Miralda-Escude and J. Lehar. Optical rings - A large number of gravitational lenses? *MNRAS*, 259:31P–34P, December 1992.
- B. Moore, F. Governato, T. Quinn, J. Stadel, and G. Lake. Resolving the Structure of Cold Dark Matter Halos. *ApJ*, 499:L5, May 1998.
- J. J. Moré and S. J. Wright. *SIAM Frontiers in Applied Mathematics 14: Optimization Software Guide*. Society for Industrial and Applied Mathematics, 1993.
- D. J. Mortlock and R. L. Webster. Using galaxy redshift surveys to detect gravitationally lensed quasars. *MNRAS*, 319:879–892, December 2000.
- D. J. Mortlock and R. L. Webster. Using the 2 degree Field galaxy redshift survey to detect gravitationally lensed quasars. *MNRAS*, 321:629–641, March 2001.

- D. C. Morton. Atomic data for resonance absorption lines. I - Wavelengths longward of the Lyman limit. *ApJS*, 77:119–202, September 1991.
- S. T. Myers et al. The Cosmic Lens All-Sky Survey - I. Source selection and observations. *MNRAS*, 341:1–12, May 2003.
- N. R. Napolitano et al. Mass-to-light ratio gradients in early-type galaxy haloes. *MNRAS*, 357:691–706, February 2005.
- R. Narayan. Gravitational lensing and quasar-galaxy correlations. *ApJ*, 339:L53–L56, April 1989.
- R. Narayan and M. Bartelmann. Lectures on Gravitational Lensing. *astro-ph/9606001*, 1996.
- J. F. Navarro, C. S. Frenk, and S. D. M. White. The Structure of Cold Dark Matter Halos. *ApJ*, 462:563, May 1996.
- N. Padmanabhan et al. Stellar and dynamical masses of ellipticals in the Sloan Digital Sky Survey. *New Astronomy*, 9:329–342, June 2004.
- C. Y. Peng, L. C. Ho, C. D. Impey, and H. Rix. Detailed Structural Decomposition of Galaxy Images. *AJ*, 124:266–293, July 2002.
- J. R. Pier, J. A. Munn, R. B. Hindsley, G. S. Hennessy, S. M. Kent, R. H. Lupton, and Ž. Ivezić. Astrometric Calibration of the Sloan Digital Sky Survey. *AJ*, 125:1559–1579, March 2003.
- W. K. Pratt. *Digital Image Processing*. Ney York: John Wiley & Sons, 1978.
- W. H. Press, S. A. Teukolsky, W. T. Vetterling, and B. P. Flannery. *Numerical recipes in FORTRAN. The art of scientific computing*. Cambridge: University Press, —c1992, 2nd ed., 1992.
- P. Prugniel and C. Soubiran. A database of high and medium-resolution stellar spectra. *A&A*, 369:1048–1057, April 2001.
- K. U. Ratnatunga, R. E. Griffiths, and E. J. Ostrander. The Top 10 List of Gravitational Lens Candidates from the HUBBLE SPACE TELESCOPE Medium Deep Survey. *AJ*, 117:2010–2023, May 1999.
- A. J. Romanowsky, N. G. Douglas, M. Arnaboldi, K. Kuijken, M. R. Merrifield, N. R. Napolitano, M. Capaccioli, and K. C. Freeman. A Dearth of Dark Matter in Ordinary Elliptical Galaxies. *Science*, 301:1696–1698, September 2003.
- A. J. Romanowsky and C. S. Kochanek. Dynamics of Stars and Globular Clusters in M87. *ApJ*, 553:722–732, June 2001.
- D. Rusin, C. S. Kochanek, E. E. Falco, C. R. Keeton, B. A. McLeod, C. D. Impey, J. Lehár, J. A. Muñoz, C. Y. Peng, and H.-W. Rix. The Evolution of a Mass-selected Sample of Early-Type Field Galaxies. *ApJ*, 587:143–159, April 2003a.
- D. Rusin, C. S. Kochanek, and C. R. Keeton. Self-similar Models for the Mass Profiles of Early-Type Lens Galaxies. *ApJ*, 595:29–42, September 2003b.

- D. Rusin and C. Ma. Constraints on the Inner Mass Profiles of Lensing Galaxies from Missing Odd Images. *ApJ*, 549:L33–L37, March 2001.
- P. Saha. Lensing Degeneracies Revisited. *AJ*, 120:1654–1659, October 2000.
- P. Saha and L. L. R. Williams. Qualitative Theory for Lensed QSOs. *AJ*, 125:2769–2782, June 2003.
- P. L. Schechter, G. S. Burley, C. L. Hull, M. Johns, H. M. Martin, S. Schaller, S. A. Shectman, and S. C. West. Active optics on the Baade 6.5-m (Magellan I) Telescope. In *Large Ground-based Telescopes. Edited by Oschmann, Jacobus M.; Stepp, Larry M. Proceedings of the SPIE, Volume 4837, pp. 619-627 (2003).*, pages 619–627, February 2003.
- P. L. Schechter and J. Wambsganss. Quasar Microlensing at High Magnification and the Role of Dark Matter: Enhanced Fluctuations and Suppressed Saddle Points. *ApJ*, 580: 685–695, December 2002.
- D. J. Schlegel, D. P. Finkbeiner, and M. Davis. Maps of Dust Infrared Emission for Use in Estimation of Reddening and Cosmic Microwave Background Radiation Foregrounds. *ApJ*, 500:525, June 1998.
- J. Schmoll, G. N. Dodsworth, R. Content, and J. R. Allington-Smith. Design and construction of the IMACS-IFU: a 2000-element integral field unit. In *UV and Gamma-Ray Space Telescope Systems. Edited by Hasinger, Günther; Turner, Martin J. L. Proceedings of the SPIE, Volume 5492, pp. 624-633 (2004).*, pages 624–633, September 2004.
- T. Schramm. Realistic elliptical potential wells for gravitational lens models. *A&A*, 231: 19–24, May 1990.
- J. L. Sersic. *Atlas de galaxias australes*. Cordoba, Argentina: Observatorio Astronomico, 1968, 1968.
- R. K. Sheth et al. The Velocity Dispersion Function of Early-Type Galaxies. *ApJ*, 594: 225–231, September 2003.
- J. A. Smith et al. The u'g'r'i'z' Standard-Star System. *AJ*, 123:2121–2144, April 2002.
- C. Stoughton et al. Sloan Digital Sky Survey: Early Data Release. *AJ*, 123:485–548, January 2002.
- M. A. Strauss et al. Spectroscopic Target Selection in the Sloan Digital Sky Survey: The Main Galaxy Sample. *AJ*, 124:1810–1824, September 2002.
- T. Treu and L. V. E. Koopmans. The Internal Structure and Formation of Early-Type Galaxies: The Gravitational Lens System MG 2016+112 at $z = 1.004$. *ApJ*, 575:87–94, August 2002.
- T. Treu and L. V. E. Koopmans. The redshift of the Einstein ring in MG 1549+305. *MNRAS*, 343:L29–L32, August 2003.
- T. Treu and L. V. E. Koopmans. Massive Dark Matter Halos and Evolution of Early-Type Galaxies to $z \sim 1$. *ApJ*, 611:739–760, August 2004.

- E. L. Turner, J. P. Ostriker, and J. R. Gott. The statistics of gravitational lenses - The distributions of image angular separations and lens redshifts. *ApJ*, 284:1–22, September 1984.
- J. A. Tyson, G. P. Kochanski, and I. P. dell’Antonio. Detailed Mass Map of CL 0024+1654 from Strong Lensing. *ApJ*, 498:L107, May 1998.
- M. Viton and B. Milliard. Two-dimensional Analytical Modeling of Distortion and Sky Background in Multifiber Spectrographs: The Case of the Norris Spectrograph at Palomar Mountain. *PASP*, 115:243–254, February 2003.
- S. J. Warren and S. Dye. Semilinear Gravitational Lens Inversion. *ApJ*, 590:673–682, June 2003.
- S. J. Warren, P. C. Hewett, G. F. Lewis, P. Moller, A. Iovino, and P. A. Shaver. A candidate optical Einstein ring. *MNRAS*, 278:139–145, January 1996.
- J. P. Willis. A spectroscopic survey for gravitational lenses. *The Observatory*, 120:427–428, December 2000.
- H. J. Witt, S. Mao, and P. L. Schechter. On the universality of microlensing in quadruple gravitational lenses. *ApJ*, 443:18–28, April 1995.
- D. G. York et al. The Sloan Digital Sky Survey: Technical Summary. *AJ*, 120:1579–1587, September 2000.